ORNL-6430

ornl

OAK RIDGE NATIONAL LABORATORY

MARTIN MARIETTA

Microstructural Evolution in Fast-Neutron-Irradiated Austenitic Stainless Steels

R. E. Stoller

OPERATED BY
MARTIN MARIETTA ENERGY SYSTEMS, INC.
FOR THE UNITED STATES
DEPARTMENT OF ENERGY

Printed in the United States of America. Available from
National Technical Information Service
U.S. Department of Commerce
5285 Port Royal Road, Springfield, Virginia 22161
NTIS price codes—Printed Copy: A17 Microfiche A01

ORNL-6430
Distribution
Category UC-25

Metals and Ceramics Division

MICROSTRUCTURAL EVOLUTION IN FAST-NEUTRON-IRRADIATED AUSTENITIC STAINLESS STEELS

R. E. Stoller

Date Published: December 1987

Prepared for the
MFE - Reactor Materials
AT 15 02 03 A

Prepared by the
OAK RIDGE NATIONAL LABORATORY
Oak Ridge, Tennessee 37831
operated by
MARTIN MARIETTA ENERGY SYSTEMS, INC.
for the
U.S. DEPARTMENT OF ENERGY
under Contract DE-AC05-84OR21400

TABLE OF CONTENTS

Contents (contd.)

Contents (contd.)

LIST OF FIGURES

Figure List (contd.)

Figure List (contd.)

Figure List (contd.)

FIGURE Page

Figure list (contd.)

FIGURE Page

Figure list (contd.)

Figure list (contd.)

Figure list (contd.)

FIGURE Page

Figure list (contd.)

LIST OF TABLES

Table List (contd.)

ACKNOWLEDGMENTS

The completion of this dissertation was made possible by the assistance of many people. The contributions of my doctoral committee Professors G. R. Odette, G. E. Lucas and C. G. Levi are gratefully acknowledged. My major research advisor, Dr. Odette, was responsible for stimulating my interest in radiation effects while I was still an undergraduate and his guidance and support were essential to this work. Dr. Lucas participated in many helpful discussions and provided some much needed comic relief at key times along the way. Technical support for this work at the University of California, Santa Barbara, was provided by Robert Lynch and Douglas Klingensmith.

During the time that I have been working in the Defect Mechanisms Group in the Metals and Ceramics Division at the Oak Ridge National Laboratory, I have had the benefit of the experience of my coworkers. I have enjoyed many productive discussions with Dr. L. K. Mansur on the theoretical aspects of this work. Discussions with Drs. D. F. Pedraza of ORNL, W. A. Coghlan of Arizona State University and A. D. Brailsford of Ford Motor Company have also been helpful. Dr. P. J. Maziasz invested a significant amount of time to provide me with some of my initial instruction in the use of the transmission electron microscope. Drs. J. Bentley, E. A. Kenik, P. S. Sklad and S. J. Zinkle provided further advice and assistance with those aspects of the work that involved transmission electron microscopy.

The technical support provided by C.H.K. DuBose, A. T. Fisher, J. W. Jones, H. R. Livesey, G. C. Marsh, N. H. Rouse and L. J. Turner at ORNL has been much appreciated. A special thanks is due to Frances Scarboro for the excellent job that she did typing and editing this dissertation.

Finally, I wish to acknowledge the patient support of my wife Robin, our families and many friends during the time that this work was in progress. Without their prayers and encouragement this work might never have been completed.

The financial support for this work was provided by the United States Department of Energy under: the Magnetic Fusion Energy Technology Fellowship Program administered by Oak Ridge Associated Universities, contract AM03-765F00034 with the University of California at Santa Barbara, and contract DE-AC05-840R21400 with the Martin Marietta Energy Systems, Inc.

MICROSTRUCTURAL EVOLUTION IN FAST-NEUTRON-IRRADIATED AUSTENITIC STAINLESS STEELS

R. E. Stoller

ABSTRACT

The general field of neutron irradiation effects is very broad. The present work has focused on the specific problem of fast-neutron-induced radiation damage to austenitic stainless steels. These steels are used as structural materials in current fast fission reactors and are proposed for use in future fusion reactors. Two primary components of the radiation damage are atomic displacements (in units of displacements per atom, or dpa) and the generation of helium by nuclear transmutation reactions. The radiation environment can be characterized by the ratio of helium to displacement production, the so-called He/dpa ratio. Radiation damage is evidenced microscopically by a complex microstructural evolution and macroscopically by density changes and altered mechanical properties. The purpose of this work was to provide additional understanding about mechanisms that determine microstructural evolution in current fast reactor environments and to identify the sensitivity of this evolution to changes in the He/dpa ratio. This latter sensitivity is of interest because the He/dpa ratio in a fusion reactor first wall will be about 30 times that in fast reactor fuel cladding.

The approach followed in the present work was to use a combination of theoretical and experimental analysis. The experimental component of the work primarily involved the examination by transmission electron microscopy of specimens of a model austenitic alloy that had been irradiated in the Oak Ridge Research Reactor. Some of these specimens had been implanted with helium and subsequently annealed at various temperatures prior to irradiation. The as-implanted-and-aged microstructures were also characterized. A major aspect of the theoretical work was the development of a comprehensive model of microstructural evolution. This included explicit models for the evolution of the major extended defects observed in neutron irradiated steels: cavities, Frank faulted loops and the dislocation network.

The results of this study indicate that the various extended defects evolve in a highly coupled manner. Both the theory and the experimental work indicate a significant infuence of helium on microstructural evolution. In particular, the theory predicts that near peak swelling may occur for the fusion He/dpa ratio due to reduced swelling incubation times. Other recent experimental data due to reduced swelling incubation times. Other recent experimental data tend to corroborate this prediction. A significant new experimental observation was that large stacking fault tetrahedra were formed in the model austenitic alloy after irradiation to 4.7 dpa at 550 and 600°C.

CHAPTER 1

INTRODUCTION

The purpose of the work described here is to provide additional understanding about the effects of fast (i.e., with greater than about 0.1 MeV of kinetic energy) neutron irradiation of austenitic stainless steels. This topic is of interest because the use of two of the four energy sources which have been identified as offering the potential for an "indefinitely sustainable" energy supply[1] — nuclear fission with breeding and controlled thermonuclear fusion of deuterium and tritium (DT) — will result in the production of fast neutrons. Components in both fast fission and DT fusion reactors will therefore be exposed to and damaged by these neutrons. This work focuses on austenitic stainless steels because they have already been extensively used in early fast breeder reactors[2,3] and are proposed for use in near-term fusion reactors.[4-6]

The general topic of this work is the microstructural changes that occur when austenitic stainless steels are exposed to fast neutrons. This radiation damage has two major components. The first is the displacement of the constituent atoms of the steel. This occurs primarily as a result of elastic collisions between these atoms and either the neutrons themselves or other energetic displaced atoms. The second component is the transmutation of the constituent atoms by nuclear reactions. The radiation damage which will occur in the

structural first wall of a DT fusion reactor is quite similar to that which occurs in fast reactor fuel cladding; however, there are a few differences between the two environments which confound direct comparisons. The principal difference is the presence of a flux peak at 14.1 MeV in the fusion neutron spectrum, while the fission spectrum has relatively few neutrons with energies greater than about 2 MeV. Since the (n,α) and (n,p) cross sections for many elements used in structural materials exhibit an energy threshold between 1 and 10 MeV, transmutant gas production in fusion reactor materials will exceed the value obtained in fission reactor irradiations by a factor of about 10 to 100. The transmutant helium is believed to be of particular significance and the work discussed below attempts to discern the implications of this helium on the extrapolation of the large radiation effects data base which has been generated in fission reactor experiments to fusion reactor conditions.

In addition to fast neutrons, nuclear fission and fusion also generate highly energetic charged particles. In the former case, the kinetic energy of the so-called fission fragments carry off about 80% of the approximately 200 MeV of energy which is released per fission while the prompt neutrons carry off only about 3%.[7] The range of the fission fragments is quite small, less than 1.0×10^{-4} m in the uranium (plutonium)-oxide fuel, while the range of the neutrons is about 0.1 to 1.0 m.[7] Since the diameter of a typical fast reactor fuel pellet is 5.0×10^{-3} m, only the neutrons significantly contribute

to the radiation damage of the cladding. In the case of a DT fusion reaction, about 17.6 MeV of kinetic energy is released. This is the most likely fusion reaction to be employed in first generation fusion reactors because the DT reaction has the lowest ignition temperature of the plausible alternatives.[8,9] The products of this reaction are an alpha particle and a neutron which carry off the kinetic energy which results from the mass defect. Using simple mass and energy conservation, one can show that the neutron will have 14.1 MeV and the alpha particle 3.5 MeV of kinetic energy. A neutron with 14.1 MeV of kinetic energy has a mean free path of about 4.5×10^{-2} m in stainless steel.[10] The radiation damage which results from the slowing down of these neutrons will therefore occur over relatively long distances in the reactor blanket structure. Because of their atomic charge of +2, the alpha particles with a peak energy of 3.5 MeV will largely lose their kinetic energy in collisions within the plasma. Those that escape the plasma will be stopped within about 6.0×10^{-6} m of the surface of the first wall facing the plasma.[11] This surface loading may cause erosion of the first wall by sputtering and blistering.[12] While these processes are probably not negligible in a DT fusion reactor with a stainless steel first wall, they do not appear to be limiting in determining the first wall lifetime.[8,13,14] Surface phenomena are described elsewhere[12,14,15] and will not be further considered in this work.

The approach of the present work was to couple experimental and theoretical analyses in order to obtain a more complete description of the factors which affect microstructural evolution. The experimental component of the work included examination by transmission electron microscopy (TEM) of a model austenitic alloy which had been neutron irradiated in the Oak Ridge Research Reactor (ORR). Some of these specimens had been preinjected with helium and subsequently annealed at various temperatures prior to irradiation. One purpose of this experiment was to determine the effect of the initial helium distribution on subsequent void swelling. The microstructures which resulted from helium injection and annealing were also characterized. A major aspect of the theoretical work was the development and use of a comprehensive rate-theory-based model of microstructural evolution. This model includes the explicit dose dependence of the major extended defects which evolve in fast neutron irradiated stainless steel: cavities, Frank faulted loops, and network dislocations. Simpler models were also used to explore the importance of parameters such as the critical cavity size for void formation.

CHAPTER 2

BACKGROUND AND LITERATURE SURVEY

Because of the broad engineering interest in the effects of fast neutron irradiation on structural materials, a substantial amount of research has been conducted in this area over the past twenty-five years. In addition to standard texts on this topic,[7,16,17] numerous international conferences have been held to discuss the ongoing research.[18] The details of the formation and evolution of the neutron-induced radiation damage microstructure are complex and are thoroughly discussed in the references just cited; the basic concepts are summarized below. This is followed by a discussion of the published literature relevant to the present work.

2.1 Generation of Primary and Extended Defects

The process of radiation damage begins with the impingement of a high energy particle such as a neutron on the crystalline lattice. If a neutron with energy E_n undergoes an elastic collision with a stationary nucleus of mass A, the kinetic energy, E_t, which can be transferred to the nucleus has a maximum value of $4AE_n/(A+1)^2$. If the scattering is isotropic, the average energy transfer will be one half of the maximum.[7,19] If E_t exceeds a value E_d, called the displacement energy, the atom is displaced from its lattice site and is referred to as a primary knock-on atom (PKA). The displacement energy

is a strong function of crystallographic direction; hence an effective value must be used for any one material.[20,21] For example, the displacement energy in the <110> direction of stainless steel has been measured to be about 18 eV (ref. 22). However, the effective value which is recommended for this material is 40 eV (ref. 23). Using this effective value of E_d for stainless steel and assuming maximum energy transfer, the minimum neutron energy required to displace an atom in this material is about 580 eV. Since both fission and fusion reactor neutron energy spectra include neutrons with energy in excess of 1 MeV, both types of facilities are capable of producing PKAs with a broad energy spectrum. The details of the PKA spectrum will vary with the neutron spectrum[24] as shown in Figure 2.1.

In collisions with 1 MeV neutrons, the average energy transfer to a PKA in stainless steel is about 69 keV. Since $E_t >> E_d$, the PKA will recoil with significant kinetic energy and be capable of displacing additional lattice atoms. In elastic collisions between such nearly equal mass atoms, any energy up to $(E_t - E_d)$ may be transferred to what is termed a secondary knock-on atom. These secondary knock-ons can in turn yield third and higher generation knock-ons until the last generation is produced with energies less than E_d. At this point the kinetic energy of the original neutron has been converted to many PKAs (and higher order knock-ons), each of which have in turn produced a number of displaced atoms in a region known as a displacement cascade. These displaced atoms will occupy the lattice interstices and are

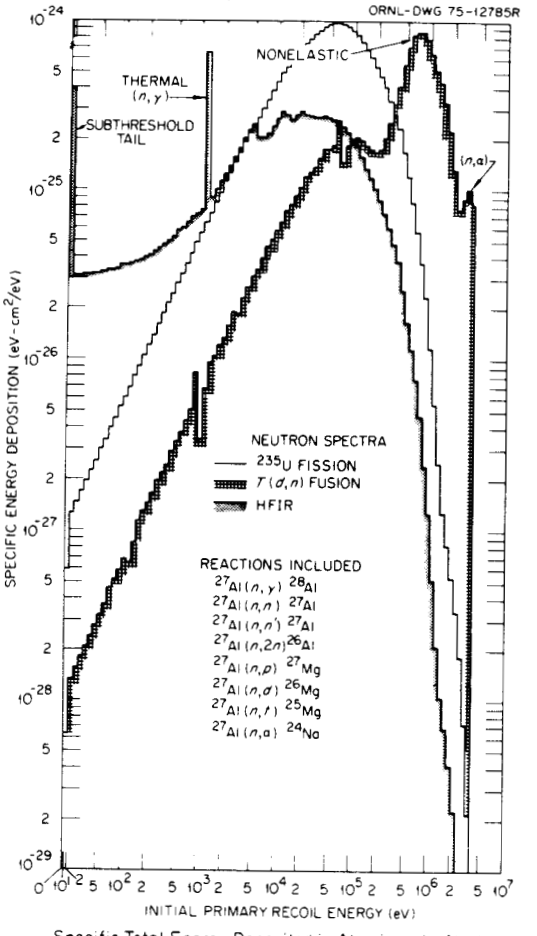

Specific Total Energy Deposited in Aluminum by Neutron Reactions (After T.A. Gabriel, ORNL).

Figure 2.1. Primary recoil energy spectra for three different neutron spectra on aluminum. The curve marked ^{235}U fission would be similar to a fast reactor spectrum; from Robinson, ref. 24.

called interstitials while their vacant lattice sites are called vacancies. An interstitial/vacancy pair thus created is referred to as a Frenkel pair. The geometry of a two-dimensional displacement cascade is shown schematically in Figure 2.2 (ref. 7).

The total neutron fluence (m^{-2} sec^{-1}) does not provide an appropriate measure of a material's accumulated radiation damage, in part because of the energy dependence of the displacement cross sections.

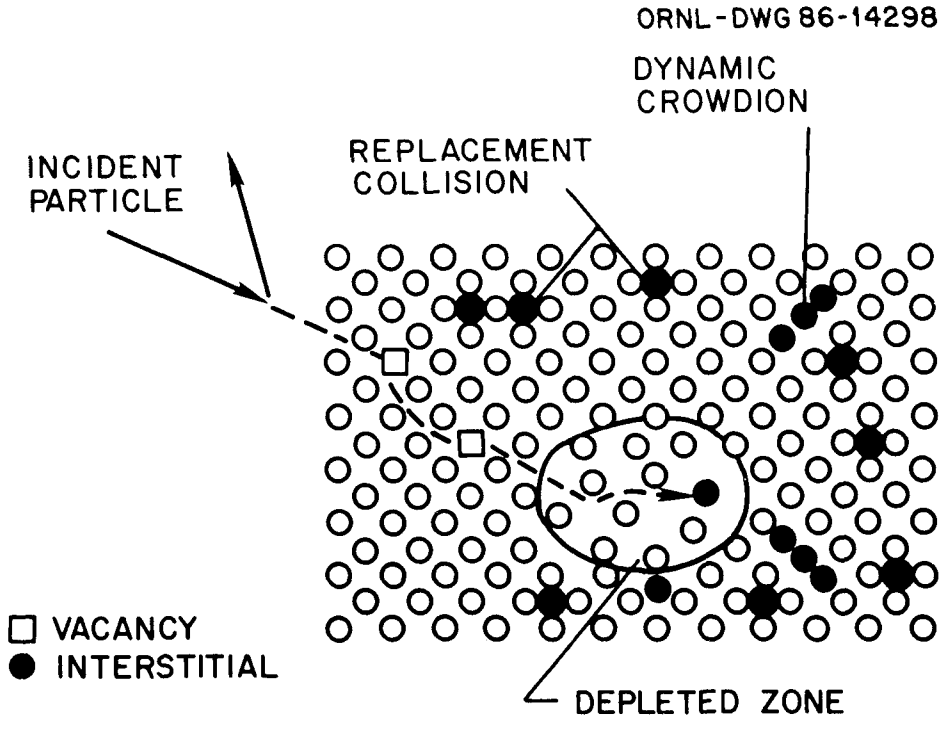

Figure 2.2. Schematic drawing of two-dimensional displacement cascade; from Olander, ref. 7.

One of the early attempts to correlate data from reactors with different neutron energy spectra involved the use of a partial neutron fluence in which only neutrons with an energy greater than some minimum were counted. Initially, this minimum energy was 1.0 MeV and later 0.1 MeV. This approach was successful to some degree, but it prevented the correlation of data from charged particle irradiations.

A more recent exposure parameter for the amount of radiation damage which has been accumulated is the number of atomic displacements that have been generated per lattice atom site (dpa). The number of displacements is not a direct measure of the residual radiation

damage because this damage is the result of a number of interacting processes. However, many of these processes are initiated by atomic displacements so that dpa can be viewed as an exposure unit with a reasonable physical basis for comparing the damage potential of both reactors with different neutron energy spectra and different charged particle irradiation environments.[7,25-27]

Various models of the displacement production process have been proposed. The simplest is that of Kinchin and Pease.[28] Their model assumed binary elastic collisions between hard sphere atoms, used a step function displacement probability which was equal to 0 for a lattice atom which received less than E_d from a collision and 1 for atoms which received greater than E_d, and accounted for the effect of nondisplacive energy losses between recoil atoms and electrons through the use of an upper cutoff energy. These assumptions have been relaxed by subsequent workers, notably Lindhard et al.[29] For high energy PKAs, most calculations support an expression for the number of displacements produced by a PKA with energy E_t, $\nu(E_t)$ as:

$$\nu(E_t) = 0.8\ T(E_t)\ /\ 2\ E_d. \qquad (2.1)$$

The so-called damage energy, $T(E_t)$, in Equation (2.1) can be estimated from Lindhard's theory[24,29] and accounts for nondisplacive electronic energy losses at high PKA energies. The most commonly used procedure for calculating the damage energy was proposed by Norgett, Robinson and Torrens (NRT).[23,24,26] For example, using the 69 keV PKA energy

computed above and taking E_d = 40 eV (ref. 23), T = 45 keV and $\nu(E_t)$ = 450 dpa NRT.

The geometry of the displacement cascade has a significant influence on the number of point defects (vacancies and interstitials) which survive the initial event and hence contribute to increasing the concentration of these defects above their thermal equilibrium values. Early researchers envisioned the cascade as having a vacancy rich central region surrounded by an interstitial rich shell similar to the one shown in Figure 2.2 (ref. 7). Subsequent computer calculations[30,31] and experimental work[32,33] have generally confirmed this picture. The separation of these two opposite defect types inhibits their mutual annihilation (recombination). Recombination of Frenkel pairs during what is termed intracascade annealing would, in the limit of 100% efficiency, largely eliminate radiation damage. This thermal rearrangement of the cascade occurs in three steps. The first step occurs within about 1×10^{-11} sec following cascade production and eliminates Frenkel pairs which are within a few atomic jump distances of one another. During the next $\sim 1 \times 10^{-8}$ sec, diffusion of mobile interstitials to vacancies results in uncorrelated recombination. The local cascade geometry continues to evolve over somewhat longer times as both vacancies and interstitials cluster and some of these clusters in turn dissolve. These clusters also act as recombination sites. A fraction of the initially produced point defects survive these intracascade annealing and clustering processes as free defects.[7,23,24]

These free defects raise the bulk concentration of vacancies and interstitials above their thermal equilibrium values.

The small defect clusters which remain as the residue of the displacement cascade can provide nuclei for the formation and growth of the extended defects discussed below. Additional clusters are formed when the diffusion of the free defects leads to encounters between defects of the same type. Depending upon whether they are comprised of vacancies or interstitials, these clusters may have various morphologies, microvoids, small platelets (dislocation loops) or stacking fault tetrahedra.[35-41] Theoretical calculations indicate that the stable defect type is a function of the material and the number of point defects in the cluster.[35-41] Such calculations have had only limited success at predicting the vacancy-type defect that is observed experimentally. This may in part be due to uncertainties about key parameters such as the stacking fault energy and the surface free energy.[35-38] In austenitic stainless steels, quenching studies have revealed primarily vacancy loops and voids.[42] One study reported a few large stacking fault tetrahedra.[43] Low densities of stacking fault tetrahedra have also been formed by plastic deformation[44,45] and by low temperature electron[46] or nickel ion[47] irradiation. There have been no reports of stacking fault tetrahedra in stainless steels that have been neutron irradiated at elevated temperatures. In the case of interstitial clusters, the stable defect is normally both calculated and observed to be a two-dimensional platelet.[39-41,48]

In addition to point defect and cluster production by atomic displacements, neutron irradiation also produces both solid and gaseous transmutants.[49-54] Solid transmutants have been postulated to influence the microstructural evolution of stainless steel by varying the fraction of minor alloying elements, notably manganese and vanadium.[52,53] However, transmutant gases are generally considered to be more important.[48,54] As stated above, in both fusion and fast reactor irradiation environments, the principal transmutant gases produced are hydrogen and helium. The generation rate of these gases is strongly dependent on the neutron energy spectrum since the relevant cross sections exhibit an energy threshold[55] as shown in Figure 2.3. Helium is

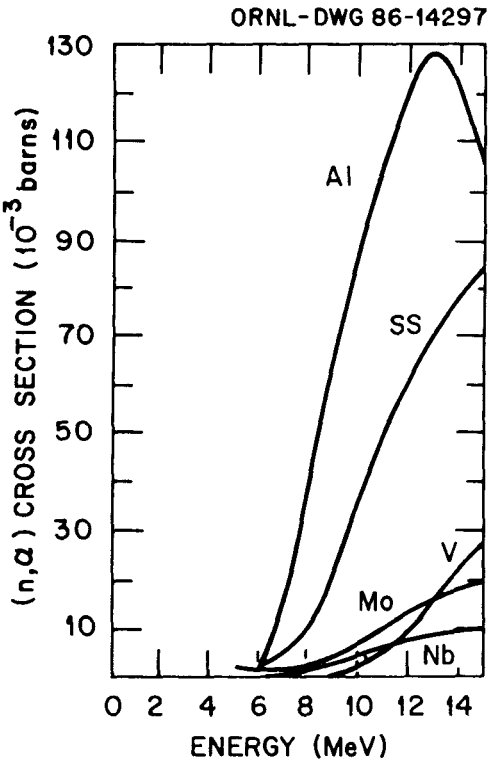

Figure 2.3. Comparison of (n,α) cross sections for several materials; from Kulcinski, et al.[55]

thought to be of greater importance than hydrogen since helium is chemically inert and essentially insoluble in metals.[56,57] Hydrogen is generally agreed to be a fast diffusing species and so is unlikely to remain free in the metal lattice.[58] There are data that indicate that hydrogen can affect the irradiation response of some materials. Bullen et al.[59] have reported that hydrogen injection prior to 14-MeV nickel ion irradiation of high purity nickel results in increased swelling, and Jones[60] has indicated that hydrogen embrittlement may increase crack growth rates in ferritic steels. However, Packan and Farrell have investigated the effect of hydrogen on void swelling in an austenitic stainless steel under nickel ion irradiation and found that it had no significant impact.[61] Since the focus of this work is austenitic stainless steel, no further discussion of hydrogen effects will be included. The role of helium will be discussed in some detail below.

Although stainless steel is a crystalline material, its structure is normally highly defected. The most common defects are a thermal equilibrium concentration of vacancies, line dislocations and grain boundaries.[62-64] These defects determine to a large degree the engineering properties of the material.[62-65] Extended defects in fast neutron irradiated stainless steel include not only these, but also Frank faulted loops and cavities.[7,18] With the exception of the grain boundaries, these extended defects can all be thought of as resulting from the agglomeration of individual point defects which have survived

the annealing of displacement cascades. Second phase particles in complex alloys can also be regarded as defect structures. In the absence of irradiation, their formation and evolution are governed by solubility limits and solute diffusivities.[66] However, neutron irradiation places the material in a nonequilibrium state in which certain phases that are normally observed thermally may be either enhanced or diminished and other phases may appear.[66,67,68] The influence of precipitates on other microstructural features will be briefly discussed below; however, precipitation as such will not be discussed here.

The two components of the irradiated microstructure of most interest here are the dislocations and the cavities. The evolution of the dislocation microstructure under irradiation is determined by the loss of network dislocation line length by climb/glide to free surfaces or mutual annihilation of dislocation dipoles and the replenishment of the network dislocations by climb sources and faulted dislocation loop growth and unfaulting. These processes require a flux of point defects to sustain them. If both vacancies and interstitials arrived at an edge dislocation at equal rates, no net climb would occur. However, it is well accepted that dislocations preferentially absorb interstitials because of the interaction of their respective strain fields,[69] leading to a greater dislocation sink strength for interstitials than for vacancies. This preference is referred to as the dislocation/interstitial bias. The bias can most simply be defined as the ratio of the capture rate of interstitials at a dislocation to the capture

rate of vacancies at a dislocation. Other components of the microstructure may also be biased toward either point defect type; the total system bias is the parameter of most interest.[70-76] In addition, calculations of the dislocation/interstitial bias have shown a dependence on the total system sink strength as well as the ratio of the dislocation sink strength to the total system sink strength.[72,73] Estimates[7,68-75] of the bias in the literature range between about 1 and 100%.

Dislocation loops are formed by the condensation of vacancies or interstitials into roughly circular disks on or between close packed planes, respectively [e.g., (111) planes in face centered cubic austenite]. The edge dislocation thus formed encloses a stacking fault and these faulted loops are called Frank loops.[7,63] These loops may grow or shrink by absorbing or emitting point defects of the appropriate type. Since the dislocation has a net bias for interstitials, only the interstitial type loops have a reasonable probability of growing very large. Because of the stacking fault, Frank loops are not mobile. However, the stacking fault can be removed by shearing the crystal above or below the faulted region. This is accomplished by the nucleation and movement of a Schockley partial dislocation across the loop.[63] The Burgers vector of the Frank loop is 1/3<111> and that of the Schockley partial is 1/6<211> leading to a Burgers vector of 1/2<011> for the unfaulted loop. The energy necessary to nucleate the partial dislocation can be provided thermally above about 550 to 600°C or mechanically due to the interaction of the strain fields of the

faulted loop and an adjacent dislocation.[35,63] This unfaulted or perfect loop is mobile and can both climb and glide to eventually become part of the dislocation network. Since mechanisms exist which can both supply and remove network dislocations and faulted loops, quasi-steady state dislocation microstructures are observed after an initial transient.[76,77] The duration of the transient and the steady state dislocation density are temperature dependent.[76] The relative fraction of the total dislocation density which is comprised of faulted and unfaulted loops is also determined by the irradiation temperature.[78]

The evolution of the cavity microstructure begins with the formation of small vacancy clusters. As discussed above, these vacancy clusters can exhibit several morphologies at small sizes. The phenomenon of void swelling in irradiated stainless steels indicates that at some point the cavity becomes the preferred defect (in fact, there was a recent report of cavities being nucleated on the corners of stacking fault tetrahedra[66]). The cavities grow by absorbing vacancies (interstitial emission is generally negligible) and shrink by vacancy emission and interstitial absorption. For small cavities the dominant process is thermodynamically determined to be vacancy emission.[79,80] Statistical fluctuations can still produce large vacancy clusters since having vacancy clusters of size (n) and mobile vacancies implies a non-zero probability of having (fewer) clusters of size (n+1) which can in turn yield clusters of size (n+2) and so on. However, homogeneous nucleation rates are computed to be several orders of magnitude

too small to explain the observed cavity densities.[79-85] Hence, heterogeneous nucleation at pre-existing internal surfaces and interfaces or as a result of solute segregation to cavity surfaces is invoked to explain the experimental results.[83-85] Cavity nucleation is also believed to be aided by residual gases[86] (e.g., N_2 and O_2) in the material from the melt and by transmutant gases produced under irradiation.[55,87] For example, the fact that helium is produced in stainless steel by (n,α) reactions has already been mentioned. Because helium is insoluble in the atomic lattice, it is likely to diffuse until it is either trapped at a pre-existing defect or clusters with other helium atoms or vacancies. Small clusters of vacancies and helium atoms are stable bubble nuclei and would provide preferred sites for nucleation of larger cavities. Theoretical calculations indicate that small clusters with approximately equal numbers of vacancies and helium atoms should be highly stable[88] and that the divacancy-monohelium complex may be particularly stable.[89] However, even when gas-assisted heterogeneous nucleation is considered, a nucleation barrier remains which must be overcome to yield cavities which are stable against vacancy emission.

In this context the terms bubble and void can be defined for the purposes of the present work. A cavity which is primarily stabilized by its gas content is termed a bubble. The gas pressure in a bubble of radius r_b at temperature T is a significant fraction of the equilibrium value of $2\gamma/r_b$, where γ is the free surface energy. A cavity

which is primarily an agglomeration of vacancies has $P<<2\gamma/r_b$ and is called a void. Experimentally, voids are generally distinguished from bubbles by the fact that voids tend to be larger and are frequently faceted while bubbles tend to be spherical. The size of spherical cavities in the grain boundaries can be used as a measure of the maximum bubble size.[48] Voids are unstable in the absence of irradiation and will disappear or shrink back to the appropriate bubble size in a postirradiation anneal while bubbles will persist due to their gas content. Bubbles produced in fast-reactor irradiations tend to be small, $r < 2.5$ nm (refs. 48,90), while void radii may range up to several hundred nanometers or more.[48,78,91,92] These concepts will be discussed in greater detail in Chapter 3.

The time dependence of the cavity microstructure tends to exhibit three fairly distinct regions.[93] There is an initial period associated with the formation of a subcritical cavity (bubble) population. During this period little or no density change as a result of the cavities is observed and the cavities may remain invisible under transmission electron microscopy (TEM) examination (i.e., $r_b \leq 0.5$ nm). Next there is a transient which is a result of some of the subcritical bubbles reaching the critical radius and beginning to grow as voids. At this point the cavities are visible under TEM and the reduction in density due to the void volume is measurable but generally less than 1%. Finally a regime of "steady state" swelling is reached as those voids which have previously nucleated grow rapidly by vacancy absorption.

In some cases the high cavity sink strength obtained in the steady state regime can suppress the effective vacancy supersaturation to a sufficient degree to prevent further void nucleation. This regime is characterized by high swelling (values of greater than 30% have been measured in fast-reactor-irradiated AISI 316 stainless steel[92,93]) and frequently by a bi-modal cavity size distribution with small subcritical bubbles and large voids.[48,76,78]

Finally, it should be noted that the discussion of the evolution of the individual components of the irradiated microstructure is somewhat artificial. In reality, the response of each component is highly coupled to the others through the competition for point defects and the influence of the total system sink strength.[76] The fact that dislocations preferentially absorb interstitials, leading to an excess of vacancies to drive void growth, is just one example of this coupling.

2.2 Effects of Transmutant Helium

The role of transmutant helium in the microstructural evolution of irradiated materials has been the subject of some debate.[48,95,96] From the time that Cawthorne and Fulton first observed void swelling,[87,88] helium has been assumed by many workers to play a key role in assisting void nucleation.[51,76,87,88,100] Recent reviewers[54,57,76,101] have discussed the results of both neutron and charged particle (with helium either preinjected or simultaneously injected with the damage producing ions) irradiation experiments in

which the total cavity density appears to increase with helium content. In some cases the dependence of the cavity density on the helium concentration could crudely be described by a simple power law.[54] Preinjected helium also appears to increase the density of small dislocation loops at low doses and in some cases the network dislocation density at higher doses.[54,57] Helium has also been reported to retard the growth of interstitial loops at low doses during charged particle irradiation.[57] This extends the time at which these loops unfault and become part of the dislocation network.

The effect of helium on cavity density has generally received the most attention because of its potential consequences on void swelling. Odette and Frei[102] and later Odette and Langley[103] investigated the effect of varying helium generation rates on bubble and void densities. They found that the bubble density was a strong function of the helium generation rate and that high bubble densities could lead to a suppression of void swelling. They suggested that metallurgical treatments which promoted a high bubble density could be used to limit swelling.[102,103] Singh and Foreman[104] have also investigated the influence of helium on void formation and found similar results. They note that their cavity density is roughly proportional to the square root of the helium generation rate as mentioned above.[54,104] The experiments which have investigated these effects will be discussed further below.

The influence of helium on precipitation in complex alloys is more subtle. Precipitation and phase decomposition are largely

governed by solute atom migration and segregation. Various solutes (e.g., Ni, Cr, Mo and Si in stainless steel) may diffuse with the radiation induced point defect fluxes to existing sinks at different rates leading to local concentration or depletion of the solute. When the local solute concentration exceeds a solubility limit, a phase change occurs. In spite of the fact that helium is a chemically inert gas, it can have various direct and indirect effects on precipitation. For example, if helium increases the total system sink strength by increasing the cavity and/or loop density it should also reduce the amount of radiation induced solute segregation taking place by distributing the available solutes to more sinks. This should lead to a finer dispersion of second phase particles and perhaps a lower precipitate volume fraction. While some observations are generally consistent with these simple arguments,[87,101] the details of the effect of helium on precipitation are more complicated and continue to be a matter of some discussion.[48,87,95,96,101,105,106]

A key parameter to consider in the attempt to extrapolate swelling data from fission to fusion conditions is the ratio of transmutant helium generated to displacements per atom produced (He/dpa ratio) in the material. The He/dpa ratio is a function of both the material selected and the neutron flux spectrum to which it is exposed as shown in Table 2.1.[48,55] In Table 2.1, HFIR refers to the High Flux Isotope Reactor and ORR refers to the Oak Ridge Research Reactor, both of which have a mixed (i.e., thermal and fast neutron) spectrum. The former of

Table 2.1. Helium/dpa ratio for various materials and reactor neutron spectra

	Type 316 Stainless Steel	Molybdenum	Vanadium
EBR-II	0.385	5.94×10^{-3}	5.7×10^{-3}
ORR	1.0–10.3[a]	--	--
HFIR	0.2–60.8[a]	0.119	9.38×10^{-3}
Fusion Reactor (3 MW/m²)	14.5	5.77	4.86

[a]Nonlinear due to buildup of ^{59}Ni; indicated values at startup and after one year.

these two reactors is of interest to the fusion materials program since the fast component of the neutron spectrum produces displacement damage at near-fusion values, ~1×10^{-6} dpa/sec, while the thermal component produces significant quantities of helium in nickel-bearing alloys by a two-step reaction:

$$^{58}Ni(n,\gamma)^{59}Ni(n,\alpha)^{56}Fe \quad . \tag{2.2}$$

This He/dpa ratio is nonlinear in time due to the buildup of ^{59}Ni, beginning at <1 appm He/dpa and saturating at ~80 appm He/dpa in a typical stainless steel. The ORR also produces significant levels of helium but at a lower dose rate. A comparison of the neutron spectra obtained in the Experimental Breeder Reactor-II (EBR-II), HFIR, ORR and a typical DT fusion reactor[4,8] is shown in Figure 2.4. Relevant neutron energy ranges are noted. Although the anticipated value of the He/dpa ratio in an austenitic stainless steel fusion reactor first

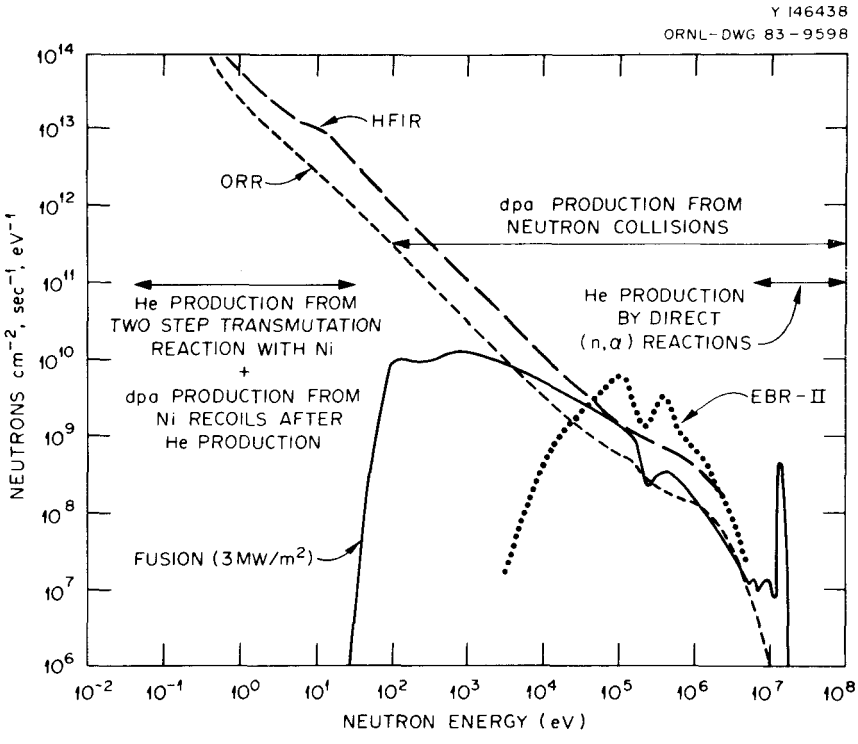

Figure 2.4. Neutron energy spectra for three fission reactors used in irradiation experiments (HFIR, ORR, EBR-II) and a typical DT fusion spectrum at 3 MW/m² wall loading.[48]

wall is bracketed by the values of this parameter in the EBR-II and HFIR, the ability to interpolate between data sets generated in these two fission reactors is complicated by the fact that both theoretical and experimental evidence indicate that cavity swelling is not a monotonic function of the He/dpa ratio.[54,107,108]

In general, the influence of helium can be summarized as tending to refine the microstructure of irradiated materials, particularly in the incubation and transition regimes; increasing both the cavity and dislocation loop densities while enhancing and refining precipitation.

Since helium is a critical factor in determining the scale of the microstructure, its indirect effects may also be observed in the high dose or steady state regime as well.

2.3 Theoretical Background

This section presents a summary of previous theoretical work that provides the background for the models discussed in Chapter 3. Three key concepts have already been mentioned: (1) the presence of a biased sink for interstitials, leading to an effective vacancy supersaturation, (2) the importance of transmutant helium in promoting bubble formation and (3) the existence of a critical cavity (bubble) size for void formation. Although their interest was in fissionable rather than structural materials, Greenwood et al.[10] suggested two of these concepts in 1959. They proposed that the formation and growth of bubbles in nuclear fuel were due to the diffusion and agglomeration of fission gas atoms and vacancies. They proposed that dislocations may absorb interstitials "more readily" than vacancies, leaving an excess of vacancies to drive cavity growth. The converse was also suggested — namely, that small gas bubbles nucleating on dislocations may require excess vacancies with the corresponding interstitials left to drive dislocation climb.[10] This latter mechanism has recently been proposed to explain the growth of Frank faulted interstitial loops under thermal annealing following helium injection.[8] Finally, Greenwood et al. also indicated that the bubble density should be strongly dependent upon the fission gas generation rate. They assumed

that a cluster containing two gas atoms and two vacancies would be a stable nucleus and, using a simple kinetic model, showed that the bubble density should be proportional to the square root of the gas generation rate.[109] This approximate dependence has often been observed experimentally.[54,104]

The so-called chemical reaction rate theory has been heavily used in the development of the theory of radiation effects. Early researchers in this area include Harkness and Li,[110] Brailsford and Bullough[111] and Wiedersich.[112] This initial work focused on deriving the appropriate sink strengths for the extended defects in the microstructure in order to permit the calculation of the rate coefficients in the theory. Brailsford and Bullough and their coworkers have continued to contribute to this work as the theory has been developed,[75,113-116] along with Mansur, Wolfer, Coghlan, Yoo, Heald, Nichols and Gösele.[70-73,117-123] The current status of the theory of sink strengths has been well presented in a recent review by that title,[115] and Mansur has written overall reviews of the theory of radiation effects.[21,74]

The use of the rate theory will be extensively described in Chapter 3; a few key points will be illustrated here. The effective medium approach of Brailsford and Bullough[111,115] is adopted. In this approach the spatial details of point defect production (cascades) and the microstructure (cavities, dislocations, grain boundaries ...) are averaged out and replaced with an effective homogeneous medium.

The properties of the medium are chosen to conserve the generation of point defects and their loss to the various sinks. The conservation equations for vacancies and interstitials are:

$$\frac{dC_{i,v}}{dt} = G_{i,v} - \alpha C_i C_v - D_{i,v} C_{i,v} \sum_j S^j_{i,v} \quad . \qquad (2.3)$$

The subscripts i and v in Equation (2.3) denote interstitials and vacancies, respectively. Their concentrations (per unit atom) are denoted by the $C_{i,v}$ and their diffusivities by the $D_{i,v}$. The generation rate, $G_{i,v}$, includes thermal emission from the extended defects whose sink strengths are denoted by $S^j_{i,v}$. The recombination coefficient, α, mathematically couples the vacancy and interstitial equations so that they must be solved simultaneously.

The appropriate sink strengths for the extended defects in the effective medium are obtained by solving a discrete diffusion problem.[7,21,74,115] It is convenient to consider these sink strengths as having three terms.[21,74] The first is a geometric term which includes the appropriate dimensions of the sink (e.g., the amount of dislocation line length per unit volume). The second term is a sink capture efficiency or bias. A simple definition of this term was given above for the dislocation/interstitial bias. A more general definition is that it is the ratio of the actual point defect current of either type to a given sink to that which would be obtained if the sink caused no strain field in the lattice that gave rise to long range interactions with the defect and if the sink were a perfect

absorber of that defect. The third term is called the multiple sink correction factor and it accounts for the correlated loss of point defects when more than one sink is present. This correction is necessary because the total sink strength in a multiple sink system is greater than the sum of their individual effective-medium sink strengths.

A simple example of an extended defect sink strength is the standard result for a straight segment of dislocation network:[7,21,66]

$$S^{n}_{i,v} = Z^{n}_{i,v} \rho_n \quad . \tag{2.4}$$

In Equation (2.4) ρ_n is the network dislocation density (m/m^3) and the capture efficiency is:

$$Z^{n}_{i,v} = \frac{2\pi}{\ell n\ (r_o/r^{i,v}_c)} \quad , \tag{2.5}$$

where r_o is essentially a diffusion length for the point defect in the medium and $r^{i,v}_c$ is the dislocation capture radius for interstitials or vacancies. The preferential attraction or bias of dislocations for interstitials follows from the fact that r^{i}_c is computed to be greater than r^{v}_c due to the interstitial's long range strain field.[66] The diffusion length in Equation (2.5) is simply the mean dislocation spacing, $(\pi\rho_n)^{-1/2}$, in the absence of the multiple sink strength correction and takes on a more complex form when this effect is included.[115]

Finally, the sink strengths may take alternate forms in two limiting cases. These cases are diffusion-controlled and reaction-

rate-controlled kinetics.[7,21,74] The former case is obtained when the transfer velocity into the sink (the last defect jump) occurs at the same rate as diffusion in the matrix, $v_t \sim (D_{i,v})/b$, where b is an appropriate lattice dimension. In this case the diffusion distance in the matrix determines the point defect current into the sink. The latter case, also known as surface-limited kinetics, occurs when the sink is a poor absorber and the last jump (or jumps) occurs at a much lower rate than matrix diffusion. For a simple distribution of N_c spherical cavities of radius r_c, these two cases yield the following sink strengths (to lowest order):[7,117]

$$S_c = 4\pi r_c N_c \quad \text{(diffusion-limited)} \quad , \tag{2.6}$$

and

$$S_c = \frac{4\pi r_c^2 N_c}{b} \quad \text{(reaction-limited)} \quad , \tag{2.7}$$

Mansur has described the influence of reaction- versus diffusion-limited kinetics on the predicted dose dependence of swelling.[74] Although the comparison with swelling data is not conclusive, most workers have used diffusion-limited kinetics.[102,103,108,115,124-126] Exceptions include Yoo and Stiegler's analysis of faulted loop growth in nickel under high voltage electron microscope (HVEM) irradiation which indicated that the kinetics were reaction limited.[127]

Typically, quasi-steady state solutions to the point defect equations are obtained by first setting the time derivatives in

Equation (2.3) to zero. This implicitly assumes that the point defect concentrations respond to changes in the sink strengths much more quickly than the sink strengths change. Calculations of the characteristic relaxation times for the point defect concentrations to reach steady state indicate that this is a valid assumption.[74] A numerical solution for Equation (2.3) by Yoo[122] is also available. Other implicit assumptions in the formulation of Equation (2.3) are that only the monodefects are mobile and that a single effective diffusion coefficient is adequate to describe the mobility of these defects. The work of Johnson[60] indicates that neglecting the mobility of small interstitial clusters should not have a significant effect on the concentrations of the monodefects. On the other hand, Yoo[128] indicates that neglecting the mobility of divacancies could lead to errors for some materials. Mansur[74] has suggested that this assumption should be carefully examined. Regarding the second assumption, Mansur and Yoo[128] have developed a methodology for computing effective diffusion coefficients which takes into account the point defect trapping by solutes. The use of this method permits the calculation of correction factors for multiple traps and varying trap distributions.

Once the point defect concentrations have been calculated, the evolution of the extended defects can be determined. To once again use a spherical cavity as an example, the radial growth velocity if one assumes diffusion-limited kinetics is:[7,21,115]

$$\frac{dr_c}{dt} = \frac{1}{r_c}\left(Z_v^c D_v C_v - Z_i^c D_i C_i - Z_v^c D_v C_v^c\right) \quad . \qquad (2.8)$$

where C_v^c is the vacancy concentration in equilibrium with the cavity surface at r_c. Equations similar to Equation (2.8) can be written for the various extended defects and the equations integrated to yield the time or dose dependence of a macroscopic parameter such as void swelling. The time step in such an integration is limited by the quasi-steady state assumption discussed in reference to Equation (2.3).

Numerous workers have compared the predictions of theoretical models based on the rate theory with experimental data. The results have generally been reasonably good. The major caveat in this last statement is a recognition of the fact that many of the physical parameters which are required in the rate theory are not well known, particularly for alloys. Hence the common approach is to try to obtain good agreement between theory and experiment while maintaining parameter values within "reasonable" limits.[108,124-126] Key parameters which exhibit some range of values in the literature include the dislocation/interstitial bias, the self-diffusion energy and the matrix surface free energy. The influence of these parameters will be discussed in detail in Chapter 3.

Typical examples of the use of the rate theory include the work by Odette and co-workers[102,103,108,130] to determine the influence of helium on void swelling, Brailsford and Bullough[131] investigating the effect of stress on swelling and Mansur and Coghlan[127] on the mechanisms by which helium alters the irradiation response of a material. Mayer, Brown and Göselle[132] have reported on their work on nucleation and growth of voids in a recent series of papers. Ghoniem et al.[133-136]

have looked extensively at the early stages of point defect clustering, also including the influence of helium. Wehner and Wolfer[137] have also described the evolution of the vacancy cluster population which provides the nuclei for subsequent void formation. Hayns[138,139] has published a model in which a hierarchy of rate equations is used to compute the homogeneous nucleation of both voids and interstitial loops.

With the exception of Hayns,[138,140] the work mentioned above has been primarily concerned with the cavity component of the irradiation-produced microstructure. The rate theory has also seen more limited use as a tool for predicting dislocation evolution. Powell[141] described a model for the simultaneous evolution of faulted loops and cavities. The nucleation of these defects was calculated using the classical nucleation theory[142] and the rate theory was used to describe their growth. A constant network dislocation density was used in this analysis. More recently, Wolfer and co-workers[126,143] have developed a phenomenological model of network dislocation evolution to explain the experimentally observed saturation network dislocation density. This model has been linked with a rate theory description of void growth and they have explored the differences between austenitic and ferritic steels.[126]

Two major shortcomings of the effective medium, rate theory approach include the spatial averaging of discrete microstructural features and both the temporal and spatial averaging of point defect generation. The ability to use the rate theory as a tool for studying radiation effects does not appear to be compromised by these

approximations. The present work will in fact demonstrate the potency of the rate theory in this regard. Nonetheless, there are examples of phenomena which are discrete in time or space which cannot then be accounted for in the simple theory. An example of such a heterogeneity is the commonly observed regions near grain boundaries which are denuded of loops or cavities.[166,168] The assumption of continuous point defect generation was relaxed in work by Brailsford, Mansur and Coghlan[166,167] in their cascade diffusion theory. This work indicated that there were a limited number of examples in which the discrete nature of point defect production was significant; one of those was cascade-induced irradiation creep. These authors found that the conventional rate theory approach was a limiting case of their analysis and concluded that it was generally quite accurate.[167]

2.4 Experimental Observations

A few general trends in the behavior of extended defects under irradiation were given in Sections 2.1 and 2.2. This section is a summary of the experimental observations which have been reported for irradiated austenitic stainless steels. The section focuses on the cavity and dislocation components of the irradiated microstructure. Recent publications[66,67,68,101,105,106] have discussed the presence and evolution of second phase precipitates in these materials in great detail. The influence of helium in moderating the formation of radiation-induced phases has received particular attention in two reviews.[66,101] While the formation of second phases can influence

the rest of the microstructure (e.g., by altering diffusivities due to solute depletion[128,148,149]), no further discussion of precipitation as such is included. Maziasz has thoroughly reviewed the radiation effects literature for solution-annealed stainless steel in a recent report.[68] Reference to his work will be made as appropriate. Early work by Bloom and Stiegler,[150] Brager and Straalsund[78] and Eyre[151] provides a good overall view of the effects of fast neutron irradiation on the microstructure of AISI type 316 stainless steel. Odette[76] has summarized and discussed in detail the observed data trends for a number of phenomena in austenitic stainless steels. Other helpful reviews of the fairly large amount of void swelling data include those by Garner[152] and Maziasz.[153]

2.4.1 Role of Helium

Because of the interest in the role that helium plays in microstructural evolution, several studies have been made of the annealing behavior of specimens which had been implanted with helium. This work typically involves the use of high energy alpha particle beams from a cyclotron. The beam energy is chosen so that the end of the range is nearly the full thickness of the specimen and the beam energy is degraded in a cyclic fashion to obtain a uniform distribution of helium throughout the specimen.[154-156] Implantation to a level of 10 to 100 appm He generates about 10^{-3} to 10^{-2} dpa (ref. 157). The work of most relevance to the present study is that by Mazey and Francis,[145]

Mazey and Nelson,[157] Smidt and Pieper,[158] Rothaut and Schroeder[159] and Maziasz.[48] Their work involved primarily "cold" (i.e., about room temperature) helium implantation of solution-annealed 316 stainless steel to levels of 1 to 1000 appm. Following the implantations, the specimens were annealed for times up to 10,000 hours at temperatures between 200 and 1100°C.

The principal observations of these annealing studies are summarized using representative data from refs. 48, 145 and 158 in Tables 2.2 and 2.3. The as-implanted materials contain a high density of small Frank faulted interstitial loops. Maziasz is the only one who has done quantitative work on the as-implanted material; he reports ~4 x 10^{23} loops/m^3 with a diameter of about 2.2 nm (ref. 48). Maziasz has also verified that these loops in the helium-implanted material are interstitial type.[48] This result is significant because Table 2.2 indicates that the loops are growing under thermal annealing. Interstitial loop growth in the absence of irradiation suggests that the material is in a nonequilibrium state with net absorption of thermal vacancies by at least one sink. The fact that helium bubbles begin to appear after 10,000 hours at 600°C (ref. 48) or 1 hour at 700 to 750°C (refs. 157–159) appears to indicate that this sink is small helium/vacancy clusters which have a high capture efficiency for vacancies as initially suggested by Greenwood et al.[109]

Although these studies covered a range of helium levels and annealing times and temperatures, a fairly consistent picture emerges

Table 2.2. Faulted loop evolution in helium-implanted and aged, solution-annealed 316 stainless steel[a,b]

Helium Implanted (appm)	Annealing Temperature (°C)	Annealing Time (hours)	Average Loop Diameter (nm)	Loop Density (10^{21} m^{-3})
100	200	1	5.0	7.0
100	500	1	4.6	6.0
100	600	1	10.9	1.8
100	650	1	36.8	0.5
100	700	1	45.0	0.14
100	725	1	59.0	0.008
100	750	0.55	99.0	0.005
100	650	1	36.5	0.5
100	650	2	52.5	0.3
100	650	4	65.5	0.2
100	650	16	81.9	0.1
10	650	1	66.2	0.008
100	650	1	36.0	0.5
1000	650	1	28.5	6.5
110	400	10,000	5.3	8.6
110	500	10,000	9.8	8.2
110	600	10,000	28	0.34
110	700	10,000	None observed	

[a]Reference 48, P. J. Maziasz.
[b]Reference 145, D. J. Mazey and S. Francis.

when the results are compared. For low (<50 appm He) helium concentrations and annealing times up to about one hour, faulted loops grow and coarsen up to about 750°C. At higher temperatures or for longer times at slightly lower temperatures the loops have all annealed out. At high helium levels (~1000 appm He), the loops grow until they unfault. The loop density tends to decrease and the average size to increase as a function of time or increasing temperature. The bubble

Table 2.3. Bubble evolution in helium-implanted and aged, solution-annealed 316 stainless steel[a,b]

Annealing Temperature (°C)	Annealing Time (hours)	Average Bubble Diameter (nm)	Bubble Density (10^{21} m^{-3})
800	1	2.5	0.44
900	1	3.9	1.8
1000	1	8.6	0.17
1100	1	15.1	0.054
900[c]	1	6.4	0.25
1000[c]	1	11.2	0.11
600	10,000	2.73	7.0
700	10,000	5.50	0.33

[a]Reference 48, P. J. Maziasz, 110 appm He.
[b]Reference 158, F. A. Smidt and A. G. Pieper, ~40 appm He.
[c]Specimen accidentally deformed; see text.

densities which form and the temperature at which they are first observed are strongly dependent on the helium level. For one hour anneals, bubbles are not seen until the annealing temperature reaches 700 to 750°C if the helium level is ≤50 appm. At ~100 to 1000 appm He, bubbles are seen as low as 600°C after one hour and the densities are much higher at all temperatures. At higher temperatures and for longer times, the bubble size distribution coarsens with a concurrent decrease in their density. Smidt and Pieper point out the effect of dislocations on bubble formation in two specimens which were accidentally deformed prior to annealing. These specimens were annealed at 900 and 1000°C and revealed both larger sizes and a lower bubble density than their undeformed counterparts (see Table 2.3). These

results will be discussed further in Chapter 4 when the annealing study from the present work is described.

2.4.2 Dislocation Structure

The dislocation structure of austenitic stainless steels is determined by thermal and mechanical treatment.[78,150,160] Two common treatments are solution annealed and 20% cold-worked. The former condition can be achieved by fairly high temperature (~1050 to 1100°C) annealing for times as short as 30 min. This results in a fairly homogeneous dislocation density on the order of 10^{12} to 10^{13} m^{-2} (ref. 48). The 20% cold worked material contains ~1 to 5 × 10^{15} m^{-2} of dislocation line length which is quite heterogeneously distributed. The two major features are a coarse distribution of microtwins, stacking faults and deformation bands along with a finer distribution of dislocation network.[161,162] These two components are reported to have different thermal stabilities. The dislocation network begins to show significant recovery and polygonization as low as 650°C while the coarse structure is stable against recrystallization up to about 900°C in short term (~10 hours) aging.[162-164]

Under fast-neutron irradiation, this dislocation structure is modified and consists primarily of three components: Frank faulted (sessile) dislocation loops, perfect (glissile) or prismatic dislocation loops, and a dislocation network. The relative fractions of these three components and the total density of dislocation line

length are functions of both the irradiation temperature and the accumulated dose.[48,78,150,151] Information concerning this dose and temperature dependence is summarized in Figure 2.5 (refs. 48,78,91, 97,150,165–168). The general trend observed for temperatures greater than about 300°C is for the low dose structure to be primarily comprised of Frank loops, followed by a transition to a mixed population of dislocation network and loops. This is consistent with the argument advanced above that the dislocation network can be generated by the growth and unfaulting of Frank loops. At temperatures greater

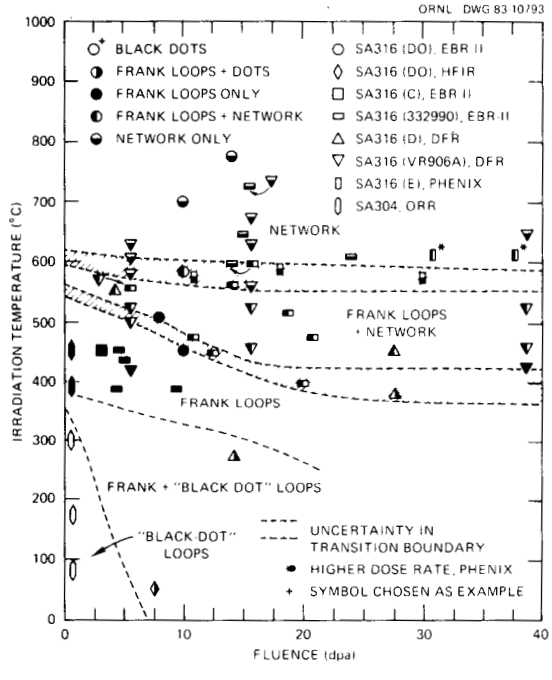

Figure 2.5. Character of dislocation structure in fast neutron-irradiated, solution-annealed austenitic stainless steel; from Maziasz.[48] Data references in legend, from top to bottom, are: (1) Bloom and Stiegler,[150] (2) Maziasz,[165] (3),(4) Brager and Straalsund,[78] (5) Cawthorne and Fulton,[97] (6) Barton et al.,[91] and Brammon et al.,[166] (7) LeNaour et al.,[167] and (8) Bloom et al.[168]

than about 600°C, few loops are observed. Figure 2.6 shows the temperature dependence of the Frank faulted loop density in AISI type 316 stainless steel. This figure includes some of the solution annealed data from Figure 2.5 (refs. 78,91,150) and additional solution annealed[169] and 20% cold worked data.[169,170] This data indicates that similar loop populations evolve in spite of the fact that the initial dislocation density is more than a factor of 100 higher in the 20% cold worked material.[161] However, Bloom and Stiegler[150] have reported a suppression of faulted loop formation in 20% cold worked materials at 10 dpa and 450°C. This is consistent with the fact that the latter authors also observed less recovery of the dislocation network at 450°C than did Brager and Straalsund.[161]

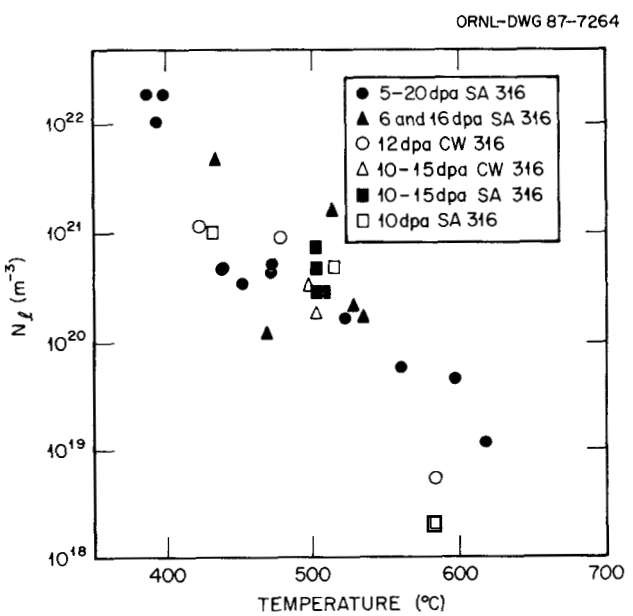

Figure 2.6. Temperature dependence of Frank faulted loop density in AISI type 316 stainless steel. Data from Brager and Straalsund,[78] Barton et al.,[91] Bloom and Stiegler,[150] Brager et al.,[169] and Brager.[170]

Brammon et al.[171] also report similar faulted loop densities in solution annealed and cold worked specimens. They indicate that at 30 dpa there was a temperature range over which the faulted loops disappeared and were replaced by unfaulted loops and network. This temperature range was 450 to 480°C in solution annealed material and 495 to 530°C in 20% cold worked material.[171]

The maximum and average faulted loop sizes have been observed to correlate with the total dislocation density.[169] In that work the average loop diameter in both solution annealed and cold worked material was approximately equal to the reciprocal of the square root of the total dislocation density.[170] This value is roughly the mean dislocation spacing and is consistent with the proposed mechanism of near contact with another dislocation segment inducing a local stress that initiates the unfaulting reaction described in Section 2.1 (refs. 35,63,169).

The network dislocation density is also observed to evolve toward a steady state value which is independent of the initial value.[76,77] This appears to be weakly temperature dependent below about 500 to 550°C and to decrease more sharply above this temperature as faulted loops no longer provide a significant source for the network.[166,171,172] Some representative data are shown in Figure 2.7 (refs. 75,91,166,172). It is difficult to determine from the literature the degree to which the value of the network density depends on temperature. Often the total dislocation density is reported and the

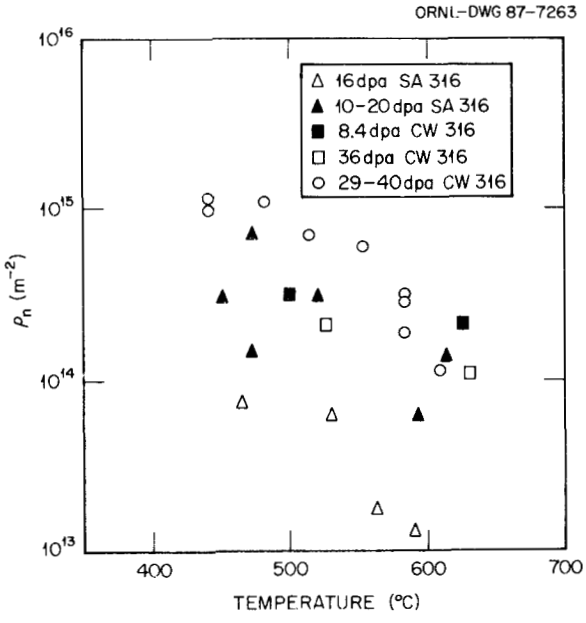

Figure 2.7. Temperature dependence of network dislocation density in fast neutron-irradiated austenitic stainless steel. Data from Brager and Straalsund,[78] Barton et al.,[91] Brammon et al.,[166] and Maziasz.[172]

partitioning between network and faulted loop line length is not clearly stated. For example, the data from ref. 166 shown in Figure 2.7 include some loop contribution. The authors report the value of the total dislocation line length and make qualitative statements about its character. They report no faulted loops above 525°C, a "few" at 512°C and increasing numbers below 500°C. They do report that the network value was 8.6×10^{14} m^{-2} at 480°C with the loop contribution raising the total to 1.02×10^{15} m^{-2} (ref. 166). With this as guidance, their data does reflect a trend of not only higher total dislocation density with decreasing temperature but also an increasing network dislocation density. This is somewhat in contradiction to the observations of Brager et al.[77] that the network density is essentially temperature independent in the range of 450 to

600°C. Some of the discrepancy may be due to the fact that the two groups of researchers were examining slightly different steels (U.K. M316 versus AISI 316). An additional factor could be that there have not been a statistically significant number of measurements of the network dislocation density at each temperature. The uncertainty in such measurements is typically rather large (e.g., $6 \pm 3 \times 10^{14}$ m^{-2} in ref. 77) due to errors in thickness measurements, dislocation invisibilities and the probable loss of dislocations to the surfaces during and after the preparation of thin foils.[183] In this case differences of a factor of 2 or 3 could easily be masked by data scatter and the question of what is "constant" becomes more subjective.

2.4.3 Cavity Structure

The evolution of the cavity component of the irradiated microstructure has received more attention than the dislocation component.[18] Maziasz[68] has summarized cavity statistics for a number of fast-reactor irradiations of solution annealed austenitic stainless steel.[78,91,97,150,166-168,174,175] Figures 2.8 and 2.9 are reproduced from his work.[68] Figure 2.8 is a diagram showing the temperature/dose regimes in which various types of cavity microstructures are observed. The distinction between bubbles and voids described in Section 2.1 is observed. Voids are described as being either precipitate-associated or free in the matrix. In the intermediate temperature range where precipitate-associated voids are formed, they tend to be formed at a lower fluence than matrix voids.

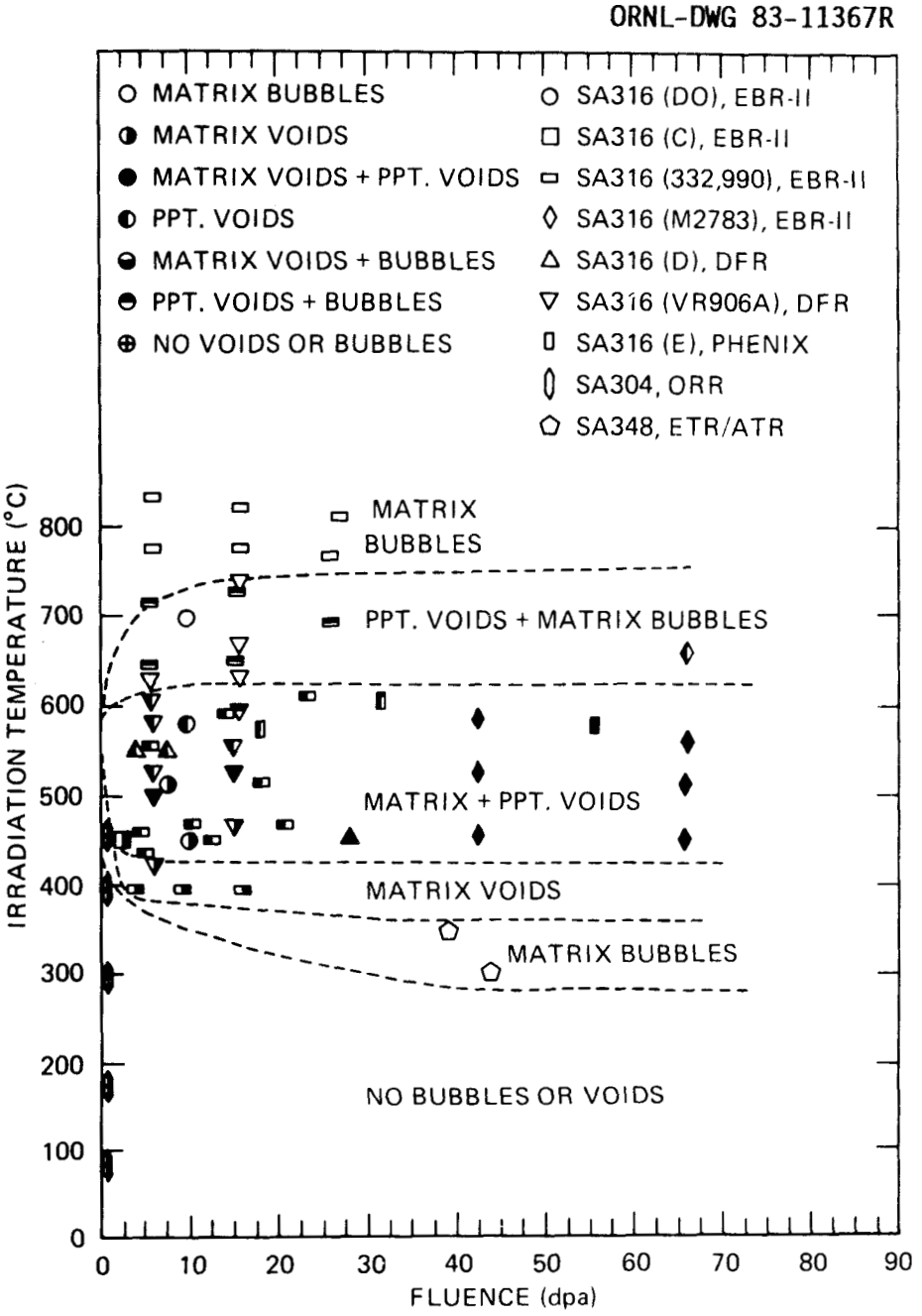

Figure 2.8. Character of cavities formed in fast neutron-irradiated, solution-annealed austenitic stainless steel; from Maziasz.[48] Data references in legend, from top to bottom, are: (1) Bloom and Stiegler,[150] (2),(3) Brager and Straalsund,[78] (4) Lee et al.,[174] (5) Cawthorne and Fulton, [97] (6) Barton et al.,[91] and Brammon et al.,[166] (7) LeNaour et al.,[167] (8) Bloom et al.,[168] and (9) Kenfield et al.[175]

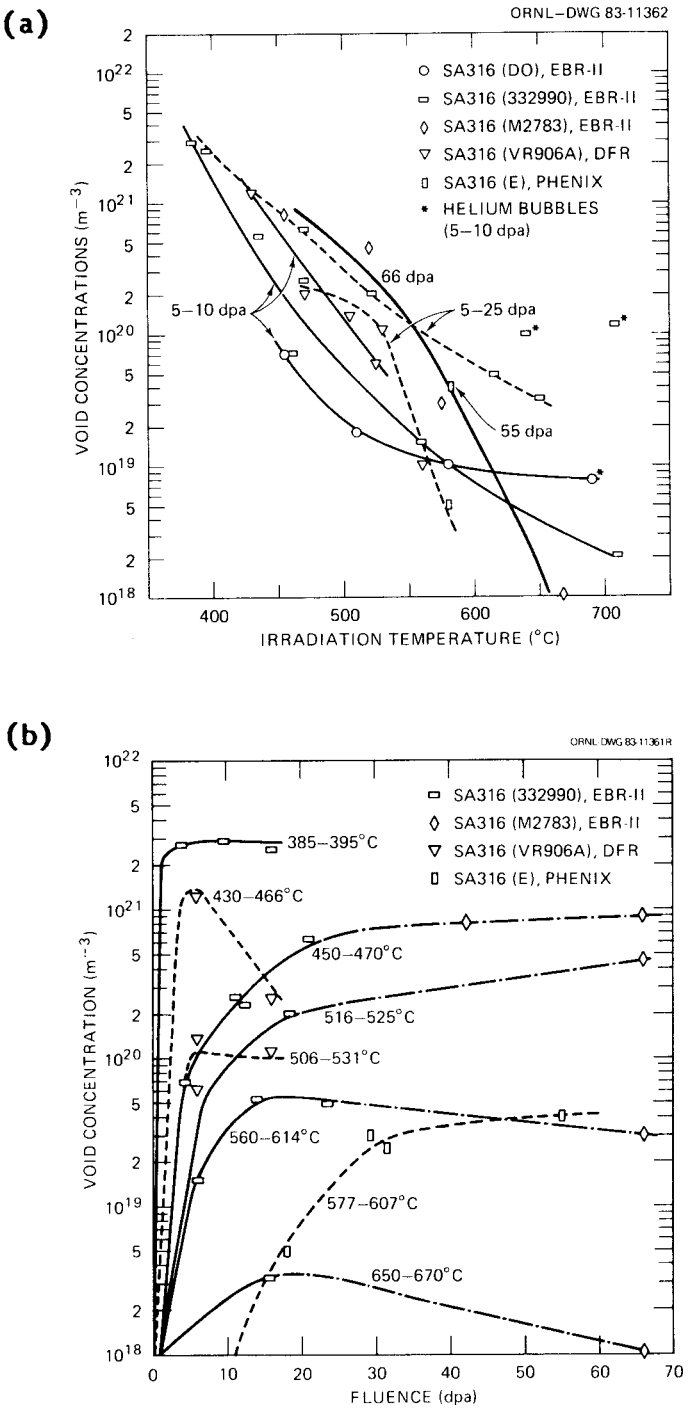

Figure 2.9. Temperature and fluence dependence of the void concentration in fast neutron-irradiated austenitic stainless steel; from Maziasz.[48] Data references in part (a) are, from top to bottom: (1) Bloom and Stiegler,[150] (2) Brager and Straalsund,[78] (3) Lee et al.,[174] (4) Barton et al.,[91] and Brammon et al.,[166] and (5) LeNaour et al.[167] Legend in (b) is consistent with (a).

Two likely causes for this observation are the precipitate acting as an efficient collection site for point defects and helium[176,177] and surface energy effects due to the precipitate/matrix interface.[108] Figure 2.9(a) and (b) show the temperature and fluence dependence of void concentration.[78,81,150,166,167] The general trends are: (1) a steep temperature dependence, sometimes with a change in slope near 500 to 550°C, and (2) the attainment of a temperature-dependent saturation value at a fairly low fluence. At high fluences, the voids reach diameters up to ~300 nm while the bubbles remain less than 5 nm (ref. 48). The bubble density may be much higher than the void density as shown in Figure 2.9(a) but their small size limits their contribution to the overall swelling.

The same general trends are also observed in 20% cold worked material. In early work the reported influence of cold working was to reduce swelling.[150,170] Patchy void formation was observed particularly in regions where the as-cold-worked dislocation network showed signs of recovery.[150] Later work following higher fluence irradiation experiments indicated that the primary influence of cold work was to extend the incubation time for void swelling and that once the incubation time had been exceeded similar void densities and swelling rates were observed.[77,166] This is consistent with the observed evolution toward a "steady state" dislocation structure which is independent of initial thermomechanical treatment as discussed above.

The scenario for void formation from helium-stabilized bubbles was described in Section 2.1. One consequence of void formation by this process should be the appearance of bi-modal cavity distributions. This would be the result of early bubble-to-void conversion and void growth leading to a lowered vacancy supersaturation. The reduced supersaturation would in turn result in an increased critical cavity radius effectively trapping a bubble population below the critical size. This result was explicit in the early modeling work of Odette et al.[102,103] and in a recent review, Mansur et al.[178] have collected an extensive list of references in which bi-modal distributions were reported in various irradiated materials. A part of Table 1 from that work[178] is reproduced in Table 2.4 and shows the broad experimental support for this mechanism of void formation. Mansur et al. pointed out that most of the references in Table 2.4 are fairly recent.[178] Earlier workers may not have observed the population of fairly small (~1 to 3 nm diameter) bubbles when using transmission electron microscopes which had more limited resolution. Therefore the phenomenon of bimodal cavity distributions may be even more general than Table 2.4 indicates.

2.4.4 Swelling Behavior

An overview of the swelling behavior of AISI type 316 stainless steel is provided by reference to the RS-1 experiment in the EBR-II.[82,83,152] This experiment was designed to irradiate a number of heats of 20% cold worked type 316 stainless steel to doses up to

Table 2.4. Reported observations of bimodal cavity size distributions in austenitic stainless steels

Alloy	Source of Irradiation	Investigators	Reference
Type 316 SS	Neutrons (EBR-II)	Brager & Straalsund (1973)	78
Type 316 SS	Neutrons (HFIR)	Maziasz et al. (1976)	179
Type 316 SS	Neutrons (EBR-II)	Maziasz & Grossbeck (1981)	95
Type 316 SS	Neutrons (EBR-II)	Hishinuma et al. (1982)	180
Type 316 SS	Neutrons (EBR-II)	Brager & Garner (1981,84)	181,182
Type 316 SS	Neutrons (HFIR)	Brager & Garner (1983,84)	96,183
Ti-modified PCA	Neutrons (HFIR)	Maziasz & Braski (1984)	184
Ti-modified PCA	Neutrons (HFIR)	Imeson et al. (1984)	185
Type 304 SS	Ions (He pre- or coinjection)	Spitznagel et al. (1982)	186
Type 316 SS	Ions (He coinjection)	Kohyama et al. (1984)	187
Austenitic Fe-Cr-Ni-Mo	Ions	Sindelar et al. (1984)	188
Type 316 SS	Ions	Sindelar et al. (1985)	189
Ti-modified 316	Ions (He coinjection, pulsing)	Lee et al. (1983)	190
Type 316 SS	Ions (He pre- or coinjection)	Levy et al. (1985)	191
Austenitic Fe-Cr-Ni	Ions (He pre- or coinjection)	Lee & Mansur (1985)	192
Type 321 SS	Ions (He pre-injection)	Mazey & Nelson (1976)	157
Austenitic Fe-Cr-Ni-Mo	Ions (He pre- or coinjection)	Packan & Farrell (1979, 83)	61,193
Austenitic Fe-Cr-Ni	Ions (He co-injection)	Agarwal et al. (1979)	194
Ti-modified 316 SS	Ions (He pre- or coinjection)	Kenik et al. (1979, 81)	107,195
Type 304 SS	Ions (He pre- or coinjection)	Choyke et al. (1978,81)	196
Type 316 SS	Ions (He coinjection)	Wood et al. (1981)	197
Type 316 SS	Ions (He coinjection)	Ayrault et al. (1981)	198
Ti-modified 316	Ions (He coinjection)	Hishinuma et al. (1981)	180

85 dpa in the temperature range of 370 to 650°C. These conditions exceeded the requirements of temperature and dose required for service as cladding material in the first core of the Fast Flux Test Facility (FFTF). Several of the heats included in the RS-1 experiment were melted and formed in accordance with the specification for FFTF first core cladding.[93] These heats were designated BB, CN-13, CN-17, X and 81615C and will be collectively referred to below as the first core heats. The RS-1 experiment also included several other heats which did not meet first core specifications because of deviations in either composition or fabrication.

The swelling of the first core heats is shown as a function of irradiation dose in Figure 2.10(a) and (b). The irradiation dose in dpa was obtained by multiplying the reported fast fluence by a conversion factor which is dependent upon the neutron spectrum flux and hence upon the axial position in the core.[152] This is reflected in different conversion factors for different irradiation temperatures. A typical spectral-averaged displacement cross section for fast-reactor irradiations is 5 dpa per 10^{26} n/m^2 (E > 0.1 MeV). The actual values in the RS-1 experiment range from 4.6 to 5.2 (ref. 152). In Figure 2.10 the data have been shown as three trend bands for the temperature ranges indicated. These temperatures do not correspond to the design temperatures mentioned above since subsequent analysis has indicated the actual irradiation temperatures deviated from the design values.[189] Most earlier analyses of these data have not taken

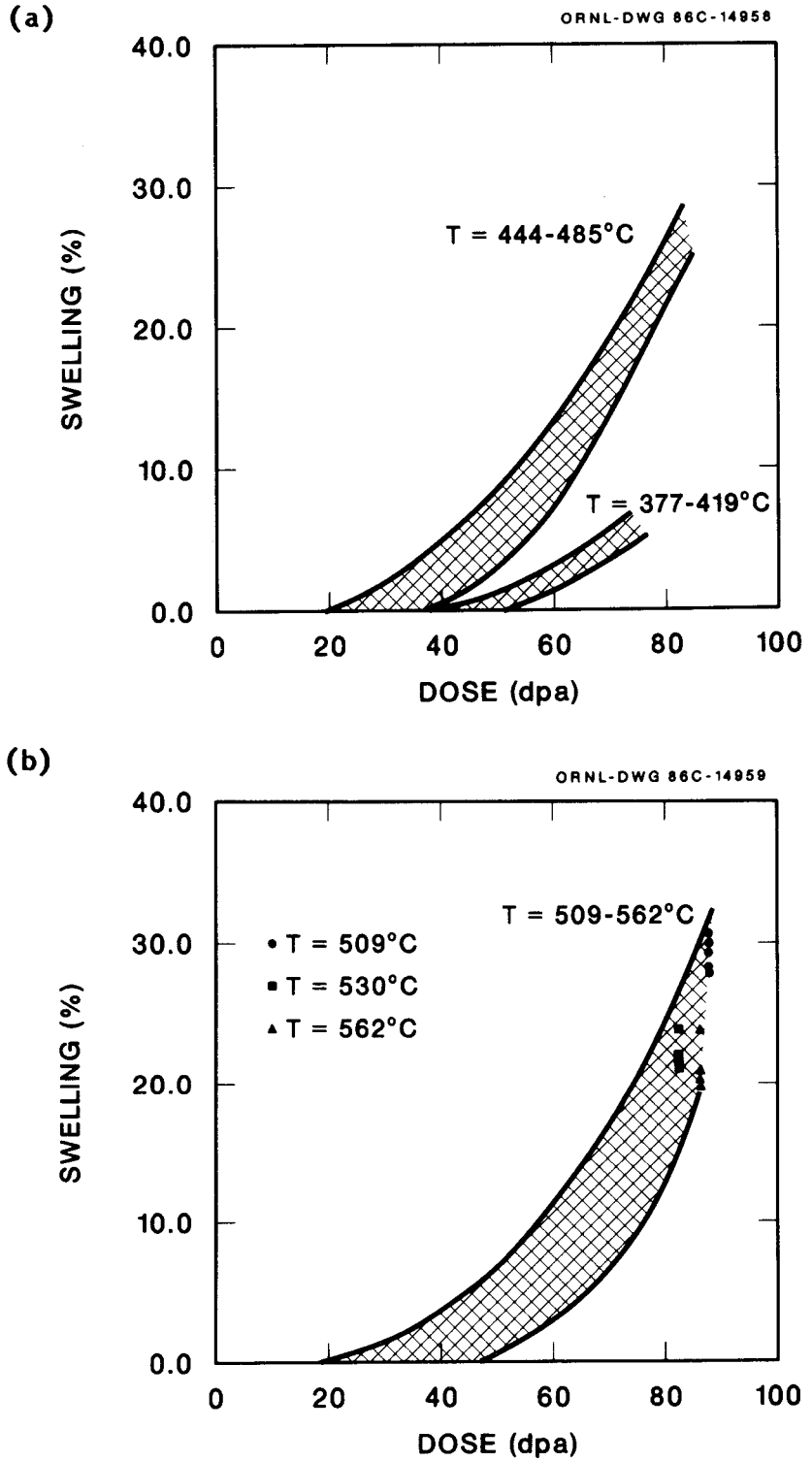

Figure 2.10. Fluence dependence of swelling of 20% cold-worked type 316 stainless steel in three temperature ranges. FFTF first core heats from the RS-1 experiment. Data from Bates and Korenko,[92] Yang and Garner,[93] and Garner.[152]

this information into account.[92,93,152,153,200] The deviations from the design temperatures increased with exposure due to unpredicted declines in the gamma heating.[199] Hence the experiment was not completely isothermal — the largest decrease was 30°C for the specimens designed to be at 650°C. This is potentially significant to the analysis of these results because of the reported sensitivity of swelling to temperature changes.[92,201,202] The temperatures used in this work are averages of the recalculated temperatures for the four discharges of the RS-1 experiment. These values are compared to the design values in Table 2.5. The actual temperatures shown in Table 2.5 reflect a significant compression of the temperature range when compared to the design values.

Table 2.5. Revised average and design irradiation temperatures in the RS-1 experiment

Temperature, °C	
Average	Design
377	370
396	400
419	433
444	467
465	500
485	533
509	567
530	600
562	650

The data in Figure 2.10 show the approximately bilinear swelling behavior referred to earlier. There is a temperature-dependent

incubation time followed by a transition to "steady state" swelling. The width of the data band is not solely due to the range of temperatures. The representative data points at each of the three temperatures in Figure 2.10(b) give an indication of the scatter at any one temperature. In addition, there are heat-to-heat variations in swelling.[76] This is illustrated by comparing Figure 2.10(b) with Figure 2.11 where all of the U.S. heats of 20%-cold-worked 316 stainless steel from the RS-1 experiment have been included. In the latter figure the scatter in the data at 80 dpa has almost doubled.

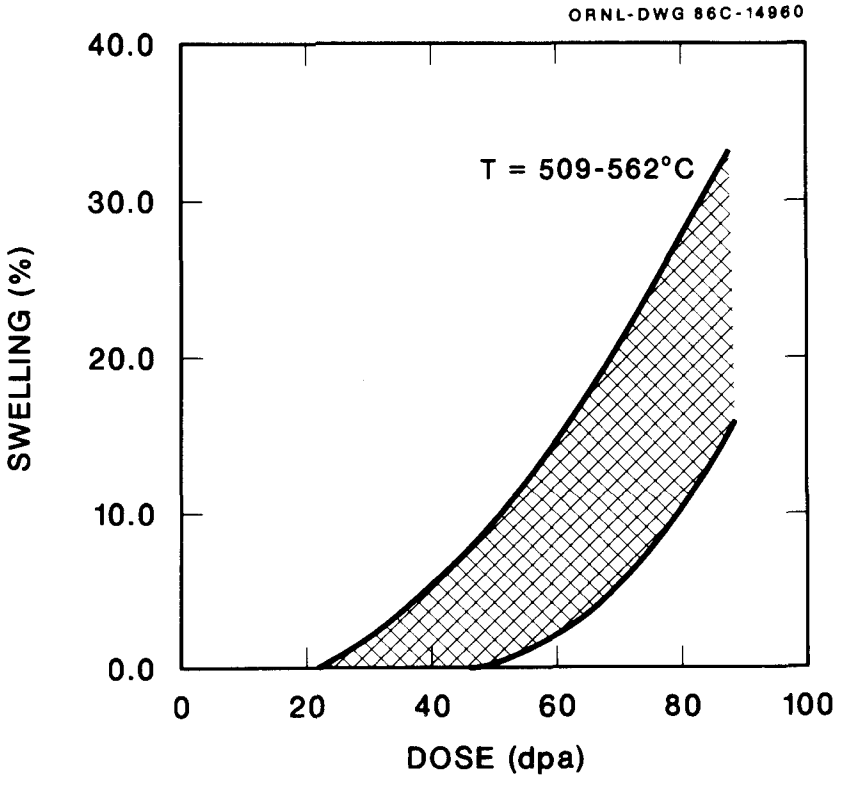

Figure 2.11. Fluence dependence of swelling at 509 to 562°C for all U.S. heats in the RS-1 experiment. Data from Bates and Korenko,[92] Yang and Garner,[93] and Garner.[152]

From an engineering standpoint, data such as shown in Figures 2.10 and 2.11 can be useful in spite of the scatter. For any reactor design, it is unlikely that the actual operating temperature of a component will be known with much greater certainty than the temperature ranges shown in these figures, and some temperature fluctuations may be anticipated. One can make conservative use of such data by using the upper bound of the data trend curves. It is more difficult to use these data for fundamental studies of the behavior of fast-neutron-irradiated materials. Nonetheless, in a sufficiently large data base, valid trends may be observed.

One attempt has been made to determine the temperature dependence of the swelling rate in the materials irradiated in the RS-1 experiment. Garner has pointed out the hazard of looking at the swelling rate when the irradiation dose is too low.[152,203] The approach followed here was to calculate the swelling rate assuming linear swelling between the values measured at the two highest doses. This dose increment was 50 to 59 dpa at 396°C, 62 to 72 dpa at 419°C, 51 to 60 dpa at 445°C, 69 to 82 dpa at 466°C, 62 to 74 dpa at 485°C, 74 to 87 dpa at 509°C, 70 to 81 dpa at 530°C, and 73 to 85 dpa at 562°C. Reference to Figure 2.10 indicates that, except for the lowest temperatures, such swelling measurements would be well beyond the incubation and transition regimes. The average linear swelling rates have been plotted in Figure 2.12 as a function of swelling. The swelling values on the abscissa of Figure 2.12 are the average of the two values over which the swelling rate was calculated. Figure 2.12(a)

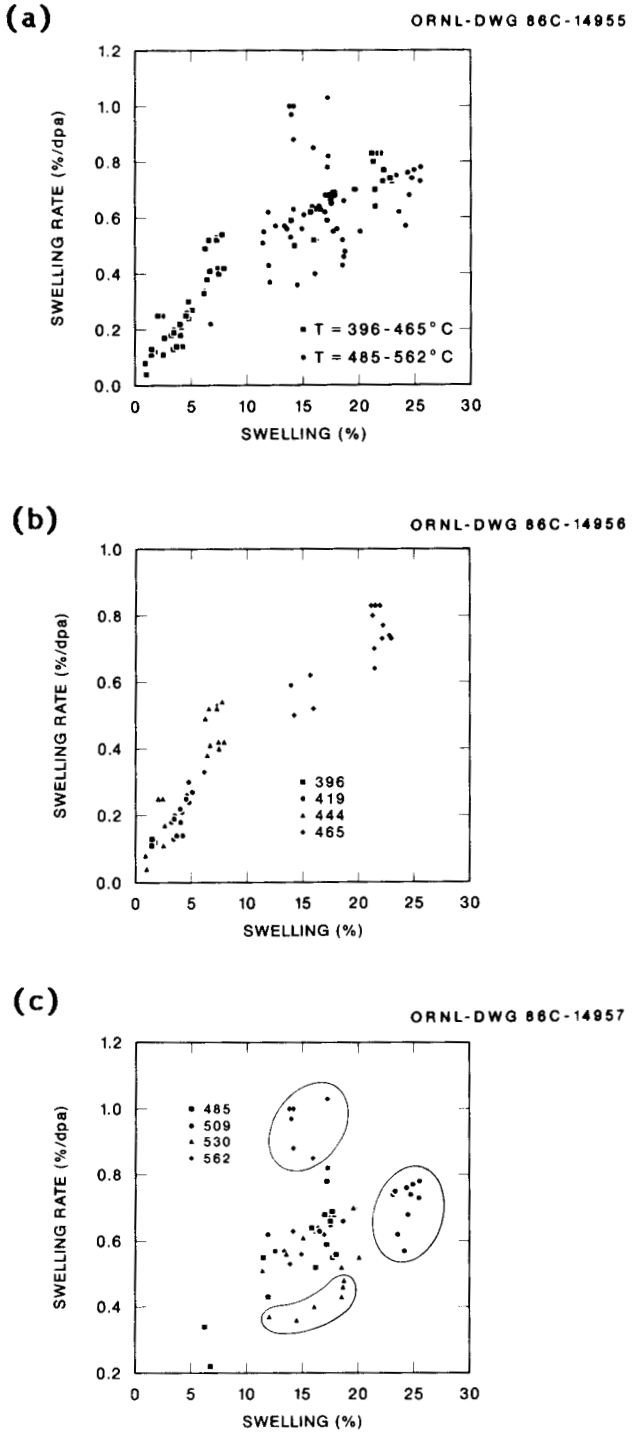

Figure 2.12. Swelling rate as a function of swelling for the indicated temperatures. Data from Bates and Korenko,[92] Yang and Garner,[93] and Garner.[152]

shows all the data broken into two rough temperature bands with most of the data approaching a value of about 0.8%/dpa at the highest swellings. The trend with swelling is clearer in Figure 2.12(b) where only the lowest four temperatures are plotted. Here the influence of the transition regime is clearly seen at the lowest swellings, as Garner indicated. No influence of temperature can be seen for these four temperatures. However, Figure 2.12(c) indicates that there may be some temperature dependence at the higher temperatures. This figure shows a region of considerable data scatter around 0.6%/dpa for all four temperatures. This scatter is to be expected given the scatter in the swelling data in Figures 2.10 and 2.11. However, there is also a clear separation of three groups of data at 509, 530 and 562°C. Data are available over the largest dose range at 509°C and the calculated swelling rates indicate that at this temperature the swelling rate is fairly constant between swellings of 12 and 25%. This supports the assumption that the calculated swelling rate of ~0.7%/dpa at 25% swelling represents a steady-state value. Therefore, the data at 562°C are particularly significant because the swelling rate is almost a factor of 2 greater than at 530°C at the same swelling and 50% higher than the 509°C data which is at an even higher swelling. Heat-to-heat variations cannot be responsible for this grouping because each temperature set has all five first-core heats included. The observed scatter at the three highest temperatures in Figure 2.12(c) do reflect specimen-to-specimen

variations at any one dose and temperature condition. These variations have been neglected in the data which were highlighted. Examining all the data indicates some overlap of the calculated swelling rates at the extremes, but this does not alter the conclusion of an apparent marked temperature dependence persisting to fairly high doses.

Four environmental or irradiation variables which are known to influence swelling are the damage rate,[187,204] He/dpa ratio,[48,54,107,193] stress[205-207] and temperature changes during irradiation.[92,201,202,208,209] Before closing this chapter, each of these four will be discussed in the light of the general theoretical concepts which are believed to govern void swelling. Some of these data will be discussed in more detail below when the results of the present work are described.

The effect of stress is perhaps the least ambiguous. Recent experiments[205-207] have shown that applied tensile stresses up to the proportional elastic limit of the material tend to decrease the swelling incubation time. Stresses in excess of the proportional elastic limit can extend the incubation time due to the introduction of additional dislocations in the specimen.[205,206] The effect is most significant at relatively high temperatures (i.e., greater than about 600°C). Garner et al.[206] summarized the results of several experiments and indicated that the following relationship described the influence of an applied hydrostatic stress, σ_H, on the incubation parameter,[93] τ, at a temperature, T:

$$\tau(T,\sigma_H) = \tau_o(T) - q(T)\ \sigma_H \quad . \tag{2.9}$$

In Equation (2.9) τ_o is the stress-free incubation parameter and q(T) is the experimentally determined stress correction factor.[208] Using the results of two heats of 20% cold-worked type 316 stainless steel, Garner et al. found $q(T) \sim 0.015 \times 10^{28}$ n/m²/MPa for T < 600°C, but that it rapidly increased at higher temperatures; q(T) = 0.061, 0.31 and 1.58 at 650, 700 and 750°C, respectively.

The temperature dependence of this effect correlates with the temperature dependence of the critical cavity size,[126,210] and stress has been shown to reduce the critical cavity size in a way which is consistent with the experimental observations.[211,212] The effect of stress is to increase vacancy emission from dislocations. This provides a small increase in the vacancy supersaturation. For high temperatures, where the supersaturation is low, this increment in the supersaturation due to stress can be significant. This would lead to a reduced critical cavity size and hence a reduced incubation time.

The effect of nonisothermal irradiation can also be understood in terms of the critical cavity size and the effect of temperature on microstructure. The dependence of swelling on temperature changes is somewhat complex, depending on whether the temperature change takes place early or late relative to the incubation time and whether the temperature increases or decreases. Yang and Garner have discussed several experiments.[92] Unfortunately, some of their analysis was

based on the erroneous, initially reported temperatures from the RS-1 experiment discussed above. This makes it difficult to determine both the sign and the magnitude of the temperature changes in some cases. The general trend in these experiments is for there to be a period following the temperature change during which the microstructures (cavity and dislocation densities) adjust to the new temperature. This is followed by swelling behavior which is characteristic of the new temperature. The influence of the previous temperature may persist if the microstructure, in particular the cavity density, does not reach the value which would be obtained in an isothermal irradiation at the new temperature.

Makin[209] has reported on a large number of high voltage electron microscope (HVEM) irradiation experiments. That work shows a strong correlation between the swelling rate at any temperature and the cavity density which has developed. He indicates that, following a change in temperature, the swelling rate is determined by the cavity density and the new temperature. Because the swelling rate is not a monotonic function of the cavity density, changes between any two temperatures can lead to either an increase or a decrease in the swelling rate.[209]

A representative example of the effect of temperature changes is provided by the data of Bates[202] which were also analyzed by Yang and Garner.[82] In one of these experiments, specimens which had been irradiated at nominal temperatures of 533, 600 and 650°C for up to about 25 dpa were reirradiated at 625°C for another 25 dpa. The

specimens which experienced the ±25°C temperature change evidenced little effect, while the specimens which experienced the 92°C temperature increase showed a clear reduction in swelling for about 15 dpa. The swelling was only about 0.5% at the time of the temperature change, and the results of the 93°C temperature increase are consistent with the behavior that would be expected if cavities which were small voids at 533°C were below the critical size at 625°C. Such cavities would shrink until subsequent irradiation had supplied additional gas to promote them to voids at the higher temperature. A second experiment involved large temperature reductions from initial values of 526 and 585°C to 416, 431 and 458°C (initial T = 526) and 423, 442, 498 and 503°C (initial T = 585°C). The temperature change was gradual and began at about 30 dpa, near the end of the incubation regime for an isothermal irradiation. The irradiation was terminated at 50 dpa. In all cases the swelling was significantly increased relative to isothermal irradiation and the increase was greater for specimens which saw greater temperature decreases. This result can also be understood in terms of the effect of temperature on the critical size. Cavities which were subcritical at the higher temperatures would exceed the critical size for unstable void growth as the temperature decreased. This would result in an abrupt termination of the incubation regime and rapid swelling.

The effect of damage rate in experiments which use charged particles to simulate neutron damage has received considerable attention because such dose rates are typically a factor of 100 to 1000 times

the fast reactor value.[74,76,213-215] However, dose rate has often been a neglected variable in neutron-irradiation experiments. These experiments typically experience dose rates which vary by at least a factor of 2 as a result of spectral differences between various locations in the reactor.[152,167,204] Recent data from the French fast breeder reactors PHENIX and RHAPSODIE have demonstrated that such relatively small variations in the dose rate can have a major effect on microstructural evolution.[167,204] That work involved irradiations at temperatures between 577 and 617°C up to about 55 dpaF (1 dpaF ~ 0.77 dpa NRT). The dose rate in these irradiations varied between 6×10^{-7} and 2×10^{-6} dpaF/sec. The major trends observed include: (1) a higher dose rate increases the total dislocation density as a result of enhanced loop formation and (2) the higher dose rate results in an extended swelling incubation time. These two results are consistent with the higher dislocation density leading to a reduced vacancy supersaturation at low doses. This would in turn increase the critical cavity size and hence increase the dose required for the cavities to become voids. The actual situation may be somewhat more complex since the higher dose rate would also tend to increase the vacancy supersaturation.

The effect of the He/dpa ratio on microstructural evolution has been examined most extensively in charged particle irradiations; the major observations have been summarized above. One significant result from a dual ion irradiation is shown in Figure 2.13 (ref. 107).

YE-13597

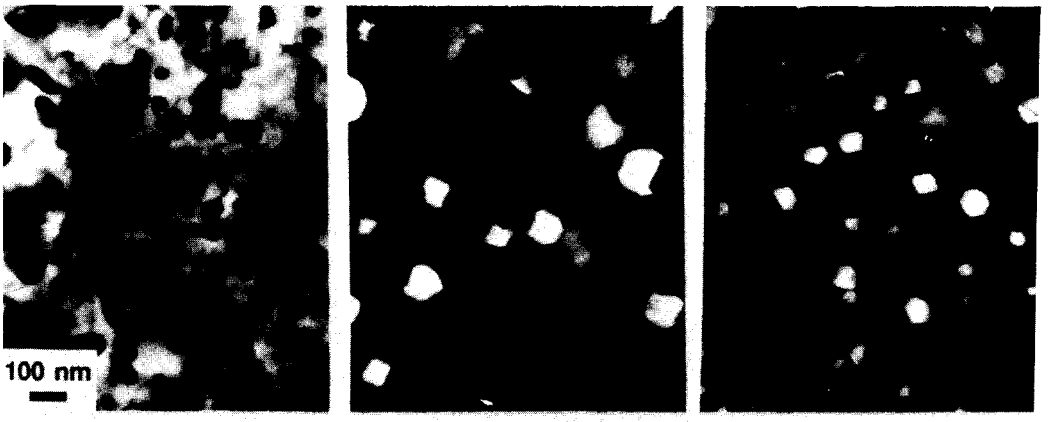

Figure 2.13. Influence of He/dpa ratio on cavity formation and void swelling in a titanium-modified type 316 stainless steel irradiated to 70 dpa at 625°C. Photographs from Kenik and Lee, ref. 107.

In this experiment, Kenik and Lee irradiated a titanium-modified type 316 stainless steel with 4 MeV Ni ions to 70 dpa at 625°C. The He/dpa ratio was varied by injecting helium to the desired level using a second accelerator. The value of 0.2 appm He/dpa represents near fast breeder conditions, and the 20 appm He/dpa simulates fusion conditions. The no-helium case provides a reference point for the others. The results indicate that swelling may not be a monotonic function of the He/dpa ratio. This observation is consistent with theoretical work which predicted a swelling peak at intermediate He/dpa ratios.[108] This follows directly from the observed He/dpa ratio dependence of the cavity density and the critical radius concept. If one adopts the low He/dpa ratio result as a reference case, small increases in the He/dpa ratio serve primarily to shorten the swelling incubation time by providing more gas to drive bubble-to-void conversion. If

incremental increases in the cavity density are also observed, then higher swelling rates could also result if the cavities do not become the dominant sink in the system. For large increases in the He/dpa ratio, an alternate path of cavity evolution may be followed. In this case high bubble densities result in an extended incubation time as the helium and vacancies must be partitioned to many sinks. If the cavities become the dominant sink, bubble-to-void conversion may be eliminated altogether and only bubble swelling would be observed.

Only a limited amount of information about He/dpa ratio effects has been obtained under fast-neutron irradiation. Most of this work has involved comparisons of irradiation experiments in the EBR-II and the HFIR. There is sufficient data from both reactors to permit direct comparisons for only one heat of solution-annealed and 20% cold-worked type 316 stainless steel, the DO-heat.[48,54,95,153,181,182,183,216] The comparison is somewhat complicated by differences in damage level and irradiation temperature as well as uncertainties about the HFIR irradiation temperatures. The dose dependence of the DO-heat swelling data is shown in Figure 2.14 (ref. 153). The data shown in Figure 2.14 indicate that the increased He/dpa ratio in the HFIR can lead to either increases (SA) or decreases (CW) in swelling relative to EBR-II. This observation can be understood if the cavity distributions for the various conditions are examined. A comparison of these cavity distributions is shown in Figure 2.15. Parts (a) and (b) of Figure 2.15 compare specimens of 20% cold-worked DO-heat that

YE-13605

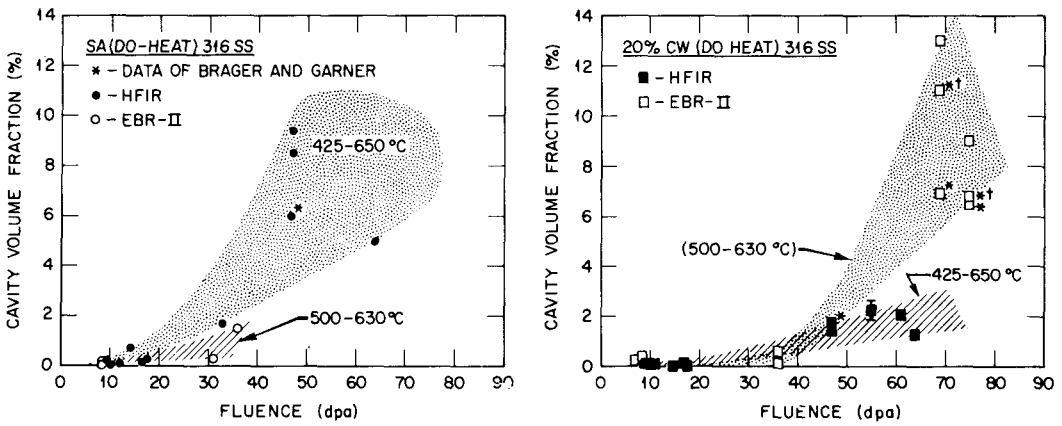

Figure 2.14. Comparison of the swelling behavior of solution-annealed and 20% cold-worked DO-heat in the HFIR and EBR-II. Figures from Maziasz, ref. 153.

were irradiated in the EBR-II (a) and HFIR (b). The irradiation temperatures were 500 to 550°C and dose was 69 dpa in EBR-II and 61 dpa in the HFIR. There is a clear qualitative difference between the cavity microstructures which have evolved. The HFIR specimen has a high density of fairly small bubbles, while the EBR-II specimen has primarily large voids, many of which are attached to precipitate particles. The apparent influence of the higher He/dpa ratio in the HFIR has been to promote bubble formation to such a degree that the bubbles have failed to reach the critical size by 61 dpa.

A comparison of solution-annealed specimens irradiated in the EBR-II and the HFIR is shown in Figure 2.15(c,d). Although the dose is somewhat lower for the solution-annealed specimens, the solution-annealed material from the HFIR is quite similar to either cold-worked or solution-annealed material in the EBR-II. The difference

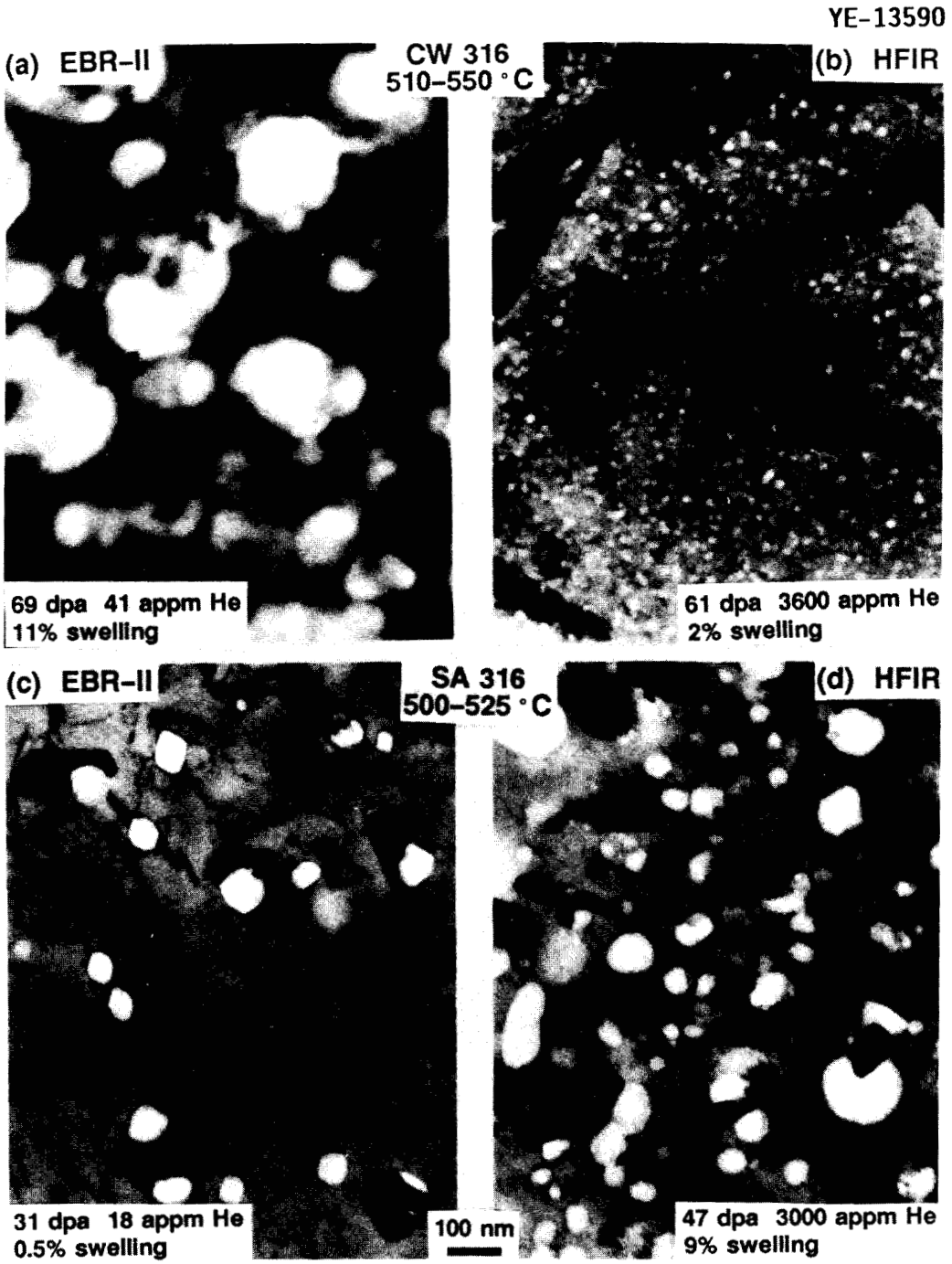

Figure 2.15. Comparison of the cavity distributions observed in the DO-heat of type 316 stainless steel after irradiation in the EBR-II (a,c) and HFIR (b,d) at 500 to 550°C. Specimens shown in (a) and (b) were initially 20% cold-worked while those in (c) and (d) were solution-annealed. (Photographs courtesy of P. J. Maziasz, ORNL).

between the cold-worked and solution-annealed material in the HFIR could be an effect of the initial dislocation density on bubble formation. Dislocations are known to provide favorable bubble nucleation sites and at low doses a higher bubble density forms in the cold-worked material. This can lead to swelling suppression by the helium and vacancy partitioning arguments advanced above. The bubble density in the solution-annealed material apparently failed to reach a sufficiently high value to suppress void formation. In this latter case the effect of the higher helium level was to shorten the swelling incubation time by promoting bubble-to-void conversion. These results tend to confirm the hypothesis advanced by Odette and co-workers[102,103] that microstructural control may be one method of suppressing (or delaying) swelling in austenitic stainless steels. Recent work by Maziasz and Braski[183,217] and by Mansur et al.[178] supports this contention.

Finally, it should be pointed out that an alternative interpretation of the high fluence fast reactor swelling data and the HFIR/EBR-II comparison has been advanced by Garner and Brager[86,153,181-183,218-221] and Garner and Wolfer.[222] These workers have focused on the effects of compositional fluctuations and the evolution of precipitation under irradiation and contend that it plays the dominant role in determining the response of irradiated alloys;[221] they indicate that microstructural evolution is due to a concurrent microchemical evolution which involves primarily carbon, silicon and nickel. They state that the average nickel content of the matrix is a reliable indicator

of having attained the "steady state" swelling rate in austenitic stainless steels. If C_C, C_{Si} and C_{Ni} are the initial atomic fractions of these alloy components, then the critical matrix nickel content is given to be $C^*_{Ni} = C_{Ni} - 3\ (C_{Si} + C_C)$ (ref. 221). For a type 316 stainless steel, $C^*_{Ni} \sim 9\%$. This nickel depletion of the matrix is a result of the formation of precipitates which are rich in both nickel and silicon. Some of these nickel- and silicon-rich precipitate phases are thermally stable (e.g., eta) and are enhanced under irradiation while others do not form thermally in type 316 stainless steel (e.g., γ' and G phase) and appear to be radiation induced.[68,88,106,223,224]

Radiation-induced solute segregation is known to play a significant role in the microstructural evolution of irradiated materials.[76] For example, point defect diffusivities are known to be sensitive to the concentrations of solutes such as silicon.[225,226] The depletion of the fast diffusing silicon would tend to increase the effective vacancy supersaturation by lowering the self-diffusion coefficient. This would in turn permit easier void formation.[227] However, the fact that nickel has been observed to segregate to void surfaces[167,228] seems inconsistent with the argument that voids preferentially form in nickel-depleted regions. Maziasz[68] has pointed out that the observed nickel depletion may be a result of void formation, and not the cause.

The influence of the He/dpa ratio on microstructural and microchemical evolution remains an unresolved controversy. While Maziasz and co-workers see significant qualitative and quantitative differences between the results of DO-heat irradiations in the HFIR and EBR-II,[48,53,95,101,228] Garner and Brager report relatively little effect.[181,182,218] The latter workers point out that the absolute swelling levels in some cases are not too different in the two reactors and believe that the progression of an inevitable microchemical evolution will eventually lead to the same behavior at any He/dpa ratio. However, a recently completed experiment lends support to the conclusion that swelling can be influenced by the He/dpa ratio via its effect on the cavity density.[230] This experiment included both solution-annealed and 20% cold-worked specimens of the U.S. fusion program's prime candidate alloy (PCA) and N-lot type 316 stainless steel. The specimens were irradiated in the HFIR for about 22 dpa at 400, 500 and 600°C. These same specimens were then irradiated at the same temperature in the FFTF for another 35 dpa. Based on experiments in the EBR-II, irradiation of the 20% cold-worked N-lot specimens to 60 dpa in a fast reactor neutron spectrum should have led to about 10% swelling. The observed swelling in the sequential irradiations was about 0.5% at 600°C and 1.8% at 500°C. The swelling of the other specimens in this experiment was similarly reduced. These observations are consistent with the high He/dpa ratio in the HFIR having led to a high bubble density that suppressed subsequent

bubble-to-void conversion in the FFTF which has a much lower He/dpa ratio. This could result from a combination of two effects: (1) the high bubble density can suppress the vacancy supersaturation leading to an increased critical cavity size and (2) the available helium must partition to more bubbles requiring more time for any one bubble to obtain the critical number of gas atoms. Higher fluence irradiation in the FFTF and microstructural examination of these specimens should help clarify these results. The resolution of this issue has significant implications for near-term fusion reactors and some of the work presented below aims to improve the theoretical understanding of the influence of the He/dpa ratio.

CHAPTER 3

THEORETICAL MODELS

This chapter contains a discussion of the theoretical models which have been developed and used in this work. The assumptions upon which these models are based and the limitations to their use are discussed where appropriate. This work builds on the foundation of the rate theory, as discussed in Section 2.3. The new work presented here includes the development of analytical expressions for helium bubble parameters using a hard sphere equation of state, a direct comparison of the importance of helium and vacancy accumulation in void nucleation and the development of a detailed composite model of microstructural evolution. Rather than foregoing a discussion of the results of the calculations until a later chapter, it seemed most natural to discuss these results as they are presented. The key results will once again be summarized in Chapter 5.

The philosophy which guided the modeling effort was to include sufficient detail so as to permit the description of the physical processes which are known to be important while avoiding unnecessary complexity. "Sufficient" detail can be defined as that level of model sophistication which permits one to predict observed data trends for the experimental conditions of interest, while "unnecessary" complexity is that which leads to a proliferation of largely unknown physical parameters. There is some trade-off involved here. Even simple models include parameters for which no well-defined value exists.

Model predictions can vary significantly depending on the values assumed for parameters such as the dislocation-interstitial bias or the matrix surface free energy. In addition, equivalent results can often be obtained with different sets of parameter values. More detailed models typically have more parameters. However, including more detail (additional physical mechanisms) can constrain the problem by limiting the range of parameter values which give rise to reasonable predictions. This will be discussed in more detail below.

3.1 Helium Equation of State

3.1.1 Introduction

Before proceeding to describe the general features of the models, the equation of state used to compute helium bubble parameters will first be discussed. The importance of transmutant helium in promoting void formation was described above; hence modeling void swelling requires solution of equations describing helium bubble behavior. The ideal gas law provides a first approximation for this purpose; however, for small bubbles the internal gas pressures are much too high to be adequately described by this simple equation of state.

The three parameters of most interest are the stable bubble radius, r_b, the critical bubble radius, r_c^* and the critical number of helium atoms, m_{He}^*. Expressions for these parameters are first derived for the ideal gas case. The use of a more complicated hard sphere equation of state is then discussed. Numerical calculations of the helium bubble parameters using the hard sphere equation of state are

presented and compared with the ideal gas results. The comparison indicates that the functional dependence of the critical bubble parameters on a variety of physical variables is generally preserved. This has permitted the formulation of two "master curves" which describe the deviation from ideal gas behavior as a function of the effective vacancy supersaturation only. The use of the master curves provides simple analytical expressions for the minimum critical radius $r_c^*(m_{He}^*)$ and m_{He}^* analogous to the ideal gas results. In addition, the helium bubble radius computed using the hard sphere equation of state was found to deviate in a systematic way from the ideal gas radius. Hence, a third master curve was developed which allows the direct calculation of the "real gas" bubble radius from the ideal gas value. A rate theory based model of void swelling was used to demonstrate that results obtained using the analytical expressions preserved the accuracy of numerical solutions.

3.1.2. Critical Helium Bubble Parameters

In the context of the rate theory description of void swelling,[74,108,231] the equation describing the growth rate of a cavity with radius r_c is:

$$\frac{dr_c}{dt} = \frac{1}{r_c} \left(Z_v^c D_v C_v - Z_i^c D_i C_i - Z_v^c D_v C_v^c\right) \quad , \tag{3.1}$$

where $Z_v^c D_v C_v$ and $Z_i^c D_i C_i$ are the point defect fluxes impinging on a cavity of radius r_c, and $Z_v^c D_v C_v^c$ is the rate of vacancy emission from

the cavity. The parameters F_s and F_v in Equation (3.1) are geometric terms used to compute the surface area ($F_s r_c^2$) and volume ($F_v r_c^3$) of nonspherical cavities.[74,231] For a sphere, $F_s = 4\pi$ and $F_v = 4\pi/3$. Values for F_s and F_v will be discussed in Section 3.3.1.1. The capture efficiencies (Z_v^c and Z_i^c) in Equation (3.1) are frequently taken to be equal to 1.0; here they reflect the multiple sink strength correction to the cavity sink strength as given in Section 3.3.1.3. The vacancy concentration in local equilibrium with the cavity is:

$$C_v^c = C_v^e \exp\left[\frac{\Omega}{kT}\left(\frac{2\gamma}{r_c} - P\right)\right] . \qquad (3.2)$$

In Equation (3.2) C_v^e is the thermal equilibrium vacancy concentration, Ω is the atomic volume, γ is the surface free energy, P is the cavity's internal gas pressure and kT has its usual meaning. In the following discussion, two types of cavities are distinguished. Cavities which are stabilized by their internal gas pressure (i.e., $P \sim 2\gamma/r_c$) are referred to as bubbles while cavities which are primarily agglomerations of vacancies, $P \ll 2\gamma/r_c$, are called voids.

3.1.2.1 Ideal Gas Results

For purposes of illustration, the ideal gas behavior will be considered first. A typical plot of Equation (3.1) is shown in Figure 3.1, where m_{He} is the number of helium atoms in the cavity and r_b and r_c^* denote the stable bubble and critical bubble radii, respectively. The parameter S is the effective vacancy supersaturation:

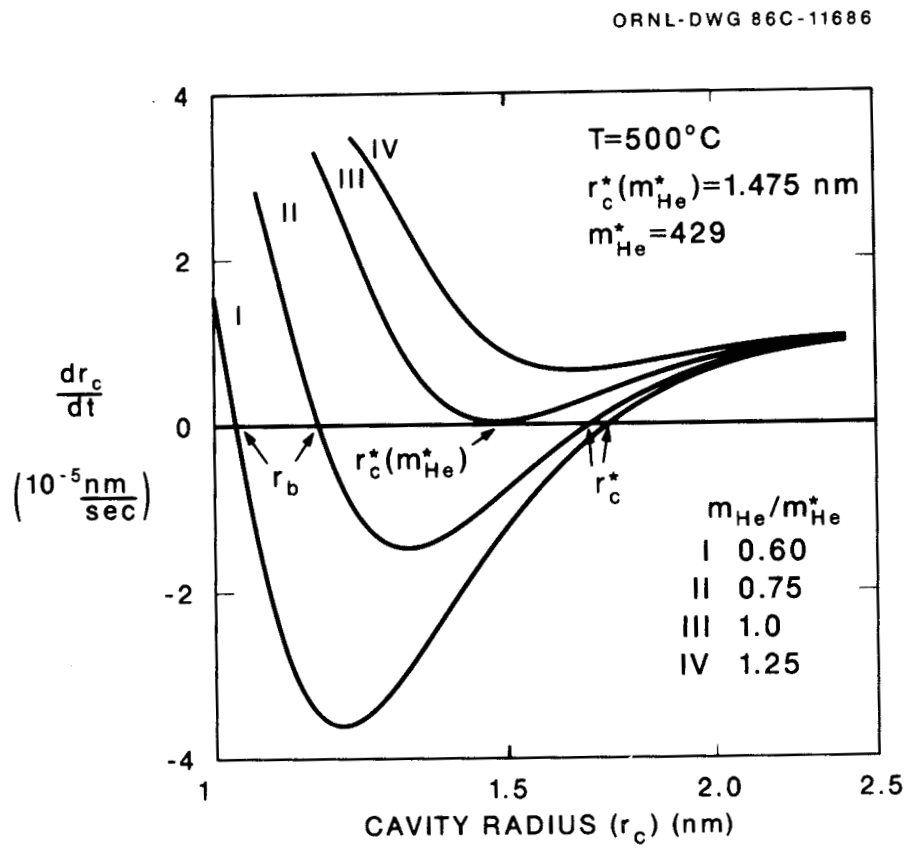

Figure 3.1. Typical plot of the cavity growth rate as a function of the cavity radius.

$$S = \frac{Z_v^c D_v C_v - Z_i^c D_i C_i}{Z_v^c D_v C_v^e} \quad . \tag{3.3}$$

Due to the irradiation-induced vacancy supersaturation, r_b generally exceeds the radius of an equilibrium bubble with the same helium content by a small fraction; hence P is somewhat less than $2\gamma/r_b$. The roots of Equation (3.1) can be obtained by substituting Equation (3.2) for C_v^c in Equation (3.1) and setting $P = m_{He}\ kT/F_v r_c^3$. Equation (3.1) then becomes:

$$r_c^3 - \left(\frac{2\gamma\Omega}{kT\ \ln S}\right) r_c^2 + \frac{m_{He}\ \Omega}{F_v\ \ln S} = 0 \quad . \qquad (3.4)$$

The curves labeled I and II, III and IV in Figure 3.1 represent three different cavity states: subcritical, critical, and supercritical, respectively. Mathematically, they describe the situations in which Equation (3.1) or Equation (3.4) have: (1) three real and unequal roots; (2) three real roots of which at least two are equal; or (3) one real root and two conjugate imaginary roots.[232] One of the three roots of Equation (3.4) is always negative. When they exist, the real and positive roots are denoted here r_b and r_c^*. The region of negative dr_c/dt in Curves I and II represents a barrier to void nucleation. If a cavity absorbs excess vacancies without a proportional increase in m_{He}, the probability of vacancy emission is increased, and the cavity (bubble) will tend to shrink back to r_b. Of course, statistical fluctuations would still allow a small number of cavities to reach r_c^*, at which time they would be considered voids. This is the process of classical nucleation. For cavities larger than r_c^*, no barrier to further growth exists, and such cavities grow unstably by vacancy absorption. In Curve III, $m_{He} = m_{He}^*$ and $r_b = r_c^*$. This case represents bubble-to-void conversion by the accumulation of transmutant helium. This is believed to be the most likely mechanism of void formation in irradiated stainless steels. For damage rates characteristic of neutron irradiation conditions, classical nucleation rates are much too low to explain the experimentally observed void densities. This is particularly true for temperatures greater than about 500°C,

even when effects such as solute segregation or heterogeneous nucleation are involved.[54,76,83-85,87] Finally, Curve IV would describe a cavity with $m_{He} > m^*_{He}$ for which only void growth is possible. In this case there are no physically realistic roots to Equation (3.4), and the void radius must be computed by integrating Equation (3.1) directly. The critical bubble parameters will be discussed further in the context of void nucleation in Section 3.2.2.2.

The critical number can be obtained by solving Equation (3.4) for the case in which $r_b = r^*_c$.[232] The critical radius is in turn found by substitution. The results are:

$$m^*_{He} = \frac{32F_v}{27}\left[\frac{\gamma}{kT}\right]^3\left[\frac{\Omega}{\ln S}\right]^2 \quad ; \tag{3.5}$$

$$r^*_c(m^*_{He}) = \frac{4\gamma\Omega}{3kT\ln S} \quad . \tag{3.6}$$

These equations reveal the important parametric dependencies of r^*_c and m^*_{He} and can be used in modeling studies to predict the point at which helium stabilized bubbles convert to voids. However, as will be shown in the next section, Equation (3.5) significantly overpredicts the value of the critical number, and Equation (3.6) underpredicts the minimum critical radius when compared to the values obtained with a hard sphere equation of state.

3.1.2.2 Results Using Hard Sphere Equation of State

The equation of state used in this study was developed by Brearley and MacInnes.[233] Compressibilities computed using their

hard sphere equation of state (HSEOS) show good agreement with the somewhat limited amount of high pressure helium data. Although this data was taken at a relatively low temperature (~65°C), the fact that the approximation of gas atoms as rigid spheres improves at higher temperatures and pressures provides confidence in the required extrapolation.[233] The equation of state has the following form:

$$\frac{PV}{m_{He}kT} = \frac{(1+y+y^2-y^3)}{(1-y)^3} \quad , \tag{3.7}$$

where $y = \pi\, m_{He} d_g^3/6V$ and d_g is the hard sphere diameter of the gas atoms. The value of d_g is determined by the interatomic potential assumed. Following Brearley and MacInnes, the modified Buckingham potential has been used and $d_g = 0.3135\ [0.8542 - 0.03996\ \ln(T(K)/9.16)]$ nm.

An examination of Equation (3.7) indicates that the real gas analog of Equation (3.4) would be a twelfth order equation rather than a cubic since $V = F_v\, r_c^3$. Hence, there is no longer an analytical solution for r_c^* and m_{He}^*. However, Equations (3.1), (3.2), and (3.7) have been implemented using a numerical solution to obtain r_c^* and m_{He}^* for a variety of irradiation conditions. In Figures 3.2 and 3.3 representative values are shown along with the ideal gas values. The irradiation parameters are typical of fast reactor conditions as discussed below in Section 3.3.1.4. The effect of the equation of state is most pronounced at the lower temperatures where high vacancy supersaturations result in small critical radii – hence high compressibilities.

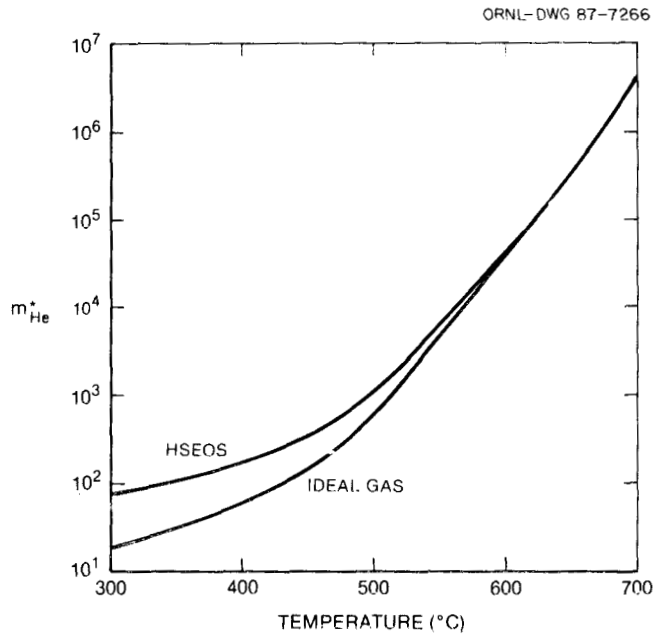

Figure 3.2. Temperature dependence of critical number (m^*_{He}) for typical fast reactor irradiation conditions. The value for ideal gas behavior and the HSEOS are shown.

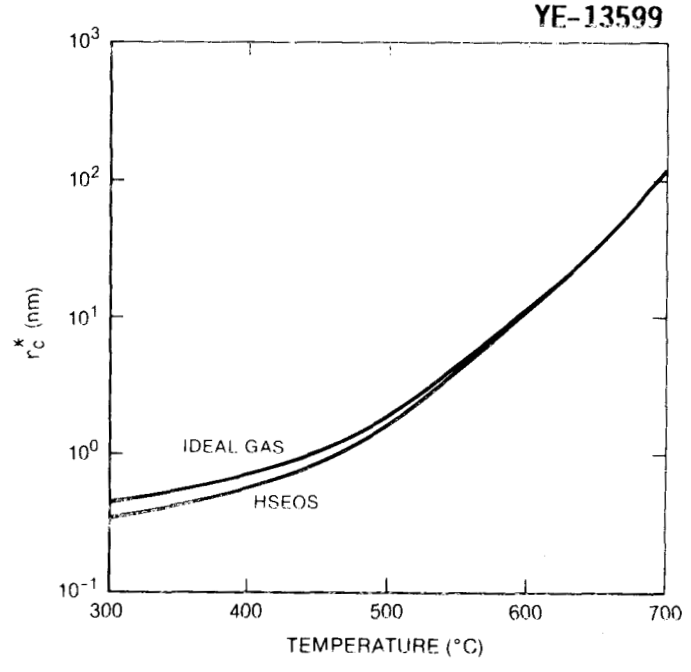

Figure 3.3. Temperature dependence of critical radius (r^*_c) for typical fast reactor irradiation conditions. The values for ideal gas behavior and the HSEOS are shown.

A further comparison is given in Figure 3.4 where the ratio of the real to ideal gas critical parameters are plotted as a function of the effective supersaturation. Using the parameters of Section 3.3.1.4 and ref. 108, effective supersaturations of 137, 4.57, and 1.19 correspond to the temperatures 400, 500, and 600°C, respectively.

The value of m^*_{He} computed using HSEOS begins to deviate significantly from the ideal gas value for temperatures less than about 550°C, and for T < 500°C, the difference exceeds a factor of 2. Thus the use of the ideal gas law to compute m^*_{He} would overpredict the dose required to achieve bubble-to-void conversion at any given helium generation rate. Alternately, the use of the ideal gas law would require the adjustment of some parameter in Equation (3.5) (e.g., the

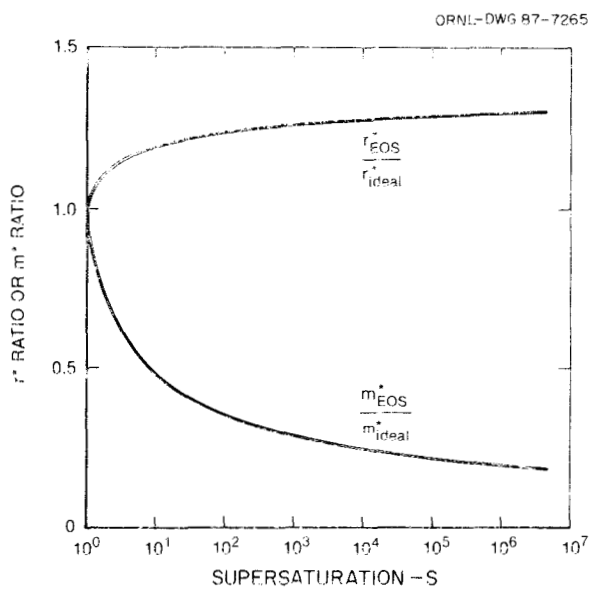

Figure 3.4. Ratio of critical bubble parameters computed with HSEOS to ideal gas values.

surface energy) in order to obtain agreement between theory and experimentally observed swelling incubation times.

The discrepancy in the predicted value for m^*_{He} increases with increasing vacancy supersaturation (decreasing irradiation temperature). Hence the impact of the choice of equation of state is potentially greatest when attempting to predict first wall swelling in near term fusion reactor designs which typically have low operating temperatures.[234] Of course, in such modeling studies this impact is somewhat mitigated by other uncertainties, notably helium partitioning.[235]

In order to eliminate the need for cumbersome iterative solutions when using the HSEOS, the results of numerous calculations of r^*_c and m^*_{He} were examined to determine their functional dependencies. It was found that for a broad range of irradiation conditions, the real gas critical number and critical radii could be computed as:

$$m^*_{He} = f_1(\Phi)\, F_v \left(\frac{\gamma}{kT}\right)^3 \left(\frac{\Omega}{\Phi}\right)^2 \quad ; \tag{3.8}$$

$$r^*_c\,(m^*_{He}) = f_2(\Phi)\, \frac{\gamma\Omega}{kT\,\Phi} \quad ; \tag{3.9}$$

where $\Phi = \ln S$ and f_1 and $f_2(\Phi)$ are real gas correction factors which approach the ideal gas values of 32/27 and 4/3, respectively, for low supersaturations. Figures 3.5 and 3.6 are plots of f_1 and f_2. Note that the range of supersaturations encompassed in these figures includes any reasonable value expected under either fast breeder or fusion conditions. Hence, the results can find broad application in a variety of modeling studies. One example of such a use will be given below.

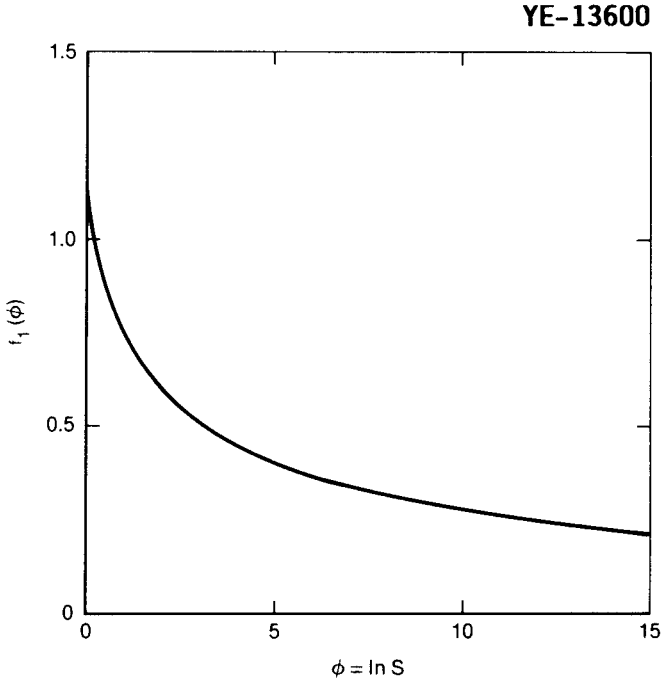

Figure 3.5. Master curve for obtaining critical number (m^*_{He}) using HSEOS.

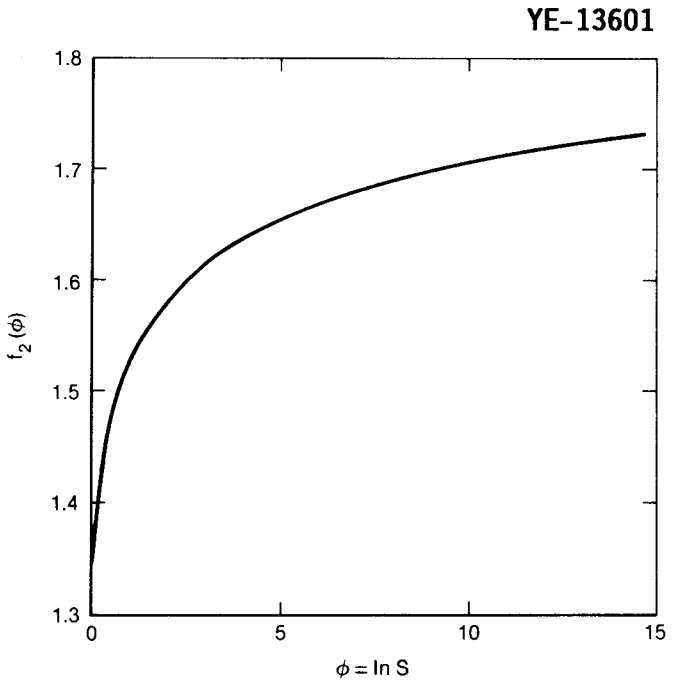

Figure 3.6. Master curve for obtaining critical radius (r^*_c) using HSEOS.

The "master" curves shown in Figures 3.5 and 3.6 are tenth order polynomial fits of the pointwise determined values of m^*_{He} and r^*_c.

$$f_1 = a_0 + a_1\Phi + a_2\Phi^2 \ldots + a_{10}\Phi^{10} \quad ; \qquad (3.10a)$$

$$f_2 = b_0 + b_1\Phi + b_2\Phi^2 \ldots + b_{10}\Phi^{10} \quad ; \qquad (3.10b)$$

The polynomial coefficients are given in Table 3.1.

Table 3.1. Polynomial coefficients for master curves in Figures 3.5, 3.6, and 3.8 [see Equations (3.8)-(3.13)]

i	a_i	b_i	c_i
0	1.1802288	1.3368825	$-7.3006207 \times 10^{-3}$
1	$-7.9391797 \times 10^{-1}$	3.8733464×10^{-1}	4.5820315
2	5.7059961×10^{-1}	$-3.2338567 \times 10^{-1}$	$-1.3153813 \times 10^{+1}$
3	$-2.7545689 \times 10^{-1}$	1.6904814×10^{-1}	$4.0631158 \times 10^{+1}$
4	8.4271137×10^{-2}	$-5.4081633 \times 10^{-2}$	$-1.1590146 \times 10^{+2}$
5	$-1.6549585 \times 10^{-2}$	1.0909847×10^{-2}	$2.3303617 \times 10^{+2}$
6	2.1091198×10^{-3}	$-1.4139331 \times 10^{-3}$	$-3.0597821 \times 10^{+2}$
7	$-1.7313693 \times 10^{-4}$	1.1733086×10^{-4}	$2.5718364 \times 10^{+2}$
8	8.8188621×10^{-6}	$-6.0190901 \times 10^{-6}$	$-1.3349066 \times 10^{+2}$
9	$-2.5326847 \times 10^{-7}$	1.7369785×10^{-7}	$3.8976532 \times 10^{+1}$
10	3.1317501×10^{-9}	$-2.1550751 \times 10^{-9}$	-4.8969485

Because of the high order of polynomial fit, two precautions should be mentioned when these master curves are used. Extrapolations outside the range of supersaturations shown in Figures 3.5 and 3.6 must be avoided. This should pose no significant limitation, however, since these figures include $1.0 < S < 3 \times 10^6$, while for either fast reactor or fusion irradiation conditions, $1.0 < S \lesssim 2 \times 10^5$ for temperatures from 300 to 700°C. More importantly, care should be taken

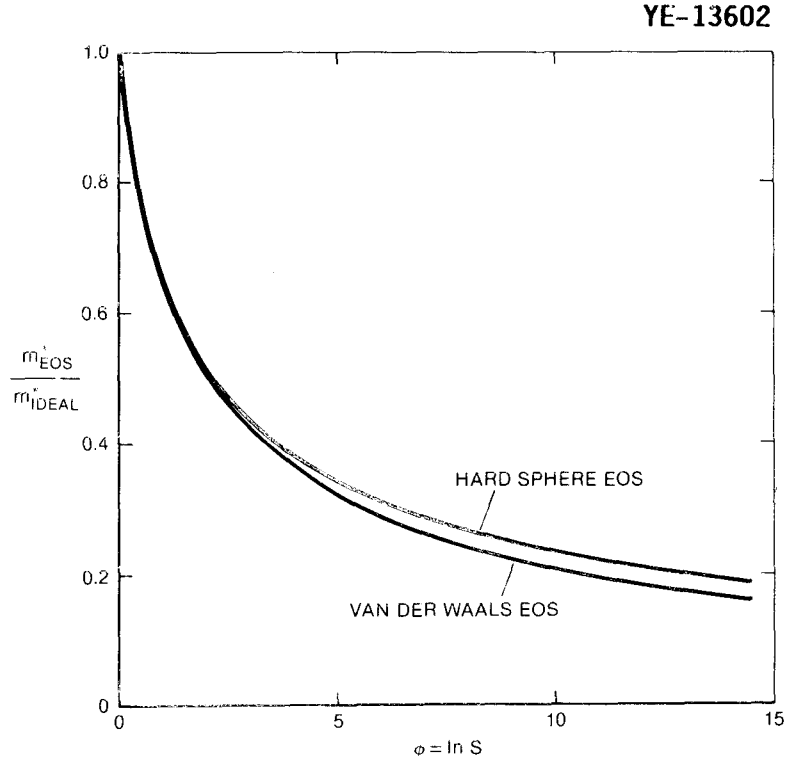

Figure 3.7. Comparison of critical number (m^*_{He}) calculations using HSEOS and a similar expression using a Van der Waals equation of state. The Van der Waals result is from Coghlan and Mansur.[234]

to include all of the significant digits listed in Table 3.1 for each coefficient in order to ensure the accuracy of the fit. Note that the zero order coefficients are not exactly equal to values obtained in the ideal gas limit. This is a result of the residual error in the polynomial fit, but the deviation is quite small (~1%).

Coghlan and Mansur have investigated r^*_c and m^*_{He} using a Van der Waals equation of state and have also derived analytical expressions for these terms.[236,237] Their expression for m^*_{He} is compared to Equation (3.8) in Figure 3.7 where the ratio of m^*_{He} computed using the

alternate equations of state to the ideal gas value is plotted as a function of the effective supersaturtion. The two expressions agree very well for supersaturations less than about 5, which corresponds to temperatures greater than about 500°C. Even for higher supersaturations, the difference is less than 20%. Both expressions tend toward the ideal gas value for very low supersaturations.

3.1.3 Stable Bubble Radius Using Hard Sphere Equation of State

In addition to the critical bubble parameters, the ability to compute r_b as a function of m_{He} is also required in order to model the swelling incubation regime. For example, r_b is used in helium partitioning calculations. For the ideal gas case, various methods can be used to find r_b from Equation (3.4); an analytical solution exists[232] or standard root-finding techniques can be applied.

The use of the HSEOS eliminates the above-mentioned analytical solution and significantly complicates root finding since the equation analogous to Equation (3.4) is now twelfth order. An effort was made to relate the ideal gas bubble radius to the bubble radius computed with the HSEOS. Figure 3.8 shows the ratio of the ideal to real gas bubble radii as a function of a reduced radius:

$$R(nm) = \left[\frac{r_b^{ideal}\ kT}{\gamma}\right]^{1/3} . \qquad (3.11)$$

The plot suggests the existence of a third master curve which will yield the real gas bubble radius directly from the ideal gas

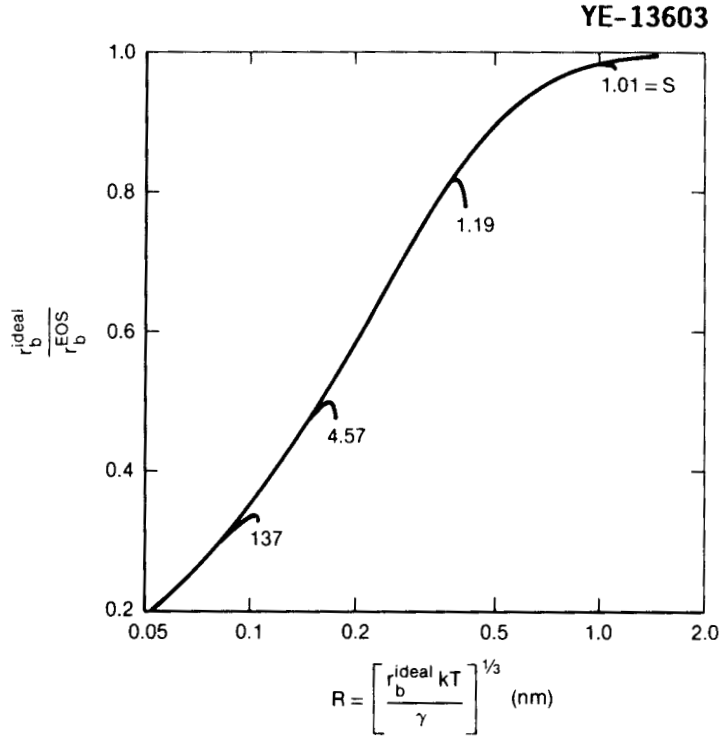

Figure 3.8. Master curve for obtaining stable bubble radius (r_b) using HSEOS from the ideal gas value.

values. The master curve was found to be the curve for no irradiation, i.e., S = 1. This curve overlays the S = 137, 4.57, 1.19, and 1.01 curves in Figure 3.8.

This master curve has also been fit using a tenth order polynomial:

$$f_3(R) = c_0 + c_1 R + c_2 R^2 \ldots + c_3 R^{10} \quad , \tag{3.12}$$

and the polynomial coefficients are given in Table 3.1. Using Equation (3.11), the real gas bubble radius can be computed as:

$$r_b^{real} = \frac{r_b^{ideal}}{f_3(R)} \quad . \tag{3.13}$$

Equations (3.11–3.13) are valid over the entire range of reasonable values of r_b ($\gtrsim$0.20 nm). The deviation of the bubble radius computed using the master curve from the actual radius is small but increases near r_c^*. The increased deviation from the master curve near $r_b = r_c^*$ is a result of the fact that as m_{He} approaches m_{He}^* the ratio of r_b to the equilibrium bubble radius (r_b^{eq}) begins to diverge from linearity. This is shown in Figure 3.9 where the ratio r_b/r_b^{eq} has been plotted as a function of m_{He} for T = 500°C, S = 4.57, $F_v = 4\pi/3$ and $\gamma = 1.588$ J/m^2. For these conditions, $m_{He}^* = 541$. This error has a negligible effect on the results of a detailed model calculation of cavity evolution as is shown in the next section.

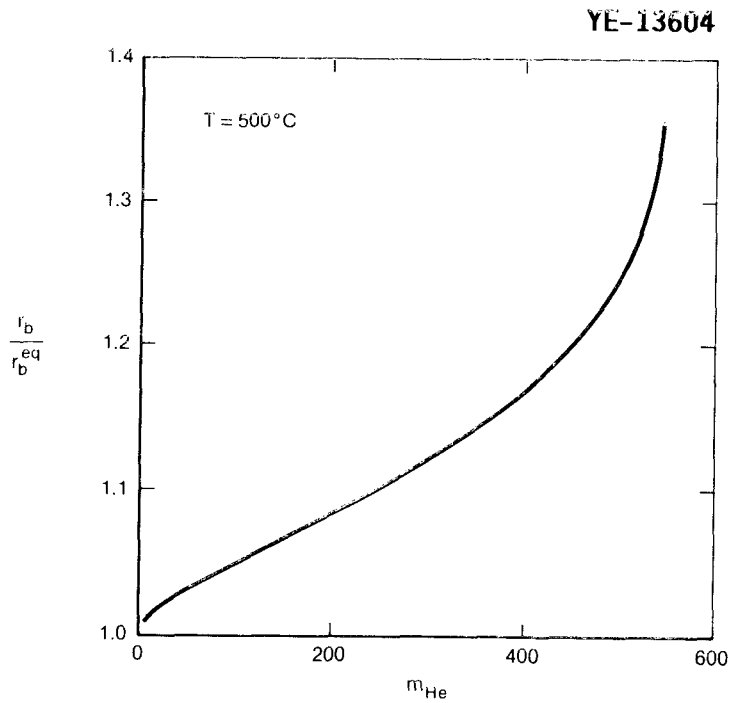

Figure 3.9. The ratio of the bubble radius under irradiation to the equilibrium bubble radius as a function of the helium content of the bubble. For these conditions, $m_{He}^* = 541$.

3.1.4. Application of Analytical Approximations

The validity of the analytical solutions developed for use with the HSEOS was tested using the rate theory model of void swelling which is discussed below. For this comparison, the model was used to predict void swelling under fast reactor irradiation conditions up to 100 dpa.[106] The helium bubble radii prior to conversion and the bubble-to-void conversion criterion were first computed numerically. The bubble-to-void conversion criterion was that the numerical search for r_b fail as a result of m_{He} exceeding m^*_{He}. Then in a modified procedure, Equations (3.11)–(3.13) were used to compute the stable bubble radius and the bubble-to-void conversion criterion was that the accumulated helium in a bubble exceed m^*_{He} as computed by Equation (3.8).

Table 3.2 compares the dose at bubble-to-void conversion, τ_c, and the swelling at 100 dpa at the indicated temperatures as calculated using the analytical approximations with the results obtained using

Table 3.2. Comparison of swelling parameters using numerical and analytical solutions

T (°C)	τ_c (dpa)		Swelling (% at 100 dpa)	
	Iterative	Analytical	Iterative	Analytical
450	45.89	47.05	24.41	24.59
500	38.46	38.51	28.77	28.78
550	34.63	34.60	35.45	35.64
600	35.31	35.10	39.53	40.08
650	44.43	43.33	28.79	30.16
700	N/A	N/A	0.18	0.19

the numerical solutions. The agreement is quite good and significant computational simplification has been gained.

3.2 Mechanisms of Void Formation

3.2.1 Introduction

A general description of void formation by two alternate mechanisms was given in Chapter 2. Here these two mechanisms will be discussed in detail and a method developed to test their relative importance for irradiation conditions typical of either fast breeder reactor core components or a DT fusion reactor first wall.

The first of these two paths is classical stochastic nucleation theory. Early researchers who applied homogeneous nucleation theory to the problem of void formation in austenitic stainless steels include Harkness and Li,[238] Katz and Wiedersich[239] and Russell.[70] Russell and co-workers have continued to develop the stochastic theory over the past ten years and have included some effects of helium and heterogeneous nucleation.[82,83,87,240,241] Wolfer and co-workers have developed a Fokker-Planck formulation of the void nucleation problem and have explored the effects of mobile di-vacancies and solute segregation to void surfaces.[84,85,242] Despite these refinements, the classical theory fails to predict the experimentally observed void densities in the intermediate to high temperature range ($450 < T < 700°C$) where measurable void swelling occurs in these steels.[81,82,85] As discussed above, an alternate mechanism has been proposed to cause void formation at these temperatures and to promote void formation at

low temperatures. This mechanism was first proposed by Sears[243] and involves the growth of small gas-stabilized bubbles until they reach a critical size beyond which further gas accumulation is not required to promote growth.

The mathematical derivation of the critical bubble parameters from the equation for the cavity growth rate has just been given in Section 3.1. Theoretical and recent experimental work has shown that the time required for such bubbles to reach the critical size correlates well with observed void swelling nucleation times.[103,108,124,182,244,245] This work will focus on the influence of transmutant helium because it is believed to be the most significant bubble-stabilizing gas. For example, Sindelar et al. have used degassed specimens to show that residual oxygen can have a major effect on void nucleation in a model austenitic alloy during heavy ion irradiation with no helium implantation.[86] However, when this same alloy is co-implanted with helium during the irradiation, the effect of the helium appears to swamp that of the oxygen.[246] Accordingly, one can envision two limiting paths for void formation on a population of subcritical helium/vacancy clusters; one is limited to growth by helium accumulation alone and the other to growth by stochastic fluctuations in the vacancy cluster population. A recent discussion concerning the relative magnitudes of these two processes provided some of the impetus for this work.[247]

3.2.2 Models of Void Formation

The two methods discussed below compute a characteristic time for nucleation or the nucleation rate per cluster for a helium/vacancy cluster with a given number of helium atoms. The number of vacancies in this cluster or bubble is computed assuming that the bubble radius is that of a stable bubble in an irradiation environment characterized by a vacancy supersaturation S given in Equation (3.3) at a temperature T. The bubble radius and the gas pressure in the bubble are computed using the hard sphere equation of state described in Section 3.1.

For both models, the point defect concentrations are computed using the conventional rate theory and the temperature dependent sink strengths for extended defects discussed in Section 3.3.1.3. The calculated sink strength of the subcritical bubble population was insignificant when compared to the other sinks in the system; therefore it is not included when computing the point defect concentrations. The calculations assume that only the mono-defects and helium gas atoms are mobile and that the only defects which the bubbles emit are vacancies. The use of the principle of detailed balance and thermodynamic equilibrium[23,24] leads to the following form for the vacancy emission rate from a cluster containing n vacancies and m helium atoms;

$$\alpha_v^n = F_s r(n-1,m)\, D_v C_v^e \exp\left\{\frac{1}{kT}\left[G(n,m) - G(n-1,m)\right]\right\} \quad . \qquad (3.14)$$

where the free energy in the equilibrium situation is:

$$G(n,m) = F_s r(n,m)^2 \gamma + mkT\ell n(P) \quad . \qquad (3.15)$$

where γ is the surface free energy, P is the pressure in the bubble and F_s is the geometric factor to account for nonspherical clusters.

3.2.2.1 Nucleation by Stochastic Fluctuations

The method developed here is similar to that of Katz and Wiedersich,[238] Clement and Wood[248] and Mansur and Wolfer.[250] In general, a family of equations can be written describing the concentrations, C_k, of discrete size classes containing k, k+1, k+2, ... up to n_v^{max} vacancies.

$$\frac{dC_1}{dt} = G_v + C_2(\beta_i^2 + 2\alpha_v^2) - C_1(\beta_v^1 + \beta_i^1) - D_v C_1 S_T^v \; ; \qquad (3.15a)$$

$$\frac{dC_k}{dt} = \beta_v^{k-1} C_{k-1} + C_{k+1}(\beta_i^{k+1} + \alpha_v^{k+1}) - C_k(\beta_i^k + \beta_v^k) \; . \qquad (3.15b)$$

In Equation (3.15), the $\beta_{i,v}^k$ terms are the interstitial and vacancy impingement rates on a cluster with k vacancies and the α_v^k have been given above.

$$\beta_{i,v}^k = F_s r(k,m) \, D_{i,v} C_{i,v} \; . \qquad (3.16)$$

C_1 of course equals C_v. The value of n_v^{max} can be arbitrarily large. A specific choice for its value will be discussed below. The term G_v in Equation (3.15a) is the total vacancy source term due to atomic dislocements and vacancy emission from extended defects. The last term in Equation (3.15a) represents the loss of vacancies to all the

other sinks in the system. The sink strengths for vacancies of the network dislocations, S_ρ^v and the subgrain structure, S_g^v are computed as described in Section 3.3.

$$S_T^v = S_g^v + S_\rho^v \quad . \tag{3.17}$$

The temperature dependence of these sink strengths is consistent with experimental observation.[108] It should be pointed out that the void nucleation rate is quite sensitive to the dislocation density as will be shown below. It is therefore important that calculations such as these include appropriate temperature dependent values of this and other microstructural parameters.

In order to simplify the equations used below, the terms which describe the shrinkage of a given cluster will be grouped together.

$$\gamma_k = \alpha_v^k + \beta_i^k \quad . \tag{3.18}$$

The nucleation regime can be defined as that region in vacancy cluster size space for which $\gamma_k > \beta_v^k$. Because of the radius dependence of the vacancy emission term and the existence of a supersaturation of vacancies under irradiation, a critical size is reached beyond which growth rather than shrinkage is the dominant process. The number of vacancies which correspond to this critical size will be designated n_v^*.

The steady state nucleation rate, J_{ss}, can be obtained from Equation (3.15) in one of two ways. The first solution involves computing what is commonly termed the constrained equilibrium cluster size distribution which is obtained by imposing the requirement that there be no net flux from one cluster size class to the next, i.e.

$$J_k = \beta_v^k C_k - \gamma_{k+1} C_{k+1} = 0 \quad , \tag{3.19}$$

for all values of $k \geq 1$. This solution requires the calculation of pseudo-free energies of formation for clusters in each size class, resulting in an exponential cluster distribution for $n \leq n_v^*$. However, this method introduces the artificial result that the number of clusters begins to increase in size classes for which $n > n^*$. The values of the cluster concentrations in the constrained equilibrium distribution are elevated relative to the steady state distribution for $n \leq n_v^*$ also; this is accounted for in the theory by the introduction of the so-called Zeldovich factor. The use of this method to compute void nucleation rates is adequately discussed elsewhere.[79,83]

The second method for obtaining the steady-state nucleation rate from Equation (3.15) is to set all of the fluxes [Equation (3.19)] equal to the steady state flux, J_{ss}. This leads to a family of equations:

$$J_1 = \beta_v^1 C_1 - \gamma_2 C_2 = J_{ss} \quad ; \tag{3.20}$$

$$J_2 = \beta_v^2 C_2 - \gamma_3 C_3 = J_{ss} \quad ; \tag{3.20b}$$

$$J_3 = \beta_v^3 C_3 - \gamma_4 C_4 = J_{ss} \quad ; \tag{3.20c}$$

$$J_{N-1} = \beta_v^{N-1} C_{N-1} - \gamma_N C_N \quad ; \tag{3.20d}$$

where, to simplify the equations, $N = n_v^{max}$.

Let the ratio $\gamma_k/\beta_v^k = \rho_k$ for all $k \geq 2$ and let $\rho_1 = 1$. Then this system of equations can be solved by multiplying the equations for J_k by the product of all the ρ_k with $k \leq i$. Hence Equation (3.20b) is multiplied by ρ_2, Equation (3.20c) is multiplied by both ρ_2 and ρ_3 and so on. If the resulting equations are summed, all the C_k are eliminated except C_1 and C_N, yielding

$$J_1 = J_{SS} = \frac{\left[\beta_v^1 C_1 - \gamma_N C_N \prod_{j=2}^{N-1} \rho_j\right]}{1 + \sum_{k=2}^{N-1} \prod_{j=2}^{k} \rho_j} \quad . \tag{3.21}$$

The term in the numerator in Equation (3.21) involving the products of the ρ_j can safely be eliminated by noting two facts. First, since the problem being considered is nucleation, the concentration of the mono-defect, C_1, will in general be much greater than C_N. In fact the distribution is approximately exponential as the constrained distribution suggests. Secondly, it has already been pointed out that the ratio of the shrinkage to growth terms, ρ_j, is less than unity for $n > n_v^*$. Hence for N sufficiently greater than n_v^* the product of the ρ_j contains many fractional terms. Therefore,

$$J_1 = J_{SS} = \beta_v^1 C_1 \left[1 + \sum_{k=2}^{N-1} \prod_{j=2}^{k} \rho_j\right]^{-1} \quad . \tag{3.22}$$

The appropriate value of N can be determined numerically to ensure that J_{SS} has converged. The advantage of using this method to compute

J_{ss} is the elimination of the Zeldovich factor and the approximations which must be made to compute it.

Each of the J_k in Equation (3.20) can be defined in an analogous way to Equation (3.21); i.e.,

$$J_k = \beta_v^k C_k \left[1 + \sum_{i=k+1}^{N-1} \prod_{j=k+1}^{i} \rho_j \right]^{-1} . \qquad (3.23)$$

The nucleation rate per cluster of a given size is then,

$$j_k = J_k / C_k = \beta_v^k \left[1 + \sum_{i=k+1}^{N-1} \prod_{j=k+1}^{i} \rho_j \right]^{-1} . \qquad (3.24)$$

The characteristic time for this process would be just the reciprocal of this fractional nucleation rate:

$$\tau_k = j_k^{-1} . \qquad (3.25)$$

The time τ_k is generally much greater than the time required to establish the steady-state cluster population. This latter time can be computed using the classical nucleation theory[78,83] and varies from 4×10^4 sec at 400°C to 3×10^5 sec at 500°C for the parameters used here. The corresponding values of τ_k will be shown below.

3.2.2.2 Nucleation by Helium Accumulation

The second void formation mechanism is that of a helium-stabilized bubble obtaining the critical number of gas atoms. This critical number of gas atoms, m_{He}^*, is a function of both the material and irradiation parameters, as shown in Equations (3.5) and (3.8).

The critical bubble size corresponding to m^*_{He} is in general not the same as the critical size associated with n^*_v discussed above. Their relationship was shown in Figure 3.1. For a fixed value of the vacancy supersaturation, the family of curves shown in Figure 3.1 represent four different levels of helium. The curves labeled I and II contain a region in radius space for which the net growth rate is negative. This region corresponds to the void nucleation barrier and the stochastic nucleation theory deals with the probability that fluctuations will permit a bubble to grow from the stable bubble radius r_b to the critical radius r^*_c. This latter radius is that corresponding to n^*_v. The curve labeled III is the curve for which $m = m^*_{He}$ and the growth rate is everywhere non-negative. The point at which curve III is tangent to the x axis is $r(m^*_{He})$ and is also the minimum critical radius. Hence the minimum critical radius is a special case of the critical size calculated from the stochastic theory.[103,124]

In order to compute a characteristic time for nucleation by helium accumulation, it is necessary to assume a model for the partitioning of helium among the various microstructural features. Since the procedure used here is similar to that which will be discussed in Section 3.3, only a brief summary will be given. The model assumes that the sink strengths for helium are the same as those for vacancies except that the dislocation sink strength for helium is reduced by a factor f^{He}_{ρ} (refs. 235,251). This parameter has a nominal value of 0.5 and is varied in the analysis to determine its effect. As mentioned above, because the sink strength of the subcritical bubbles is small,

it is neglected when computing the matrix helium concentration C_{He} but the subgrain structure is included. The total system sink strength for helium is then:

$$S_T^{He} = S_g^v + f_\rho^{He} S_\rho^v \quad , \tag{3.26}$$

and C_{He} can be computed at steady state as

$$C_{He} = \frac{G_{He}}{D_{He} S_T^{He}} \quad , \tag{3.27}$$

where G_{He} is the helium generation rate and D_{He} is the helium diffusivity.

The formation of bubbles on dislocations is accounted for by permitting a fraction of the helium trapped by dislocations to be "piped" to bubbles. This fraction, f_b^{He}, is treated as a parameter in the analysis.

Based on the foregoing helium partitioning model, the arrival rate of helium atoms at a bubble with a radius r(n,m) is

$$\beta_{He} = D_{He} C_{He} \left[\bar{F}_s r(n,m) + \frac{\bar{f_b^{He} f_\rho^{He} S_\rho^v}}{N_c} \right] \quad , \tag{3.28}$$

where N_c is the total number of bubbles among which the helium from the dislocations is partitioned. This bubble density is taken from ref. 108 and reflects experimentally observed values. The temperature

dependent expression for N_c is given in Table 3.3. The radius, r(n,m) is computed as discussed in the previous section using Equations (3.11–3.13).

Equations (3.27) and (3.28) can be combined to eliminate the helium diffusivity.

$$\beta_{He} = \frac{G_{He}}{\Omega N_c S_T^{He}} \left[F_s r(n,m) N_c + f_b^{He} f_\rho^{He} S_\rho^v \right] \quad . \tag{3.29}$$

The characteristic time for a bubble containing m helium atoms to reach the critical number is then:

$$\tau_{He} = \int_m^{m_{He}^*} \beta_{He}^{-1} \, dm \quad . \tag{3.30}$$

Table 3.3. Material and irradiation parameters used in comparison of void formation mechanisms

E_v^f	1.50 eV	γ^a	2.025–8.75 × 10^{-4} T (°C) J/m²
$E_v^{m^a}$	1.40 eV	$\rho_n(T)^a$	2.0 × 10^{18} exp[-0.016 T(°C)] m^{-2}
D_v^o	8 × 10^{-4} m^{-2} sec^{-1}	$N_c(T)$	2.53 × 10^{25} exp[-0.023 T(°C)] m^{-3}
E_i^m	0.85 eV	$Z_i^{n^a}$	1.25
D_i^o	8 × 10^{-5} m^{-2} sec^{-1}	$f_b^{He^a}$	0.5
G_{dpa}	0.25 × 10^{-6} dpa/sec[b]	$f_\rho^{He^a}$	0.5
G_{He}	3.5 × 10^{-13} He/atom/sec		

[a]Parameter varied in analysis.

[b]Equivalent to a 10^{-6} dpa/sec dose rate with a cascade efficiency of 0.25.

$$\tau_{He} = \frac{\Omega N_c S_T^{He}}{G_{He}} \sum_{i=m}^{m_{He}^*} \left[F_s r(n,i)\, N_c + f_b^{He} f_\rho^{He} S_\rho^v \right]^{-1} . \qquad (3.31)$$

3.2.3 Results and Discussion of Calculations

The results compared in this section were computed as discussed above using the set of material and irradiation parameters listed in Table 3.3. The values of certain of the parameters listed in the table have been varied in the analysis and they will be discussed further in the text. Bias terms other than the effective network dislocation/interstitial bias (Z_i^n) have been set to 1.0. Representative values of n_v^*, r_c^*, m_{He}^*, and $r_c^*(m_{He}^*)$ which were computed at 400, 450 and 500°C using the base parameter set from Table 3.3 are listed in Table 3.4. These parameter values are similar to those which have been used previously in rate theory simulations of void swelling.[103,108,245]

Table 3.4. Typical critical cluster parameters

T (°C)	m_{He}^*	$r_c^*(m_{He}^*)$ (nm)	$m = 0$		$m = 0.9\, m_{He}^*$	
			n_v^*	r_c^*	n_v^*	r_c^*
400	33	0.574	121	0.692	95	0.638
450	98	0.890	481	1.10	353	0.989
500	576	1.82	4718	2.35	3387	2.10

Figure 3.10 provides a base case for comparison of the two alternate nucleation times as well as showing their temperature dependence. The void swelling incubation time should be approximately in the range of 10 to 50 dpa for the fast reactor conditions which are considered here. The values of the characteristic void nucleation times for both mechanisms are plotted in Figure 3.10(a) and (b) as a function of m/m^*_{He}. The major differences between the two are the much greater temperature dependence and size dependence of the stochastic nucleation path. The relative magnitude of the two nucleation rates is shown in Figure 3.10(c) where the ratio of the nucleation times has been plotted. In order for the nucleation times for the two processes to be comparable, the ratio of m/m^*_{He} must be about 0.80 for 400°C and greater than 0.95 for 500°C. For lower gas contents the nucleation time due to helium accumulation is always much less than that for the stochastic process.

The parametric dependence of the ratio of the nucleation times at 450°C is shown in Figures 3.11 and 3.12. The parameters which have been varied are the dislocation-interstitial bias, the network dislocation density, the self-diffusion coefficient, the surface energy and the two parameters in the helium partitioning model. The values of the parameters are indicated in the appropriate figure; in each case, all other parameters were maintained as listed in Table 3.3. The dependence seen in Figure 3.11(a–c) is a result of the vacancy supersaturation varying in response to the parameter changes. Increases

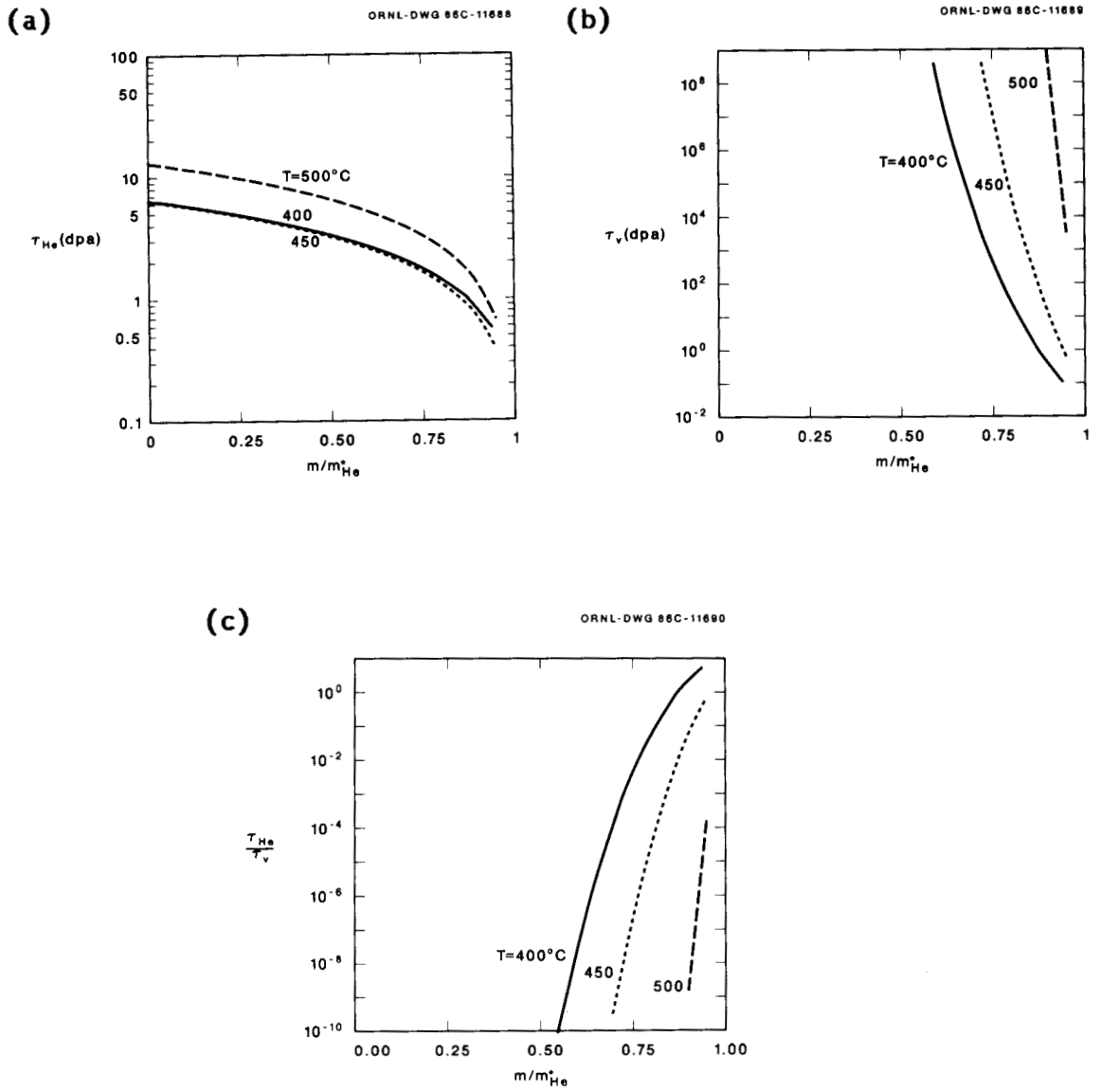

Figure 3.10. Characteristic nucleation times for the helium accumulation process (a), stochastic theory (b) and their ratio (c) at 400, 450 and 500°C.

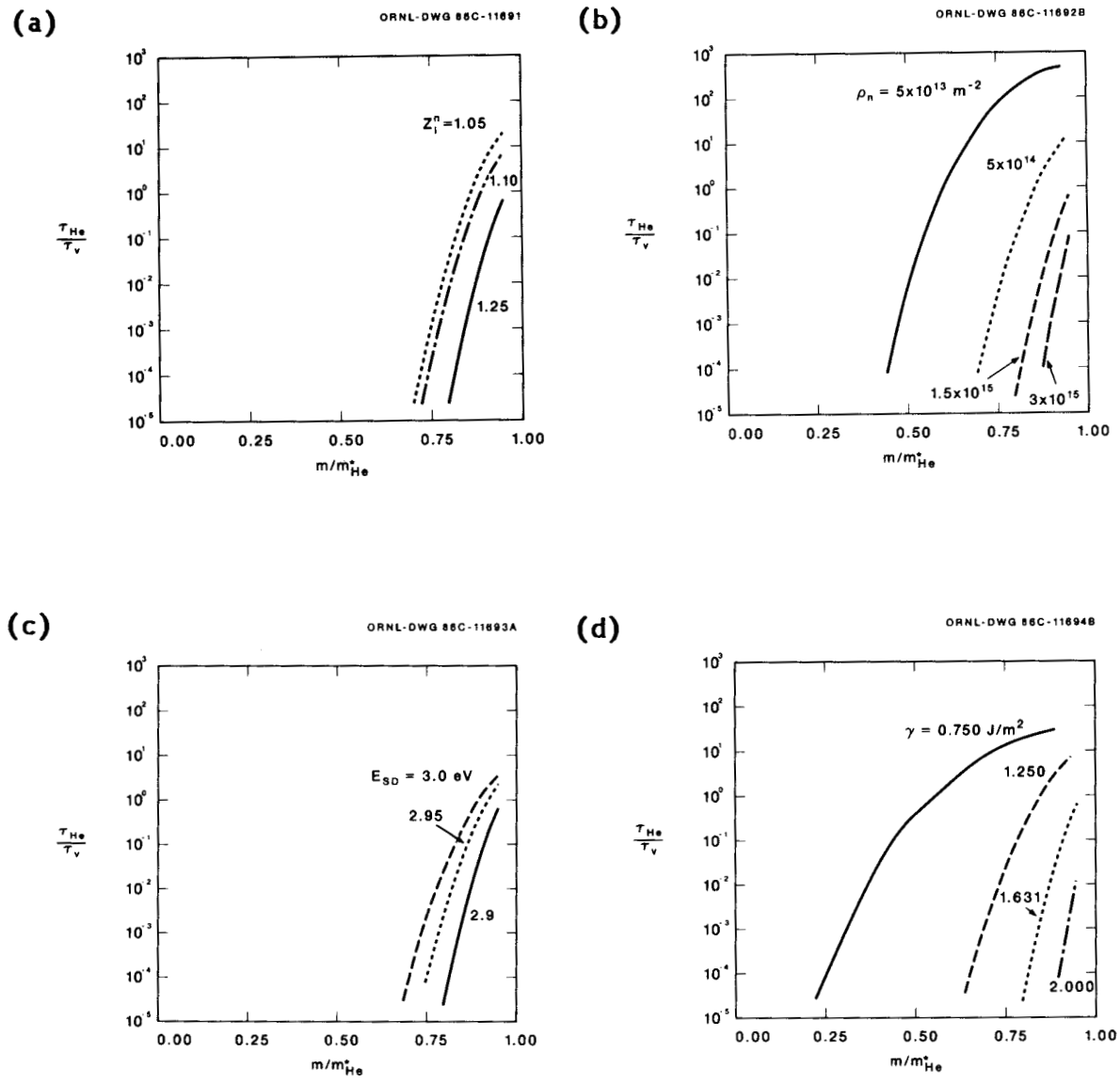

Figure 3.11. Parametric variation in the ratio of the nucleation time by helium accumulation to that by the stochastic theory at 450°C. The parameters are the dislocation-interstitial bias (a), the network dislocation density (b), the activation energy for self-diffusion (c) and the surface energy (d).

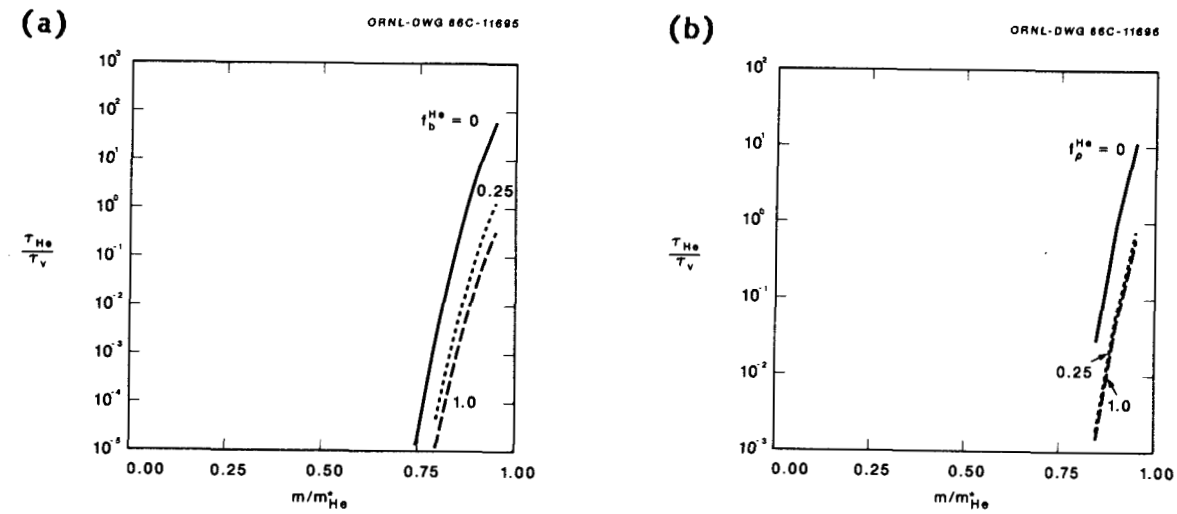

Figure 3.12. Dependence of the nucleation time ratio on the parameters in the helium partitioning model; fraction of dislocation-trapped helium piped to bubbles (a) and the fractional reduction in the dislocation sink strength for helium (b).

in the vacancy supersaturation increase nucleation by both mechanisms, but the nucleation rate by helium accumulation increases to a greater degree. Although the rate of helium absorption by a subcritical cluster is not a function of the supersaturation [Equation (3.29)], the critical number of gas atoms is reduced [Equation (3.8)]. Similarly while the critical number of gas atoms increases as the cube of the surface energy, higher surface energies also lead to increased vacancy emission [Equations (3.14–3.15)] and the net result of a higher surface energy is to decrease the stochastic nucleation rate relative to the helium mechanism [Figure 3.11(d)].

The results are much less sensitive to the parameters in the helium partitioning model. Note that the vertical axis scaling has been changed between Figures 3.12(a) and (b) in order to show the dependence. The fraction of dislocation-trapped helium which is directly "piped" to bubbles has only a modest effect on the ratio of the nucleation times [Figure 3.12(a)] while varying the dislocation sink strength for helium has even less effect [Figure 3.12(b)] as long as it is greater than zero.

These results provide a clear comparison of the two complementary nucleation paths which can lead to void formation in irradiated materials. The details of the results are certainly model dependent, and parameter variations can selectively favor one process over the other. But the overall conclusions seem sound since the comparison is so striking. Because the critical cluster sizes are relatively small for the temperatures discussed here, the characteristic nucleation times which have been computed should be somewhat less than the time at which measurable swelling is observed. However, even with moderate amounts of gas the stochastic nucleation theory predicts relatively long nucleation times at intermediate temperatures. At higher temperatures, the stochastic theory fails to predict finite nucleation rates with reasonable material parameters. This result is already evident in the values shown for 500°C in Figure 3.10(b) and is in striking disagreement with the fact that void formation persists up to 700°C in austenitic stainless steels.[152] Observed void swelling

incubation times are much more consistent with the helium accumulation process as shown in Figure 3.10(a).

The role of fluctuations begins to be significant when a sufficiently large fraction of the critical number of gas atoms has been accumulated. However, at 400°C this fraction is already about 0.8 while at 500°C it is greater than 0.95. With these levels of helium, voids can nucleate due to fluctuations in a relatively short time as shown in Figures 3.10(b) and (c). This result is highlighted in Figure 3.13 where, based on the present sensitivity studies, the material parameters have been chosen to maximize the influence of the stochastic path; a low bias (Z_i^n = 1.01), a high network dislocation

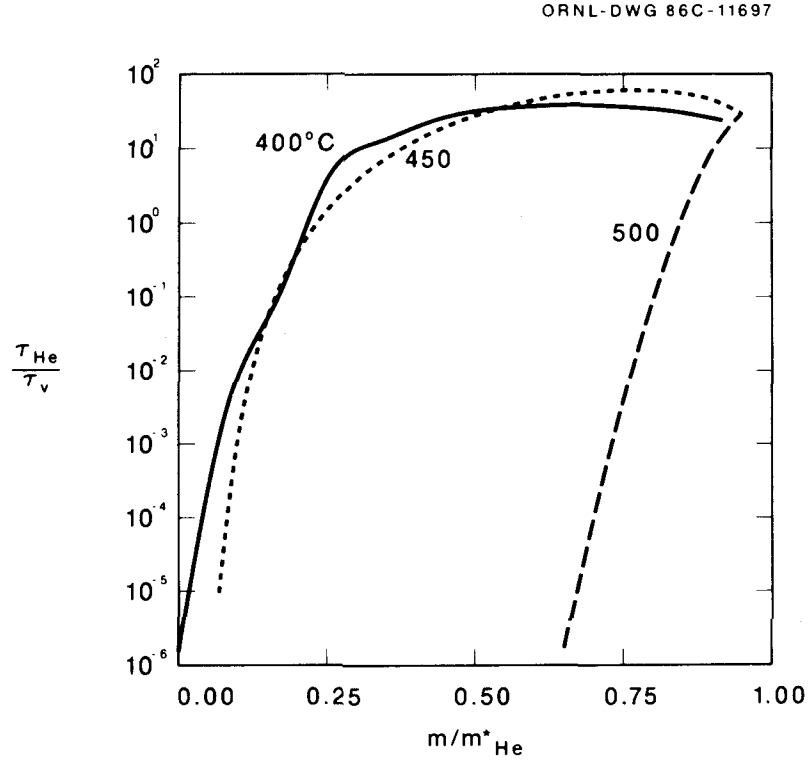

Figure 3.13. Temperature dependence of the nucleation time ratio with parameters chosen to minimize the influence of helium; Z_i^n = 1.01, E_{SD} = 3.0 eV, ρ_n = 1.5 x 10^{15} m^{-2} and γ = 1.0 J/m^2.

density (ρ_n = 1.5 × 10^{15} m^{-2}), a high self-diffusion energy E_{SD} = 3.0 eV) and a low surface energy (γ = 1.0 J/m^2). Even in this extreme case a relatively large amount of gas is required for stochastic fluctuations to make a significant contribution to the void nucleation rate. At 400°C, 20% of the critical number of gas atoms is required and at 500°C over 80%. Fluctuations can hasten the final stages of void nucleation, but only if sufficient gas is available to assist the earlier stage. Hence, the void formation time is still limited by the time required to obtain nearly the critical number of gas atoms.

This conclusion highlights the importance of the role that transmutant helium plays in void formation. For temperatures of technological interest (i.e., 350 < T < 600°C), an examination of Figures 3.10 to 3.13 indicates that fluctuations will contribute to the void nucleation rate only for cavities which are already near the critical size. At low temperatures the two processes contribute more equally to the total nucleation rate with the gas driven process dominant for smaller clusters. These conclusions support earlier work which explored the concept of the critical number of gas atoms and suggested that void formation was largely due to helium-stabilized bubbles reaching the critical radius rather than due to stochastic fluctuations.[108,124,192,244,245,252] The present work also provides a justification for the neglect of stochastic void nucleation in the models which are to be presented next.

3.3 Models of Microstructural Evolution

This section describes the specific models of microstructural evolution which have been developed in the present work. Two general models will be discussed. The first is a model of cavity evolution in which the dislocation structure is treated in a simple parametric manner. This model's swelling predictions were calibrated using the results of the RS-1 irradiation experiment[82,83,152] and good agreement was achieved. Then the model was used to examine the influence of both material and irradiation parameters on void swelling. One of these parameters was the He/dpa ratio. The predictions of the model indicated that simple interpolation between swelling data sets from the EBR-II (~0.3 appm He/dpa) and the HFIR (~70 appm He/dpa) could lead to highly nonconservative swelling predictions for a DT fusion reactor first wall (~10 appm He/dpa). These predictions have also been used to generate a family of design curves for 20% cold-worked type 316 stainless steel. The second model to be discussed includes an explicit treatment of the time dependence of both Frank faulted loops and the dislocation network. The cavity evolution model has been coupled with the dislocation evolution model to yield a comprehensive description of microstructural evolution. The predictions of the more complex model have been shown to agree with data from a broad range of fast reactor experiments. This indicates both the power of the rate theory as an analytical tool and the importance of microstructural control as

a tool for controlling the irradiation response of austenitic stainless steels. The simpler model will be discussed first and this discussion will include those aspects which are common to both models. Some of the assumptions and limitations of the chemical reaction rate theory have already been described above. Some additional discussion will be added here in the context of the more simple model but similar caveats apply equally to the more complex one.

3.3.1 Description of Cavity Evolution Model

The calculation of point defect sink strengths was described in Section 2.3. Here a first order effective medium approach has been adopted.[75,118] The sinks which have been included are bubbles, voids, dislocations, subgrain structure and transient vacancy clusters in the form of microvoids formed by the collapse of displacement cascades. The total dislocation density is expressed as a time independent function of temperature and no distinction is made between the faulted loop and network components. Except for the dislocations, equal capture efficiences (biases) for vacancies and interstitials have been used to calculate the extended defect sink strengths. As discussed below, an effective dislocation/interstitial bias has been introduced as a separate parameter to account for both the dislocation preference for absorbing interstitials and the effect of any other preferentially biased sinks. In this case the dislocation/interstitial bias can be thought of as representing an effective overall system bias. Before giving the general description of the model, two specific aspects will

be discussed – precipitate effects and the helium partitioning model. These two components are included in the same way in the more complex model to be discussed in the next section.

3.3.1.1 Precipitate Effects

There are several possible mechanisms by which precipitation of second phase particles can influence bubble-to-void conversion and void swelling. Some of these were mentioned in Chapter 2 and a partial list would include:

1. Lattice compositional changes leading to changes in sink capture efficiencies or self-diffusion parameters.[177,188,225,226,253]

2. Transient misfit strain effects at matrix-precipitate interfaces in which tensile strains could promote and compressive strains suppress bubble-to-void conversion by altering the critical size.[130,254,255]

3. Misfit strains leading to interfaces which are biased for either vacancies or interstitials.[255]

4. Point defect and helium collector effects.

5. Surface energy effects at matrix-precipitate interfaces leading to nonspherical cavities.[176,177]

In principle, each of these can be modeled but here item (5) and helium collection effects from item (4) have been examined. Item (1) is approximately accounted for in the choice of "effective" parameters which represent an appropriate average value. The helium collector

mechanism will be discussed in Section 3.3.1.2. The surface energy effect has been studied in detail in the literature for stress-induced creep cavity nucleation.[256,257] This mechanism can be modeled using a single parameter, β, which is a function of the relevant surface energies:

γ, the matrix surface free energy; γ_p, the precipitate surface free energy; and γ_{mp}, the matrix-precipitate interfacial energy.

$$\beta = \cos\left[\frac{\gamma_{mp} - \gamma_p}{\gamma}\right] \quad . \tag{3.32}$$

The volume (V_β) and the surface area (A_β) of the nonspherical cavity are given as:

$$V_\beta = F_v r^3 \quad , \tag{3.33}$$

and

$$A_\beta = F_s r^2 \quad , \tag{3.34}$$

where

$$F_v = \frac{\pi}{3}(2 - 3\cos\beta + \cos^3\beta) \quad , \tag{3.35}$$

and

$$F_s = 2\pi(1 - \cos\beta) \quad . \tag{3.36}$$

Equations (3.35) and (3.36) are appropriate for cavities which are growing on a larger precipitate. The cavity is nonspherical in this case because of the energy credit obtained by the destruction of

matrix-precipitate interface as the cavity grows. The parameter β is the contact angle of the cavity with the precipitate. For example, for a cavity which is a hemisphere, $\beta = 90°$, $F_s = 2\pi$ and $F_v = 2\pi/3$. There are very little data on values for either γ_p or γ_{mp} for the phases which appear in austenitic stainless steels. In general one might expect $\gamma \sim \gamma_p > \gamma_{mp}$ since the matrix-precipitate interface involves fewer broken atomic bonds than a free surface; although interface misfit strains could raise γ_{mp}. To a first approximation one might expect γ_{mp} to be on the order of the grain boundary free energy. Based on this assumption and a very limited amount of data,[88,258,259] a reasonable range of values for β might be 60 to 120°. An intermediate value of $\beta = 82°$ has been used here. This corresponds to a reduction in F_v by 0.4 and in F_s by 0.434 from their maximum values of $4\pi/3$ and 4π, respectively and is generally consistent with the observed shape of bubbles that are attached to precipitates.[255] One example of a precipitate-associated cavity is shown in Figure 3.14. The result of this reduced volume for a given radius is a reduction in the critical number of gas atoms for those bubbles attached to precipitates; Equation (3.8) shows that the critical number is linear in F_v.

Although Mansur and co-workers[176,177] have developed a model to describe point defect collection at matrix-precipitate interfaces, the precipitates have not been included here as point defect sinks for several reasons. First, there is not sufficient data characterizing the size and number densities of the various precipitates to permit a

YE-13592

Figure 3.14. Typical example of cavity-precipitate association. Large void on G phase and bubbles on phosphide phase in background. Photograph courtesy P. J. Maziasz, ORNL; solution-annealed PCA after 15 dpa irradiation in the FFTF at 500°C.

confident calculation of their sink strength at various temperatures and doses. Explicit modeling of the evolution of these particles was beyond the scope of the present work. Second, the literature suggests that incoherent interphase boundaries may be inefficient sinks, at least for vacancies.[254] Hence, the various precipitates might be expected to have different sink efficiencies and these efficiencies may be a function of precipitate size (and therefore dose) due to the buildup and relaxation of misfit strains. Finally, a preliminary attempt to include the point defect collection mechanisms in the present model indicated that the predictions of the model were significantly perturbed. This is clearly an area in which further theoretical development is warranted as data become available.

3.3.1.2 Helium Partitioning

In the models discussed here, voids are formed as a result of bubbles obtaining the critical number of helium atoms. It is therefore important that this work include an appropriate treatment of helium partitioning among the various microstructural sinks. This helium partitioning model is based on a conservation equation which includes the helium generation rate (G_{He}), the helium diffusivity (D_{He}) and the sink strengths of the extended defects for helium (S^j_{He}). The atomic concentration of helium in the matrix (C_{He}) is computed from the steady-state solution of the following conservation equation:

$$\frac{dC_{He}}{dt} = G_{He} - D_{He}C_{He} \sum_j S^j_{He} \quad . \tag{3.37}$$

This equation is similar to Equation (2.3) which is used to obtain the vacancy and interstitial concentrations.

The helium sinks in Equation (3.37) include bubbles, voids, dislocations and the subgrain structure. Because of the observation of void-precipitate association discussed above, precipitates are permitted to act as helium collectors for precipitate-associated cavities. Guided by very limited data in the range of approximately 500 to 600°C a constant sink strength of 4×10^{14} m^{-2} is used for the precipitate helium collectors.[54] Typically 10% of the cavities are assumed to be associated with precipitates. Reference to the preceding section and Equation (3.8) indicates that these cavities will preferentially become voids due to the enhanced helium collection and a reduced critical

number of gas atoms. This void formation is delayed by a precipitate formation time, τ_p, to take into account the observed temperature dependent time required for phase decomposition to take place under irradiation. A simple model which is linear in temperature has been applied:

$$\tau_p = 0.16\ [700 - T(°C)]\ \text{dpa} \quad . \tag{3.38}$$

This leads to a precipitate formation time of 40 dpa at 450°C, decreasing to zero at 700°C. For temperatures less than 450°C, 40 dpa is used. This is presently a very simple model, but it is reasonably consistent with the existing data.[56]

For the other sinks in Equation (3.37), the sink strength for helium is assumed to be the same as that for vacancies. The value of these sink strengths will be given in the next section. One exception to this assumption is the dislocations. Helium partitioning work by Spitznagel and co-workers[235] and by Hall[260] has indicated that dislocations do not appear to capture helium as efficiently as their sink strength for vacancies would indicate. Here the dislocation sink strength for vacancies is reduced by a factor, f_ρ^{He}, to account for their observations. The influence of f_ρ^{He} on bubble-to-void conversion has been discussed above and a nominal value of 0.5 was used in this work. As shown in Figure 3.15, bubbles are frequently observed attached to dislocations; therefore, the present model further assumes that a fraction of the helium trapped by dislocations is "piped"[56] to matrix bubbles. The influence of this parameter has also been

YE-13591

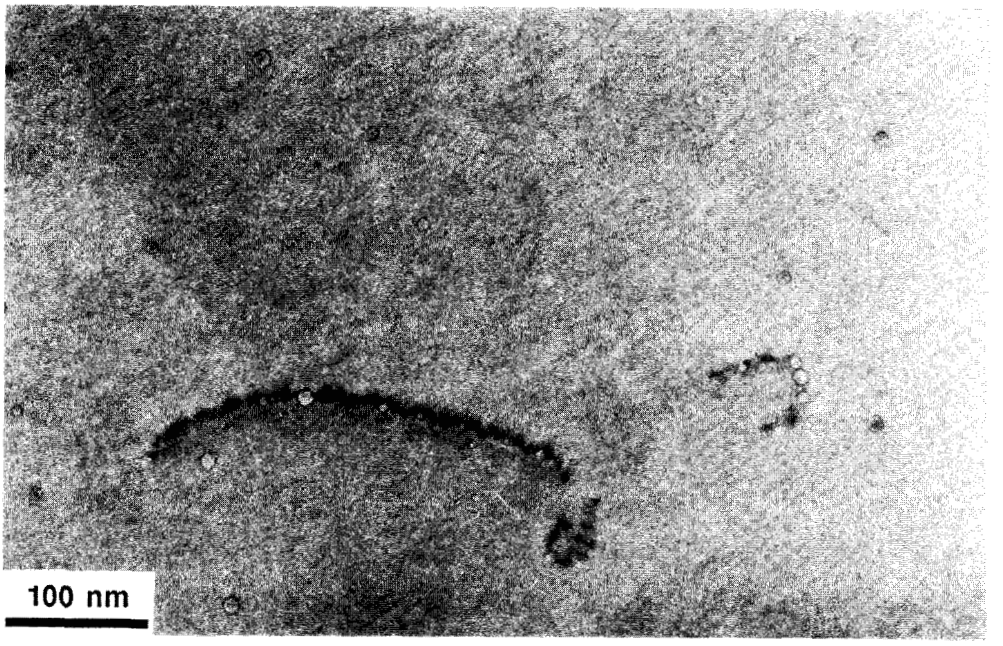

Figure 3.15. Typical example of helium-stabilized bubbles attached to dislocation segments. Solution-annealed, austenitic alloy P7, helium implanted to 65 appm He and aged for one hour at 850°C.

discussed in Section 3.2 and it was taken to be 1.0 in the calculations which will be discussed below.

The matrix helium concentration reaches a steady state level after about 10^4 to 10^5 sec (ref. 88) of irradiation. This is true even at low temperature because of irradiation-enhanced diffusion.[88,108] In this case it is appropriate to use the steady state solution of Equation (3.37). This solution was given in Equation (3.27). Although helium is partitioned to all the sinks mentioned above, it is

the bubbles which are of the most interest. Consistent with the scheme just outlined, the total amount of helium allocated to a bubble during an increment of time, Δt, is:

$$\Delta He_{mb} = F_s r_b D_{He} C_{He} \left[\frac{S^{mb}_{He} + f_\rho S^{\rho}_{He}}{S^{mb}_{He}} \right] \Delta t \quad , \tag{3.39}$$

for a matrix bubble and

$$\Delta He_{pb} = S^{ppt}_{He} D_{He} C_{He} \Delta t \quad , \tag{3.40}$$

for a precipitate-associated bubble when the time is greater than τ_ρ. S^{mb}_{He} is the total matrix bubble sink strength for helium, S^{ρ}_{He} is the dislocation sink strength for helium and S^{ppt}_{He} is the precipitate sink strength mentioned above. Once a matrix bubble is converted to a void, the dislocation is assumed to climb and/or glide away and a matrix void absorbs helium at a rate determined by its own sink strength:

$$\Delta He_{mv} = F_s r_{mv} D_{He} C_{He} \Delta t \quad . \tag{3.41}$$

Precipitate-associated voids continue to absorb helium as shown in Equation (3.40). At any time the amount of helium which has been generated can be compared with the cumulative totals of the helium allocated to the various sinks to ensure conservation of gas atoms.

When the steady state assumption is invoked, the results of the helium partitioning model and the computed bubble-to-void conversion times are independent of the assumed helium diffusivity. This can be seen by combining Equation (3.27) and each of the Equations (3.39) through (3.41). The helium diffusivity is eliminated.

3.3.1.3 Sink Strengths and Rate Equations for Point Defect Concentrations

A general conservation equation describing the concentrations of vacancies and interstitials was given in Equation (2.3). The specific equations used in this work are:

$$\frac{dC_i}{dt} = \eta G_{dpa} - \alpha C_i C_v - D_i C_i \sum_j S_i^j \quad , \tag{3.42}$$

for the interstitials and

$$\frac{dC_v}{dt} = G_v - \alpha C_i C_v - D_v C_v \sum_j S_v^j \quad . \tag{3.43}$$

The vacancy generation rate, G_v, is given in terms of the damage rate, G_{dpa} (dpa/sec), as:

$$G_v = \eta G_{dpa} (1 - \chi) + D_v \sum_j S_v^j C_v^j \quad . \tag{3.44}$$

In Equations (3.42) through (3.44) C_i and C_v are given in units of atomic concentration (number/atom), D_i and D_v are the point defect diffusivities (m^2/sec), α is the recombination coefficient (sec^{-1}).

the $S^j_{i,v}$ are the point defect sink strengths of the extended defects of type j and the C^j_v are the vacancy concentrations in equilibrium with the extended defects. This latter term is used to compute vacancy emission rates in Equation (3.44). The interstitial and vacancy diffusivities are:

$$D_{i,v} = D^o_{i,v} \exp\left(-E^m_{i,v}/kT\right) \quad . \tag{3.45}$$

Values for the migration energies, $E^m_{i,v}$, and the pre-exponential terms will be discussed below. The cascade efficiency, η, is the fraction of the initially created point defects that survive intracascade annealing. A fraction, χ, of the remaining vacancies is assumed to form microvoids as a result of cascade collapse. Values for these cascade parameters are taken from computer simulation results, as discussed below.[20,34,261]

Using the first-order, effective medium approach as discussed above,[74,75,115] the sink strengths are calculated as:

$$S^c_{i,v} = F_s \sum_j r^j_c N^j_c \left(1 + r^j_c S^t_v\right) \quad , \tag{3.46}$$

for all the cavities (bubbles and voids),

$$S^{mv}_{i,v} = F_s r_{mv} N_{mv} \left(1 + r_{mv} S^t_v\right) \quad , \tag{3.47}$$

for the microvoids with a radius, r_{mv},

$$S^g_{i,v} = \frac{6 S^o_v}{D_g} \quad , \tag{3.48}$$

for the subgrain structure with a subgrain diameter, D_g,

$$S_v^d = \frac{2\pi}{\ell n(r_o/r_c)} \rho_d \quad , \tag{3.49}$$

and

$$S_i^d = \frac{2\pi}{\ell n(r_o/r_c)} Z_i^d \rho_d \quad , \tag{3.50}$$

for the dislocations. The subscripts i and v once again denote vacancy and interstitial, respectively. The total system sink strength for vacancies, S_v^t, is:

$$S_v^t = (S_v^{o^2} + S_v^{g^2})^{\frac{1}{2}} \quad , \tag{3.51}$$

where

$$S_v^o = S_v^d + S_v^c + S_v^{mv} \quad . \tag{3.52}$$

As discussed in Chapter 2, the dislocation capture radius, r_c, in Equations (3.49) and (3.50) is larger for interstitials than for vacancies giving rise to the dislocation/interstitial bias. Here the same value of the capture radius has been used for both defects and the effective dislocation bias, Z_i^d, is introduced as a separate parameter. The value of r_c is taken as four times the magnitude of the Burgers vector[63,262] and the dislocation cell size, r_o, is set to the mean dislocation spacing, $r_c = (\pi\rho_d)^{-\frac{1}{2}}$.

Vacancy emission from the bubbles and voids is calculated using Equation (3.2) and for the other sinks as follows:

$$C_v^{mv} = C_v^e \exp\left(\frac{2\gamma\Omega}{r_{mv}kT}\right) \quad , \tag{3.53}$$

for the microvoids which are assumed to be clusters of vacancies only, and

$$C_v^g = C_v^d = C_v^e \quad , \tag{3.54}$$

for the subgrain structure and dislocations. The gas pressure in the cavities is computed using the equation of state discussed in Section 3.1.2.2 and C_v^e is the bulk thermal equilibrium vacancy concentration, taken as $C_v^e = \exp(-E_v^f/kT)$. E_v^f is the vacancy formation energy.

Equations (3.42) and (3.43) are solved at steady state as discussed above. The presence of the recombination term requires that the two equations be solved simultaneously. A solution is obtained by solving Equation (3.42) for C_i and substituting into Equation (3.43). This yields an equation which is quadratic in C_v which can be solved algebraically. C_i is then found by back-substitution for C_v into Equation (3.42).

A population of small (~0.25 nm radius) helium-vacancy clusters is assumed to form very early in the irradiation. The total density of these clusters is based on experimentally observed trends,[166,170,263]

$$N_c^t = 2.53 \times 10^{26} \exp\left[-0.023\ T\ (°C)\right]\ m^{-3} \quad . \tag{3.55}$$

These small helium-vacancy clusters grow initially as bubbles at a rate which is primarily determined by the helium generation and partitioning

rates. As discussed in Section 3.3.1.1, a constant fraction of 0.1 of the total density is assumed to be associated with precipitates that form after a temperature-dependent incubation time. The total cavity density is typically divided into two or three size classes, one of which contains the precipitate-associated cavities. If and when the cavities in any one size class exceed the critical size given by Equation (3.9) they are considered to have converted from bubbles to voids. Prior to their conversion to voids, the bubble radius is calculated using Equation (3.13) and after conversion the void radius is found by integrating Equation (3.1) with the initial condition that $r_c = r_c^*$. The LSODE (Livermore Solver of Ordinary Differential Equations)[266] subroutine package has been used to carry out the numerical integrations in this work. The time step in the integration is limited to ensure that the steady state assumption for Equations (3.42) and (3.43) is not violated and that the amount of helium partitioned to a bubble in a given time step is small relative to its current helium content.

The number of microvoids is computed by first determining the lifetime, τ_{mv}, of a spherical vacancy cluster with a radius, r_{mv};

$$\tau_{mv} = - \frac{r_{mv}^2}{D_v C_v - D_i C_i - D_v C_v^{mv}} \quad , \tag{3.56}$$

and the microvoid generation rate, G_{mv} ;

$$G_{mv} = \frac{G_{dpa}\,\eta X}{\Omega\, n_v} \quad . \tag{3.57}$$

The number of vacancies in a microvoid is:

$$n_v = \frac{4\pi}{3\Omega}\, r_{mv}^3 \quad . \tag{3.58}$$

The microvoid density, N_{mv}, is then found by integrating the following equation:

$$\frac{dN_{mv}}{dt} = G_{mv} - N_{mv}\,\tau_{mv}^{-1} \quad . \tag{3.59}$$

The total dislocation density is expressed as a time independent function of temperature:

$$\rho_d = 1.99 \times 10^{18} \exp\,[-0.016\ T(°C)]\ m^{-2} \quad . \tag{3.60}$$

Thus no distinction is made between faulted loops and network dislocations and the dislocation transient is ignored. Equation (3.60) provides a reasonable fit to the observed temperature dependence of the dislocation data discussed in Chapter 2.[166,172] Finally, the subgrain size is also temperature dependent. In 20%-cold-worked material the subgrain size simulates the observed coarse cell structure which was discussed in Chapter 2.[160-164] At 500°C and below the subgrain size is set to 1.0×10^{-6} m, increasing to 1.25×10^{-6}, 3.0×10^{-6}, 7.75×10^{-6} and 1.70×10^{-5} m at 550, 600, 650 and 700°C, respectively.

To be rigorously correct, the sink strengths of the cavities, the microvoids and the subgrain structure should be greater for interstitials than for vacancies.[75,116] This is a result of the multiple sink correction term in Equations (3.46) and (3.47) for the spherical sinks and is intrinsically the case for the subgrains in Equation (3.48). In Equations (3.46) and (3.47) S_v^t should be replaced by S_i^t and in Equation (3.48) S_v^o should be replaced by S_i^o when computing the sink strengths for interstitials. S_i^t and S_i^o are defined by equations analogous to Equations (3.51) and (3.52). Thus the existence of a single biased sink results in an apparent bias for all sinks when multiple sink strength corrections are included. To simplify the present analysis, all bias effects have been subsumed into the single effective dislocation bias and the sink strengths have been computed using Equations (3.46) through (3.52). The influence of the multiple sink correction terms was investigated further with the comprehensive model which will be discussed below.

3.3.1.4 Parameter Choices and Model Calibration

Perhaps the major uncertainty in all theoretical modeling studies is due to the use of material and irradiation parameters which are not well determined.[78] Some of these parameters were discussed in this context in Chapter 2. A partial list of these parameters would include material properties such as the activation energy for self-diffusion, the matrix surface free energy and the dislocation/interstitial bias and irradiation parameters such as the cascade efficiency. In many

cases these parameters have been measured in either pure material or simple alloys and the values applied to complex alloys. The influence of alloy composition is either ignored or extrapolated from measurements at a few compositions. In other cases no direct measurements are available and values are inferred from indirect observations. Even in the best of cases, experimental uncertainties typically lead to a large enough range of "reasonable" values for any given parameter that model predictions can be significantly affected. Finally, the use of the theory to help define the range of parameter values is hindered by the fact that changes in one parameter can often be offset by a corresponding change in another. For example, when bulk recombination is ignored and dislocations are the major point defect sink, the effective vacancy supersaturation given by Equation (3.3) takes the following simple form:

$$S = \frac{\eta\, G_{dpa}}{S_i^d\, D_v C_v^e} \left(Z_i^d - 1\right) \quad . \tag{3.61}$$

Clearly, changes in the cascade efficiency can be directly offset by changes in the bias or the dislocation density. If the temperature dependence of the dislocation density is not adequately represented, changes in the self-diffusion energy will compensate for it. One advantage of the more complex model to be discussed in Section 3.3.2 is that simple relations such as Equation (3.61) do not arise because

of the explicit dose and temperature dependence of the major microstructural sinks. However, even in the comprehensive model, some limited parameter variations could be offset by changes in other parameters. This will be discussed in more detail below, but the result of the uncertainties is that it is generally impossible to arrive at a unique set of model parameters when using the theory to match the observations in any one data set. Therefore, with even a well-calibrated model, any extrapolation from the existing data base should be carried out with great care.

The models developed here are subject to the uncertainties just discussed. In addition, the most serious assumptions in the model are the very limited treatment of possible precipitate effects on void formation and growth, the use of a simple temperature-dependent precipitate incubation time, the use of a temperature-independent precipitate sink strength and the neglect of possible microchemical effects on point defect diffusivities and sink capture efficiencies. In spite of these approximations, the model is able to predict the broad trends in the breeder reactor swelling data base and it is believed that the model provides a useful tool for increasing our understanding of the physical mechanisms responsible for void swelling and for exploring the sensitivity of swelling to parameters which may be of interest but which are not easily investigated experimentally. For example, the model will be used to examine the influence of the He/dpa ratio in the range of values which will be observed in a DT fusion reactor. In

this sense, theoretical models provide a complementary tool to experimental investigation and neither is adequate without the other.

The parameters used to calibrate the cavity evolution model are summarized in Table 3.5 and they will be discussed in turn below. The data set chosen for this calibration was from the RS-1 experiment which was discussed in Section 2.4. The data are from immersion density measurements of the 20%-cold-worked FFTF first core heats of type 316 stainless steel. This data set was chosen to minimize scatter from heat-to-heat variations and because it covers a broad dose and temperature range.

Experiments to measure the self-diffusion coefficient in austenitic alloys are typically conducted at quite high temperatures (T = 1000 to 1400°C) (refs. 225,226,265). Extrapolation of these results to temperature in the range 300 to 700°C is uncertain since relatively small changes in the activation energy will lead to diverging values of the self-diffusion coefficient at these lower temperatures. The value of the activation energy is known to be sensitive to composition[168] and typical values range from ~2.6 to 3.2 eV in various austenitic alloys.[225,226,266,267] Here an intermediate value of 2.9 eV has been used with a pre-exponential of 8.0×10^{-5} m^2 sec^{-1} (refs. 265, 267). The partitioning of the activation energy for self-diffusion between the vacancy formation and migration energies influences the results of the present model primarily for temperatures greater than about 600 to 650°C. Recently, Garner and Wolfer[222] have

Table 3.5. Material and irradiation parameters used in calibration of cavity evolution model

Material Parameters	
Vacancy energies: Formation, E_v^f	1.5 eV
Migration, E_v^m	1.4 eV
Interstitial migration energy, E_i^m	0.5 eV
Diffusivity pre-exponentials:	
Vacancy, D_v^o	8.0×10^{-5} m^2/sec
Interstitial, D_i^o	8.0×10^{-6} m^2/sec
Recombination coefficient, α	$2 \times 10^{20} D_i$ sec^{-1}
Dislocation-interstitial bias, Z_i^d	1.22
Surface free energy, γ	$1.620 - 7.0 \times 10^{-4}$ T(°C) J/m^2
Total sink densities:	
Dislocation, ρ_d	$1.99 \times 10^{18} \exp[-0.016\ T(°C)]$ m^{-2}
Cavity, N_c^t	$2.53 \times 10^{26} \exp[-0.023\ T(°C)]$ m^{-3}
Subgrain size, d_g	T < 500°C 1.0×10^{-6} m T = 550°C 1.25×10^{-6} m T = 600°C 3.0×10^{-6} m T = 650°C 7.75×10^{-6} m T = 700°C 1.70×10^{-5} m
Precipitate-associated cavity fraction, f_p	0.1
Precipitate:	
Sink Strength, S_p	4.0×10^{14} m^{-2}
Nucleation time, τ_p	0.16 [700 − T (°C)] dpa
Geometric terms for cavity volume and surface area:	
Precipitate-associated	$\beta = 82.3°$; $F_v = 0.40$; $F_s = 0.434$
Matrix	$\beta = 180°$; $F_v = F_s = 1.0$
Irradiation Parameters	
Damage rate, G_{dpa}	10^{-6} dpa/sec
Helium generation rate, G_{He}	3.5×10^{-13} He/atom/sec
Cascade efficiency, η	0.333
Fraction of vacancies clustered in microvoids, χ	0.8
Microvoid radius, r_{mv}	0.525 nm; T = 375°C 0.600 nm; T = 400°C 0.750 nm; T > 450°C

cited measurements of E_v^f which indicate that $E_v^f \sim 1.8$ and $E_v^m \sim 1.1$ in nickel[268,269] and suggest that these values be used for type 316 stainless steel. However, measurements of E_v^m in both high purity Fe-Cr-Ni austenitic alloys and in type 316 stainless steel indicate that $E_v^m \sim 1.3$ to 1.4; hence $E_v^f \sim 1.5$ to 1.6 (refs. 270,271). These latter values are more appropriate for this study and values of $E_v^m = 1.4$ and $E_v^f = 1.5$ have been used. The predictions of the cavity evolution model are not sensitive to the value of the interstitial migration energy.[272] Values of E_i^m measured in pure materials are typically fairly low, on the order of 0.1 to 0.2 eV (ref. 273), and such values have normally been used in theoretical studies of void swelling. However, recent measurements of E_i^m in austenitic stainless steel indicate that an activation energy as high as 0.9 eV may be more appropriate in these complex alloys.[270,274,275] An intermediate value of $E_i^m = 0.5$ eV was used in this work with a pre-exponential term of 8.0×10^{-6} m^2 sec^{-1}.

There have been only a very limited number of measurements of the surface free energy in austenitic stainless steels.[258,259] Murr and co-workers have reported measurements in type 304 stainless steel obtained using the method of zero creep deformation of thin wires at high temperatures.[259] A linear fit to their data in the range of 1000 to 1400°C yields the following expression:

$$\gamma(T) = 4.05 - 1.75 \times 10^{-3}\, T(°C)\ J/m^2 \quad . \qquad (3.62)$$

This leads to values of the surface energy between 2.8 and 3.5 J/m^2 when extrapolated to the 300 to 700°C temperature range. This is much higher than the nominal 1.0 J/m^2 which has typically been used in previous studies of void swelling. A lower surface energy can be rationalized on the basis of the presence of surface-active gases such as oxygen,[38,276,277] but the amount of reduction which should be applied is unclear. This is particularly true in complex alloys where the presence of oxygen-gettering elements such as carbon, silicon and titanium appears to strongly limit the influence of oxygen.[276] The 1.0 J/m^2 value has been used in the past largely because such a low value was required in order to obtain reasonable void nucleation rates from the classical stochastic theory as discussed in Section 3.2.2. The results of that same section indicated that a higher, temperature-dependent surface free energy was consistent with void formation via the conversion of critically sized, helium-stabilized bubbles. The value used here retains the temperature dependence of Equation (3.62), but the magnitude is reduced by a factor of 0.4.

The parameters which describe the net fraction of the initially produced point defects which survive intracascade annealing and cascade collapse are given in Equations (3.42) through (3.44). Here $\eta = 0.333$ and $\chi = 0.8$. These values are consistent with the results of detailed computer modeling of the evolution of the displacement cascade.[20,38,261] The microvoid radius, r_{mv}, has been used to obtain agreement between the model predictions and low temperature swelling data. The temperature dependent values of r_{mv} are given in Table 3.5. Predicted

swelling is essentially independent of the microvoid parameters above about 450°C, but below this temperature the presence of these transient vacancy clusters reduces the vacancy supersaturation by acting as a recombination site for point defects. This use of a variable microvoid radius is somewhat ad hoc, but it can be thought of as a surrogate for the other vacancy cluster parameters which may be temperature dependent. For example, the morphology of the stable vacancy cluster is known to be temperature dependent in face-centered cubic materials.[38,278,280]

Bulk, uncorrelated recombination of vacancies and interstitials due to point defect diffusion is accounted for in Equations (3.42) and (3.43) by the term proportional to what is called the recombination coefficient, α. The results presented below indicate that bulk recombination is important only when the total system sink strength is fairly low, $\alpha C_v > D_i \sum_j S_i^j$. This generally occurs only at high temperatures. While most vacancies and interstitials do recombine, this recombination takes place at point defect sinks rather than in the matrix. Neglecting the temperature dependence of the extended defects led some early researchers to the erroneous conclusion that bulk recombination was responsible for the low temperature swelling cutoff.[75,111,131] This error was pointed out by Bullough and Hayns[75] and discussed in more detail by Hayns.[281] Two alternate methods can be used to compute the recombination coefficient. The first is a continuum approach in which both types of point defects are considered to be a small

permanent sink of radius r_α for the opposite defect.[282,283] This leads to a diffusion profile around the sink and

$$\alpha = \frac{4\pi r_\alpha}{\Omega} (D_i + D_v) \quad . \tag{3.63}$$

Since $D_i >> D_v$, the recombination coefficient can generally be conveniently expressed in terms of the interstitial diffusivity only. The second approach is a discrete atomistic description in which the recombination coefficient is expressed as a function of the vacancy and interstitial jump frequencies and a geometric term referred to as the combinatorial number[7] or the recombination cross section.[283,284] This geometric factor is related to the number of atom positions around a given point defect from which the opposite defect can cause spontaneous recombination in a single jump. These two approaches have been shown to yield similar results.[283] Theoretical calculations of r_α lead to values ranging from 0.14 (ref. 284) to 1.07 nm (ref. 283). Using Equation (3.63) and neglecting D_v, these estimates of r_α would correspond to values of α/D_i between 1.6×10^{20} and 1.2×10^{21} m^{-2}. Recent measurements of the recombination volume in high-purity austenitic steels indicate that $r_\alpha \approx 0.845$ nm, leading to $\alpha/D_i = 9.25 \times 10^{20}$ m^{-2} (ref. 285). A value on the low end of this range has been used in this calibration, $\alpha/D_i = 2 \times 10^{20}$ m^{-2}.

With the other parameters fixed, as just discussed, the dislocation-interstitial bias, Z_i^d, was used as the final calibration parameter to obtain agreement between the predicted swelling and the

RS-1 swelling data. Because Z_i^d directly affects the vacancy supersaturation [Equation (3.61)], it influences the critical number of gas atoms [Equation (3.8)]; hence, it influences the bubble-to-void conversion times. The steady-state swelling rate can also be shown to be approximately linearly dependent on $(Z_i^d - 1)$ (ref. 74). Therefore, variations in the assumed bias have about the largest overall effect on model predictions. Theoretical calculations of Z_i^d suggest a fairly broad range of possible values, $Z_i^d \approx 1.01$ to 2.0 (refs. 69–75,286). Unfortunately, it is not possible to determine a precise value for the bias from experimental measurements of a parameter such as the swelling rate because the bias appears as a product with the cascade efficiency. With the cascade efficiency fixed, as discussed previously, the bias was used to fit the model's predicted steady-state swelling rates to rates observed in the RS-1 experiment. This required $Z_i^d = 1.22$, which is near the middle of the range of theoretical values.

The swelling predictions of the cavity evolution model are compared with the RS-1 swelling data[92,93,152] in Figure 3.16. For the results shown here, two cavity size classes have been used — one matrix class and one precipitate-associated class. The use of more than two size classes has a minimal impact on the predicted swelling as long as the total cavity density and the precipitate-associated fraction remain constant. Although the model is fairly simple, the temperature and fluence dependence of the data is well tracked. Both

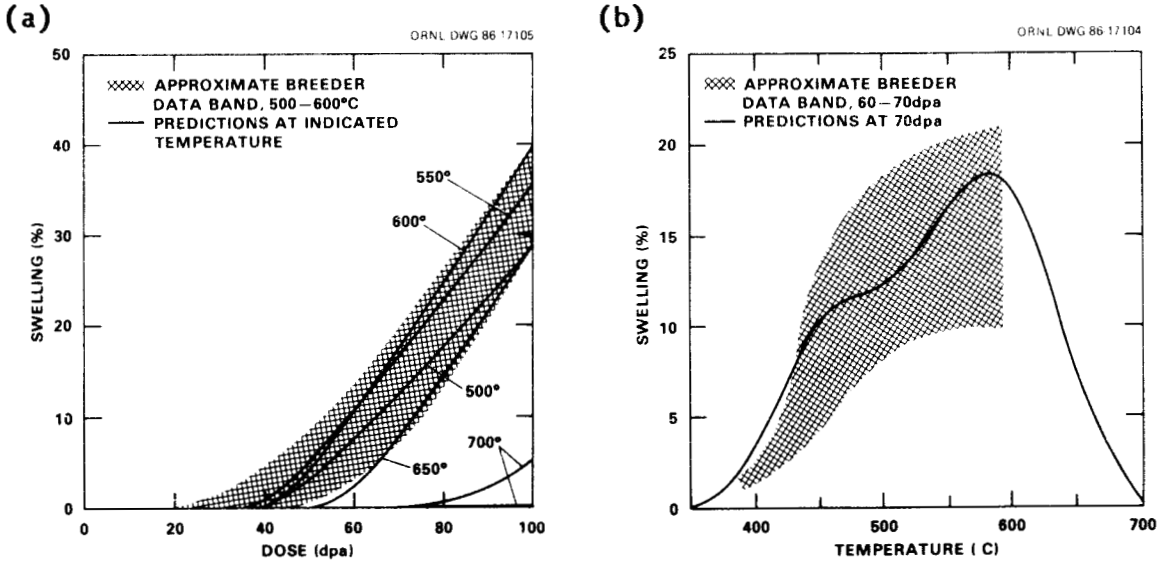

Figure 3.16. Comparison of RS-1 swelling data and predictions of cavity evolution model. RS-1 data from Bates and Korenko,[92] Yang and Garner,[93] and Garner.[152]

the incubation times and the steady-state swelling rates observed in the data are well represented by the model.

The incubation time in Figure 3.16 is primarily a function of the rate at which the subcritical bubbles absorb helium and the precipitate incubation time. Point defect partitioning to the various sinks gives rise to a temperature-dependent vacancy supersaturation and critical number of gas atoms, as shown in Figure 3.17. The value of m^*_{He} shown in Figure 3.17 is for a spherical (matrix) bubble (i.e., $F_v = 4\pi/3$). Because of the increasing dependence of the critical

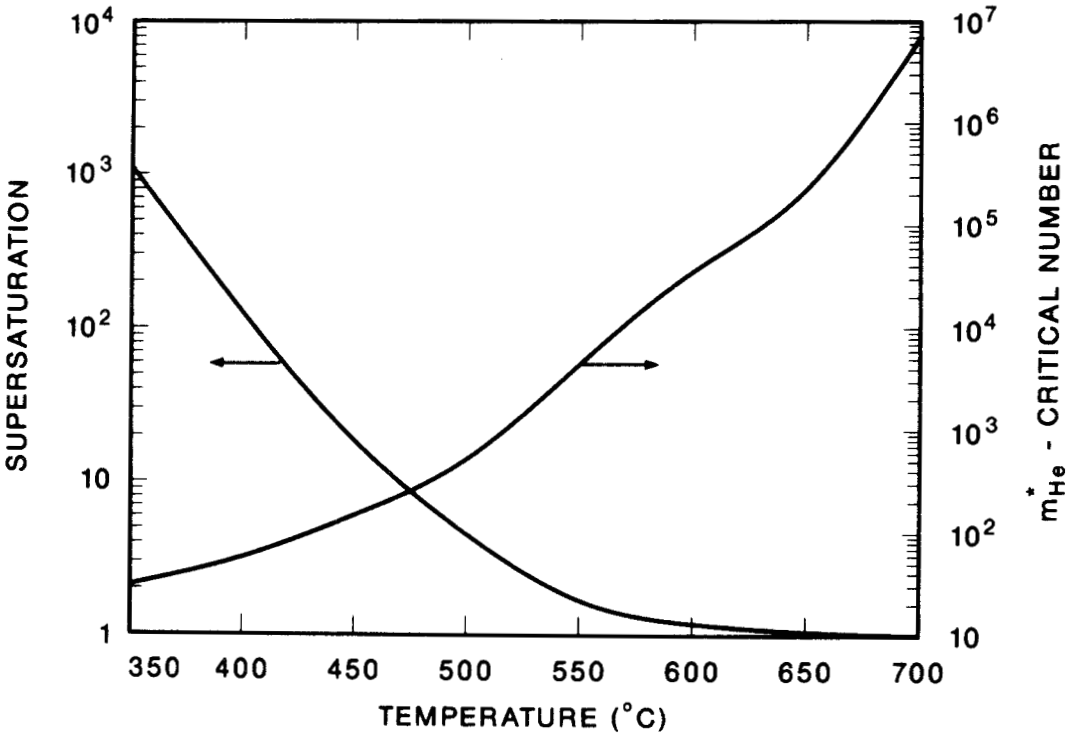

Figure 3.17. Temperature dependence of effective vacancy supersaturation, S, and critical number of gas atoms, m^*_{He}, using nominal model parameters.

number on temperature above about 500°C, two patterns of bubble-to-void conversion are observed. At 400 to 450°C swelling is due to the conversion of matrix bubbles to voids while at higher temperatures the precipitate-associated cavities are responsible for the swelling. The lag time for bubble-to-void conversion following precipitate formation increases from about 6 dpa at 500°C to 36 dpa at 650°C. Hence, the model indicates that, for the set of parameters used here (typical of commercial austenitic steels), swelling at low temperatures can be due to helium accumulation alone, while at higher temperatures the increased critical cavity size requires void-precipitate association in order to observe swelling at doses less than about 100 dpa.

At both high and low temperatures the early conversion of either bubble size class tended to prevent the other from converting. This is due to the increasing cavity sink strength which begins to suppress the vacancy supersaturation. This in turn causes the critical size for the remaining bubble size class to increase at a rate that is greater than the helium accumulation rate. A typical example of this phenomenon is shown in Figure 3.18 where the effective vacancy supersaturation and critical number of gas atoms at 500°C are plotted as a function of irradiation dose for both matrix and precipitate-associated cavities. The helium content of the cavities is also shown. The change in slope of the supersaturation and critical number curves

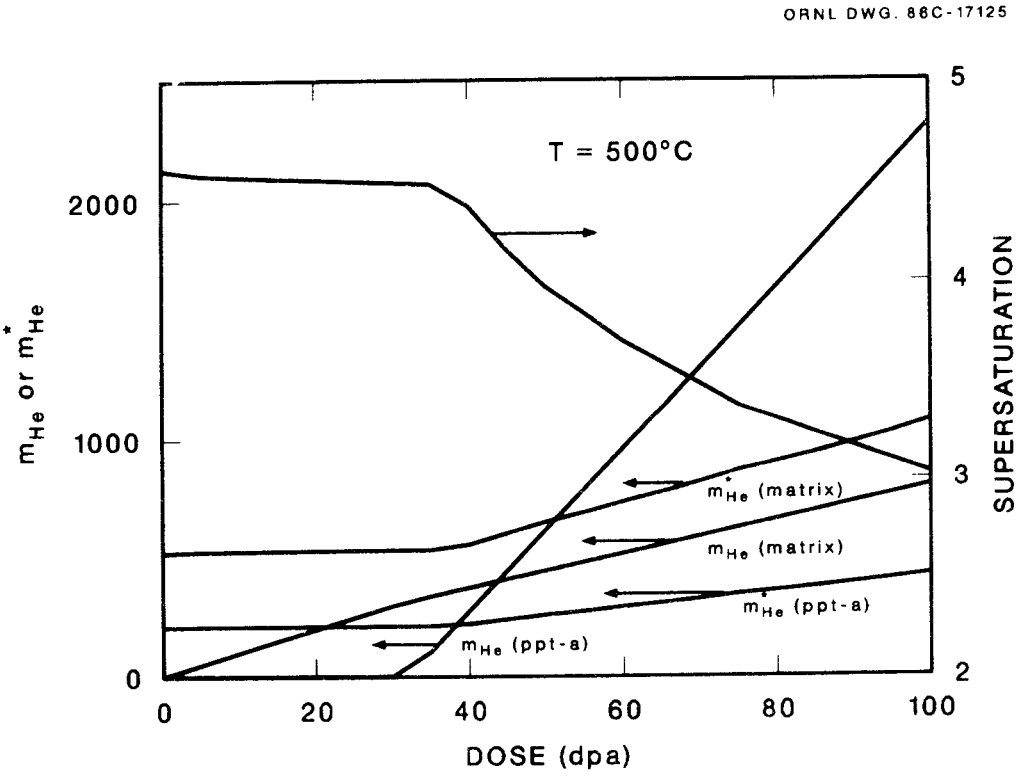

Figure 3.18. Dose dependence of the effective vacancy supersaturation, S, and critical number of gas atoms, m^*_{He}, at 500°C.

at about 45 dpa is a result of the conversion of the precipitate-associated bubbles to voids. The significance of this effect will be explored further in the next section.

At 700°C the model does not predict void formation out to 100 dpa with the nominal parameters. This is shown in the lower of the two curves labeled 700°C in Figure 3.16. Increased thermal vacancy emission reduces the effective vacancy supersaturation at such high temperatures to a very low level. This leads to a large critical number as shown in Figure 3.17. However, the predictions of the model at 700°C are quite sensitive to small changes in model parameters. Increasing the vacancy formation energy by as little as 0.03 eV and slightly reducing the dislocation density or the recombination coefficient raises the vacancy supersaturation to a sufficient degree that swelling begins at about 85 dpa as the upper of the two curves labeled 700°C in Figure 3.16 indicates. A somewhat higher value for the self-diffusion energy is consistent with the measurements mentioned above.[285,286] A somewhat lower dislocation density would be in agreement with values observed in recrystallized steels and is within the range of observed values for irradiated type 316 stainless steel (cf. Figure 2.7). The sensitivity to dislocation density may explain in part the fact that void formation is highly nonuniform in cold-worked materials. This will be discussed further when the predictions of a more comprehensive model are described in Section 3.3.2.

3.3.1.5 Parametric Analysis: Cavity Density and He/dpa Ratio

Because of the interest in the potential effects of the He/dpa ratio on swelling in austenitic stainless steels, the calibrated cavity evolution model has been used to explore the influence of this parameter. The most systematically observed effect of the He/dpa ratio is the formation of higher cavity densities at higher helium levels.[56,57] This was discussed in Chapter 2, and ref. 54 indicated that the total cavity density could be approximately described by a simple power law, $N_c^t \alpha (He/dpa)^p$. Simple theory suggests that the exponent p should be about 0.5 (ref. 109) while experimental observations typically fall in the range of 0.2 to 1.0 (refs. 54,57,104). For the present analysis p has been treated as a variable parameter and the He/dpa ratio has been varied between the low value of 0.35 appm He/dpa listed in Table 3.5 to a high value of 70 appm He/dpa. For austenitic stainless steels the former value is typical of EBR-II and the latter value is typical of the HFIR. The He/dpa ratio in a DT fusion reactor first wall falls between these two limits (~10 appm He/dpa). The total cavity density was scaled from the value listed in Table 3.5,

$$N_c^t (He/dpa) = N_c^t (0.35) \left[\frac{He/dpa}{0.35} \right]^p . \qquad (3.64)$$

The values of the other model parameters remained fixed.

The dose dependence of the predicted swelling with a He/dpa ratio characteristic of the HFIR and a DT fusion reactor first wall is

compared to the EBR-II base case in Figure 3.19. Three values of the cavity scaling exponent are represented at 450, 550, and 650°C. For the HFIR simulation, the dose dependence of the He/dpa as described by Simons[50] is included. Incubation times and in some cases steady-state swelling rates vary as a function of both the He/dpa ratio and the cavity density. At 450 and 650°C there is a fairly monotonic decrease in swelling as the cavity density (p) is increased in both environments. At 550°C the behavior is more complex, with peak swelling near a value of p = 0.5 for the DT fusion case. The sensitivity of the HFIR and fusion swelling predictions at 75 dpa to the cavity density is shown explicitly in Figure 3.20. The bubble-to-void conversion pattern is indicated in Figure 3.20 by the labels m,p and n/c for matrix, precipitate-associated and no conversion, respectively. The EBR-II base case swelling is also shown for comparison. Although the details of the swelling behavior are dependent on both temperature and the He/dpa ratio, a broad trend of enhanced swelling (relative to EBR-II) is observed for p up to about 0.5 to 0.7 for HFIR and p = 0.6 to 0.9 for DT fusion. This enhanced swelling is primarily a result of reduced incubation times at the higher He/dpa ratios. In a few cases, conversion of additional classes of bubbles to voids leads to higher swelling rates as well. However, at the highest cavity densities, swelling is reduced. The reduced swelling is due to extended incubation times and in some cases to lower swelling rates. The incubation times are extended as a result of a higher cavity sink strength, leading to a reduced vacancy supersaturation; hence, the critical

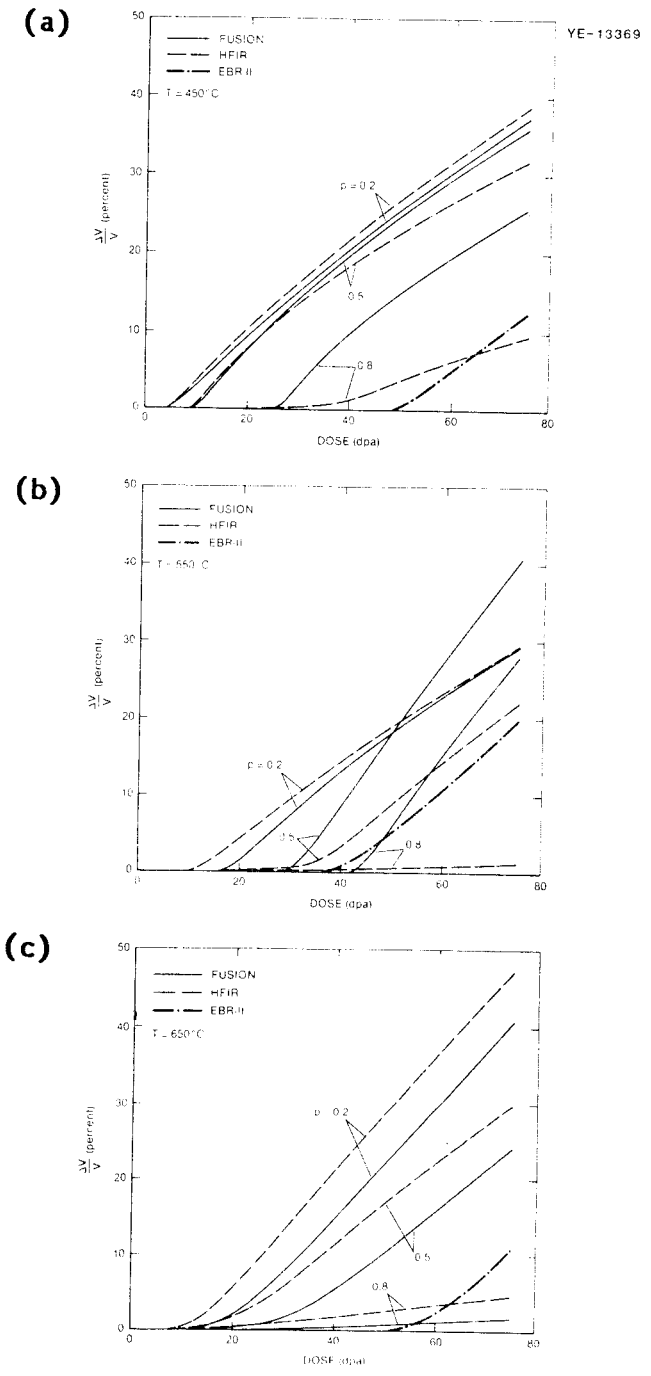

Figure 3.19. Comparison of predicted dose dependence of swelling for EBR-II, HFIR and DT fusion. See text for explanation of the parameter, p.

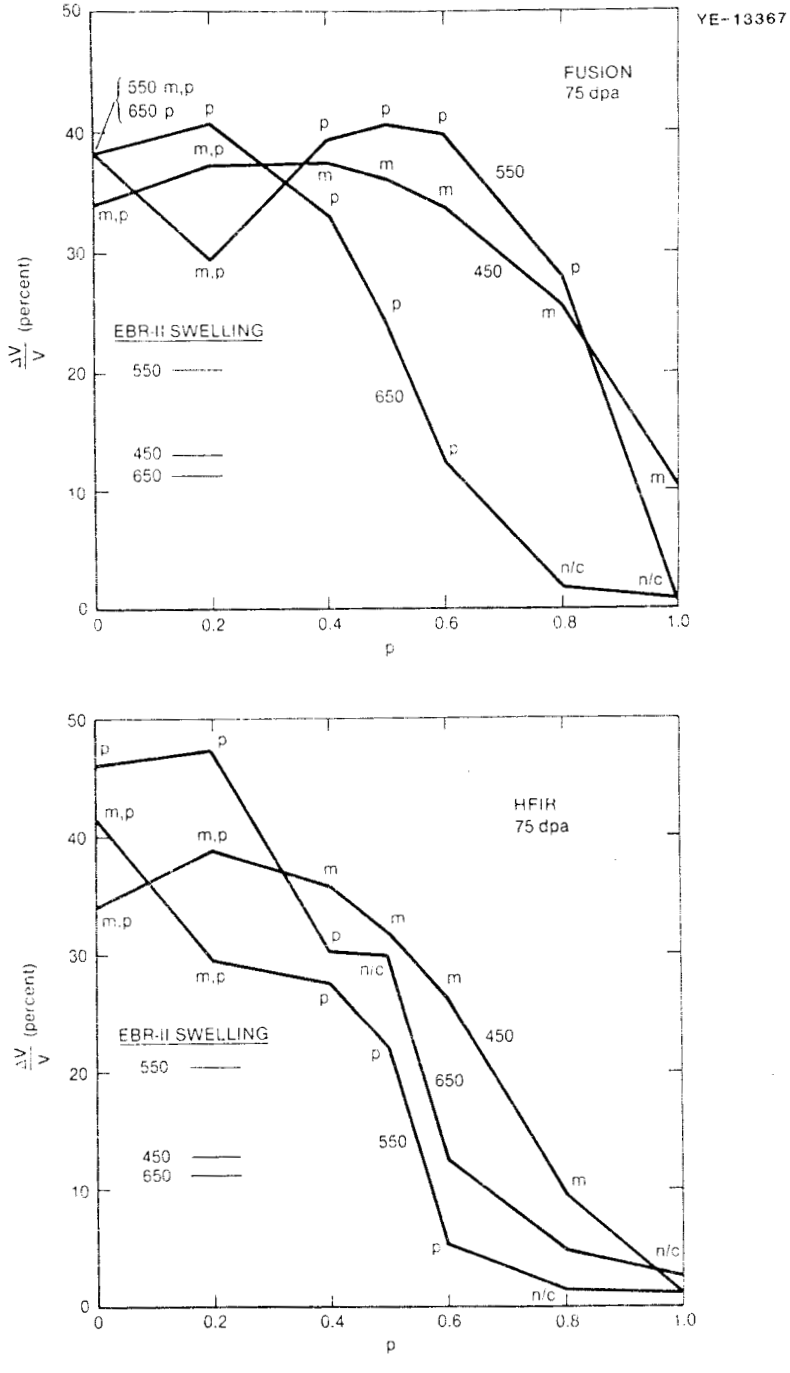

Figure 3.20. Predicted swelling at 75 dpa for HFIR and DT fusion as a function of the cavity scaling exponent, p. See text for explanation of notation.

number of gas atoms is increased. At the same time, the available helium must partition to more cavities. Reduced swelling rates are also the result of an increased cavity sink strength. As discussed in Chapter 2, the peak swelling rate occurs when the cavity and dislocation sink strengths are nearly equal.[74] The early conversion of a high density of matrix cavities (e.g., p = 0.8 at 450°C) can suppress the later formation of precipitate-associated voids which would otherwise cause rapid swelling. Therefore, there may be a critical value of the cavity density which will give rise to a bifurcation in the path of cavity evolution. The tendency for the system to follow the low swelling path for a given value of p is enhanced by high temperatures and a high He/dpa ratio.

In Figure 3.21, the ratio of the incubation time (dose to 1% swelling), τ, and the quasi-steady-state swelling rates (at 75 dpa), $\dot{S}$, for DT fusion relative to EBR-II are shown for p = 0.2, 0.5 and 0.8. For p = 0.2 and 0.5, the difference between EBR-II and DT fusion is primarily due to the reduced incubation time. At 550°C, the swelling rate is somewhat enhanced as well. For p = 0.8, both the swelling rates and the incubation times are affected. The magnitude and the sign of the effect vary with temperature. The explicit dependence of the predicted swelling on the He/dpa ratio is shown in Figure 3.22 for p = 0.2, 0.5 and 0.8. The predicted swelling at 75 dpa for 450, 550 and 650°C is compared with the EBR-II base case. These calculations indicate nonmonotonic swelling behavior with He/dpa ratio. Except for the highest value of p and the highest temperature, the predicted

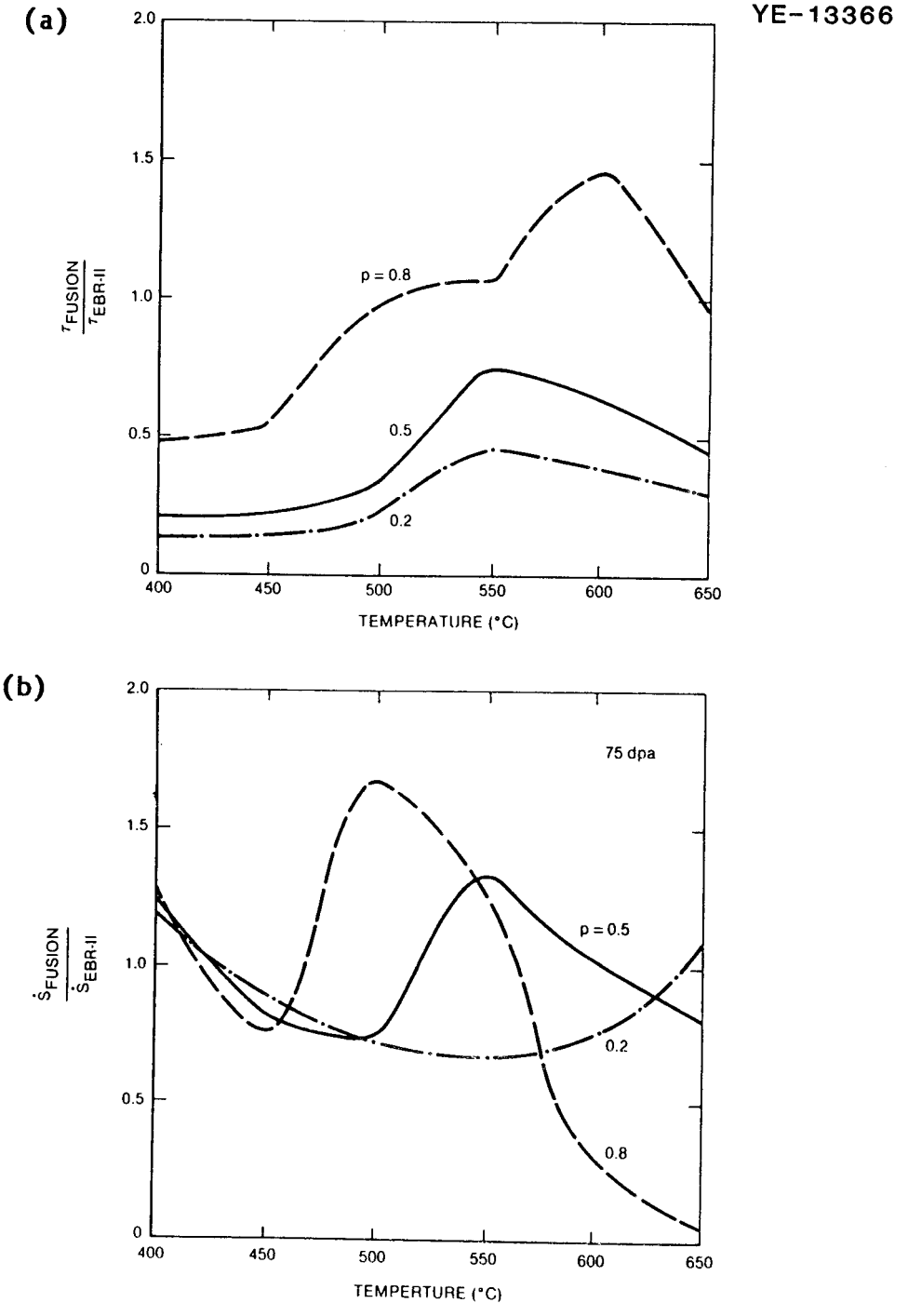

Figure 3.21. Temperature dependence of predicted incubation dose (τ = dose to 1% swelling) and steady state swelling rate ($\dot{S}$ = swelling rate at 75 dpa) for DT fusion normalized to EBR-II.

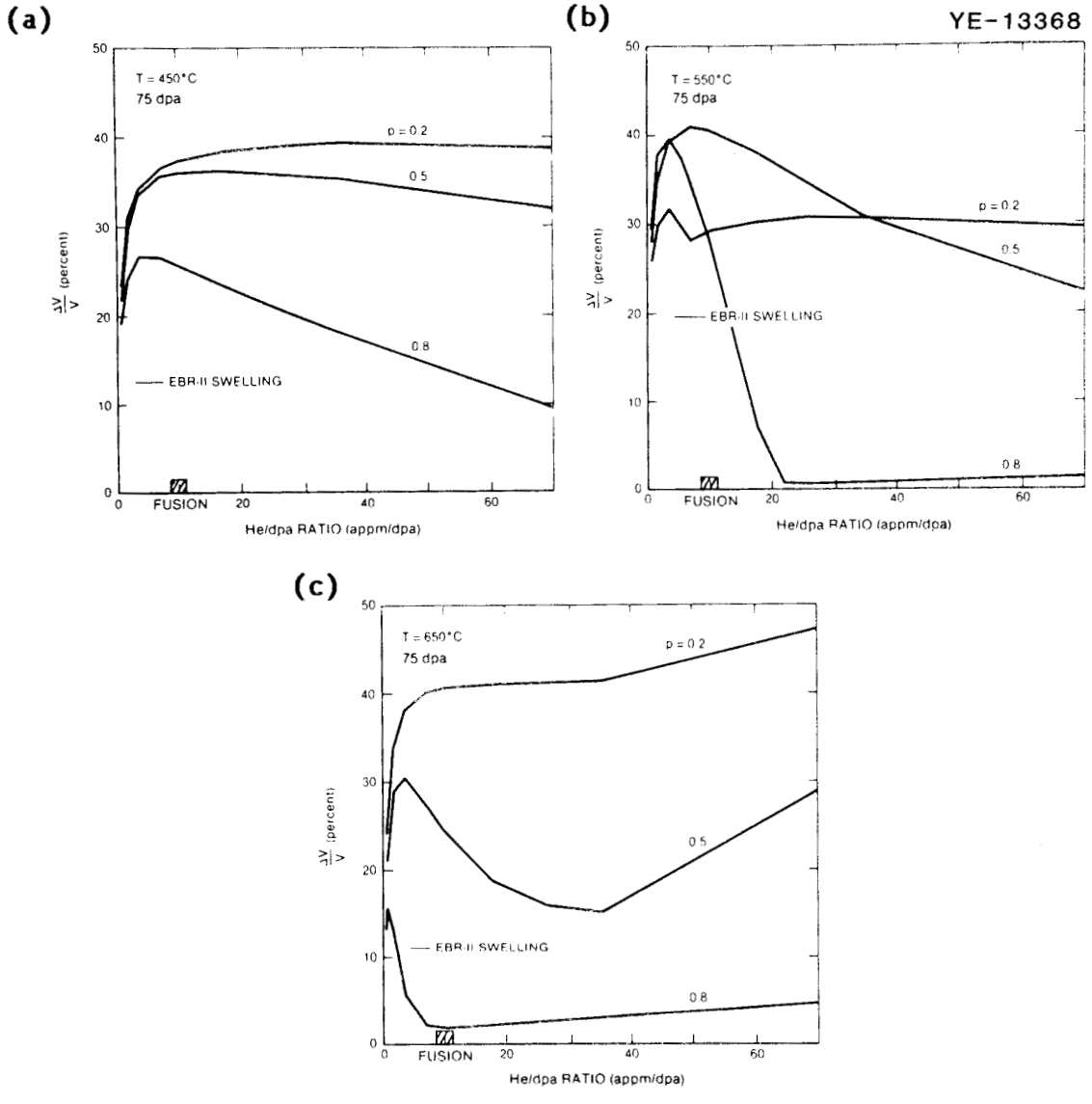

Figure 3.22. Dependence of the predicted swelling at 75 dpa on the He/dpa ratio.

swelling appears to peak near the DT fusion He/dpa ratio. This result suggests that a simple interpolation or extrapolation of swelling data obtained in either the EBR-II (0.35 appm He/dpa) or the HFIR (70 appm He/dpa), or both, may lead to significant errors in predicting swelling in a DT fusion reactor first wall.

It should be emphasized once again that the specific values of the predicted swelling are sensitive to model assumptions and parameters. However, the general trends which are predicted are a consequence of the physical mechanisms discussed above and not the details of the model. In particular, the dependence of swelling on the He/dpa ratio is believed to be real. The predicted bifurcation in the cavity evolution path is quite consistent with the observed swelling of 20%-cold-worked DO-heat in the HFIR and EBR-II, as discussed in Chapter 2. Finally, type 316 stainless steel has been irradiated in the ORR in an experiment in which the neutron spectrum was tailored to yield a He/dpa ratio of about 10 (ref. 287). Initial examinations of specimens from this experiment indicate that swelling is significantly greater than was observed in the same heats of material irradiated in the HFIR or the FFTF (He/dpa ~ 0.5).[288]

3.3.1.6 Development of Model-Based Design Equations

The results of the previous section have been used to develop a set of model-based design equations for the swelling of 20% cold-worked type-316 stainless steel in a DT fusion reactor. This set of equations complements two data-based design equations which have also

been formulated.[288,290] These two data-based equations arose from the two different interpretations of the results of irradiations of 20% cold-worked DO-heat, as discussed in Chapter 2. One of these equations emphasizes the results of HFIR irradiation[288] while the other emphasizes the EBR-II results.[290] In developing the model-based design equations, values of p = 0.2, 0.5 and 0.8 in Equation (3.64) were used. This attempts to set crude mechanistic limits on the predictions. The He/dpa ratio was set to 10 appm He/dpa with a damage rate of 10^{-6} dpa/sec. The other parameters from Table 3.5 also apply. Hence, the design equations are appropriate for components near the reactor first wall.

For temperatures up to 600°C and doses to 100 dpa, the predicted swelling values, S, were fit using a function of the following form:

$$S(T,d) = A(T)[d - \tau(T)] - B(T)[d - \tau(T)]^a \quad , \qquad (3.65)$$

for $d > \tau$, where T is the irradiation temperature (°C), d is the dose (dpa) and A, B and τ are temperature-dependent parameters used to fit Equation (3.65) to the swelling curves. The parameter A is approximately equal to the predicted maximum swelling rate and τ corresponds to the dose required to reach 1% swelling. A value of the exponent a = 1.25 is required to yield the proper curvature in the swelling curves. Best-fit values of A, B and τ were computed using a nonlinear least-squares regression program for each of the three values of p. Individual fits for A, B and τ as a function of temperature were then

obtained in each case. These functions are given below in Equations (3.66) to (3.68).

For the p = 0.2 case:

$$A(T) = 1.285 \exp\left[-\frac{(T-500)^2}{8100}\right] + 0.80 \exp\left[-\frac{(T-615)^2}{500}\right] + 0.09 \exp\left[-\frac{(T-380)^2}{2000}\right], \quad (3.66a)$$

$$B(T) = 0.225 \exp\left[-\frac{(T-500)^2}{5300}\right], \quad (3.66b)$$

$$\tau(T) = 23.5 \exp\left[-\frac{(T-250)^2}{7250}\right] + 5.88 + \tau'(T), \quad (3.66c)$$

$$\tau'(T) = \begin{cases} 0, & T < 490°C \\ 18.6\ [1.0 - \exp\{-\frac{(T-490)^2}{2000}\}], & T \geq 490°C . \end{cases} \quad (3.66d)$$

For the p = 0.5 case:

$$A(T) = 1.08 \exp\left[-\frac{(T-450)^2}{6500}\right] + 1.12 \exp\left[-\frac{(T-555)^2}{3550}\right] + 0.04 \exp\left[-\frac{(T-400)^2}{500}\right], \quad (3.67a)$$

$$B(T) = 0.235 \exp\left[-\frac{(T-485)^2}{7400}\right] + 0.035 \exp\left[-\frac{(T-400)^2}{900}\right] + 0.04 \exp\left[-\frac{(T-540)^2}{1000}\right], \quad (3.67b)$$

$$\tau(T) = 8.5 + 16.5 \exp\left[-\frac{(T-300)^2}{8700}\right] + 24.5 \exp\left[-\frac{(T-558)^2}{2100}\right] . \quad (3.67c)$$

For the p = 0.8 case:

$$A(T) = 1.07 \exp\left[\frac{(T-426)^2}{5050}\right] + 1.30 \exp\left[-\frac{(T-500)^2}{1250}\right] + 1.40 \exp\left[-\frac{(T-550)^2}{1450}\right] , \quad (3.68a)$$

$$B(T) = 0.20 \exp\left[\frac{(T-430)^2}{5200}\right] + 0.22 \exp\left[-\frac{(T-505)^2}{1900}\right] + 0.20 \exp\left[-\frac{(T-555)^2}{1200}\right] - \text{AMAX1}[0.0,\ 3.1 \times 10^{-3}\ (T-550)] , \quad (3.68b)$$

$$\tau(T) = \begin{cases} 53.0 \exp\left[-\frac{(T-342)^2}{4800}\right] + 42.5 \exp\left[-\frac{(T-500)^2}{4500}\right] ; & T < 500°C \\ 42.8 + 7.0 \times 10^{-4}\ (T-500)^2 ; & T \geq 500°C . \end{cases} \quad (3.68c)$$

In Equations (3.66) to (3.68), $\exp(a) = e^a$ in order to simplify the notation and the FORTRAN function AMAX1 is used to prevent the use of negative values in the last term in Equation (3.68b).

The model-based equations are compared with the two data-based equations in Figure 3.23. In the case of the HFIR-based equation, a 50°C temperature shift has been applied in plotting the results since this equation was developed prior to the discovery that the actual

ORNL DWG 86C-17127

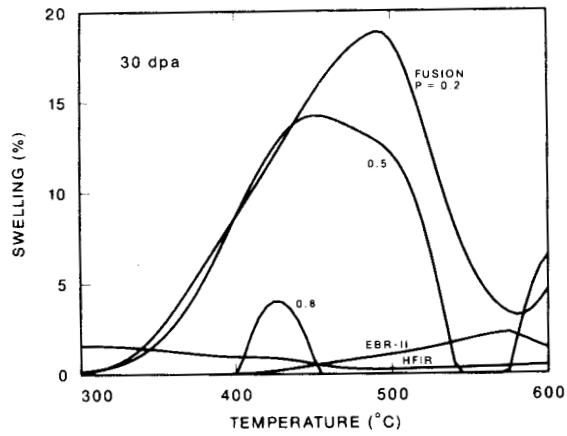

ORNL DWG 86C-17128

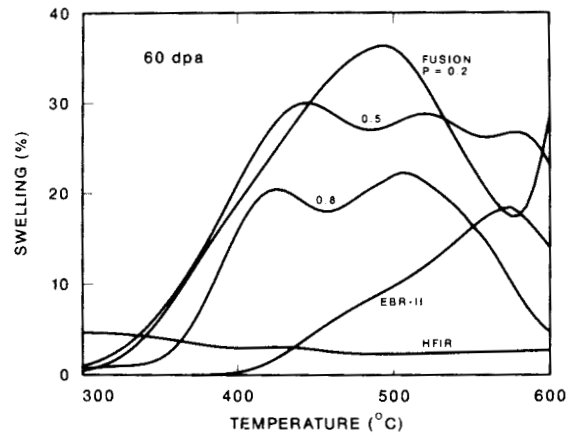

ORNL DWG 86C-17129

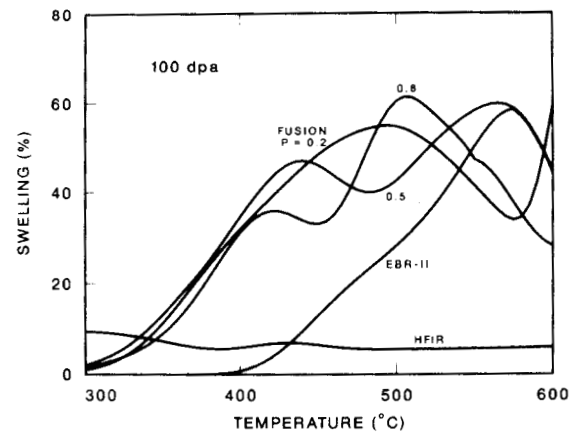

Figure 3.23. Comparison of alternate design equations for the swelling of 20% cold-worked type-316 stainless steel in a DT fusion reactor first wall. The curves for the model-based equations reflect the value of p, as indicated.

irradiation temperatures in the HFIR were systematically higher than originally thought.[54,201] The curves shown for the EBR-II-based equation do not include the helium bubble swelling contribution that the authors recommended;[200] this term would yield a small amount of swelling at low temperatures (<0.5% at 100 dpa at 300°C).

The comparison shown in Figure 3.23 re-emphasizes the key result discussed in the preceding section (i.e., that neither EBR-II nor HFIR may provide a conservative estimate of swelling in a DT fusion reactor first wall). Dose and temperature regimes are observed in which each of the three alternate design equations predicts the highest swelling. However, the model-based interpolation (at the appropriate He/dpa ratio) generally predicts much higher swelling than the two data-based equations.

3.3.2 Description of Comprehensive Microstructural Model

The comprehensive model discussed here is built on the foundation of the simpler model just described. The cavity evolution component of the model is identical to that described in Section 3.3.1. Here the assumption of a time-independent dislocation density has been relaxed and an explicit treatment of the evolution of both Frank faulted dislocation loops and the dislocation network are included.

3.3.2.1 Rate Equations with Time-Dependent Dislocation Density

In order for the model to include the time dependence of the dislocation structure, the rate equations given above for vacancies and

interstitials [Equations (3.42) and (3.43)] are modified to include the presence of di-, tri-, and tetra-interstitial clusters and Frank faulted dislocation loops. Additional rate equations describe the interstitial cluster concentrations and the evolution of the faulted loops and the dislocation network.

The assumptions discussed in Section 3.3.1.3 apply here as well, along with the following:

1. Only the monodefects are assumed to be mobile. Although the mobility of the small interstitial clusters can be included in a simple manner, their mobility has been shown to have no significant effect on the point defect calculations.[40]

2. The tetra-interstitial is a stable radius for Frank faulted loop formation. The di- and tri-interstitials may thermally dissociate by emitting a single interstitial.[41]

In Section 3.3.1, parameters related to the total dislocation density were designated by a subscript or superscript d where appropriate. Here, because the network and faulted loop components are distinct, the letter n will be used in reference to network parameters and the letter ℓ for loop parameters.

The rate equations are as follows:

$$\frac{dC_v}{dt} = G_v - \beta_v^2 C_2 - \beta_v^3 C_3 - \beta_v^4 C_4 - \alpha C_1 C_v - D_v C_v (S_v^n + S_v^\ell + S_v^c + S_v^{vcl} + S_v^g) \quad , \quad (3.69)$$

$$\frac{dC_1}{dt} = \eta G + C_2(2r_d^2 + \beta_V^2 - \beta_1^2) + C_3(r_3^d - \beta_1^3) - \beta_1^1 C_1$$

$$- \beta_1^4 C_4 - \alpha C_1 C_V - D_1 C_1 (S_1^n + S_1^\ell + S_1^c + S_1^{vcl} + S_1^g) \quad , \qquad (3.70)$$

$$\frac{dC_2}{dt} = \beta_1^1 \frac{C_1}{2} + C_3(\beta_V^3 + r_3^d) - C_2(\beta_V^2 + \beta_1^2 + r_2^d) \quad , \qquad (3.71)$$

$$\frac{dC_3}{dt} = \beta_1^2 C_2 + \beta_V^4 C_4 - C_3(\beta_V^3 + \beta_1^3 + r_3^d) \quad , \qquad (3.72)$$

$$\frac{dC_4}{dt} = \beta_1^3 C_3 - \beta_V^4 C_4 - C_4 \tau_4^{-1} \quad . \qquad (3.73)$$

In Equations (3.69) through (3.73), the $\beta_{1,V}^j$ and $r_{2,3}^d$ are rate constants for the impingement of point defects on interstitial clusters of size j and the thermal dissociation of di- and tri-interstitials, respectively, $S_{1,V}^\ell$ is the faulted loop sink strength, τ_4 will be discussed below and most of the other terms have already been defined. Variable definitions are summarized in Table 3.6.

$$\beta_{1,V}^j = \frac{z_{1,V}^j D_{1,V} C_{1,V}}{a_0^2} \quad . \qquad (3.74)$$

$$r_{2,3}^d = \frac{D_1}{a_0^2} \exp\left(-\frac{E_{2,3}^b}{kT}\right) \quad . \qquad (3.75)$$

Table 3.6. Variable definitions in comprehensive model

Parameter	Value/Units
Lattice parameter, a_o	3.58×10^{-10} m
Atomic volume, Ω	1.15×10^{-29} m^3 $(a_o^3/4)$
Burgers vector magnitudes	
Network dislocation, b_n	2.53×10^{-10} m $(a_o/\sqrt{2})$
Faulted loop, b_ℓ	2.07×10^{-10} m $(a_o/\sqrt{3})$
Diffusivities	
Vacancy, D_v	m^2/sec
Interstitial, D_i	m^2/sec
Concentrations	
Vacancy, C_v	No./atom
Thermal equilibrium vacancy, C_v^e	No./atom
Interstitial, C_i	No./atom
Di-interstitial, C_2	No./atom
Tri-interstitial, C_3	No./atom
Tetra-interstitial, C_4	No./atom
Extended defects	
Sink strengths, $S_{i,v}^j$	m^{-2}
Equilibrium vacancy concentrations, C_v^j where j = c for cavities, = n for network dislocations, = ℓ for faulted loops, = g for subgrains, = vcl for microvoids,	No./atom

$$S_{i,v}^{\ell} = \frac{2\pi}{\ell n(r_o/r_c)} \sum_j 2\pi r_\ell^j N_\ell^j Z_{i,v}^{\ell}(r_\ell^j) \quad . \tag{3.76}$$

The $Z_{i,v}^{\ell}(r_\ell)$ are effective faulted loop bias factors for interstitials and vacancies. Values for the binding energy of the second and third interstitial in a cluster ($E_{2,3}^b$) and for the combinatorial numbers ($z_{i,v}^j$) in Equation (3.74) will be discussed below.

The present model distinguishes between the small interstitial clusters and the larger faulted loops by treating their evolution differently. The τ_* term in Equation (3.73) is the lifetime of a tetra-interstitial against growth to the size of the first faulted loop size class. If r_* is the radius of the tetra-interstitial and r_1^ℓ is the radius of loops in the first size class,

$$\tau_* = \int_{r_*}^{r_1^\ell} \left(\frac{dr_\ell}{dt}\right)^{-1} dr_\ell \quad , \tag{3.77}$$

$$\frac{dr_\ell}{dt} = \frac{B}{b_\ell} \{Z_i^\ell(r_\ell) D_i C_i - Z_v^\ell(r_\ell) D_v [C_v - C_v^\ell(r_\ell)]\} \quad , \tag{3.78}$$

in which $C_v^\ell(r_\ell)$ is the vacancy concentration in equilibrium with a faulted loop of radius r_ℓ, b_ℓ is the magnitude of the Burgers vector of the faulted loop ($b_\ell = a_o/\sqrt{3}$) and $B = 2\pi/\ell n(r_o/r_c)$.

$$C_v^\ell(r_\ell) = C_v^e \exp\left[- \frac{\Omega}{kT} \left(\frac{Gb_\ell}{4\pi(1-\upsilon)r_\ell} \ell n \left(\frac{4r_\ell}{b_\ell}\right) + \frac{\gamma_{sf}}{b_\ell} \right) \right] \quad . \tag{3.79}$$

The first term in the exponential in Equation (3.79) is the elastic energy opposing loop growth due to the increasing dislocation line length while the second term is due to the stacking fault; G is the shear modulus, υ is Poisson's ratio and γ_{sf} is the stacking fault energy. Here the calculation of the vacancy generation rate using Equation (3.44) also includes vacancy emission from the faulted loops using Equation (3.79).

The use of the term $C_4\tau_4^{-1}$ in Equation (3.73) permits a mathematical transition between regions in which alternate descriptions of interstitial loop evolution are used. As shown in Equations (3.70) to (3.73), a discrete clustering calculation is done for sizes up to the tetra-interstitial. However, this description would necessitate integrating greater than 10^4 rate equations if it were used for loops up to the maximum size observed experimentally. The evolution of the larger loops is instead given by equations of the form,

$$\frac{dN_i^\ell}{dt} = N_{i-1}^\ell \tau_i^{-1} - N_i^\ell \tau_{i+1}^{-1} \quad , \tag{3.80}$$

where N_i^ℓ is the number of loops in a given size class with radius r_i^ℓ and the τ_i are given by Equation (3.77) with the appropriate loop radii used as the limits of the integration. The loop size space between r_4 and the maximum loop radius is divided into a discrete number of size classes. This latter discretization provides a practical description of the continuum distribution. The number of size classes required to preserve the essential features of the loop distribution can be determined numerically. Figure 3.24 is a plot of the loop density and loop line length at 450°C as a function of the number of size classes used. These parameters are essentially independent of the number of size classes when greater than about 15 are used.

It remains to be shown that Equation (3.73) provides a mathematically appropriate boundary condition between the two regions. For the interstitial clusters up to size four, Equations (3.69)–(3.73) provide

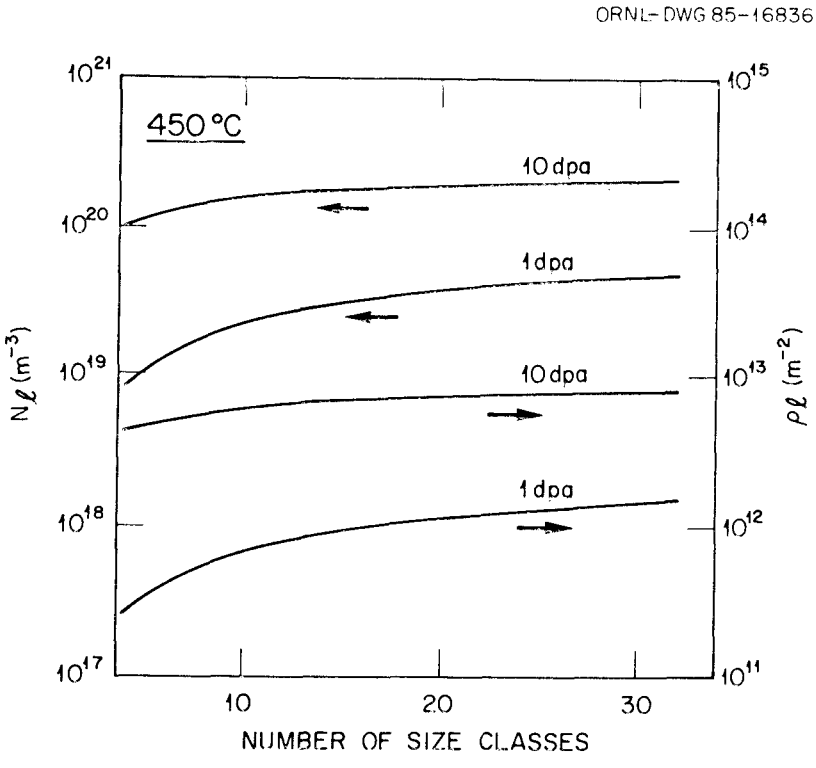

Figure 3.24. Faulted loop number density (N_ℓ) and faulted loop line length (ρ_ℓ) as a function of the number of loop size classes.

an exact representation of the physical processes involved in clustering. Therefore, the net forward current (J_+) obtained from Equation (3.73) provides a precise measure of a source term for the region in which the continuum description is used. This same current can also be exactly calculated for the discretized continuum distribution using the continuity equation. The continuity equation yields the following result:

$$\frac{\partial}{\partial t}[n(r)] = -\frac{\partial}{\partial r}[\dot{r}n(r)] \approx \frac{-\dot{r}(r+\delta r)n(r+\delta r) + \dot{r}(r)n(r)}{\delta r} \quad . \qquad (3.81)$$

If $r = r_s$, $r + \delta r = r_s$, $n(r) = C_s$ and $n(r + \delta r) = C_s$, then Equation (3.81) yields:

$$J_+ = \frac{\dot{r}(C_s)C_s}{\delta r} \quad , \tag{3.82}$$

$$J_+ = \frac{C_s B}{b_2(r_s - r_s)} \{Z_1^{\ell}(r_s)D_1C_1 - Z_V^{\ell}(r_s)D_V[C_V - C_V^{\ell}(r_s)]\} \quad , \tag{3.83}$$

where Equation (3.78) has been substituted for $\dot{r}(C_s)$. Alternately, J_+ from Equation (3.73) is given by $C_s\tau_s^{-1}$.

$$C_s\tau_s^{-1} = C_s / \frac{b_{\ell}}{B} \int_{r_s}^{r_1^{\ell}} \{Z_1^{\ell}(r_{\ell})D_1C_1 - Z_V^{\ell}(r_{\ell})D_V[C_V - C_V(r_{\ell})]\}^{-1} \, dr_{\ell} \, . \tag{3.84}$$

$$C_s\tau_s^{-1} = \frac{C_s B}{b_{\ell}} \frac{1}{(r_1^{\ell} - r_s)} \{Z_1^{\ell}(r_s)D_1C_1 - Z_V^{\ell}(r_s)D_V[C_V - C_V^{\ell}(r_s)]\} \quad , \tag{3.85}$$

where the integral has been approximately evaluated by the values of the integrand at the lower limit times dr. In the limit as r_1^{ℓ} approaches r_s (the radius of the penta-interstitial), Equations (3.83) and (3.85) are equal by inspection. This equality is subject to the assumption that the integrand in Equation (3.84) is only a weak function of r_{ℓ}. This condition is met by noting that $D_V C_V^{\ell}(r_{\ell}) \sim 0$ for small loops and that in the present model the biases are not size dependent for the smallest loops. Finally, it is worth noting that the values in Figure 3.24 for 32 size classes correspond to the case where $r_1^{\ell} = r_s$.

The model for the evolution of the dislocation structure includes four components, two of which are solely due to the irradiation and two of which are thermal. The thermal components are a high temperature climb source term (Bardeen-Herring sources) and a thermal annihilation term due to stress-directed preferential thermal emission of vacancies. Models of this type have been developed for the study of creep processes.[202,203] Network dislocations can be recovered by climb and glide processes leading to annihilation. The present model assumes that climb is the rate controlling process. The climb velocity of an edge dislocation subject to a stress, σ, is given by Nix et al.[204] as

$$v_{cl}^{\sigma} = \frac{2\pi}{\ell n(r_o/r_c)} \frac{\Omega}{b_n kT} D_v C_v^e \sigma \quad . \tag{3.86}$$

Adopting the model of Gibbs,[205] the stress is assumed to be an internal (back) stress due to a population of immobilized dislocations

$$\sigma = A G b_n \rho_i^{1/2} \quad , \tag{3.87}$$

where A is nominally 0.4 and ρ_i is the density of pinned dislocations. The average climb distance is taken as the mean dislocation spacing

$$d_{cl} = (\pi \rho_n)^{-1/2} \quad . \tag{3.88}$$

Using Equations (3.86) to (3.88), one obtains a lifetime against annihilation due to this climb-glide process as

$$\tau_{th} = \frac{d_{cl}}{v_{cl}^{\sigma}} = \left[A' \frac{2\pi^{3/2}}{\ell n(r_o/r_c)} \frac{\Omega G D_v C_v^e}{kT} \rho_n \right]^{-1} \quad . \tag{3.89}$$

In Equation (3.89) $A\rho_i^{1/2}$ has been set to $A'\rho_n^{1/2}$ and the parameter A' was used to fit thermal recovery data.

The dislocation network can also be regenerated as the result of sources that act by dislocation climb and from the emission of dislocations at precipitate interfaces.[167] It would be difficult to model these dislocation generation processes in detail. As a first-order approach, a model was developed for the generation of network dislocations by the so-called Bardeen-Herring sources.[62] Bardeen-Herring[62] sources for network dislocations are similar to the Frank-Read source except that the former are climb-driven while the latter are glide-driven.[63] The source is shown schematically in Figure 3.25 in which a pinned dislocation segment is bowed due to an applied stress. After climbing a sufficient distance, the source will collapse leaving a dislocation loop and the original line segment once again able to generate succeeding loops. For simplicity, the source may be assumed to generate $2\pi L$ of new dislocation line length after

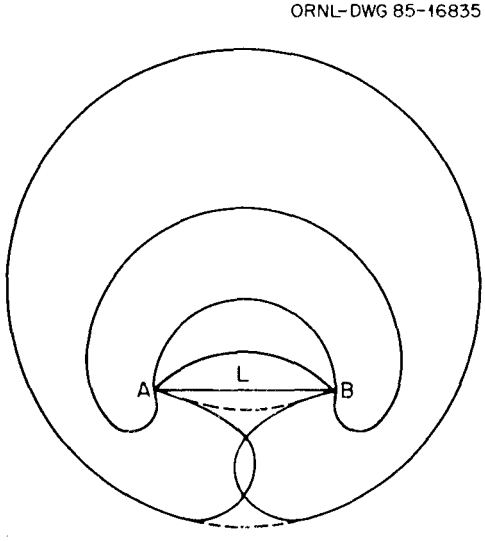

Figure 3.25. Schematic drawing of Bardeen-Herring dislocation source (after ref. 62).

climbing a distance L. The time to generate this new line length (τ_{gen}) is defined by analogy to Equation (3.89). The climb velocity is given by Equation (3.86) and the generation rate is then

$$R_{th}^{\rho_n} = \frac{2\pi L}{\tau_{gen}} S_D = \frac{2\pi L v_{cl}^{\sigma}}{L} S_D \quad , \tag{3.90}$$

$$R_{th}^{\rho_n} = 2\pi v_{cl}^{\sigma} S_D \quad , \tag{3.91}$$

in which S_D is the thermal source density. In cold worked materials the subgrain structure as well as the network dislocations provide potential sources of this type. The thermal source density was also used as a fitting parameter.

The thermal dislocation source and annihilation terms were calibrated using tensile data obtained at 450, 550 and 650°C for AISI 316 stainless steel. This data included yield strength measurements (2% offset) for both 20% cold-worked and solution annealed material as well as 20% cold worked material aged for 4000 hr at the test temperature.[163] Assuming that the hardening increment due to network dislocations varies as $(\rho_n)^{1/2}$ (ref. 296) and that this is the primary cause of the increased yield strength of the cold-worked material relative to the solution annealed material, the ratios shown in Table 3.7 are obtained from the data. The model's predictions for these same ratios are also listed. These were obtained by computing the dislocation evolution with $G_{dpa} = 0$ in the model. These values are also consistent with transmission electron microscope observations on the same

Table 3.7. Results of thermal dislocation evolution model

Dislocation Density Ratio:	Cold Worked + 4000 hr at T / As Cold-Worked	
Test Temperature T (°C)	Data	Model
450	0.73	0.99
550	0.41	0.41
650	0.054	0.053

heat of steel after thermal aging. The parameters used to obtain these results are listed in Table 3.8. They are discussed further in the section on Model Calibration.

Table 3.8. Thermal dislocation evolution parameters

Modified back-stress term, A′ 0.05	
Temperature (°C)	Source Density S_D
550	2.0×10^{21} m^{-3}
600	9.7×10^{20} m^{-3}
650	1.2×10^{20} m^{-3}
700	2.0×10^{19} m^{-3}

Under irradiation, the growth and unfaulting of Frank loops provide an additional source of network dislocations. The model assumes that the maximum loop size is governed by the geometrical constraint that the loop unfaults upon contacting another loop or network dislocation;[169] hence

$$r_{unf}^{\ell} = (\pi \rho_t)^{-1/2} \quad , \tag{3.92}$$

where ρ_t is the total (i.e. loop line length plus network) dislocation density. As the loops grow into this size class, they are no longer considered Frank loops and a dislocation line length $2\pi r^{\ell}_{unf} N^{\ell}_{unf}$ is added to the dislocation network. The time constant for this process is given by Equation (3.77) with the appropriate limits of integration. The rate at which new dislocation line length is generated by this mechanism is:

$$R^{\rho_n}_{irr} = 2\pi r^{\ell}_{unf} N^{\ell}_{unf} \tau^{-1}_{unf} \quad . \tag{3.93}$$

Network dislocations can also be annihilated by bias driven climb of point defects generated by irradiation. The climb velocity for this process is:

$$v^{irr}_{cl} = \frac{1}{b_n} [Z^n_i D_i C_i - Z^n_v D_v (C_v - C^n_v)] \quad , \tag{3.94}$$

where the superscript n denotes the relevant parameter for network dislocations. By reasoning similar to that which leads to Equation (3.89), the dislocation lifetime for this process is:

$$\tau_{irr} = \frac{b_n}{(\pi \rho_n)^{1/2}} [Z^n_i D_i C_i - Z^n_v D_v (C_v - C^n_v)]^{-1} \quad . \tag{3.95}$$

The lifetimes given in Equations (3.89) and (3.95) are added using an electrical resistance analog to yield the total lifetime time of network dislocations:

$$\tau_T = (\tau^{-1}_{irr} + \tau^{-1}_{th})^{-1} \quad . \tag{3.96}$$

With this formulation of τ_T, the shorter of the two dislocation lifetimes primarily determines the rate of dislocation annihilation. This finally leads to a rate equation describing the evolution of the dislocation network as

$$\frac{d\rho_n}{dt} = 2\pi(v_{cl}^{\sigma} S_D + r_{unf}^{\ell} N_{unf}^{\ell}) - \rho_n \tau_T^{-1} \quad . \tag{3.97}$$

The thermal dislocation evolution parameters in Equation (3.97) could be expected to be altered by irradiation. For example, the Bardeen-Herring source density is likely to be dependent on the neutron fluence and the thermal climb velocity could be altered to reflect the irradiation-induced point defect currents. However, since the thermal dislocation model was calibrated independently of the irradiation, these parameters have not been subsequently modified for the work discussed here. This component of the dislocation evolution model should be viewed as being in a somewhat preliminary state of development.

3.3.2.2 Calibration of Comprehensive Model

The sensitivity of the comprehensive model to parameter variations will be discussed in some detail in the next section. In order to provide a base case for purposes of comparison, the RS-1 swelling data was used once again to provide a calibration point for the swelling predictions. The predicted dislocation parameters were compared with the microstructural data discussed in Chapter 2. The base

parameter set was obtained by starting with the values in Table 3.5 where applicable and adding the parameters which the dislocation evolution model required. In some cases, adjustment of the parameters from Table 3.5 was required. These adjustments and the choice of values for the additional parameters will now be discussed. Table 3.9 lists the values for the modified and the new parameters.

The parameters in Table 3.9 which have been changed from the values in Table 3.5 include the vacancy formation energy (E_v^f), the interstitial migration energy (E_i^m), the recombination coefficient (α), the surface free energy (γ) and the vacancy cluster parameters (χ and r_{mv}). The values for all these parameters still fall within the range of "typical" values as discussed in Section 3.3.1.4. The changes generally reflect better agreement with values measured in austenitic alloys and also indicate the interrelationship of the various parameters. For example, the increase in E_v^f required that both γ and α also be increased in order for the model's predictions to track observed data trends. As a result, all three of these parameters are nearer to their theoretical values. The increased interstitial migration energy is a result of a new dependence in this more comprehensive model. As discussed above, the results of the simple theory are not dependent on E_i^m. However, the swelling predictions of the present model are dependent on E_i^m via its influence on the predicted faulted loop density and the subsequent effect on the network dislocation density. The sensitivity of the model's predictions to E_i^m will be shown

Table 3.9. Material and irradiation parameters used in calibration of comprehensive model

Material Parameters	
Vacancy energies: Migration, E_v^m	1.4 eV
Formation, E_v^f	1.6 eV
Interstitial migration energy, E_i^m	0.85 eV
Binding energies:	
Di-interstitial, E_2^b	1.35 eV
Tri-interstitial, E_3^b	1.75 eV
Interstitial/vacancy combinatorial number for interstitial clusters	$z_i^1 = 63$, $z_i^2 = 90$, $z_i^3 = 110$, $z_i^4 = 127$ $z_v^2 = 33$, $z_v^3 = 38$, $z_v^4 = 42$
Recombination coefficient, α	$2 \times 10^{21} D_i$ sec^{-1}
Surface free energy, γ	$3.24 - 1.4 \times 10^{-3}$ T(°C) J/m^2
Stacking fault energy, γ_{sf}	1.5×10^{-2} J/m^2
Initial dislocation density, $\rho_n(0)$	3.0×10^{15} m^{-2} — 20% cold worked 3.0×10^{13} m^{-2} — solution annealed
Interstitial bias	
Network dislocation, Z_i^n	1.25
Faulted loop, Z_i^ℓ	1.50
Poisson's ratio, ν	0.3
Shear modulus, G	Temperature-dependent value from ref. 297
Irradiation Parameters	
Cascade efficiency, η	0.333
Fraction of vacancies collapsed into microvoids, χ	0.6
Microvoid radius, r_{mv}	T = 350°C 7.0×10^{-10} m T = 400°C 7.5×10^{-10} m T > 450°C 8.0×10^{-10} m

below. Briefly, the use of the lower, pure material value for E_i^m results in faulted loop densities which are much lower than is experimentally observed. This reduced loop density leads to a lower network dislocation density since the source term is reduced. The predicted swelling can be either increased or decreased, depending upon the dose and temperature at which the comparison is made. The value of $E_i^m = 0.85$ given in Table 3.9 is in agreement with recent measurements of this parameter in austenitic steels.[270,274,275] One possible explanation for this higher interstitial migration energy in the alloys is the effect of solute trapping.[272] The fact that the model requires such a value for E_i^m is encouraging. As the model became more complex, through the introduction of additional physical mechanisms, more parameters were introduced. However, the model also became somewhat "stiffer" with respect to arbitrary parameter choices. For example, reference to Equation (3.61) indicates that relative changes in Z_i^n and η can be used to offset one another in a simple model. This is no longer the case in the present model since the various sinks have different dependencies on these parameters. The cavity and dislocation evolution are not independent, but are coupled in a complex way via their mutual effect on the point defect concentrations.

An example of this coupling is shown in Figure 3.26 where the dose dependence of swelling is plotted for various assumed dislocation densities at 400 and 550°C. For both temperatures the results of the present model with the time (dose) dependent dislocation density are compared with results obtained with three time-independent values.

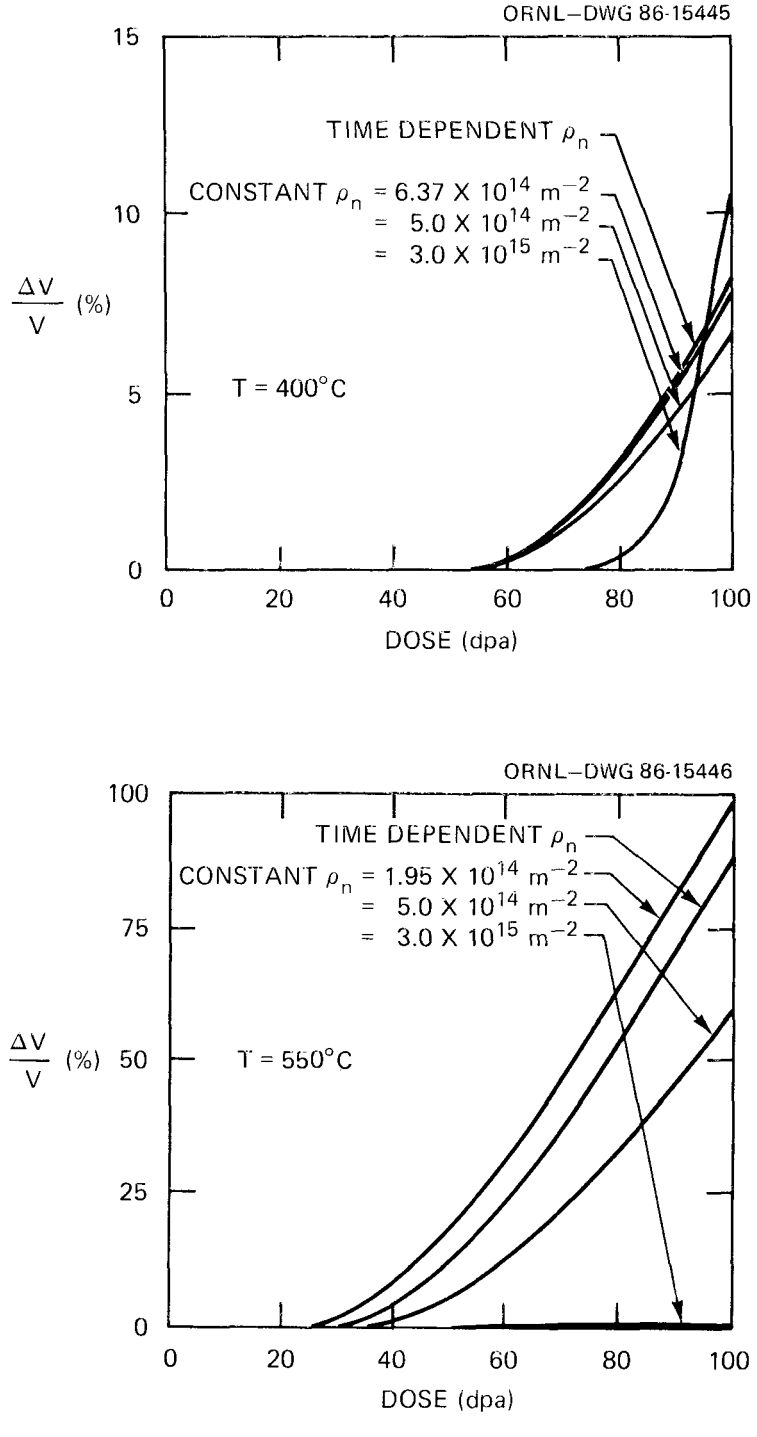

Figure 3.26. Comparison of predicted swelling at 400 (a) and 550°C (b) with dose-dependent and various constant network dislocation densities.

The values of 6.37 and 1.95 $\times$ 10^{14} m^{-2} are the "steady-state" values which evolve in the present model at 400 and 550°C, respectively. The other two values (5.0 $\times$ 10^{14} and 3.0 $\times$ 10^{15} m^{-2}) are used to help show the sensitivity of the predicted swelling to what has been termed a typical steady-state value in this temperature range[7] and the as-cold-worked value. Significant variations in the incubation time and swelling rate are observed in Figure 3.26. The behavior at 400°C is particularly complex. This effect is due to the balance of point defect partitioning between the network dislocations and the other microstructural sinks; in particular, the small, highly pressurized helium bubbles. When the dislocations are the dominant sink, increases in the dislocation density reduce the vacancy supersaturation [see Equation (3.61)]. This increases the critical bubble size and extends the incubation time for void swelling. The influence of the dislocation/interstitial bias is less significant because most point defects are recombining at the dislocations. On the other hand, when dislocations are not the dominant sink and a high gas pressure reduces vacancy emission from the bubbles, an increased dislocation density will result in an increased supersaturation. This is shown in Figure 3.27 where the effective vacancy supersaturation, S [Equation (3.3)], is plotted as a function of the dislocation density for 400 and 550°C. The nonmonotonic swelling behavior with dislocation density at 400°C shown in Figure 3.26(a) is a result of the maximum in the effective supersaturation at ~1 $\times$ 10^{15} m^{-2} shown in Figure 3.27. This result emphasizes the

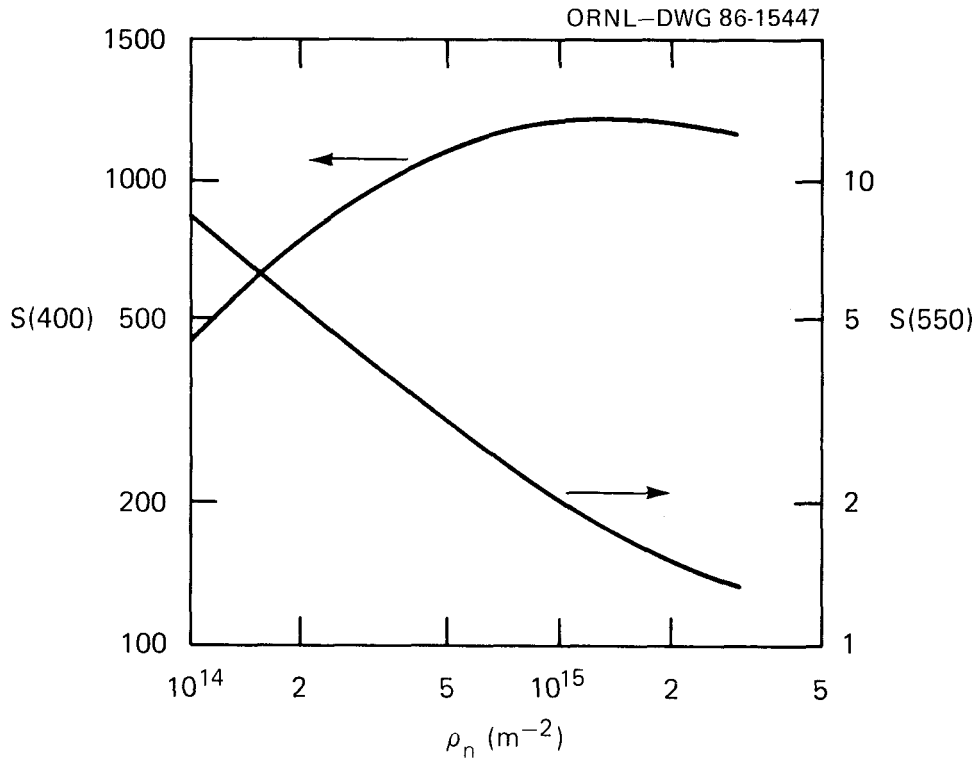

Figure 3.27. Effect of assumed network dislocation density on the effective vacancy supersaturation at 400 and 550°C.

importance of using appropriate temperature-dependent values for the various sink parameters in modeling studies.

There are several parameters used in the present work which have not been required in more simple models. These include the thermal dislocation evolution parameters in Equations (3.89) and (3.91) and the parameters used in the rate equations for interstitial clusters – Equations (3.69) through (3.75). The choice of the values for interstitial clustering parameters was guided by the results of more

detailed clustering calculations.[38-41,133,140,207,208] In Equation (3.74), the values chosen for the combinatorial numbers ($z^j_{i,v}$) depend on the geometrical configuration of the point defects and the adjacent atom sites. For example, Hayns[140] follows Damask and Dienes[208] and uses a value of 84 for the interstitial-interstitial (z^i_i) combinatorial while Olander[7] suggests a value "between 100 and 200." A more detailed analysis led Johnson[40] to a value of $z^i_i = 56$. Here the combinatorial numbers were calculated so that the values of the tetra-interstitial sink strength obtained from the combinatorial analysis was the same as if it had been calculated assuming the tetrainterstitial was a faulted loop. This led to $z^i_i = 63$, as shown in Table 3.9. Varying z^i_i in the range of 56 to 84 and scaling the other combinatorial numbers appropriately did not have a major influence on the predictions of the model. The last interstitial binding energies shown in Table 3.9 for the di- and tri-interstitials are in agreement with theoretical values of these parameters.[41,208] Varying these binding energies within a reasonable range of values influences the temperature dependence of the predicted loop density. The network dislocation density and cavity swelling are affected to a lesser degree as shown in the next section. The predicted dislocation density under irradiation is sensitive to the thermal dislocation evolution parameters (Table 3.8) only for temperatures above about 550°C when faulted loops cease to contribute significantly to the dislocation network. To a first approximation, the source density, S_D, should be about

equal to L^{-3} where L is the mean spacing of dislocation pinning points. If other dislocations provide the primary pinning sites, then L should be roughly proportional to $\rho_n^{-1/2}$. In this case, the maximum and minimum values of S_D given in Table 3.8 would correspond to pinned dislocation densities of 1.6×10^{14} and 7.4×10^{12} m^{-2}.

3.3.2.3. Predictions of Comprehensive Model

This section describes the predictions of the comprehensive model using the parameters discussed above (Tables 3.5, 3.8 and 3.9). The equations for the small interstitial clusters [Equations (3.71) through (3.73)] are coupled with the point defect equations [Equations (3.69) and (3.70)] so that the simple, algebraic solution presented in Section 3.3.1.3 cannot be used here to calculate the point defect concentrations. Instead, a numerical solution has been implemented using the method of false-position. After obtaining the point defect and interstitial cluster concentrations at steady state, the rate equations for the various extended defects were integrated using the LSODE subroutine package.[264]

Predicted values for void swelling, network dislocation density and faulted loop density are shown in Figure 3.28(a-c) as a function of irradiation temperature at 50 and 100 dpa for 20% cold-worked material. The temperature range shown in Figure 3.28 includes the operating temperatures of fast reactor core components. These predictions compare well with fast reactor irradiation data as shown in the

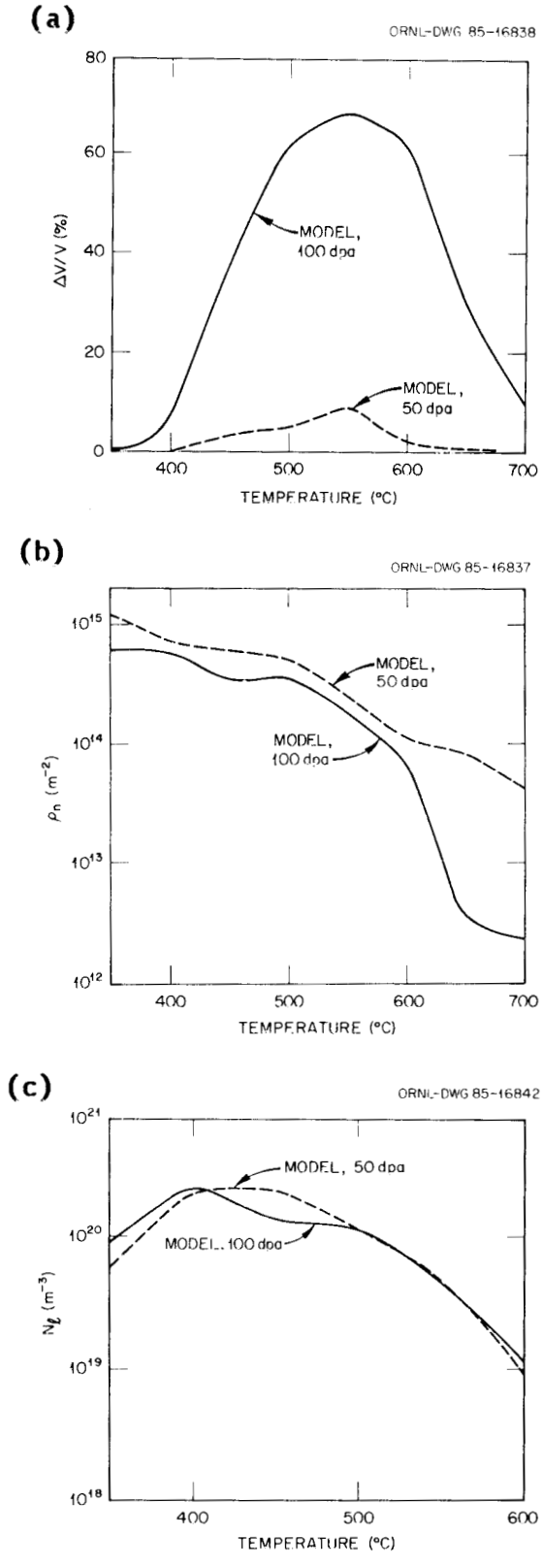

Figure 3.28. Temperature dependence of model predictions of swelling (a), network dislocation density (b) and faulted loop density (c) at 50 and 100 dpa.

next three figures. The swelling data shown in Figure 3.29 once again is from the RS-1 experiment in the EBR-II.[82,83,152] Figure 3.29(a) compares swelling data in the range of 40 to 60 dpa with the predictions of the model. This intermediate fluence is just beyond the swelling incubation dose, so the predicted swelling is highly dependent on dose. This can be seen by comparing the theoretical curves for 45 and 50 dpa in Figure 3.29(a). The predicted swelling incubation doses are quite consistent with the data. A comparison of the theory and the RS-1 data at high dose is shown in Figure 3.29(b). The fact that there is good agreement between the theory and the data at ~70 dpa indicates that the predicted swelling rates (~1%/dpa in the peak swelling region) are consistent with observation also. The model predictions of swelling at temperatures greater than 650°C shown in Figures 3.28(a) and Figure 3.29 are also consistent with recent observations.[152] The influence of transient vacancy clusters reduces low-temperature swelling here in the same way as it did in the earlier cavity evolution model. The clustering fraction (χ) has been reduced from 0.8 to 0.6 and the cluster radii have been slightly increased. This results in the microvoids being less important than they were in the more simple model. It appears that the dynamic nature of the dislocation structure in the present model helps to suppress the vacancy supersaturation at low doses and low temperatures. Hence, the higher clustering fraction in the cavity evolution model acted as a surrogate for the inadequately represented dislocation evolution.

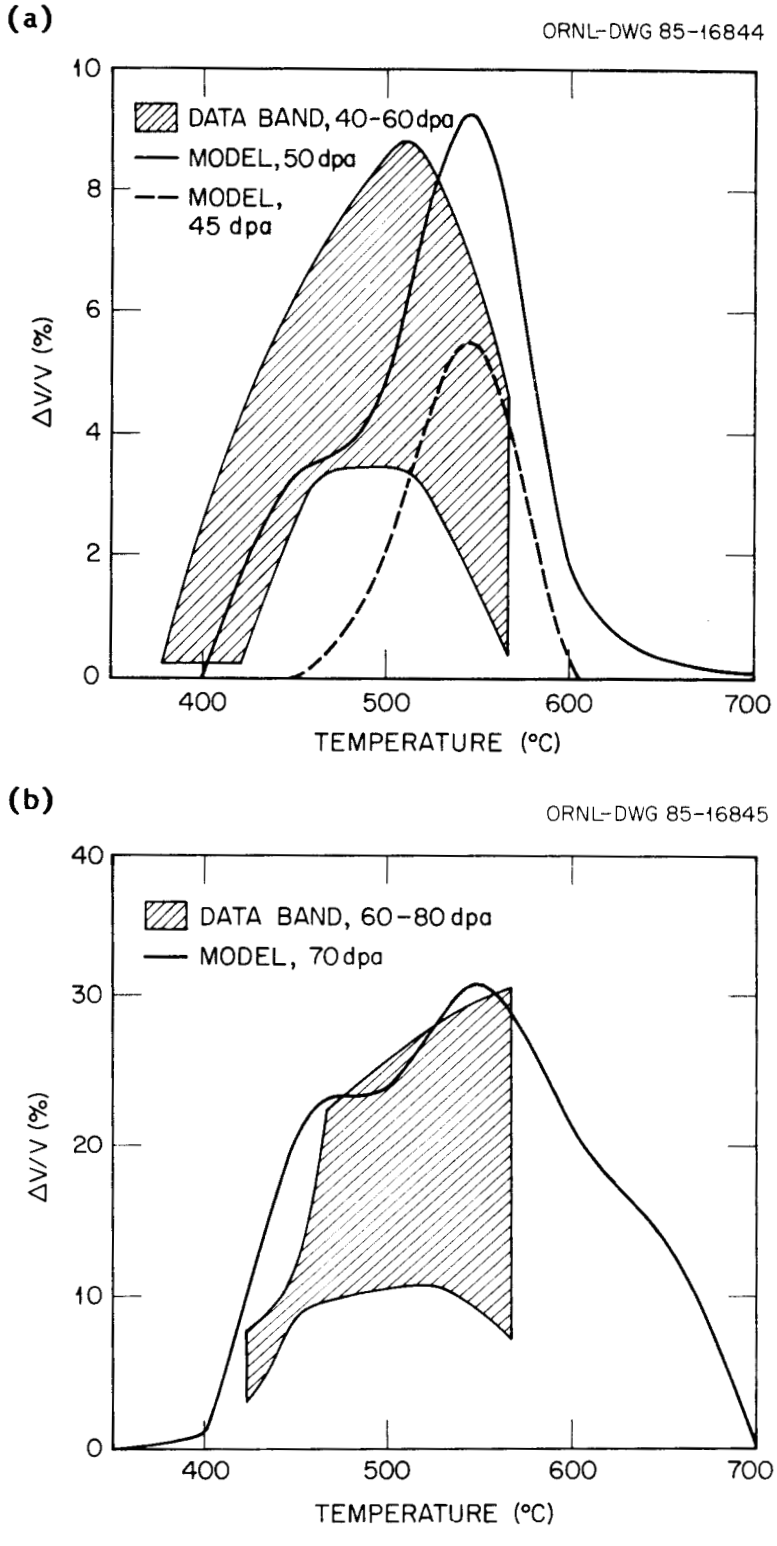

Figure 3.29. Comparison of predicted swelling and fast reactor data at an intermediate (a) and high (b) fluence.[82,83,152]

There is less data with which to compare the model's predictions of dislocation and faulted loop densities. Figure 3.30 compares dislocation densities for M316 stainless steel irradiated in the Dounreay Fast Reactor and the DO-heat of 316 stainless steel irradiated in the EBR-II.[166,172] The agreement is quite good. The results are also consistent with other reported values for AISI 316 stainless steel irradiated in the EBR-II.[78] Predicted faulted loop densities are compared with data from several sources in Figure 3.31. The data are for AISI 316 stainless steel irradiated in both the solution-annealed and cold-worked conditions at doses between about 6 and 16 dpa (refs. 78, 91,150,169,170). The data from ref. 169 include varying stress levels. The predicted curves reflect the peak faulted loop density for both solution-annealed and 20% cold-worked starting conditions. The data are reasonably well represented by the predictions except at low temperatures where the loop density is somewhat low.

Although the thermal dislocation evolution model was calibrated independently, the predictions of the model for fast-neutron-irradiation conditions can be sensitive to the thermal dislocation model parameters. This sensitivity is shown in Figure 3.32 where the thermal source density, S_D, has been varied from the nominal value which was determined during the thermal calibration. For temperatures greater than 550°C, the curves labeled "Low S_D" and "High S_D" in Figure 3.32 were calculated with a 10% decrease and increase in this parameter, respectively. For 550°C and below, the value was varied by

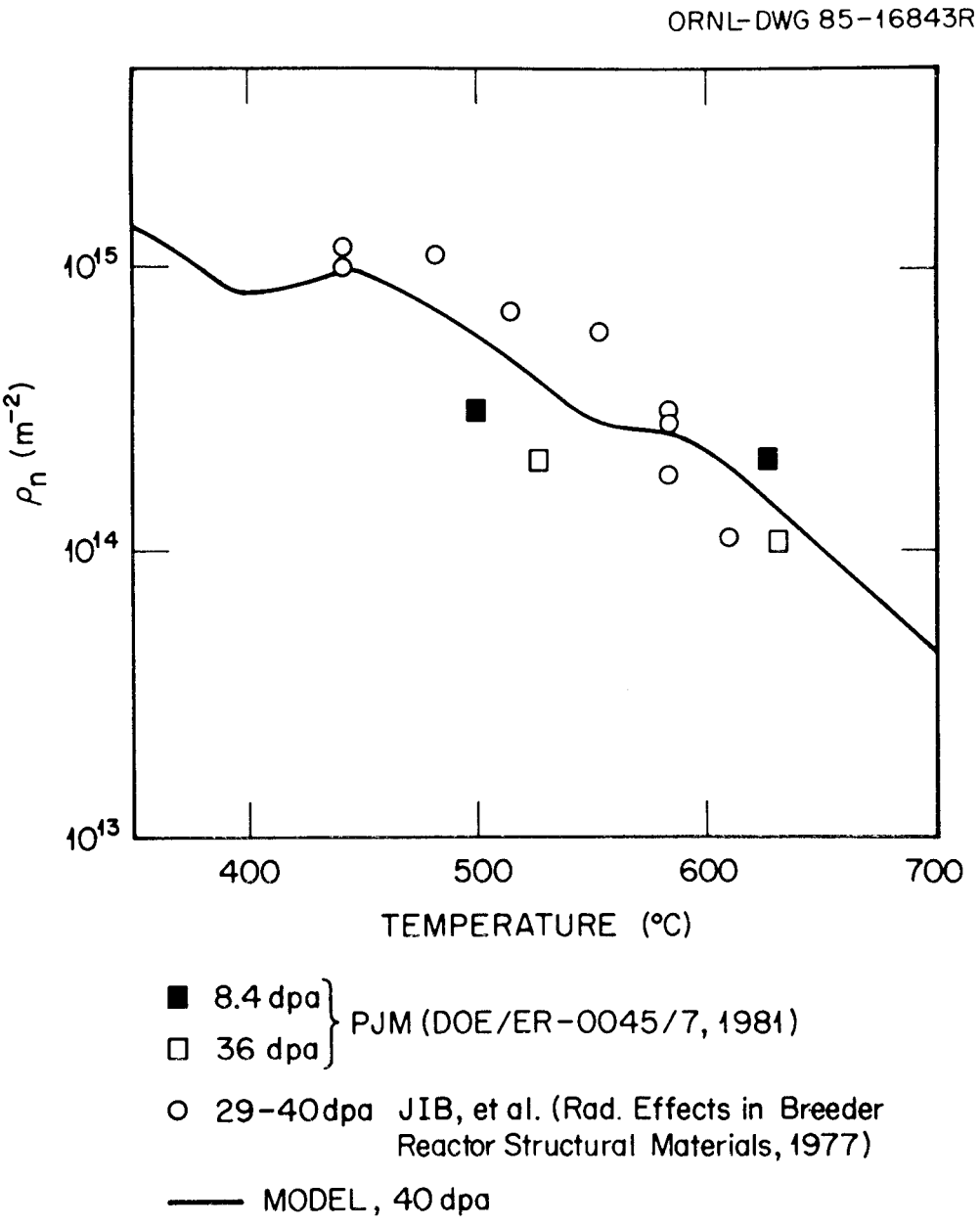

Figure 3.30. Comparison of predicted network dislocation density and fast reactor data at 40 dpa (refs. 166,172).

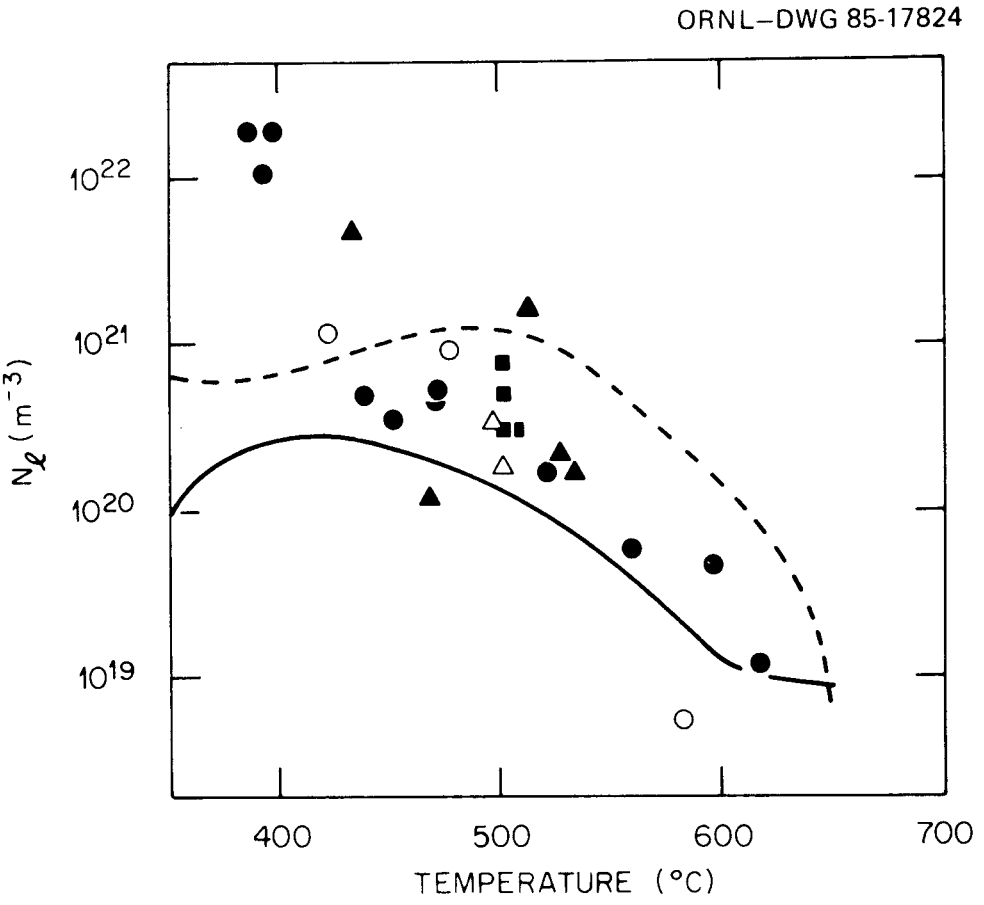

Figure 3.31. Comparison of predicted maximum faulted loop density and low fluence fast reactor data.[78,81,150,160,170]

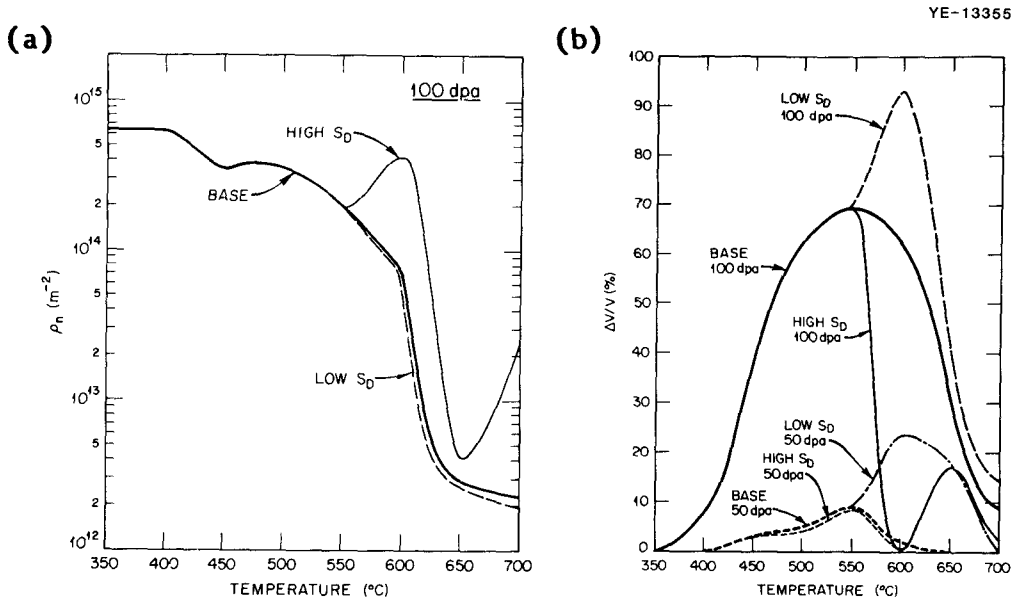

Figure 3.32. Influence of the thermal dislocation source density (S_D) on the predicted network dislocation density (a) and void swelling (b) at 50 and 100 dpa (see text for range of parameter variations).

a factor of 10 with little effect. This is a temperature regime in which little thermal recovery occurs. However, at about 575 to 625°C, the predictions are quite sensitive to S_D. This is a temperature range in which the microstructure of the material begins to recover in the absence of irradiation. This occurs largely because of increased thermal vacancy diffusion. Under irradiation, the vacancy supersaturation decreases in this temperature range for the same reason. Hence, the behavior of the material under irradiation begins to appear more like the thermal behavior, and therefore the sensitivity of the model

predictions in this transition regime is not surprising. The temperature range over which this transition occurs is known to be dependent on alloy composition.[172] Therefore, the predictions of the present model at the higher temperatures reflect the specific heat (DO) which was used to calibrate the thermal dislocation evolution model. The sensitivity of the predicted swelling shown in Figure 3.32(b) to the network dislocation density may explain in part the observation that swelling is fairly heterogeneous in cold-worked materials.

During the calibration, the model was also used to compare alternate descriptions of the faulted loop/interstitial bias factor, Z_i^{ℓ}. If interstitial absorption at faulted loops is diffusion limited, the long-range strain fields associated with the loop would give rise to an interstitial bias that was dependent on the loop radius.[70,72] On the other hand, if interstitial absorption was reaction-rate limited, a constant bias factor would be obtained.[127] The temperature dependence of the predicted faulted loop density at 50 and 100 dpa and the maximum faulted loop density are shown in Figure 3.33. Results are compared for the size-dependent bias of Wolfer and Ashkin[70] and the constant value of $Z_i^{\ell} = 1.50$. The calculated size-dependent bias has been modified so that it asymptotically approaches the value of the network dislocation/interstitial bias as the loop radius becomes large and at small sizes a maximum value of 3.5 was used.[133] The predictions using the size-dependent bias are clearly too high at the higher temperatures when compared to the data shown in Figure 3.31. This result is in

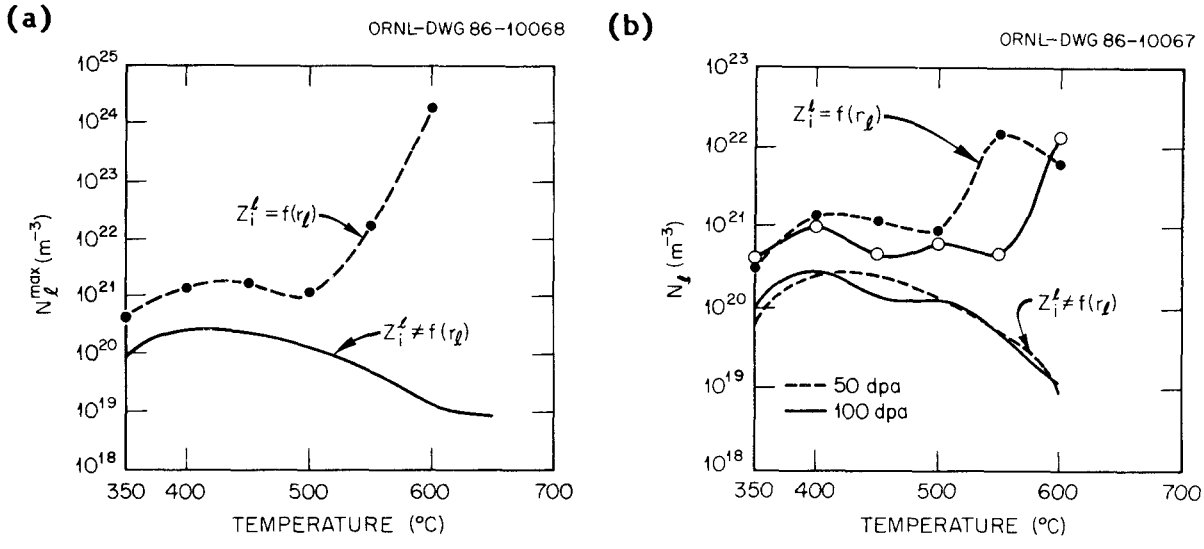

Figure 3.33. Comparison of predicted faulted loop densities obtained using a constant faulted loop/interstitial bias (Z_i^ℓ = 1.5) and a size-dependent bias (from ref. 70).

agreement with an analysis of loop growth in nickel during electron irradiation performed by Yoo and Stiegler.[127]

The fluence dependence of the model predictions at 500°C is shown in Figures 3.34(a) and (b) for 20% cold-worked and solution-annealed material, respectively. The coupling of the evolution of the various microstructural features is clearly seen. After an initial transient, the microstructure reaches a state which is independent of the initial condition. The incubation time for swelling is not primarily associated with the dislocation transient but rather with the time required for the cavities to accumulate the critical number of helium

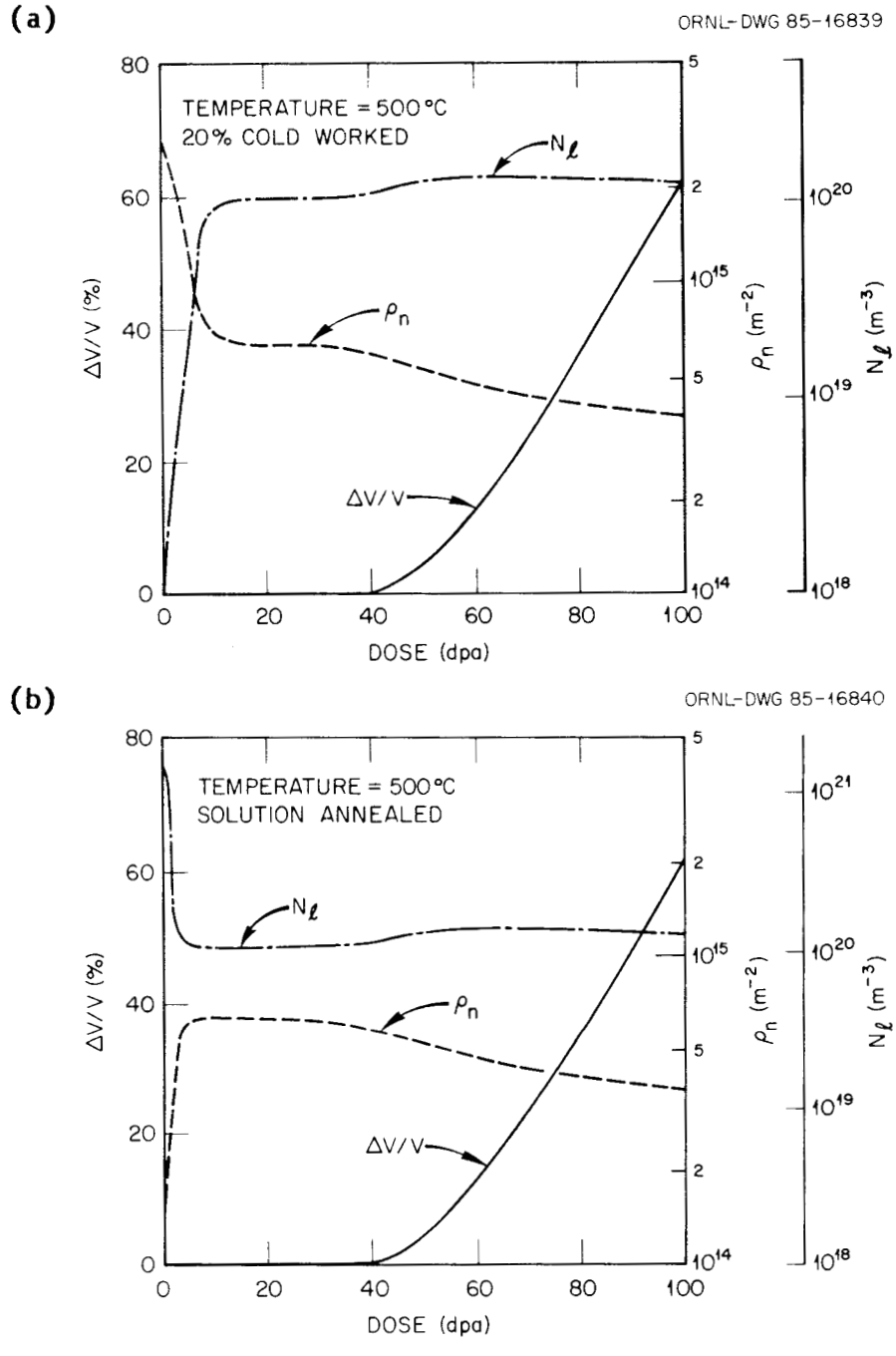

Figure 3.34. Dose dependence of predicted swelling, network dislocation density and faulted loop density at 500°C for 20%-cold-worked (a) and solution-annealed material (b).

atoms. Following the initiation of void swelling, additional recovery occurs as the cavity sink strength begins to increase. A regime in which the swelling rate is approximately constant and fairly high occurs when the cavity and dislocation sink strengths have similar values. When such parity occurs, the maximum theoretical swelling rate is observed.[74] Although it is not shown in Figure 3.34, at high doses the cavity sink strength exceeds the dislocation sink strength and the swelling rate begins to decrease as predicted by theory.[74] The near coincidence of the values for the solution-annealed and cold-worked material at low doses may be somewhat artificial. The model does not include an explicit cavity nucleation calculation and the same initial cavity densities were used for both materials. Some data indicate that void densities at low doses are higher for solution-annealed material,[170] and neglecting this difference may influence the model's predictions at low doses.

The evolution toward a saturation microstructure has been observed.[76,77,300] This was discussed in Chapter 2. The predicted low dose peak in the faulted loop number density in solution-annealed material has also been observed;[170] however, Brager and Straalsund have reported similar high values at low doses in 20% cold-worked stainless steel,[161] in conflict with the predictions shown in Figure 3.34. Note that on the dose scale of Figure 3.34(b) the early transient in the faulted loop density occurs very quickly. The actual value of the predicted loop density is zero when the dose is zero.

While the initial recovery of the network dislocation density in the 20% cold-worked material appears to be in agreement with the available data,[77,161] the initial transient appears to occur too quickly in the solution-annealed material.[77] The thermal dislocation source term may be the cause of the too rapid buildup of the network dislocation density for the solution-annealed simulation. The source density (S_D) values were developed for 20% cold-worked material and implicitly reflect a near-steady-state value for the network dislocation density, as discussed above. Hence, for the solution-annealed material, the values of S_D may be too high at low doses. Explicit dislocation density dependence in S_D may be required to improve the agreement with the solution-annealed data. The simple dislocation recovery model described above could also be responsible for some of the deviations from the data. This model implicitly assumes that all of the dislocation line length is homogeneously distributed in the material. In fact, the as-fabricated, cold-worked microstructure is quite heterogeneous with two primary features: a coarse distribution of microtwins, stacking faults, and deformation bands along with a finer distribution of network dislocations.[161] These two features are reported to have different thermal stabilities with the coarse structure stable up to the recrystallization temperature while the fine distribution anneals out at much lower temperatures. The use of a single "effective" climb distance for network dislocation annihilation may be insufficient to account for the varying thermal stabilities and spatial orientation of the dislocations in the material.

3.3.2.4. Sensitivity of Comprehensive Model to Parameter Variations

The previous section has demonstrated that the model can successfully predict a variety of fast reactor data when reasonable input parameters are used. The sensitivity of the predictions of the model to small changes in the values of key parameters will now be examined. The general trend of these results is consistent with the key concept discussed above (viz., that void swelling and microstructural evolution are primarily controlled by point defect partitioning). In the context of the rate theory, the point defect sink strengths determine this partitioning. As a result of their mutual influence on the point defect concentrations, the evolution of any one sink is coupled to the others. The primary example of this coupling is that of the cavities and the dislocations, but the other sinks can also play a significant role. To help demonstrate this coupling, the influence of the multiple sink strength corrections on the predicted void swelling and network dislocation density will also be examined.

In each of the examples shown below, the influence of a specific parameter variation will be demonstrated by comparing the predicted swelling, network dislocation density and faulted loop density with the results obtained using the basic parameter set discussed in the previous section. These latter values are denoted in these figures by the designation "base case." Because the swelling incubation dose is the parameter that limits the engineering use of materials, the work discussed in Sections 3.2 and 3.3.1 emphasized those factors that

influence the incubation dose. In the results that follow here, more emphasis is placed on the behavior of the model predictions at higher doses. Variations in the swelling shown at 50 dpa do reflect changes in the incubation behavior since the incubation dose is in the range of 35 to 50 dpa for the base case parameters. The results shown at 100 dpa provide a measure of the model's sensitivity to parameter variations at a dose well beyond the incubation dose. This limit is useful to determine which parameters influence the swelling rate and to explore the coupled evolution of the microstructural features in the "steady-state" regime.

The influence of the interstitial migration energy, E_i^m, on model predictions is shown in Figure 3.35(a-c). The faulted loop density shown in Figure 3.35(c) is the maximum value observed out to 100 dpa. The values of the swelling and network dislocation density are at the doses shown in the figure. These results were mentioned above and the dependence of swelling at intermediate temperatures [Figure 3.35(a)] is a result of the variation in the faulted loop density which in turn has a strong effect on the network dislocation density [Figure 3.35(b)]. The complex temperature dependence of the effect on void swelling at 100 dpa is in agreement with the arguments advanced above when discussing the impact of various dislocation densities on the vacancy supersaturation (cf. Figure 3.27). At low to intermediate temperatures, dislocations are the dominant sink initially. In this temperature regime, a reduced E_i^m leads to a lower dislocation density, a

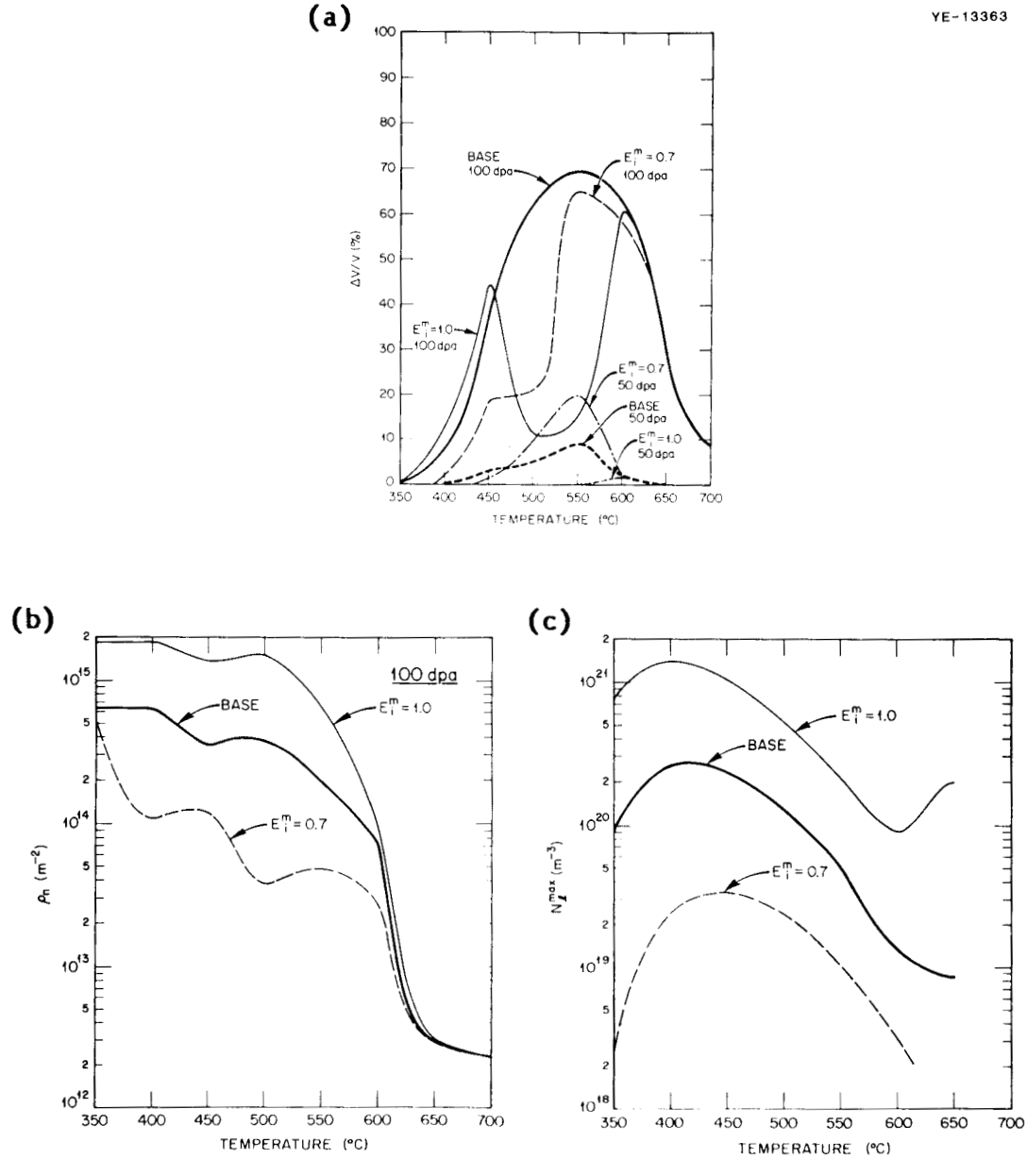

Figure 3.35. Influence of the interstitial migration energy (E_i^m) on the predicted swelling (a), network dislocation density (b) and maximum faulted loop density (c).

higher vacancy supersaturation and therefore a reduced incubation time. Increasing E_i^m has the opposite effect and the swelling predicted at 50 dpa is shifted accordingly. However, once swelling begins, the increasing cavity sink strength approaches the value of the dislocation sink strength and a higher swelling rate is observed with the higher dislocation density at low temperatures due to more effective partitioning of the vacancies to the cavities. At intermediate temperatures, lower cavity densities lead to a lower cavity sink strength at a given swelling and so the high dislocation density does not promote the more rapid swelling seen below 450°C and swelling is greater for the lower dislocation density. Above about 600°C, the faulted loop density falls rapidly and the predicted swelling is not dependent on E_i^m.

The di-interstitial binding energy, E_2^b, has an effect on the predicted microstructural parameters which is similar to the interstitial migration energy. The results obtained when E_2^b is varied about its nominal value of 1.35 eV are shown in Figure 3.36(a-c). The influence on the swelling incubation time and the peak swelling rate is once again due to changes in the faulted loop evolution. The influence of the tri-interstitial binding energy, E_3^b, is relatively minor, as shown in Figure 3.37(a-c). At much lower values of E_3^b ($\leq$ 1.2 eV), the predicted loop density is again too low and the response of the model begins to be similar to that shown for E_2^b. For higher values of E_3^b little change from the base case is observed.

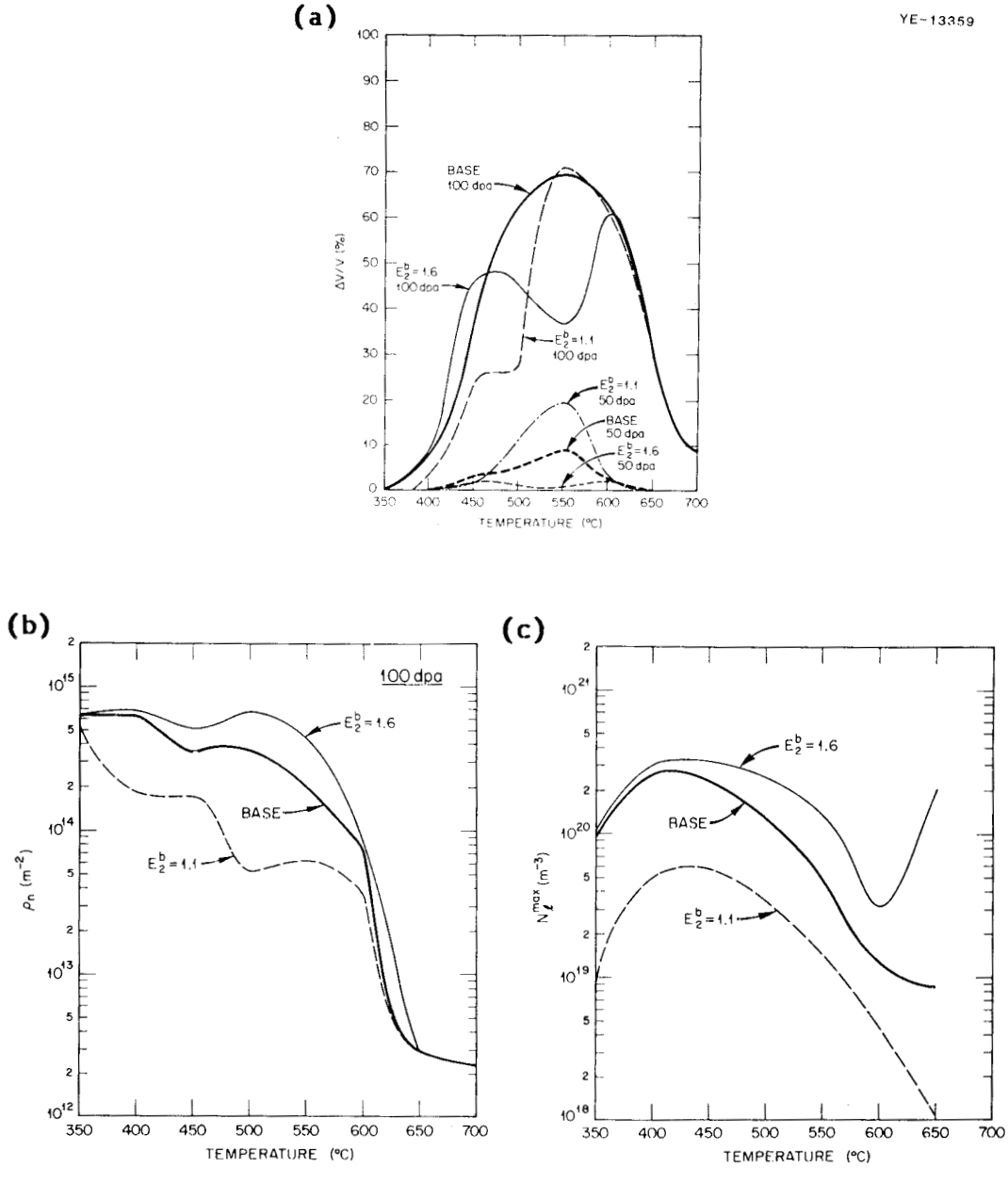

Figure 3.36. Influence of the di-interstitial binding energy (E_2^b) on the predicted swelling (a), network dislocation density (b) and maximum faulted loop density (c).

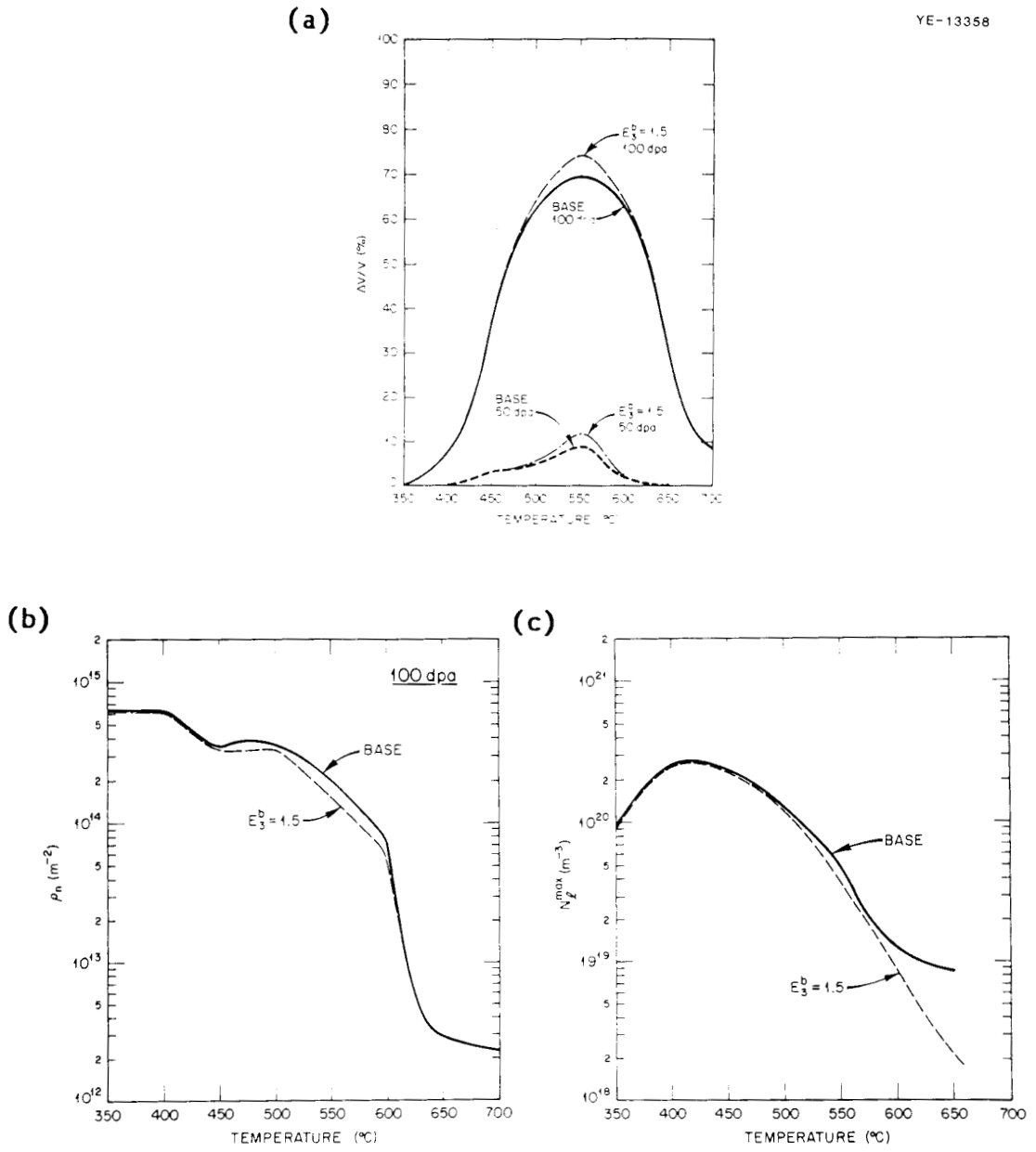

Figure 3.37. Influence of the tri-interstitial binding energy (E_3^b) on the predicted swelling (a), network dislocation density (b) and maximum faulted loop density (c).

The effective vacancy supersaturation is inversely proportional to the self-diffusion coefficient [Equation (3.3)] and the critical number of gas atoms for bubble-to-void conversion is inversely proportional to the square of the natural logarithm of the supersaturation [Equation (3.8)]. Therefore, the self-diffusion coefficient has its most direct effect on the swelling incubation time. The sensitivity of the model to changes in the activation energy for self-diffusion is shown in Figure 3.38(a-c). The influence of both the absolute value of E_{SD} (2.9 and 3.0 eV) and the partitioning of the self-diffusion energy between vacancy migration and formation are shown ($E_{SD} = E_v^m + E_v^f$). As expected, increasing the self-diffusion energy increases the maximum level of swelling and increases the peak swelling temperature. For a given self-diffusion coefficient, increasing the vacancy formation energy relative to the vacancy migration energy increases the predicted swelling at high temperature. In both of these two cases the primary influence of the changes in the self-diffusion parameters is to alter the swelling incubation time rather than the swelling rate.

For the case of the increased self-diffusion energy, a higher effective vacancy supersaturation is obtained under irradiation since the self-diffusion coefficient is reduced [see Equation (3.3)]. When the self-diffusion energy is held constant and the vacancy migration energy is reduced, the higher vacancy diffusion coefficient leads to a lower vacancy concentration under irradiation. Bulk recombination is therefore reduced and a somewhat increased supersaturation is also

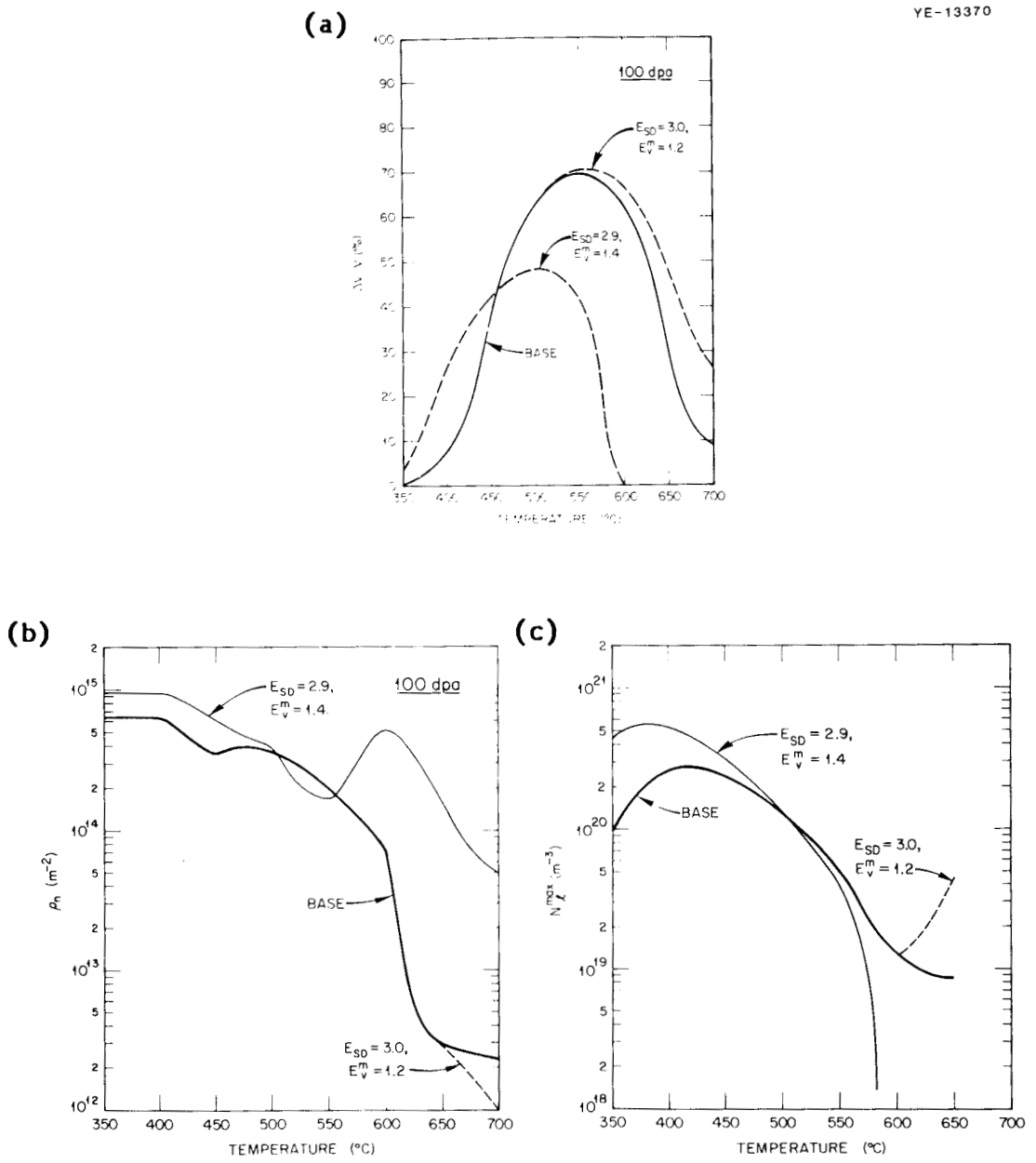

Figure 3.38. Influence of the self-diffusion energy (E_{SD}) and vacancy formation energy (E_v^f) on the predicted swelling (a), network dislocation density (b) and maximum faulted loop density (c).

obtained at the higher temperature where bulk recombination is responsible for annihilating a significant fraction of the point defects. These higher supersaturations reduce the critical number of gas atoms required for bubble-to-void conversion [see Equation (3.8)]. The dislocation climb velocity is also a function of the self-diffusion coefficient [Equations (3.86) and (3.94)]. Therefore, the temperature dependence of the predicted swelling can be further altered because of the coupled evolution of the cavities and dislocations. Generally higher dislocation densities are predicted as a result of the reduced supersaturations. At low temperatures this higher dislocation density helps to promote swelling while at high temperatures swelling is reduced as discussed in Section 3.3.2.2.

The model is, of course, quite sensitive to the network dislocation/interstitial bias, Z_1^n. This is shown in Figure 3.39(a–c). Because the dislocation climb velocity increases with Z_1^n [Equation (3.94)], the network dislocation density is reduced when the bias is increased. This leads to enhanced loop formation which helps to minimize the reduction in the network. Swelling is increased with a higher bias as a result of both a reduced incubation time and an increased steady-state swelling rate. The bias effect is greater at the higher temperatures where the dislocations become the dominant sink in the system. The low swelling at high temperatures with a bias of 1.20 is a result of an unrecovered dislocation network suppressing the vacancy supersaturation. The effect of the network dislocation/interstitial bias can be complex. This is shown in Figure 3.40(a) where the

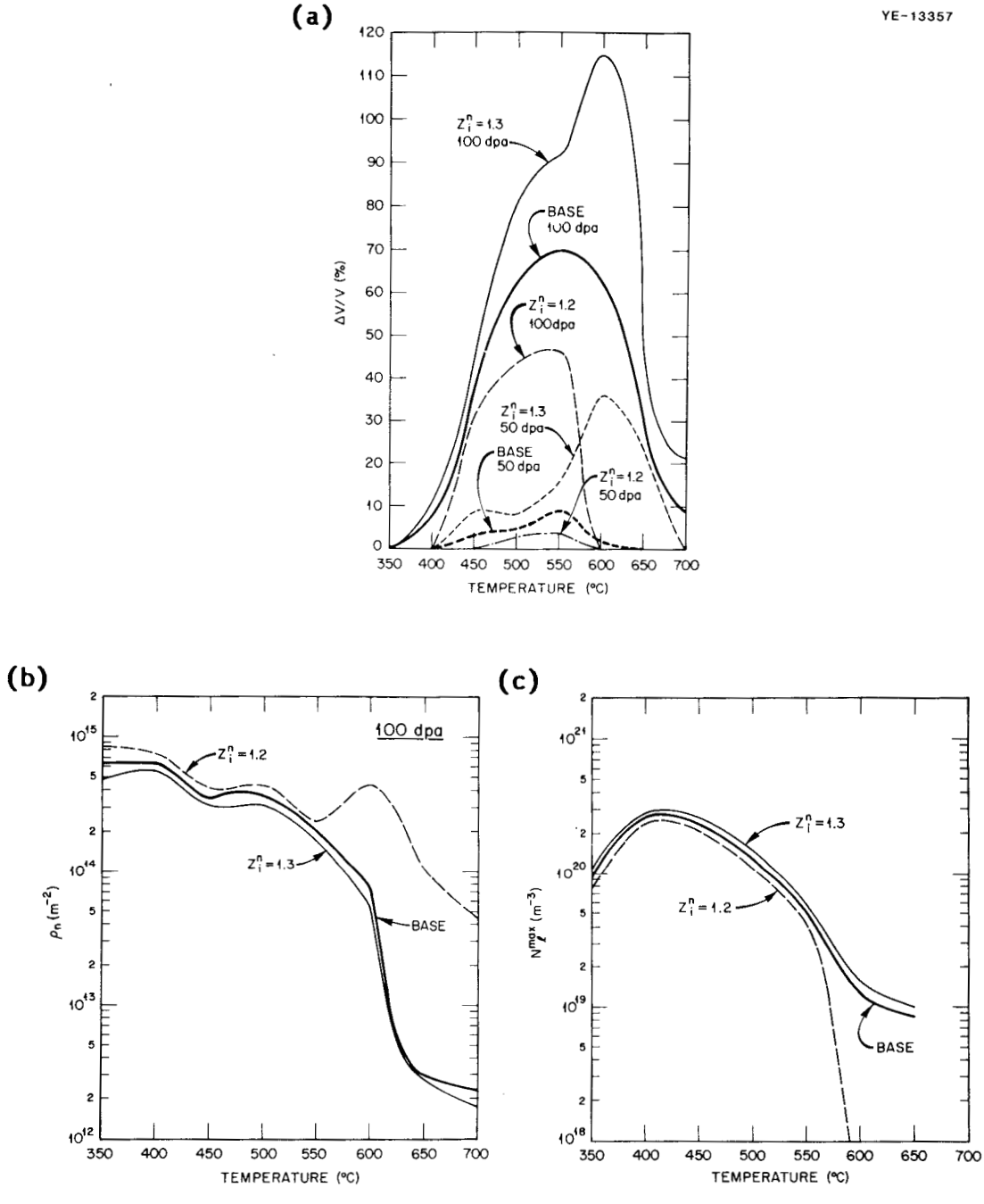

Figure 3.39. Influence of the network dislocation/interstitial bias (Z_i^n) on the predicted swelling (a), network dislocation density (b) and maximum faulted loop density (c).

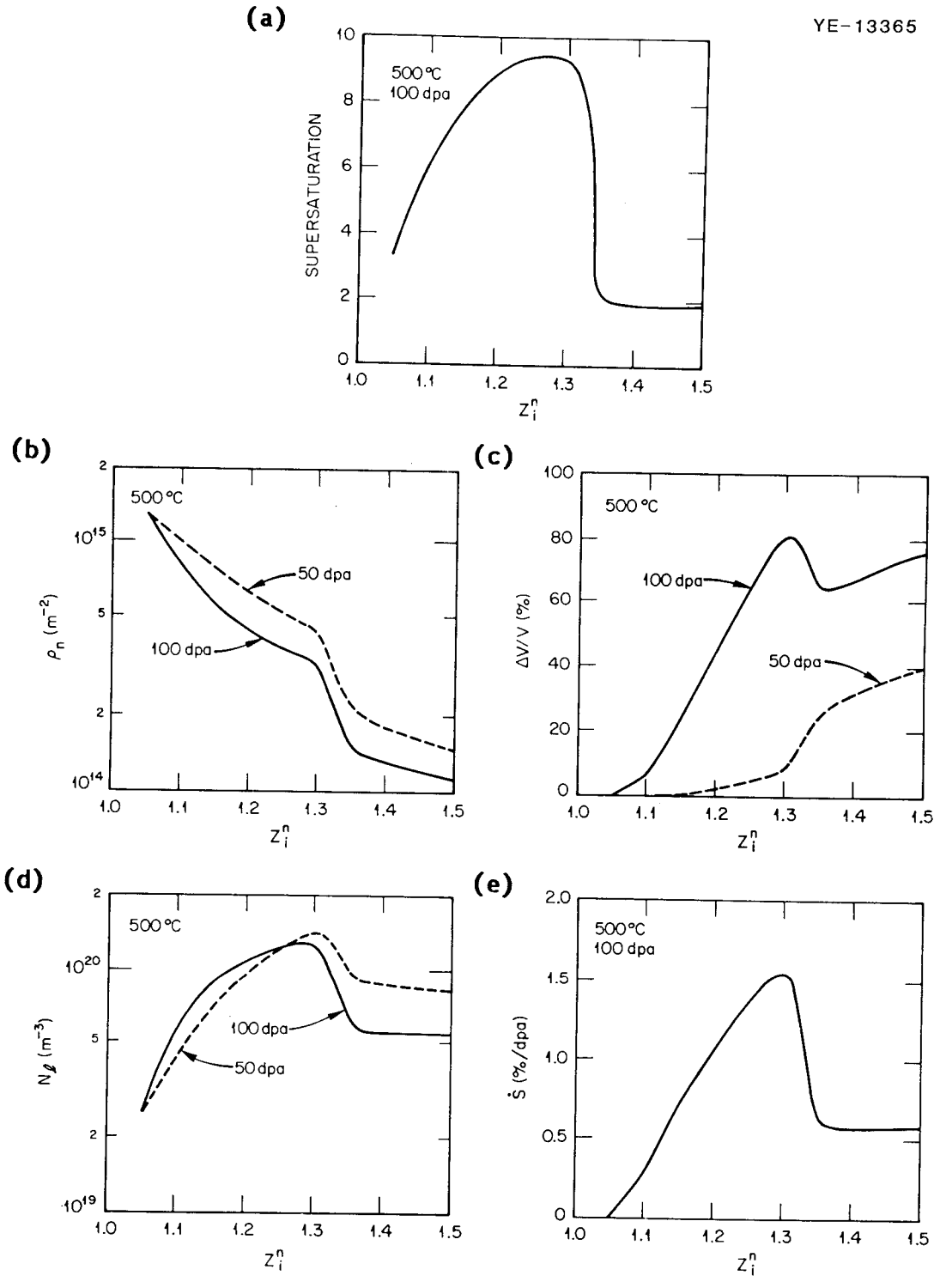

Figure 3.40. Influence of the network dislocation/interstitial bias (Z_i^n) at 500°C on the effective vacancy supersaturation (a), network dislocation density (b), swelling (c), faulted loop density (d), and swelling rate (e) at the indicated doses.

vacancy supersaturation has been plotted as a function of the bias; note that the nominal value used here is 1.25. The supersaturation initially increases with bias, and the expected changes in the microstructural parameters and the steady-state swelling rate are observed [Figure 3.40(b–e)]. The rapid reduction in the supersaturation for biases greater than about 1.3 is due to the conversion of a large number of matrix bubbles to voids. This "over-nucleation" (compared with the base case) leads to additional recovery of the dislocation network and a reduced swelling rate. Without the additional dislocation recovery for $Z_i^n > 1.3$, a somewhat greater swelling rate than that shown in Figure 3.40(e) would have been observed.

The model is less sensitive to the Frank faulted loop/interstitial bias as shown in Figure 3.41. Varying the strength of this bias $(Z_i^\ell - 1)$ by a factor of 20% results in a maximum change in the peak faulted loop density of about 40%. The higher loop bias leads to a reduced loop density and a higher network dislocation density because the loops grow and unfault at a higher rate. At intermediate temperatures the lower loop bias leads to enhanced swelling because of the lower dislocation density; this result is similar to the case for an increased Z_i^n discussed above. At lower and higher temperatures the opposite dependence on Z_i^ℓ is observed; swelling is higher for the higher loop bias. At 550°C, network dislocations are the dominant sink and the reduced network dislocation density with $Z_i^\ell = 1.4$ leads to a somewhat shorter incubation time and an initially higher swelling rate. At 650°C, network dislocations are not dominant once recovery

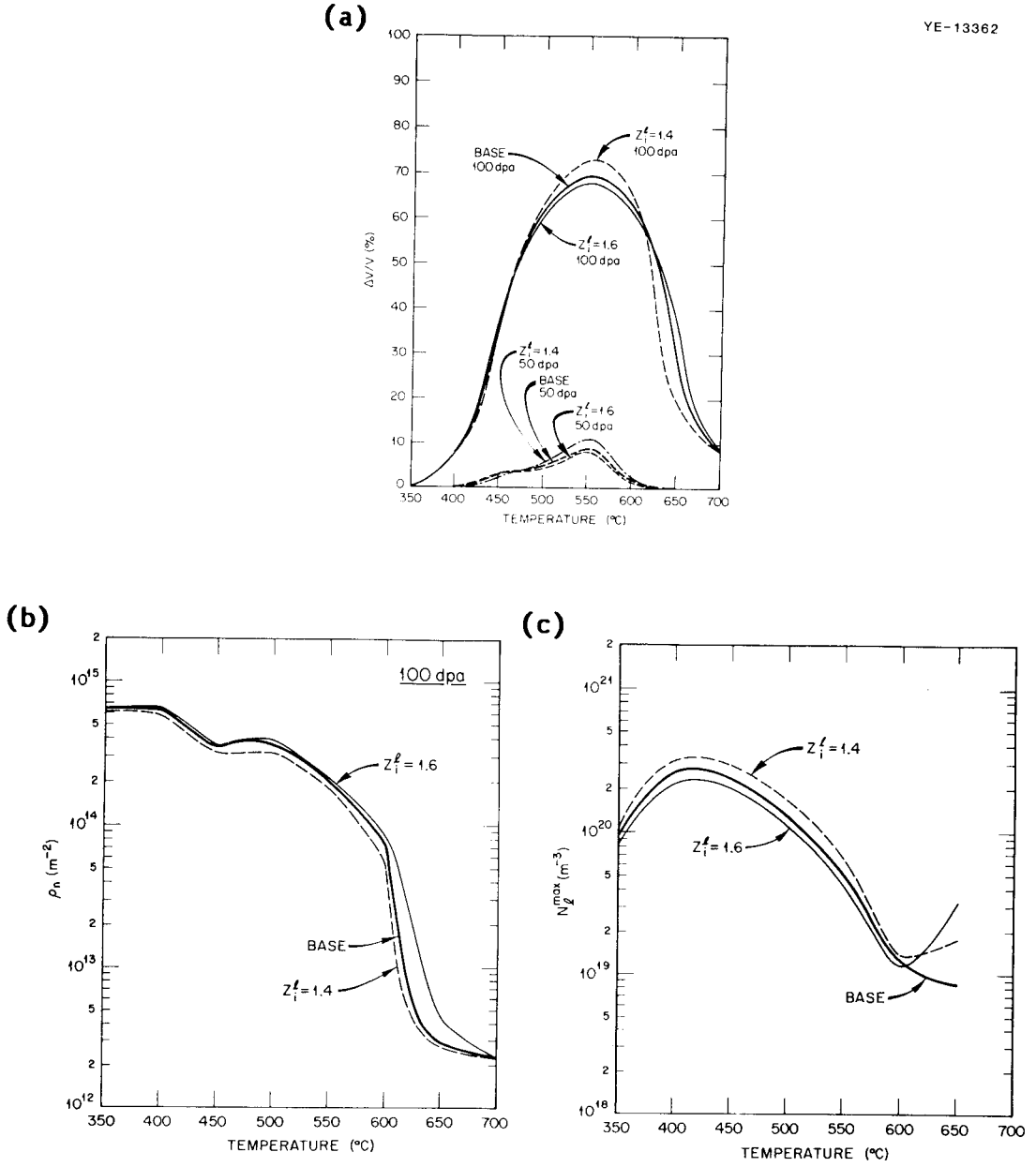

Figure 3.41. Influence of the Frank faulted loop/interstitial bias (Z_i^ℓ) on the predicted swelling (a), network dislocation density (b) and maximum faulted loop density (c).

has occurred and the higher dislocation density with $Z_i^\ell = 1.6$ leads to a higher swelling rate. Comparing the predicted temperature dependence of swelling in Figures 3.39(a) and 3.41(a) illustrates the differences between varying Z_i^n with a constant network dislocation density and varying the dislocation density with a constant Z_i^n. The predicted network dislocation density is very similar for the case of $Z_i^n = 1.3$ in Figure 3.39(b) and $Z_i^\ell = 1.4$ in Figure 3.41(b); yet the predicted swelling is quite different.

The dependence of the model on the cascade efficiency (η) is similar to the dependence on Z_i^n. The effect of a 20% increase or decrease in η is shown in Figure 3.42. This general similarity is predicted by relations such as Equation (3.61) for the case when dislocations are the dominant sink. However, this simple equation neglects the influence of Z_i^n and η on the dislocation density. Therefore, some differences are observed between Figures 3.39(a) and 3.42(a), even in the intermediate temperature range where the network dislocations are dominant. At the highest and lowest temperatures, these differences increase. Overall, the predicted dependence on Z_i^n and η is too similar to permit the model to be used to discriminate between the two parameters when fitting experimental data.

The major effect of the surface free energy (γ) is to influence the swelling incubation time as predicted by Equation (3.8). In addition, at low temperatures the surface free energy influences the lifetime of the transient vacancy clusters by determining the rate at which they emit vacancies [Equation (3.53)]. This affects the vacancy

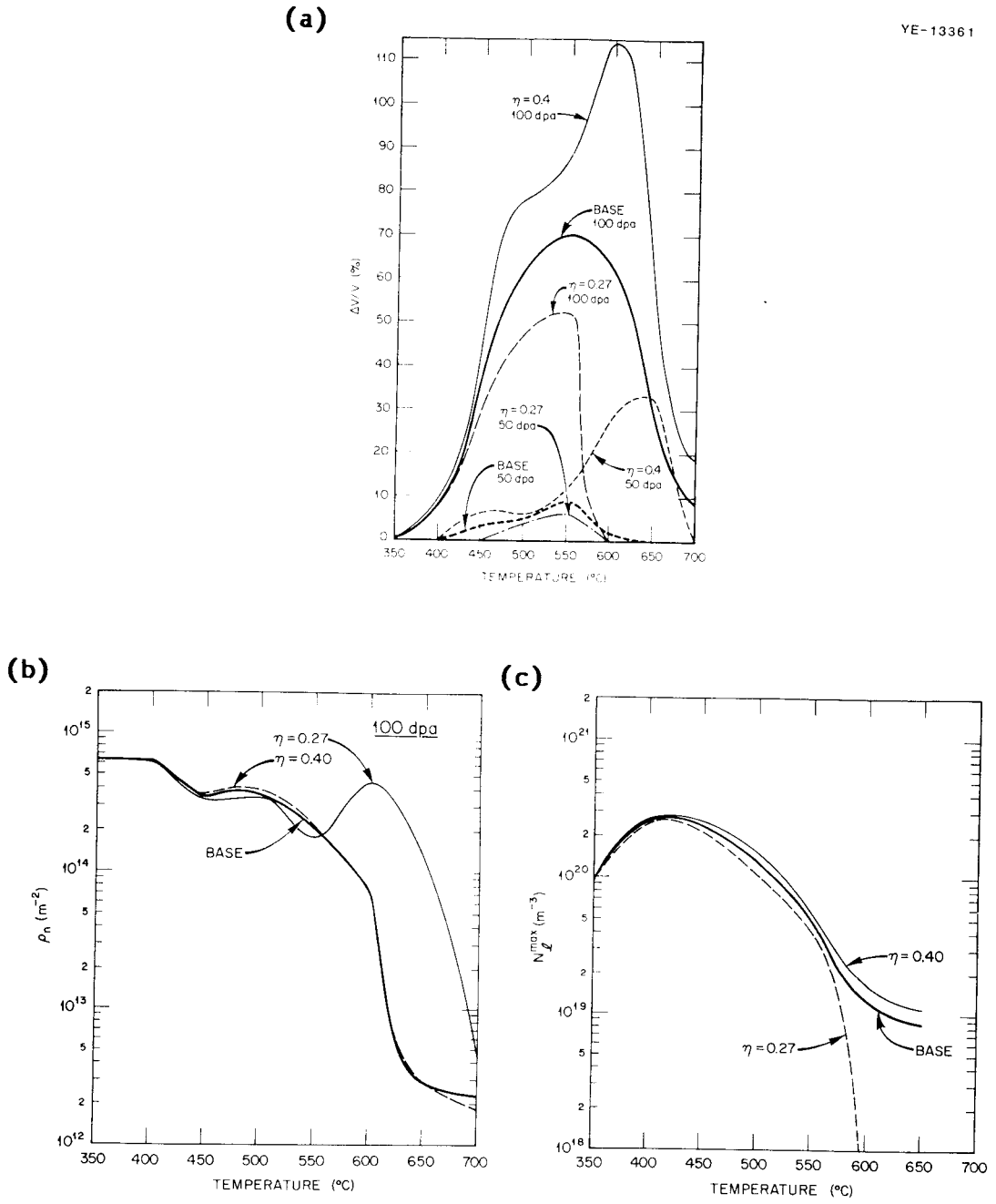

Figure 3.42. Influence of the cascade efficiency (η) on the predicted swelling (a), network dislocation density (b), and maximum faulted loop density (c).

supersaturation which in turn also alters the critical number of gas atoms needed for bubble-to-void conversion. In order to separate the direct surface energy effect on the critical size from the indirect effect of the vacancy clusters, the results shown in Figure 3.43 were obtained by varying the surface energy of the cavities while the surface energy of the vacancy clusters remained at the nominal value. Although this use of two different surface energies was for the sake of convenience, it may be physically realistic. If the surface free energy is reduced as a result of adsorbed gases or solute segregation, the appropriate value of the surface energy for the transient vacancy clusters is less likely to be affected. This same argument suggests that the actual surface energy could be time (dose)-dependent. Compared to Figure 3.43(a), the use of a single surface energy results in increased swelling below 500°C when $\gamma = 0.9\gamma(T)$ and reduced swelling below 500°C when $\gamma = 0.7\gamma(T)$. At low temperatures, the variations in vacancy supersaturation (due to altered vacancy emission from the vacancy clusters) have a greater effect on the critical size than do the direct variations in the surface energy. Because the surface energy affects primarily the incubation time in either case, the results shown in Figure 3.43(a) at 50 dpa are somewhat more sensitive to γ than the results at 100 dpa. Of course, the conversion of a higher density of bubbles to voids with the lower γ can lead to a reduced steady-state swelling rate. Although the surface free energy can have no direct effect on dislocations, the fact that the evolution

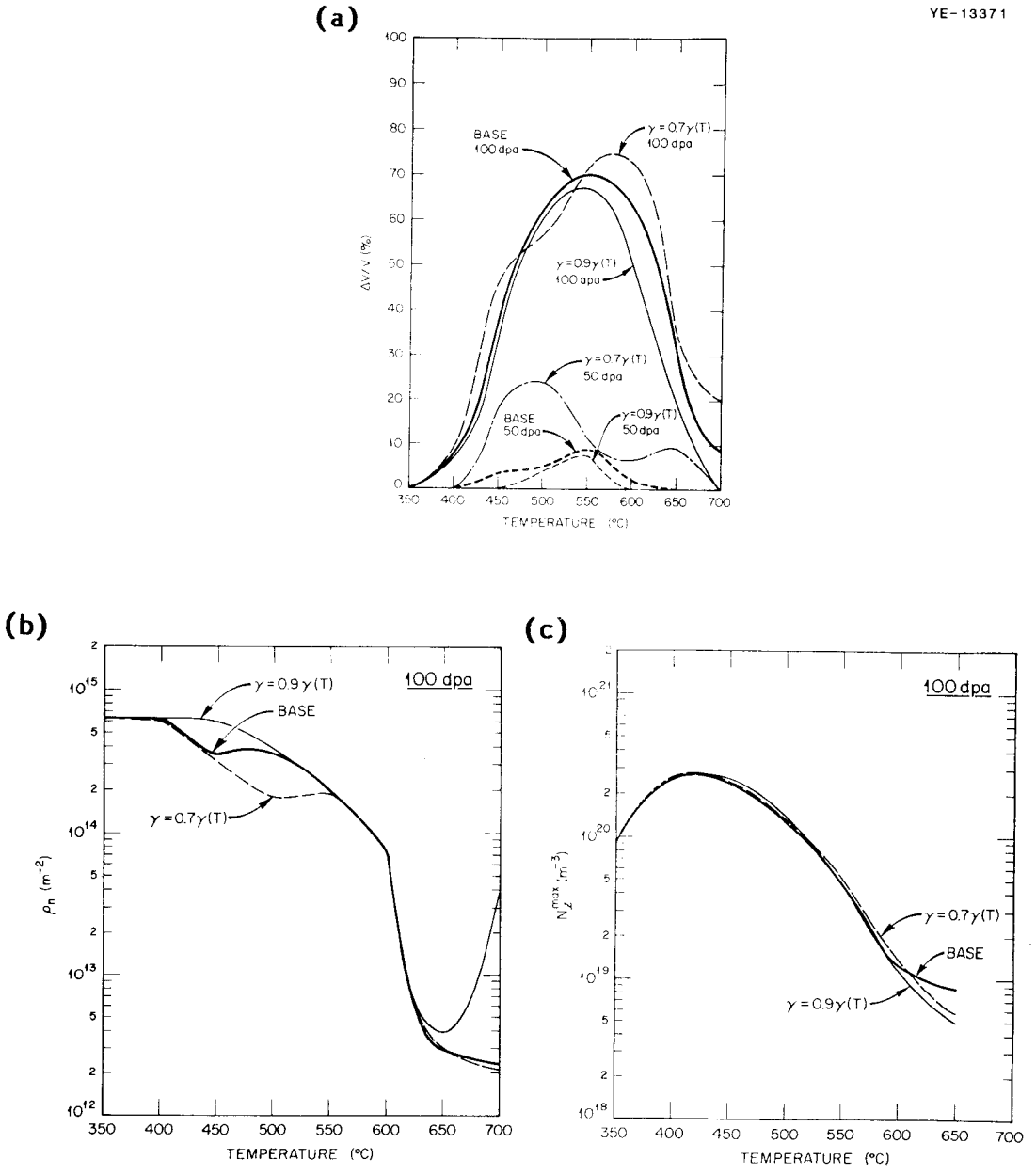

Figure 3.43. Influence of the surface free energy (γ) on the predicted swelling (a), network dislocation density (b), and maximum faulted loop density (c).

of the various sinks is coupled leads to an indirect effect. The changes in the cavity evolution are reflected in slightly altered values for the dislocation parameters as shown in Figure 3.43(b) and (c). The greatest effect is on the network dislocation density between 450 and 550°C.

The fact that bulk recombination is not important at low to intermediate temperatures has already been discussed. This is demonstrated in Figure 3.44. Here the recombination coefficient (α) has been varied by a factor of 4 from the nominal value. Below 550°C, no influence on the predicted swelling is observed in Figure 3.44(a). Above 550°C, the effect increases so that at 700°C the predicted swelling with the lowest value of α is more than double that of the

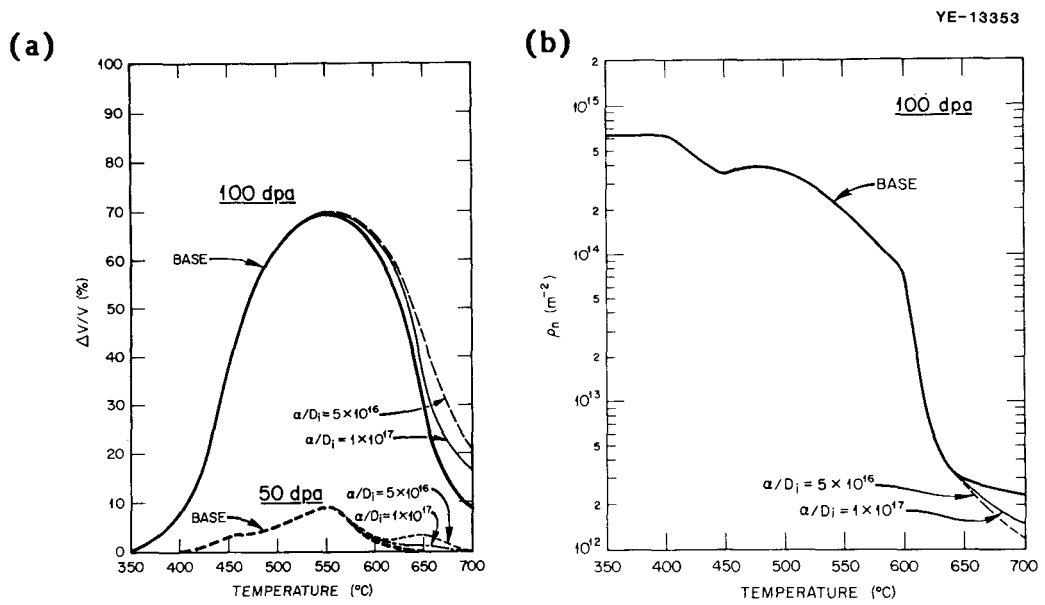

Figure 3.44. Influence of the recombination coefficient (α) on the predicted swelling (a) and network dislocation density (b).

base case. The network dislocation density shows even less influence of the recombination coefficient — less than a factor of 2 at 700°C and no effect below 650°C. The faulted loop density is not shown in Figure 3.44 because there was essentially no change in this parameter with α. These results indicate that previous modeling work which has frequently neglected bulk recombination did not incur any significant error as a result, at least for temperatures up to about 600°C.

The influence of the transient vacancy clusters (microvoids) at low temperatures is illustrated in Figure 3.45. These clusters reduce the effective vacancy supersaturation by acting as a neutral recombination site. The fraction of the cascade-produced vacancies which survive

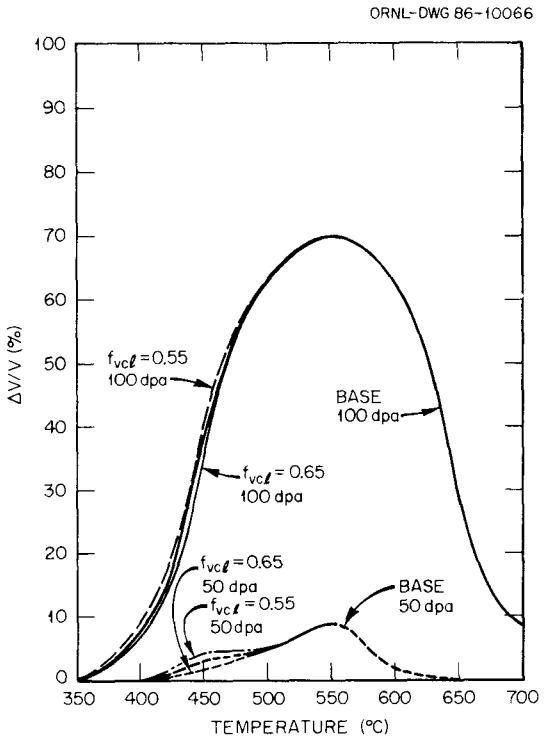

Figure 3.45. Influence of the fraction of surviving cascade-produced vacancies which collapse to form transient vacancy clusters (f_{vcl}) on the predicted swelling.

intracascade annealing and collapse to form microvoids (f_{vcl}) determines the degree to which the effective vacancy supersaturation is reduced. The effect is primarily on the incubation time for bubble-to-void conversion and is significant only at temperatures less than about 500°C. At higher temperatures, vacancy emission limits the microvoid lifetime. Because of the steepness of the swelling curve between 400 and 500°C in Figure 3.45, the apparent effect is somewhat minimized. At 450°C, the difference between the highest and lowest swelling at 100 dpa is about 7%, or 20% of the absolute swelling value which is predicted with the base case parameters.

The subgrain size has a significant influence on the predicted microstructural evolution, particularly at the higher temperatures. This effect is shown in Figure 3.46(a–c) for both 20% cold-worked and solution-annealed material. The subgrain diameter was increased from the nominal temperature-dependent value given in Table 3.5 to a constant, larger value of 10^{-4} m in order to obtain the comparison shown in Figure 3.46. For the nominal values of the subgrain diameter, and depending upon the temperature, only about 2 to 15% of the total number of point defects are absorbed in the subgrain structure. Although this is a small fraction, the amount is significant because the presence of this neutral sink permits the more efficient partitioning of vacancies and interstitials to different sinks at low doses when the cavity sink strength is low. Specifically, in the absence of this neutral sink, the network dislocation density remains fairly high out to >50 dpa since the absorption of nearly equal numbers of vacancies

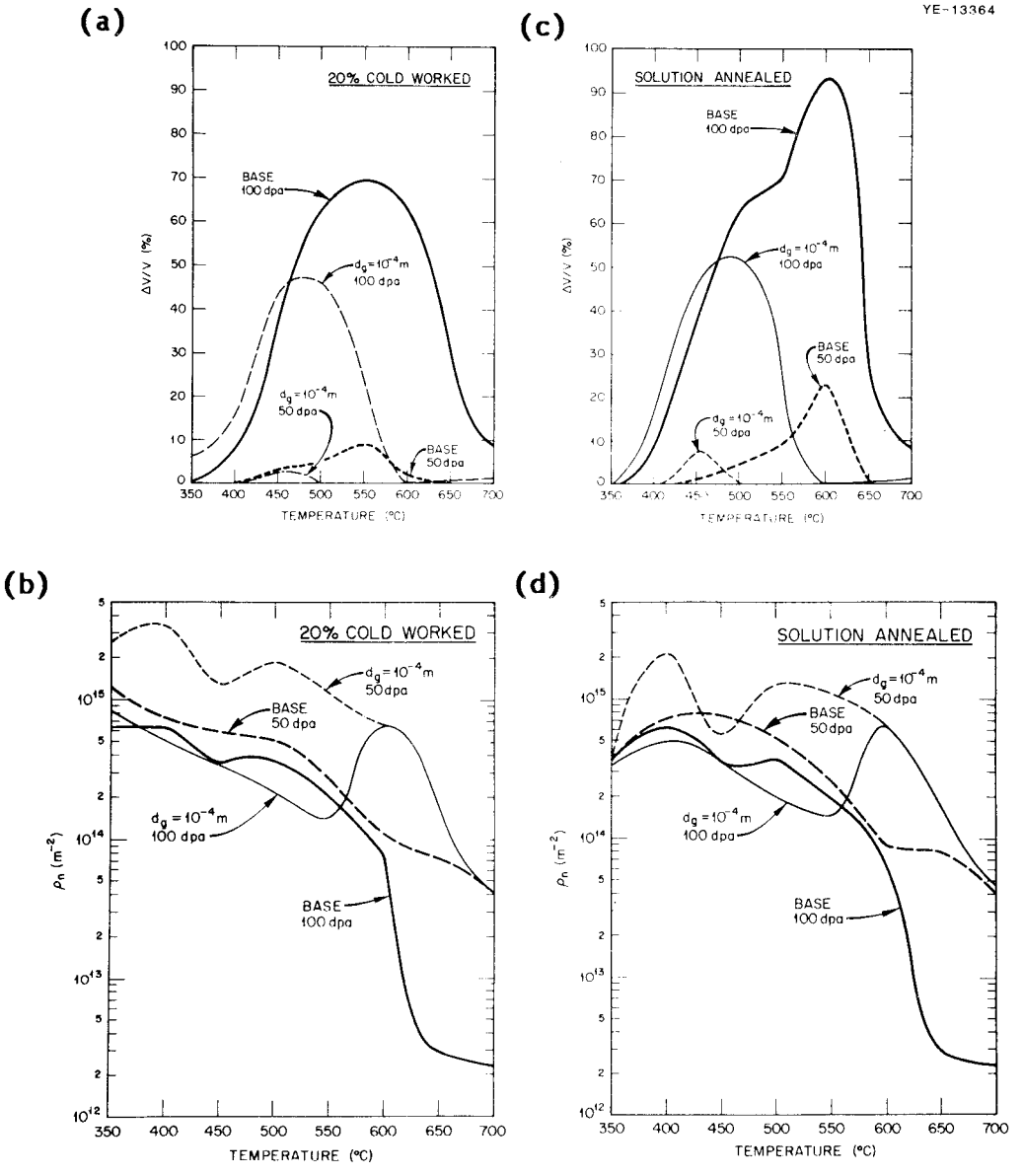

Figure 3.46. Influence of the subgrain diameter (d_g) on the predicted microstructure for 20% cold-worked (a,b) and solution-annealed (c,d) material.

and interstitials by network dislocations results in little net climb and therefore little dislocation annihilation in the present model. This suppresses the vacancy supersaturation and leads to extended incubation times above 450°C. Below 450°C, the behavior is more complex. As discussed above, the higher dislocation density can lead to higher effective vacancy supersaturations at low temperatures. This tends to reduce the swelling incubation time. In addition, at low temperatures the critical number of gas atoms for bubble-to-void conversion is small (see Table 3.4). This makes the swelling incubation time more sensitive to changes in the sink structure at these temperatures because of the partitioning of helium to the various sinks. This can change the bubble-to-void conversion dose for a given size class as well as the number of size classes that convert to voids. The swelling rate at high doses is also affected since both the dislocation density and the void density are altered. This influence of the subgrain structure is similar to that observed in fast-neutron-irradiated aluminum and reported recently by Horsewell and Singh[301] and van Witzenburg and Mastenbroek.[302] The influence of the subgrain structure on the peak faulted loop density is less severe. The higher network dislocation density slightly suppresses loop formation in the 20% cold-worked material and in the solution-annealed material at low and high temperatures. At intermediate temperatures in solution-annealed material, the peak loop density is somewhat higher. This is due to the fact that the loops grow more slowly (for the same reason that the network dislocations climb more slowly) and build in the

dislocation network at a slower rate. Solution-annealed material typically has a fairly large grain size; therefore, the smaller subgrain sizes given in Table 3.5 would be inappropriate for this material. The fact that the model may not adequately represent solution-annealed material has already been discussed and these results are shown here only for purposes of comparison.

The calculation of the multiple sink correction terms to the point defect sink strengths of the cavities and the subgrain structure was discussed in Section 3.3.1.3. The degree to which these correction factors influence the results is shown in the next four figures. None of the correction terms examined in these figures showed any significant influence on the peak faulted loop density, so only the swelling and network dislocation results are included. In order to show the sensitivity of the model to the alternate expressions for the cavity and subgrain sink strengths, no attempt was made to recalibrate the model when the various expressions were used. Because some recalibration could certainly permit the results to more closely track the base case predictions, these results should not be used in a simple way to judge how appropriate is any one formulation of the sink strengths.

In Figure 3.47, the effect of neglecting the multiple sink strength correction term to the cavity sink is shown [see Equation (3.46)]. This results in a reduced cavity sink strength at any given swelling and should yield a lower swelling rate. Little change is seen in the bubble-to-void conversion time because for small cavities the

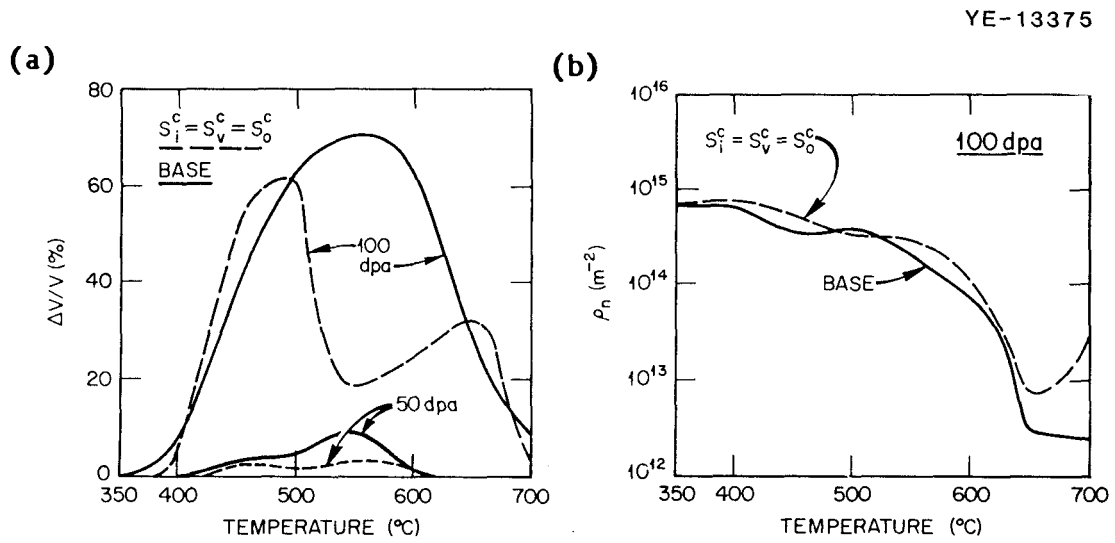

Figure 3.47. Effect of neglecting the multiple sink correction to the cavity sink strength on the predicted swelling (a) and network dislocation density (b).

correction term approaches 1.0. The large changes shown in the predicted swelling at 100 dpa are due to the same point defect partitioning effects which have been discussed previously. Although the neglect of the correction term would lead to a reduced swelling rate for a given microstructure, the dislocation density is altered by the reduction of the cavity sink strength. The swelling can then be either increased or decreased, depending on the temperature and the sign of the change in the dislocation density.

Including the effectively biased cavity sink strength correction terms yields the results shown in Figure 3.48. Here the correction terms reflect the fact that the total system sink strength for interstitials is greater than that for vacancies. Two analogous equations

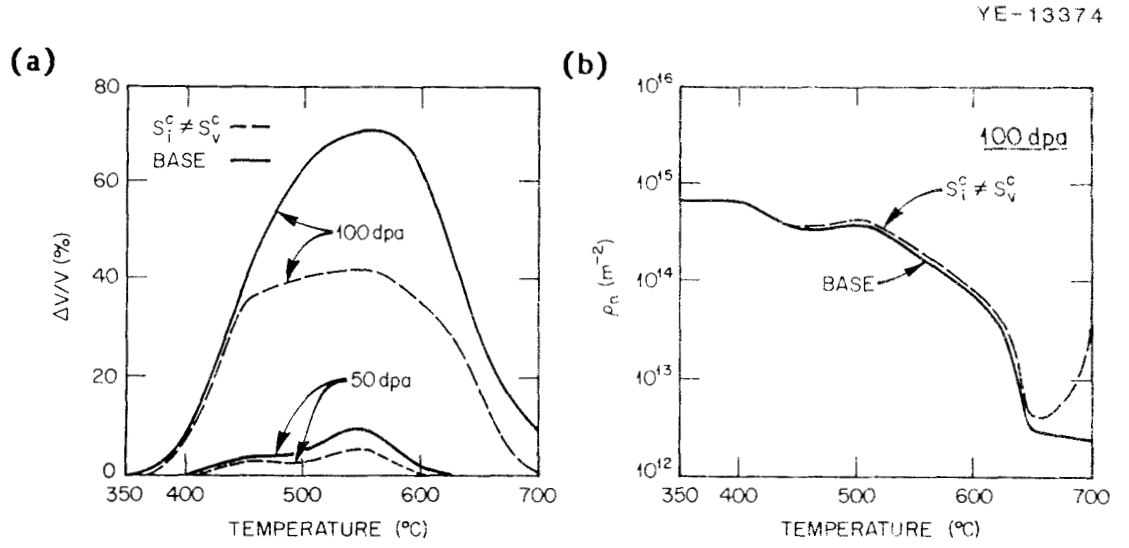

Figure 3.48. Effect of including the biased multiple sink corrections to the cavity sink strength on the predicted swelling (a) and the network dislocation density (b).

replace Equation (3.46) and $S_i^c > S_v^c$. Once again, the correction terms approach 1.0 for small cavities and little change in the incubation time is observed. The steady-state swelling rate is reduced as a result of the higher cavity sink strength for interstitials. The effect is smallest at low temperatures where the high void density yields smaller radii for a given level of swelling. This reduces the degree to which the predicted swelling is dependent on the irradiation temperature. The fact that cavity growth still occurs when $S_i^c > S_v^c$ is due to the higher bias of the network and faulted loop dislocations. The network dislocation density is once again altered by the modified cavity sink strength. Somewhat higher network dislocation densities are associated with the lower swelling levels.

The sink strength of the subgrain structure is inherently a function of the other sinks in the system [see Equation (3.48)]. When this sink strength is corrected to reflect the system bias, the results shown in Figure 3.49 are obtained. The importance of the subgrain structure at high temperatures was discussed above and was shown in Figure 3.46. A similar influence is seen here. When the subgrain structure is a neutral sink, it permits point defect partitioning to drive dislocation recovery. This increases the vacancy supersaturation, thereby decreasing the critical number of gas atoms sufficiently to permit bubble-to-void conversion. When the subgrain structure is no longer neutral, dislocation recovery and void swelling are delayed. The coupling of the cavity and dislocation evolution leads to a certain degree of synergism since the conditions that yield the lower

YE-13373

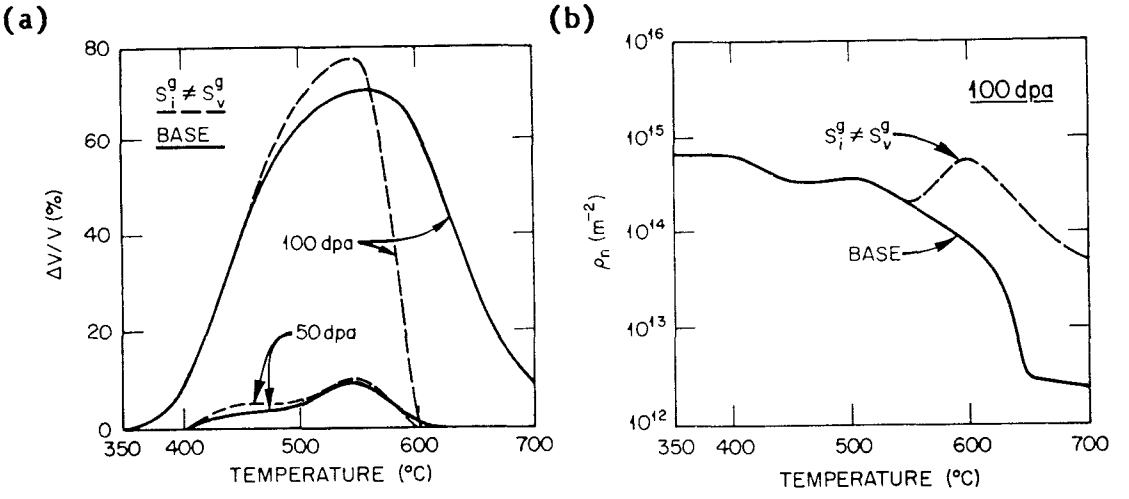

Figure 3.49. Effect of including the biased subgrain sink strengths on the predicted swelling (a) and the network dislocation density (b).

supersaturations also lead to slower bubble growth and therefore delay the time at which the bubbles would provide a significant neutral sink strength.

Finally, in Figure 3.50 the results are shown which were obtained with both the cavity and the subgrain sink strengths reflecting the system bias. The predicted swelling generally lies between the values shown in Figures 3.48 and 3.49. The strongest effect is once again observed at high temperatures where the lack of sufficient dislocation recovery has suppressed swelling out to 100 dpa. The fact that these results should not be used as a basis for determining the relative validity of the various expressions for the cavity or subgrain sink strengths has already been mentioned. The point which is significant

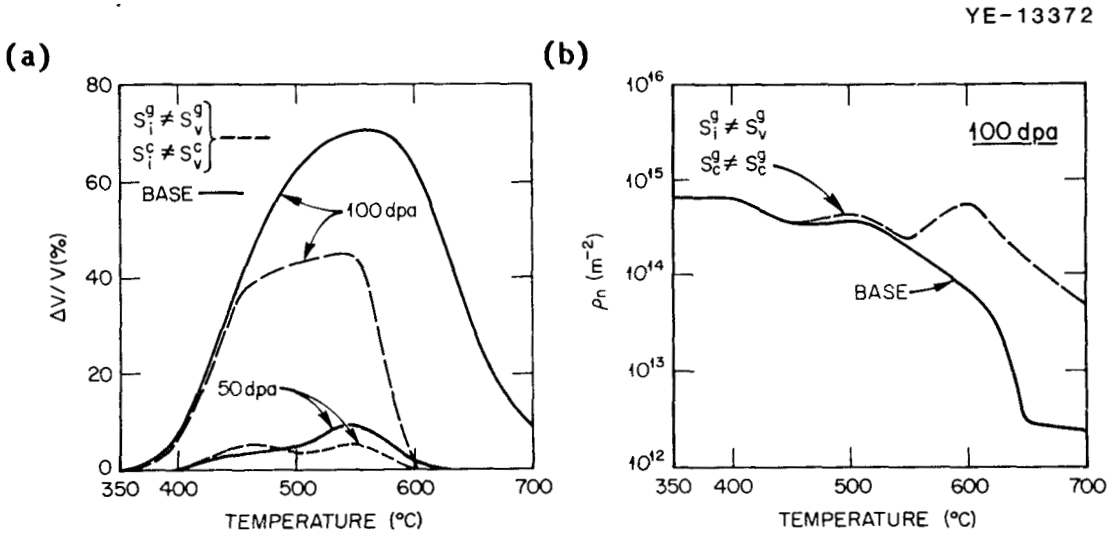

Figure 3.50. Effect of including both the biased subgrain sink strength and the biased multiple sink correction to the cavity sink strength on the predicted swelling (a) and network dislocation density (b).

is that which is independent of the details of the sink strengths - namely, that the tendency of a material to exhibit void swelling is largely determined by the balance of the microstructural sinks and point defect partitioning.

3.3.2.5 Extrapolation of Comprehensive Model to Fusion He/dpa Ratio

A simple extrapolation of the cavity evolution model discussed in Section 3.3.1.5 indicated a complex dependence of swelling on the He/dpa ratio and the cavity density. A similar extrapolation was carried out using the comprehensive model and the results are shown in Figures 3.51 and 3.52. Here the model has been used to predict swelling at conditions which would be characteristic of an austenitic stainless steel, DT fusion reactor first wall (i.e., 10^{-6} dpa/sec and 10 appm He/dpa). The influence of the cavity density was explored by again assuming the simple power law dependence of the cavity density on the He/dpa ratio [Equation (3.64)].

The predicted swelling, network dislocation density and maximum faulted loop density are shown in Figure 3.51 for a value of $p = 0.5$. The general trends include a reduced incubation time at all temperatures and enhanced swelling at high doses for both low and high temperatures. At intermediate temperatures, the predicted swelling for fusion is reduced at high doses. Related changes are observed in the predicted values of the dislocation parameters. The higher cavity density leads to a greater neutral sink strength. This enhances dislocation recovery so that the predicted dislocation density at 100 dpa is lower out

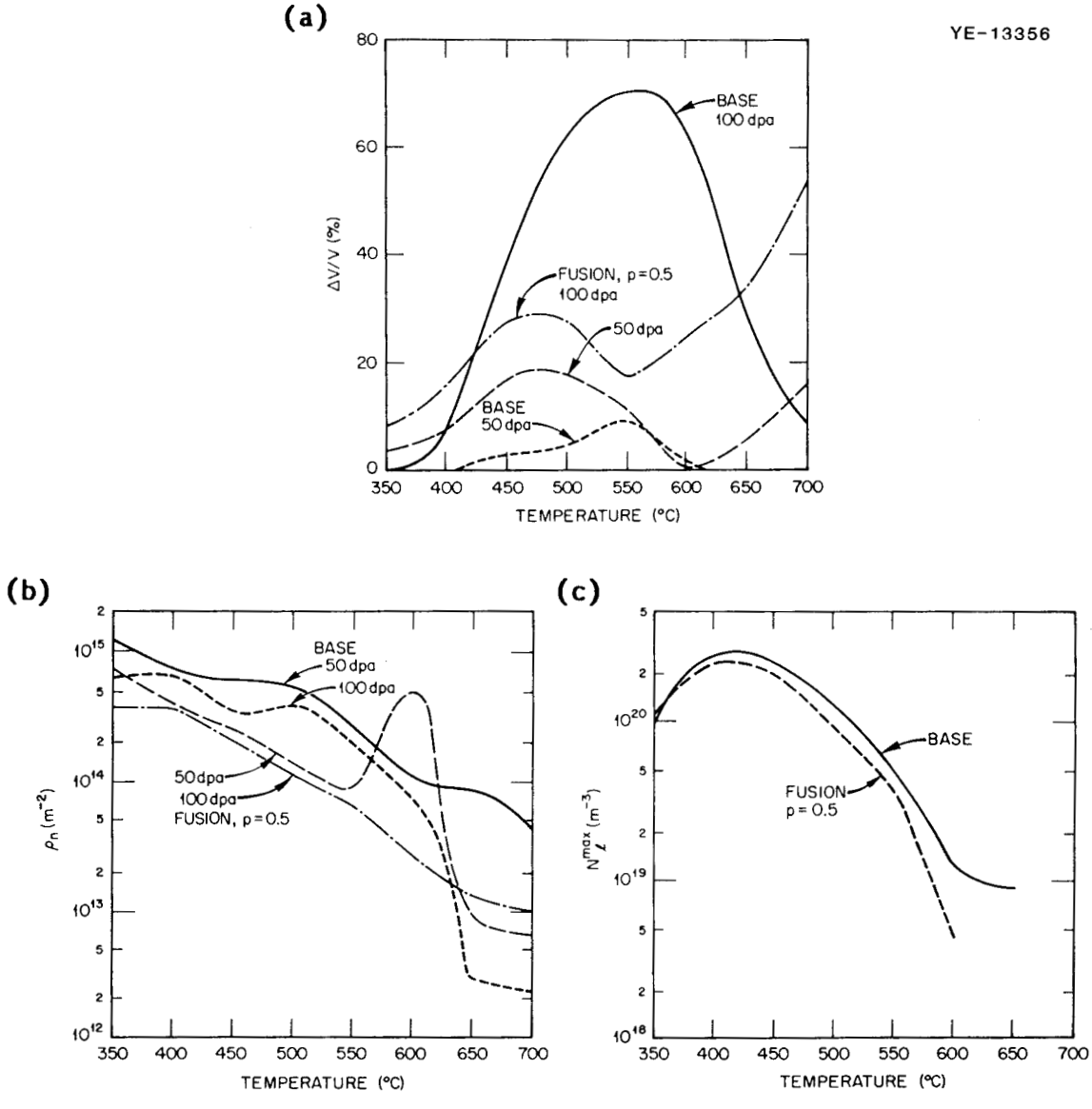

Figure 3.51. Model predictions of void swelling (a), network dislocation density (b) and peak faulted loop density (c) for fusion conditions with p = 0.5. Base case is from fast-reactor calibration.

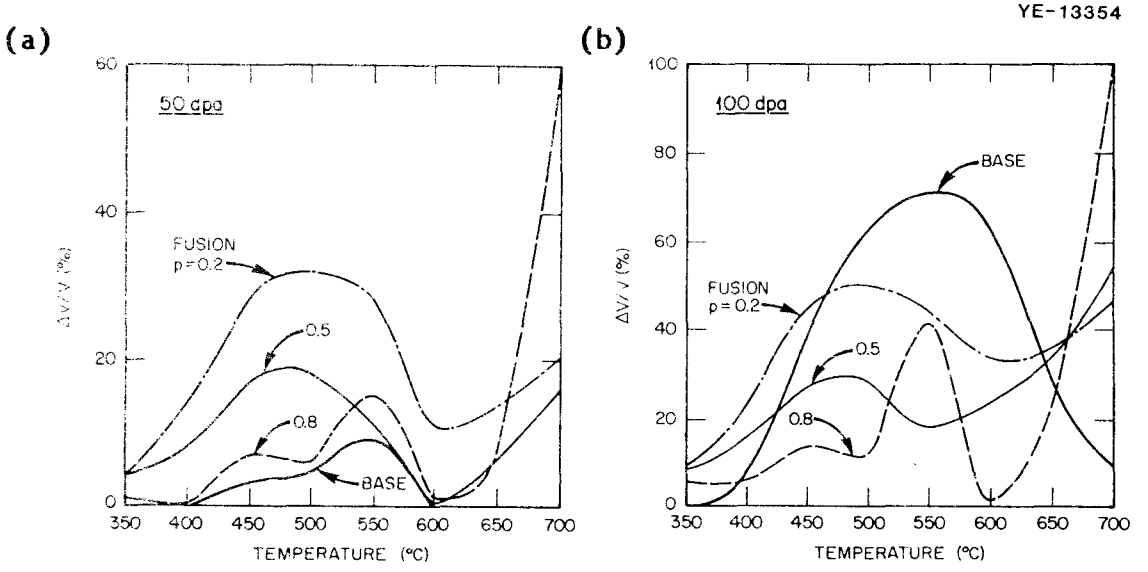

Figure 3.52. Effect of cavity density on predicted swelling for fusion conditions at 50 (a) and 100 dpa (b).

to about 650°C. There is some support for this prediction of a lower network dislocation density in the reported values for one heat of AISI type 316 stainless steel (DO heat) which has been irradiated in reactors which generate both low (EBR-II) and high (HFIR) levels of helium.[88] The explicit temperature dependence of the predicted swelling on the cavity density is shown in Figure 3.52. The details of the predicted swelling are complex and no doubt model dependent, but the major trends observed in Figure 3.51 are maintained.

Two prominent features of the predictions in Figures 3.51 and 3.52 are a reduced incubation at all temperatures and enhanced low temperature swelling. Similar predictions were made with the cavity

evolution model. The potential significance of these predictions lies in the fact that only a very limited amount of dimensional instability can be accommodated in typical fusion reactor designs;[8,238] therefore, the incubation time is a parameter of more engineering significance than the peak swelling rate. Further, recent conceptual reactor designs have tended to move toward lower operating temperatures where fast-reactor-irradiation data have indicated relatively little swelling.[8,182,238,303] These expectations of low swelling at the DT fusion He/dpa ratio may prove unwarranted.

3.4 Summary

The theoretical work presented in this chapter has emphasized the major role of microstructural sink balances and point defect partitioning in determining the path of microstructural evolution and void swelling. This indicates the need to use values for the microstructural parameters which reflect their temperature and dose dependence. The neglect of the temperature dependence has been shown to lead to particularly misleading results since different sinks are dominant in different temperature regimes. The influence of even a relatively minor, neutral sink such as the subgrain structure has been shown to be important under certain conditions. The fractions of the total number of vacancies that survive intracascade annealing ($\eta\ G_{dpa}$) at 100 dpa which have been absorbed at the various sinks are shown in Figure 3.53. The curve labeled "cavities" in Figure 3.53 includes both bubbles and voids. An analogous plot at the dose of the first

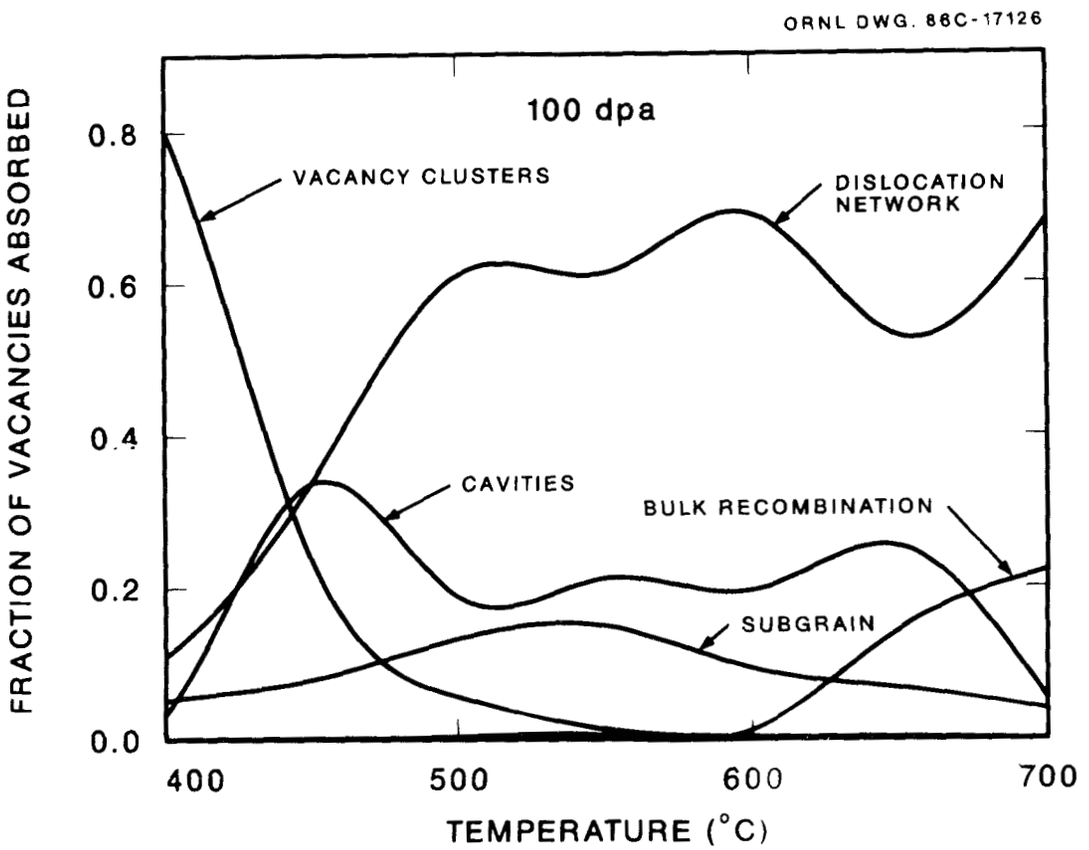

Figure 3.53. Fraction of total vacancies lost to various point defect sinks at 100 dpa, 20% cold-worked material.

bubble-to-void conversion would yield ≤1% vacancy absorption at the cavities with the network dislocation fraction proportionally higher. A plot of the fractional interstitial absorption would be similar to Figure 3.53. The relative fraction of net vacancy and interstitial absorption at 650°C and 100 dpa is detailed in Table 3.10. A comparison of the cumulative (to 100 dpa) and instantaneous (at ~100 dpa) fractions gives an indication of how the sinks have evolved in time. The effect of the dislocation/interstitial bias is seen in that the

Table 3.10. Net point defect absorption fractions at 650°C and 100 dpa

Point Defect Sink	Fractional Absorption, %			
	Vacancies		Interstitials	
	Cumulative	Instantaneous	Cumulative	Instantaneous
Bulk recombination	14.51	23.04	14.51	23.04
Vacancy clusters	0.42	0.64	0.42	0.64
Bubbles	3.96	6.05	3.96	6.05
Voids	21.52	57.35	20.71	56.19
Subgrains	6.77	6.90	5.98	6.71
Dislocation network	52.84	6.06	54.42	7.37

voids and subgrains absorb a net excess of vacancies while the dislocation network absorbs more interstitials. Table 3.10 reflects the fact that at any instant in time, stable bubbles absorb equal numbers of vacancies and interstitials. This verifies the need for a gas influx to drive bubble growth. The increase in bubble volume is so small that the cumulative net vacancy absorption is not seen in the first three significant figures in Table 3.10. Bulk recombination consumes equal numbers of both defect types, and the transient vacancy clusters are also shown to be a recombination site.

The importance of minor sinks and small changes in the point defect partitioning behavior can be pointed out by noting how small a fraction of the total defects produced finally survive and contribute to void swelling. The predicted swelling for the case summarized in Table 3.10 represents the net survival of only 0.29% of the initially produced vacancies (100 vacancies/atom). While 10.53 vacancies/atom

were initially absorbed at voids, 65.53% were lost to re-emission and 31.75% were recombined due to interstitial absorption. At lower temperatures the relative fractions of void-absorbed vacancies which are re-emitted and recombined are reversed, but only a similarly small fraction of the total survive. For example, at 450°C and 100 dpa, 98.23% of the 11.04 vacancies/atom that are absorbed at voids are then lost to recombination, while only 0.26% are lost to emission. The sensitivity of the predicted swelling to a number of irradiation, material and microstructural parameters has been shown to be due to the way these parameters alter the system sink balance. The sink balance in turn determines the net number of vacancies that survive and cause swelling. Because such a small fraction of the total generated survive, small changes in the absolute number of vacancies which survive can give rise to large changes in the predicted swelling.

The important role of transmutant helium in promoting void formation has been demonstrated by comparing the characteristic times for void formation from two alternate nucleation paths. The first path was classical nucleation due to stochastic fluctuations in the vacancy cluster population, and the second was bubble growth driven by helium accumulation. Part of this work included the development of a simplified procedure and the necessary analytical solutions to permit the calculation of the bubble parameters while using a hard-sphere equation of state for the helium. With material parameters typical of austenitic stainless steels, the role of fluctuations was shown to be significant

only when the bubbles were near the critical size for bubble-to-void conversion. The model of cavity evolution developed and used here has therefore included only the helium accumulation path.

The development and use of two models of microstructural evolution under fast-neutron irradiation have been described. A computer code that incorporates these two models is listed in Appendix A. The models share a common foundation in the chemical rate-theory description of the relevant physical processes. Similar treatments of helium partitioning and the effects of cavity-precipitate association are included in both models. The initial model developed focused on cavity evolution. Other components of the microstructure were treated in a parametric and time-independent fashion. In spite of this simplification, the model was able to predict the observed swelling behavior of fast-reactor-irradiated 20% cold-worked type 316 stainless steel. This matching of data and theory was obtained while using reasonable model parameters. The calibrated model was then used to explore the influence of the He/dpa ratio on void swelling and a surprising result was obtained. The model predicted a peak in the swelling versus He/dpa ratio curve near the DT fusion relevant value of 10 appm He/dpa. Recent results from an experiment in which the neutron spectrum was modified to yield this He/dpa ratio in a fission reactor appear to confirm this prediction.[288] Slightly over 1% swelling was measured in a 25% cold-worked, titanium-modified type 316 stainless steel at 500°C and only 12 dpa. Such a level of swelling in this material would not

be observed in a fast fission reactor (~0.3 to 1.0 appm He/dpa) until greater than 75 dpa (ref. 153).

This cavity evolution model was then incorporated into a more complex microstructural model. The comprehensive model included the explicit dose-dependence of the dislocation network and of Frank faulted dislocation loops. A model which described the evolution of the dislocation network under thermal annealing was also developed and included. Data from fast-reactor irradiation experiments were once again used to calibrate and determine the validity of the microstructural models. The comprehensive model was able to simultaneously predict values for swelling, network dislocation density and faulted loop density which were in substantial agreement with the data. The required model parameters were shown to be in agreement with measured values where such measurements are available or to be consistent with the expected range of values for those parameters which have not been directly measured. The comprehensive model has exhibited new or altered sensitivity to certain model parameters when compared with the cavity evolution model. This led to some parameter changes (e.g., E_1^m) in order for the two models to predict similar swelling while permitting the comprehensive model to match the observed dislocation densities. This modified parametric sensitivity is believed to be physically meaningful because the model demonstrates the complex way in which the evolution of the various sinks is coupled. The predictions of the more simple theory neglect this interaction and this has

been shown to lead to erroneous conclusions in certain cases. After investigating the parametric dependencies of the comprehensive model, it was also used to predict the swelling behavior of a 20% cold-worked, DT fusion reactor first wall. The key results here were a much reduced incubation time for void swelling at the fusion He/dpa ratio and enhanced swelling at the lower temperatures. Taken together with the predictions of the cavity evolution model when it was used to explore the He/dpa ratio dependence of swelling, these results indicate that the consideration of swelling in fast reactors can lead to nonconservative estimates of swelling in DT fusion reactor components.

CHAPTER 4

EXPERIMENTAL

The experimental work that was undertaken to complement the theoretical modeling discussed previously is described here. This component of the work involved the examination of irradiated specimens of a model austenitic alloy by transmission electron microscopy (TEM), immersion density and microhardness. The austenitic alloy was originally prepared at the Oak Ridge National Laboratory and was designated P7.[304] The major constituents of the P7 alloy (in weight fractions) are: 0.17Cr-0.167Ni-0.025Mo, with less than 0.001 of any minor element and the balance iron.[304] These weight fractions are similar to that of an AISI type-316 stainless steel with the exception of the nickel, which would have a nominal concentration of 12% (ref. 160, Vol. 1). In order to study the behavior of austenitic steel without the complicating effects of carbide precipitation, the weight fraction of carbon in P7 was reduced to ~10^{-5} (ref. 304). This preparation resulted in a high level of residual oxygen in the alloy, ~1000 appm (ref. 188). The high swelling of P7 observed in a variety of charged-particle and neutron irradiation experiments[61,188,193,246,304-308] appears to be partly a result of this high oxygen content.[47]

4.1 Irradiation Conditions

The material examined here was irradiated in two reactor experiments. The first experiment was the MFE-II experiment in the ORR.[309]

The P7 was irradiated in the form of TEM disks, 3 mm in diameter and 0.254 mm thick, in both the solution annealed (SA) and 20% cold-worked (CW) conditions. Some specimens were uniformly implanted with helium at room temperature and subsequently annealed for one hour at various temperatures prior to irradiation. These preirradiation treatments were designed to permit the observation of the influence of various initial microstructures on the subsequent response of the material to neutron irradiation. Early work had shown that helium preinjection suppressed void formation in the EBR-II and that postinjection annealing at 750°C had enhanced void swelling relative to uninjected controls.[310] The experimental matrix planned for alloy P7 in the MFE-II experiment is shown in Table 4.1. None of the 20% cold-worked specimens were annealed following their helium implantation in order

Table 4.1 Planned Experimental Matrix for Alloy P7 in the MFE-II experiment[a,b]

	Helium (appm)	Irradiation Temperature (°C) 450	550	650
SA	0	n.a.	n.a.	n.a.
	10	n.a.,600, 700,800	n.a.,700, 750,800	n.a.,700, 800,900
	30	n.a.,600, 700,800	n.a.,700, 750,800	n.a.,700, 800,900
20% CW	0	n.a.	n.a.	n.a.
	10	n.a.	n.a.	n.a.
	30	n.a.	n.a.	n.a.

[a]Temperatures are one hour, post-helium-implantation annealing temperatures.
[b]n.a. denotes not annealed.

to prevent recovering the as-cold-worked dislocation structure. The MFE-II experiment was planned to reach a total exposure of 10 dpa. This would have resulted in the generation of about 138 appm He in alloy P7 by neutron-induced transmutation reactions.

The helium implantations and postinjection heat treatments for the MFE-II irradiated specimens were carried out at the Argonne National Laboratory,[309] but no unirradiated controls were maintained. Therefore, as part of this work, helium implanted and aged control specimens were prepared. Strips of 20 and 24% cold-worked P7, 0.254 mm thick, were obtained from archival material. TEM disks (3 mm diameter) were mechanically punched from the 0.254-mm-thick sheet and subsequently laser engraved for identification purposes. The 24% cold-worked disks were solution-annealed at 1050°C for one hour. Helium implantations were carried out at the Crocker Nuclear Laboratory on the campus of the University of California at Davis, using their 1.93 m isochronous cyclotron. Approximately uniform through-thickness helium levels were obtained by passing a 57 MeV alpha-particle beam through a rotating graphite wheel.[311] The thickness of the graphite degrader varied linearly from 0.508 to 1.27 mm to yield alpha particles with energies uniformly distributed between 0 and 38 MeV on the target material. Calculations with the EDEP code[312] indicate that the range of a 38 MeV alpha particle in P7 should be ~0.22 mm so that all of the particles should be stopped in the target. EDEP calculations also indicate that helium implantation to a level of 30 appm would result in about 10^{-2} dpa.

The helium implantations were carried out at near room temperature in order to prevent helium diffusion. Temperature control was achieved by mounting the disks in a water-cooled fixture that consisted of two blocks of aluminum. To accommodate the TEM disks, the base block had recesses 0.25 mm deep milled in a close packed array on 3.36 mm centers. The recesses were 3.05 mm in diameter. The cover block had 2.54 mm holes drilled in corresponding positions to expose one face of the specimens to the beam. Good thermal contact with the base block was provided by the use of a thin (0.1 mm) layer of pure indium between the block and the samples. The indium foil was very malleable and deformed to fill the recess below the sample when the cover block was bolted to the base block. Figure 4.1 is a schematic

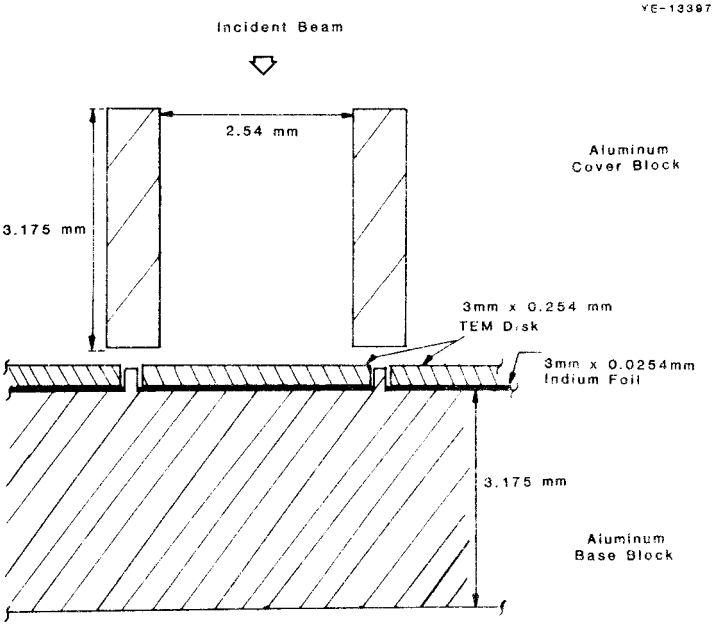

Figure 4.1. Cross-section view of a single segment of the fixture used to clamp TEM disks during helium implantation.

drawing of one segment of the mounting fixture. The indium foil also provided a crude temperature monitor since it melts at a low temperature, ~156°C. A limited amount of indium melting was observed behind some of the samples when they were removed from the fixture. Typically a small circular area less than 1 mm in diameter at the center of these disks had been wetted by melting indium. This indicates that the maximum specimen temperature during the helium implantation was ≤200°C. TEM observation of the as-implanted specimens confirmed this low temperature.

Following the implantation, the relative helium level of each disk was determined by autoradiography and densitometry. The absolute helium level was determined from the total cyclotron beam current. Due to the nonuniform cross section of the cyclotron beam, the actual helium levels in the 10 appm set of specimens varied from 5.3 to 15.8 appm He and the 30 appm set varied from 16.5 to 39.1 appm He. The helium levels of the MFE-II irradiated specimens exhibited a similar range of values. Prior to the postimplantation anneals, the specimens were individually wrapped in 25-μm-thick tantalum foil to prevent oxidation. The wrapped specimens were encapsulated in quartz tubes. The tubes were vacuum evacuated to a pressure of ~1.3×10^{-3} Pa and back filled with helium to a pressure of ~5.3×10^{4} Pa.

The second set of neutron irradiated specimens examined here were obtained from an in-reactor fracture experiment by Bloom and Wolfer.[305] This novel experiment involved the use of a "driver" tube made from the high swelling alloy P7 to strain tensile specimens made from lower

swelling engineering alloys. The tube used in this work (designated X3) was irradiated at 650°C to a total dose of 12.5 dpa in the EBR-II.[305] Only about 4 appm He would have been generated during this irradiation. The measured density decrease in this specimen was 4.7% (ref. 305), and Farrell and Packan later measured about 6% void volume by TEM.[306] The potential influence of the high oxygen content of alloy P7 is evident in the results of Bloom and Wolfer[305] where they show greater swelling in P7 than in a similar "pure 316 stainless steel" (the MS heat). The MS heat was also fabricated with a low level of carbon, but the weight fraction was only reduced to 5×10^{-5} (ref. 313). Although no oxygen analysis has been reported for the MS-heat, it is reasonable to assume that this heat would have had a lower level of oxygen than the P7 heat because the high oxygen level in P7 was a result of the treatment used to eliminate carbon. Material from the X3 driver tube was used in a postirradiation annealing experiment to study the kinetics of void and dislocation recovery.

4.2 Specimen Preparation and Examination Procedures

Specimens were prepared for TEM examination in a Tenupol twin-jet electropolishing unit. A solution of seven parts methanol to one part sulfuric acid (by volume) was used as the electrolyte. The polishing conditions were an electrolyte temperature of -20°C and an applied voltage of 17 V dc leading to a polishing current of ~120 mA. A typical P7 specimen with an initial thickness of 0.254 mm required 7 to

8 minutes to polish. Because of the residual radioactivity in the neutron irradiated specimens, all sample preparation was done in a specially designated laboratory at the Oak Ridge National Laboratory (ORNL).

Several transmission electron microscopes were used to examine specimens in this work. The JEOL 200 CX at the University of California, Santa Barbara (UCSB) and the Philips EM430 at ORNL were used most extensively. These microscopes were operated at accelerating voltages of 200 and 300 keV, respectively. To a lesser degree, the JEOL 100CX (at 120 keV) and the Hitachi HV-1000 (at 1000 keV) at ORNL were also used. Standard TEM techniques[173,316] were used to characterize the observed microstructures. Typical investigations involved tilting the specimens to obtain appropriate, low-order g vectors [e.g., (111), (200) or (220)] to photograph the various defects. Fairly strong diffraction conditions were employed to image the dislocation structure ($s \sim 0$). Cavities were normally imaged in absorption contrast with $s \gg 0$. A through-focus series of images were used to verify that the spherical defects were cavities.[173,316] In some of the micrographs shown below, cavities are shown underfocus (dark Fresnel fringe outside, bright inside) while in others they are shown overfocus (light Fresnel fringe outside, dark inside).

Foil thicknesses were obtained by either stereomicroscopy, thickness fringes with $s = 0$, or the use of a new x-ray technique.[315] This latter technique was developed by Kesternich[315] and requires the use of a standard specimen of known thickness to obtain a calibration

curve of specimen thickness versus emitted x-ray intensity. For thicknesses up to several hundred nanometers, Kesternich has shown that the x-ray intensity is linear in specimen thickness.[316] The calibration specimen for this work was an austenitic stainless steel disk supplied by Kesternich. All x-ray measurements were made with the specimen tilted (drum tilt) toward the x-ray detector by 20°. A standard beam current was obtained by adjusting the first condenser lens and the gun tilts until the camera exposure meter indicated a 20-sec exposure time with the beam at crossover and passing through the hole in the TEM specimen. The average x-ray count rate (less background) was determined by integrating the total number of counts between 4.2 and 20 keV for 10 sec (detector live time) using the EDAX energy dispersive x-ray detector on the EM430. The error in thickness measurements obtained in this way should be less than 5% (ref. 315). Magnification calibrations for the various microscopes were obtained by photographing a calibration grating with a known spacing of 2160 lines per mm.

Defect densities and sizes were measured on positive prints with a total magnification of 1 to 5 x 10^5. Normally 50 to 100 defects of the type in question were measured on any one print to obtain the size distributions discussed below. An electromagnetic digitizing pad was coupled to a microcomputer and used to measure the defects. Areal densities were converted to volumetric densities using the measured foil thicknesses.

Specimens for the postirradiation annealing experiment were cut from the X3 driver tube in the form of 0.51-mm-thick slices. Disks 3 mm in diameter were then punched from these slices. The disks were individually wrapped in tantalum foil and encapsulated in quartz tubes as discussed above. A series of isothermal anneals at 750 and 900°C were performed for times up to 210 hours. An isochronal annealing curve for 1 hour anneals between 600 and 1042°C was also obtained. After annealing, the specimens were mounted in Araldite GY502 epoxy resin for microhardness measurements. The mounted specimens were mechanically polished to a high gloss using successively finer abrasives; the final polishing step was with 0.5 μm alumina powder. Standard diamond pyramid microhardness (dph) measurements were made using a Kentron microhardness tester at loads of 500 and 1000 g. Each indent was measured 8 to 10 times using a 16× filar eyepiece and a 20× objective lens. The operation of the Kentron unit was checked before each use by measuring the microhardness of a Tukon reference block which had a hardness similar to the irradiated P7; the dph of the reference block was 169 to 172.

Following the microhardness measurements, the mounted specimens were repolished to remove the indents. The specimens were then removed from the epoxy mount using successive soakings in methyl chloride and 90°C N-N dimethyl formamide. For some specimens, additional mechanical abrasion was used to remove the last of the epoxy. The density of the specimens was measured by immersion density. The net weights of the specimens were obtained in a bath of a commercial

fluorocarbon (3M Company, Fluorinert FC-43). Experience with this microdensitometer at ORNL indicates that the absolute error in the density of a TEM-disk-size specimen is less than 10^{-3}. The density of selected specimens from the MFE-II experiment was also measured in the microdensitometer.

4.3 Experimental Results

4.3.1 Helium-Implanted and Aged MFE-II Controls

The unirradiated control specimens were examined by transmission electron microscopy to determine the preirradiation microstructure of the specimens that had been irradiated in the MFE-II experiment. Verification of the level of helium implanted was obtained for two specimens that had calculated helium concentrations of 5.3 and 39.0 appm He. The helium content of these specimens was determined by vaporization and mass spectrometry to be 7.12 ± 0.13 and 51.6 ± 1.2 appm He, respectively. Two ~1 mm disks were punched from both specimens to permit redundant analyses to be performed. These two measurements agreed within <4%. The mass spectrometry was performed by the Energy Systems Group of Rockwell International.[316] The 30% difference between the calculated and measured helium levels has not been resolved. This discrepancy is of no consequence to the present work since the influence of variations in helium content at these levels was not under examination. Values for helium concentrations quoted below have been increased by 30% from the nominal calculated values.

The as-implanted microstructure of both the solution annealed and 20% cold-worked specimens consisted of a high density of small "black-dot" clusters. In the case of the cold-worked specimen, the as-cold-worked microstructure also remained. These observations confirm the fact that the specimen temperatures remained fairly low during the helium implantation. A representative micrograph of the black-dot damage is shown in Figure 4.2. This is typical of helium implanted materials as discussed in Chapter 2.[48,145,157,158] The work of Maziasz indicates that most of the black-dot clusters are small interstitial loops.[48]

During thermal annealing, the as-implanted microstructure of the solution annealed material evolved to yield larger Frank faulted

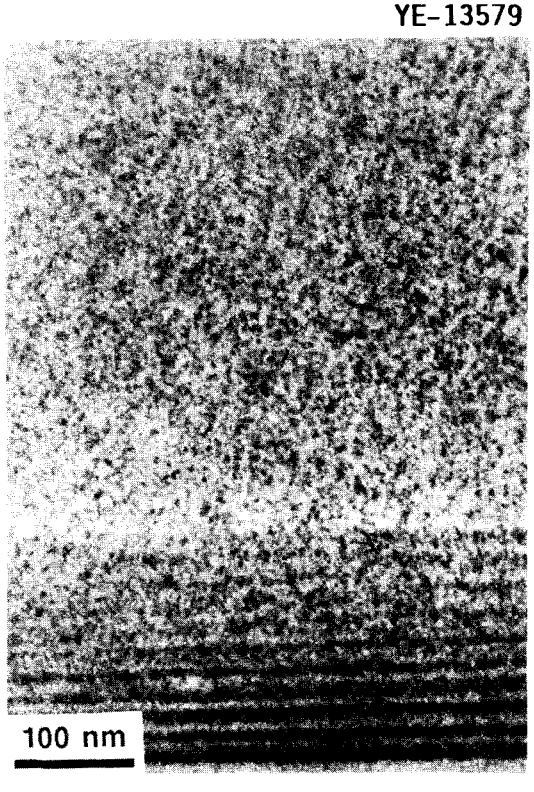

Figure 4.2. Black-spot damage observed in solution-annealed P7 after room temperature helium implantation to ~40 appm He.

interstitial loops and small helium bubbles. The temperature dependence of these two defect types is shown in Figure 4.3. These data are summarized in Table 4.2. When multiple measurements were made on the same sample, the data plotted in Figure 4.3 are a volume average of the individual measurements. The helium levels in the specimens annealed for one hour at 600, 700, 750, 800 and 900°C were 32, 44, 37, 47 and 41 appm, respectively. The observed bubble and faulted loop densities are generally consistent with the earlier work discussed in Chapter 2.[48,145,157-158]

Table 4.2. Summary of bubble and faulted loop microstructures observed in solution-annealed P7 after helium implantation and annealing

Helium Implanted (appm)	One-Hour Annealing Temperature (°C)	Defect Density, m^{-3}		Average Radius, nm	
		Bubble	Loop	Bubble	Loop
32	600	n.o.[a]	2.59×10^{21}	n.o.	3.46
44	700	8.25×10^{21}	2.32×10^{20}	0.82	24.7
37	750	6.33×10^{21}	1.49×10^{20}	1.09	25.4
47	800	6.66×10^{21}	n.o.	1.57	n.o.
41	900	2.15×10^{21}	n.o.	1.99	n.o.

[a]n.o. denotes not observed.

Representative micrographs of the annealed specimens are shown in Figures 4.4 and 4.5. The faulted loops coarsen and grow for temperatures up to 750°C. The fact that the loops are faulted is confirmed by imaging the loops in bright field with the stacking faults visible (g_{200} or g_{111}) and by dark field images using the <111> satellite streaks near the g_{200} reflections.[173,314] The number of interstitials

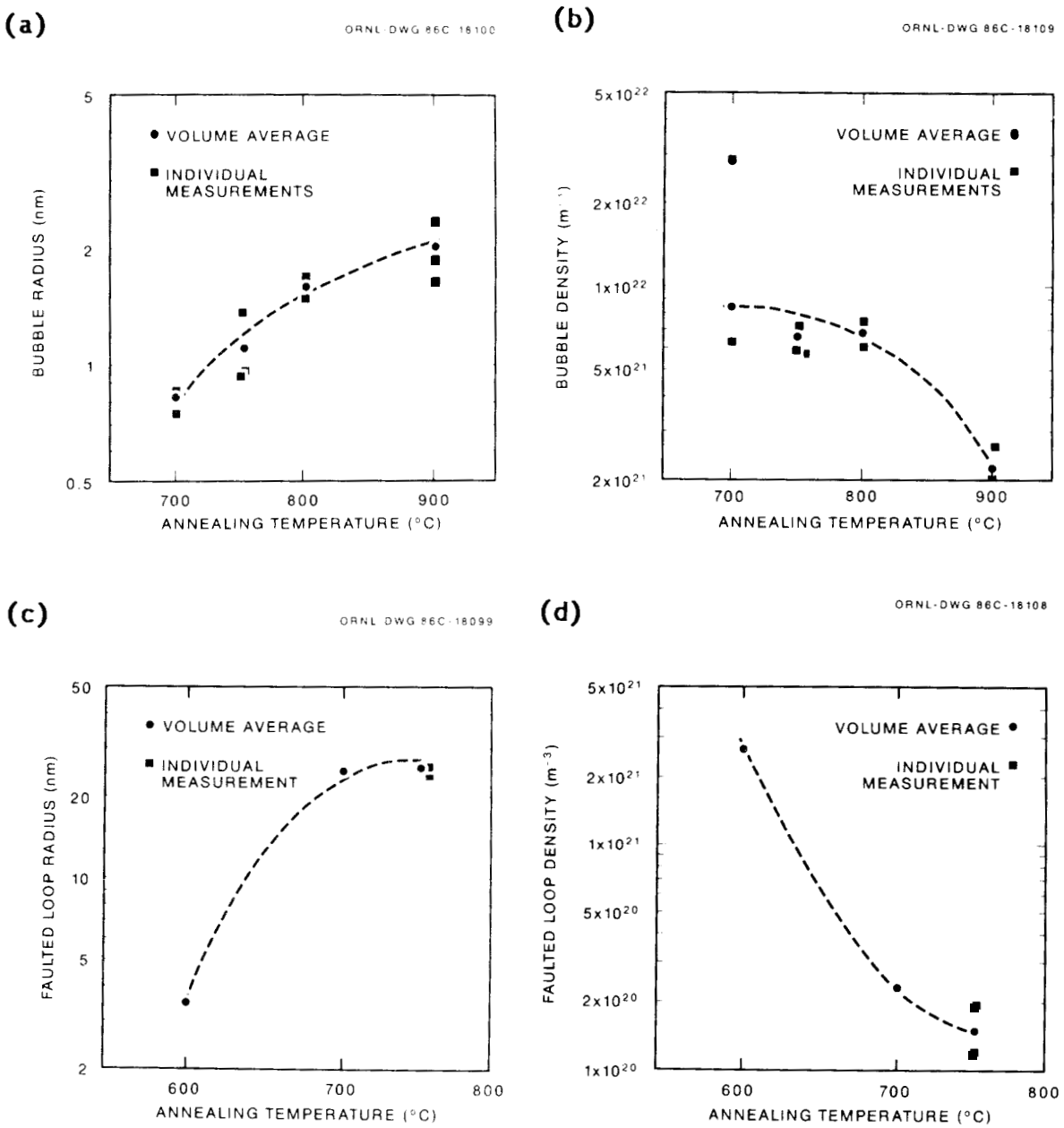

Figure 4.3. Observed average bubble radius (a), bubble density (b), faulted loop radius (c), and faulted loop density (d) after ~40 appm He implantation and subsequent annealing for one hour at the indicated temperature.

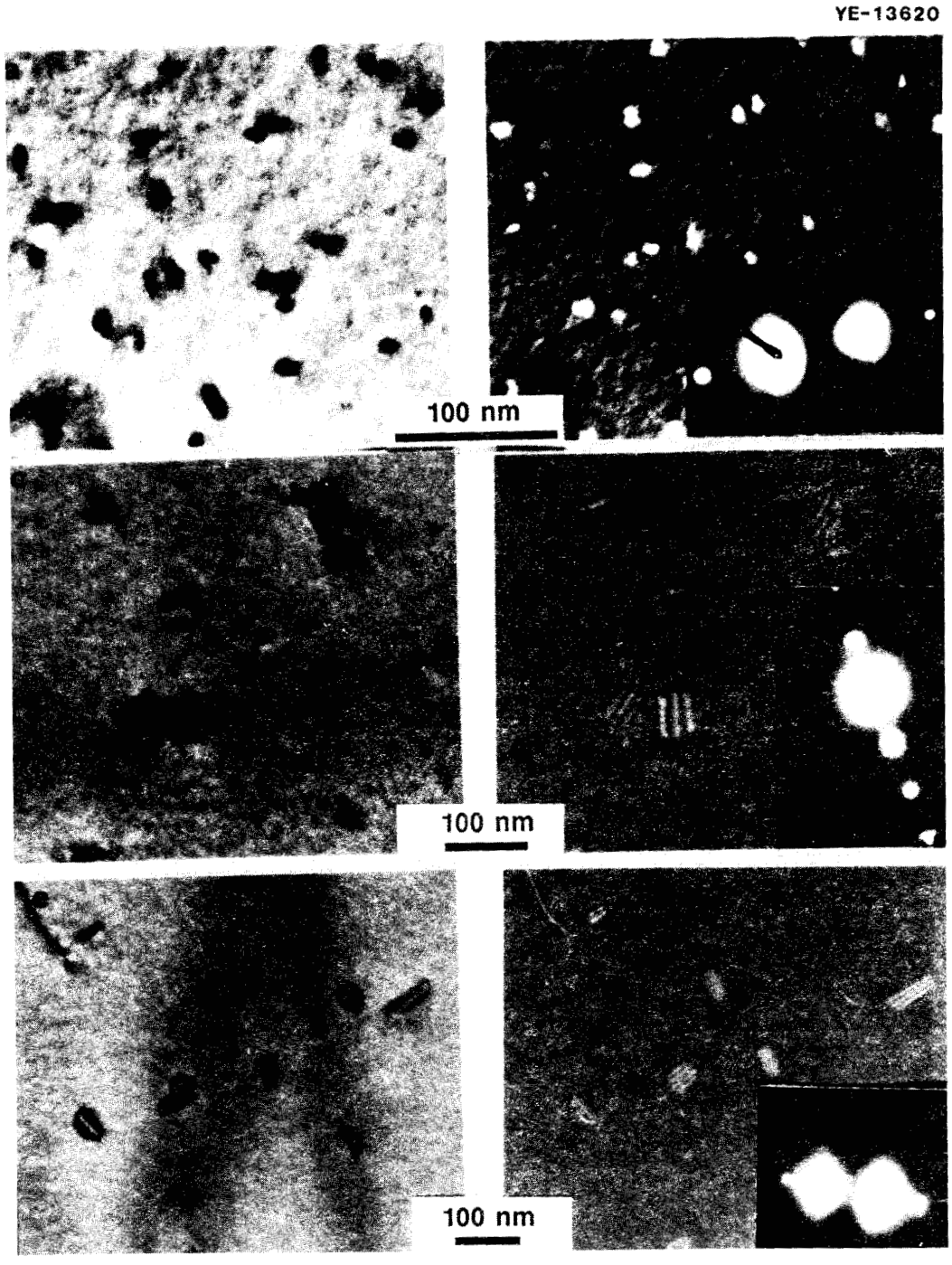

Figure 4.4. Faulted loop microstructure observed in solution-annealed P7 after annealing for one hour at 600 (a,b), 700 (c,d), and 750°C (e,f). A bright field and dark field pair is shown for each temperature. Level of helium implantation is ~40 appm.

YE-13587

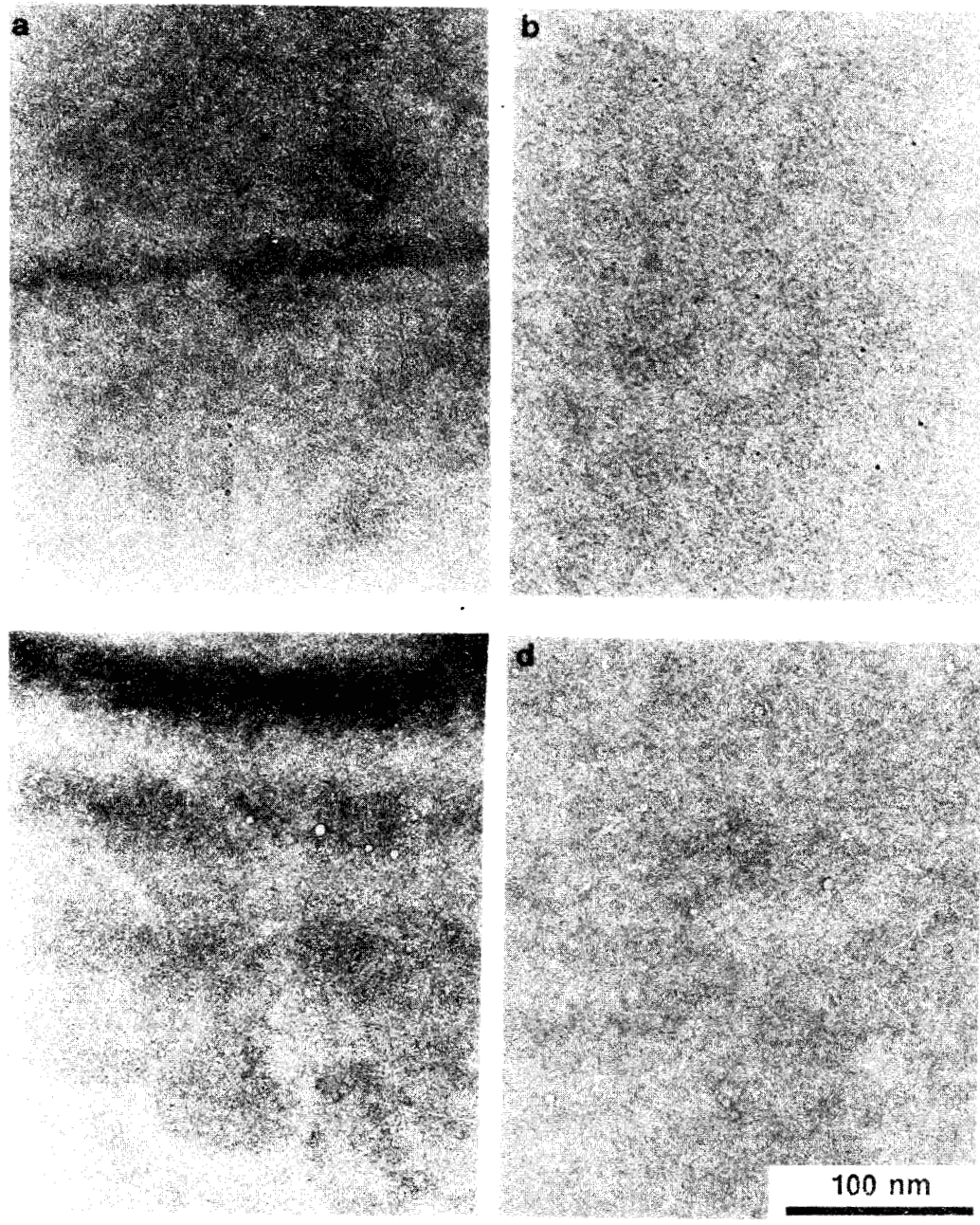

Figure 4.5. Bubble microstructure observed in solution-annealed P7 after annealing for one hour at 700 (a), 750 (b), 800 (c), and 900°C (d). Level of helium implantation is ~40 appm.

contained in the faulted loops was calculated assuming close packing on {111} planes. The interstitial content of the loops is 2.13×10^{-5} per atom after the 600°C anneal, 9.92×10^{-5} per atom after the 700°C anneal and 6.44×10^{-5} per atom after the 750°C anneal. The fact that the interstitial content of the loops increased during thermal annealing suggests that small helium-vacancy clusters may be effectively overpressurized and are absorbing a net vacancy flux until they reach equilibrium.[48,165] These small clusters remained invisible after a one-hour anneal at 700°C.

Several observations by other researchers[156-159] of apparent enhanced faulted loop stability during thermal annealing following helium implantation were discussed in Chapter 2. Shiraishi et al.[217] have recently reported a similar effect in type-316 stainless steel that had been irradiated to a low dose in a reactor with a primarily thermal neutron spectrum. By varying the concentration of boron in their steel, they were able to vary the amount of transmutant helium generated during the irradiation. In the specimens that had higher levels of boron, leading to 11 to 490 appm He, they observed faulted loop and bubble growth during a 30-min postirradiation anneal at 750°C. However, in a specimen with only 5 appm He, the radiation-produced defect clusters annealed out. This result is also consistent with the early work of Barnes and Mazey.[218] Using a cyclotron-produced beam of alpha particles, they implanted helium into a stack of thin copper foils. During postimplantation anneals at 350°C, they observed that small dislocation loops and black spot damage annealed

out in most of the foils. But in the foil in which the helium came to rest, the growth of faulted loops and small bubbles was observed.

The bubble distributions are characterized by growth at an approximately constant bubble density up to 800°C. Above 800°C the distribution coarsens and the density is reduced. This evolution of the bubble size distribution is shown in Figure 4.6. The helium content of the bubbles in the annealed specimens was calculated assuming that the bubbles were in mechanical equilibrium with the solid at the annealing temperature. The hard-sphere equation of state described in Chapter 3 was used to compute the gas pressure. The value chosen

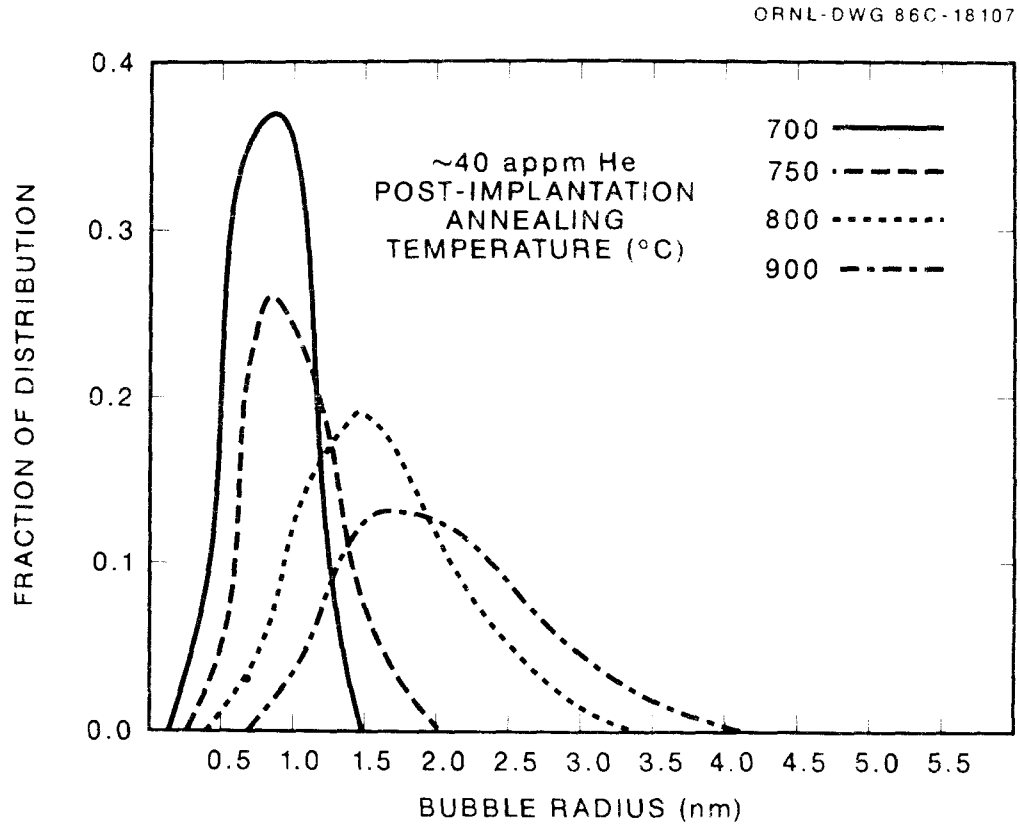

Figure 4.6. Influence of postimplantation annealing temperature on the observed bubble size distribution, ~40 appm He.

for the surface free energy has a large influence on the calculated helium content. When the temperature-dependent surface free energy used in Chapter 3 is applied here, about one-third of the implanted helium appears to be in the bubbles after the 700°C anneal, about two-thirds after the 750°C anneal, and essentially all of the helium is accounted for in the bubbles for the 800 and 900°C anneals.

The bubble and loop distributions are sensitive to the level of helium implanted as well as the annealing temperature. The specimen shown in Figure 4.7 was implanted with ~65 appm He and then annealed

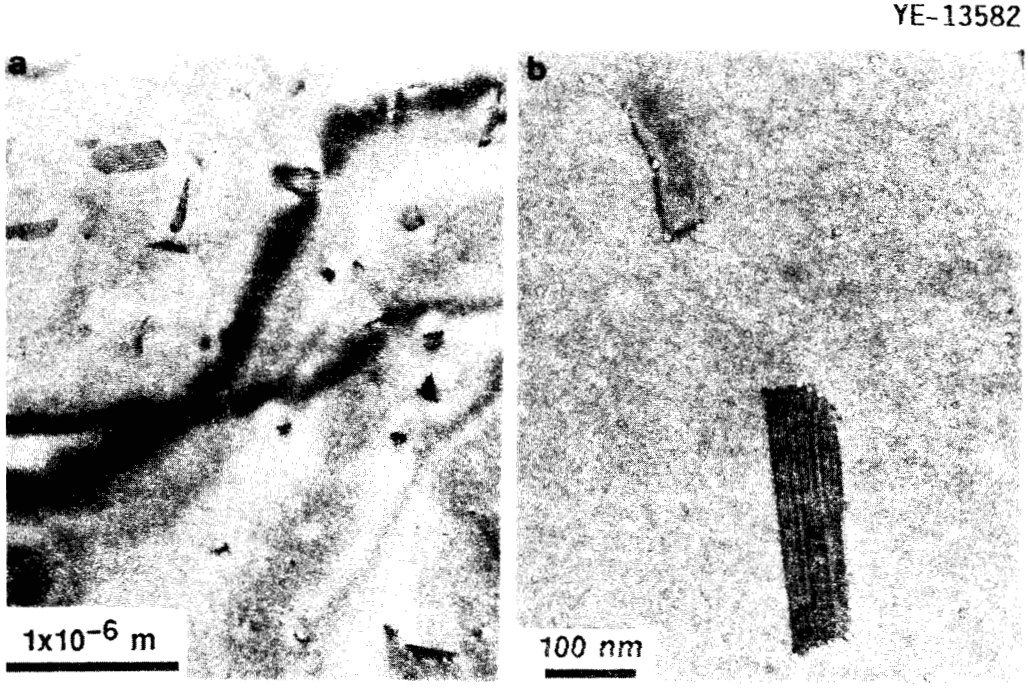

Figure 4.7. Bubble and faulted loop microstructures observed in solution-annealed P7 after annealing for one hour at 850°C; level of helium implantation is 65 appm.

for one hour at 850°C. The data shown in Figures 4.3, 4.4 and 4.5 would indicate that no loops should be observed and that ~4 x 10^{21} bubbles/m^3 with an average radius of 1.8 nm should be observed. Instead, the higher helium level has resulted in a lower than expected bubble density, 1.8 x $10^{21} m^{-3}$, and a larger than expected average size, 2.6 nm. A number of large faulted loops also have survived. The loop density is ~8 x 10^{18} m^{-3} with an average radius of 130 nm. The radius of the largest loops observed in this specimen exceeded 200 nm. All of the loops and many of the dislocation line segments were well decorated with bubbles as the example in Figure 4.7(b) indicates. The average size of the bubbles on dislocations and the loop perimeters was about 30% greater than the average bubble size in the matrix. This fact, along with the unusual loop stability, provides additional support for the concept of sympathetically coupled growth of bubbles and Frank loops that was mentioned above.

4.3.2 Results of the MFE-II Experiment

The MFE-II experiment failed to reach the planned damage level of 10 dpa. The peak damage for P7 alloy TEM disks was about 4.7 dpa with 65 appm He generated during the irradiation.[319] The actual irradiation temperatures also deviated from the design values; the temperatures achieved in the experiment were 350, 550 and 600°C.[320] Finally, a number of specimens were lost when the experiment was disassembled. Because of these facts, the value of the experiment was severely limited. The low exposure produced insufficient swelling at

most of the irradiation conditions to determine whether the various post-helium-implantation heat treatments had a significant impact. The initial examination of the specimens indicated that the incubation time for void formation was shortest at 550°C and that little information could be obtained from the 350 and 600°C irradiated specimens. Therefore, the discussion below will emphasize the results at 550°C. The TEM observations of the specimens irradiated at 550°C are summarized in Table 4.3. Brager and coworkers have also examined a few specimens of alloy P7 from the MFE-II experiment.[321-323] Their results will be referred to for purposes of comparison when it is appropriate.

Table 4.3. Summary of microstructures observed in alloy P7 after irradiation to 4 dpa at 550°C in the MFE-II Experiment

Helium Implanted (appm)	Post-Helium Implantation Anneal T (°C)	Cavity Parameters			Dislocation[a] Density (m^{-2})
		Density (m^{-3})	Radius (nm)	Volume Fraction (%)	
		20% Cold-Worked			
0	--	1.2×10^{21}	2.9	0.05	1.2×10^{14}
		Solution-Annealed			
0	--	2.3×10^{20}	10.8	0.19	3.3×10^{13}
50	--	not observed		$<10^{-2}$	1.7×10^{13}
36	750	$\sim 6 \times 10^{21}$	1.2	$<10^{-2}$	1.5×10^{13}
42	750	9.9×10^{21}	1.8	$<10^{-2}$[b]	1.5×10^{13}
		6.8×10^{21}	11.7	0.49[c]	
17	800	$\sim 6 \times 10^{21}$	~ 1.2	$<10^{-2}$	1.5×10^{13}

[a]See text for information on loop component.
[b]Bubbles throughout grains (see text).
[c]Local region near grain boundary (see text).

The microstructure of the specimens irradiated at 350°C was primarily comprised of small Frank faulted loops. This is shown in Figure 4.8 (a) and (b) for the solution annealed material that was irradiated without helium preinjection. The average loop radius was 7.0 nm and the loop density was 3.7×10^{22} m^{-3}. No cavities were observed, but the residual strain contrast from the high density of faulted loops could have obscured bubbles with radii less than about 1 to 2 nm. The specimen that was irradiated in the as-helium-injected condition was similar. Cavities were observed in a specimen that was annealed at 800°C following implantation of 37 appm He. This specimen is shown in Figure 4.8(c). The cavity size distribution in this specimen is nearly unchanged from the unirradiated control [Figure 4.5(c)]; the cavity density was 7.7×10^{21} m^{-3} and the average cavity radius was 1.28 nm. The fact that the density is slightly higher and the average radius slightly smaller than in the control specimen is consistent with the different levels of helium that were injected. Calculations using the models discussed previously predict that the critical bubble radius should be about 0.8 nm for the 350°C irradiation. The observation of an apparently stable bubble distribution with a mean radius larger than 0.8 nm indicates either that the low temperature irradiation conditions are not well modeled or that the supercritical cavities are growing very slowly at this temperature. The model does predict that voids will grow very slowly after being formed at 350°C and a prolonged, low-

YE-13585

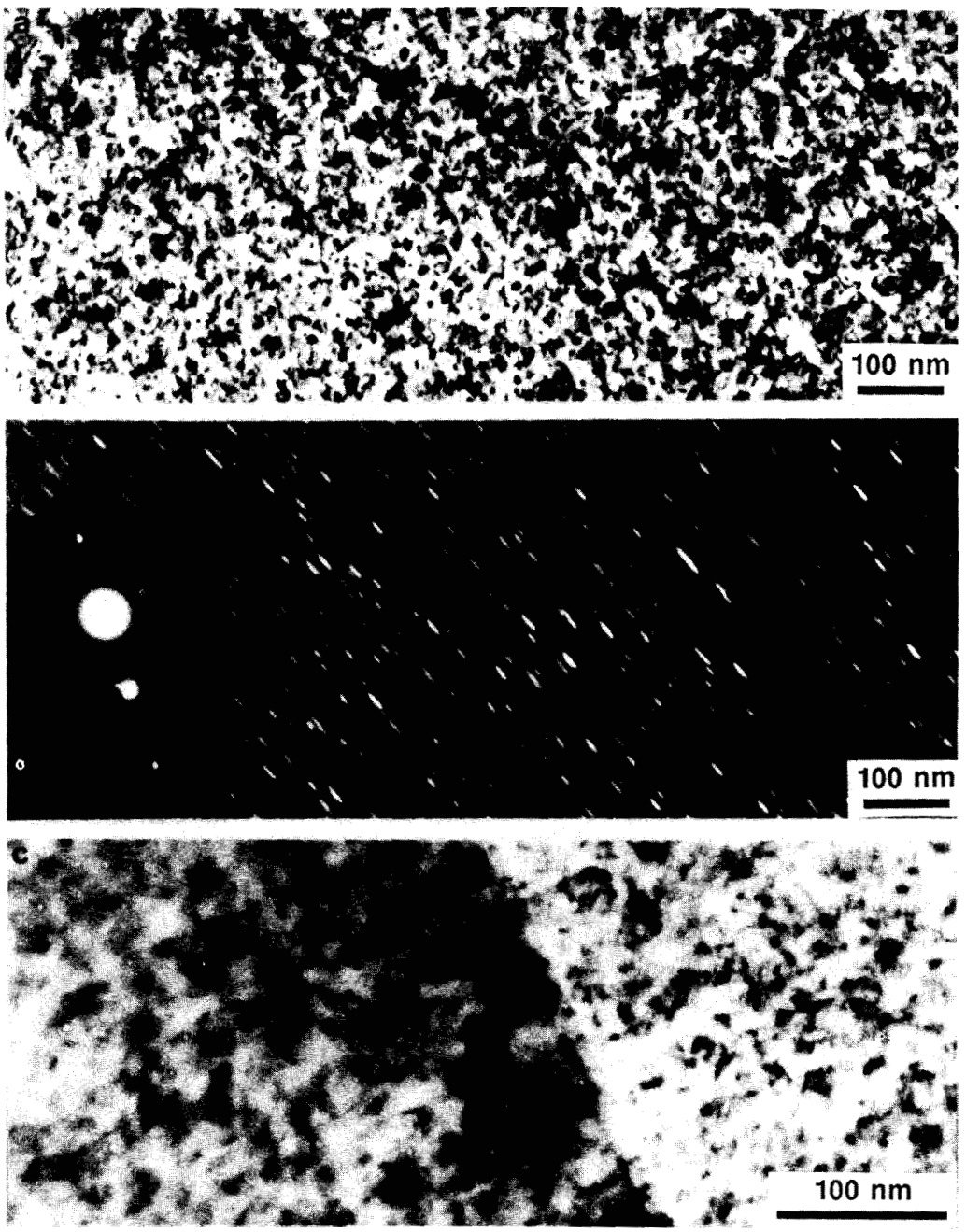

Figure 4.8. The microstructure of solution-annealed P7 observed after irradiation to 4.7 dpa at 350°C. Parts (a) and (b) are a bright field and dark field comparison of a specimen irradiated with no helium preinjection and (c) shows a specimen that was preinjected with 37 appm He and aged for one hour at 800°C.

swelling transient regime at this low temperature is consistent with the data shown in Figure 2.10.

The specimens irradiated at 600°C also showed little swelling. Cavities were observed in the solution annealed material that received no helium preinjection and in a specimen that had 32 appm He implanted followed by an 800°C anneal. These two specimens are shown at high magnification in Figure 4.9. Both cold working and helium preinjection without a subsequent anneal suppressed the formation of visible cavities. The cavities in the specimen without helium preinjection [Figure 4.9(a)] appear to be helium-stabilized bubbles. The bubble density is 7.5×10^{21} m^{-3} and the average bubble

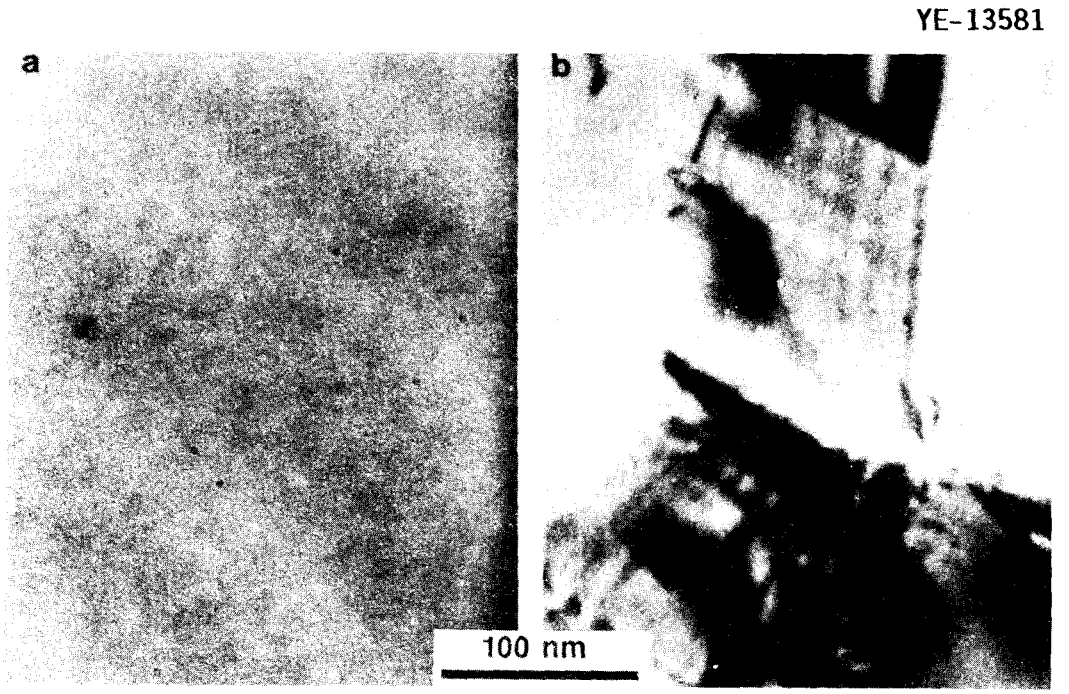

Figure 4.9. The microstructure of solution-annealed P7 observed after irradiation to 4.7 dpa at 600°C. A specimen irradiated with no helium preinjection is shown in (a), and (b) shows a specimen that was preinjected with 32 appm He and aged for one hour at 800°C.

radius is 1.2 nm. This distribution is consistent with all of the transmutant helium (65 appm) being contained in the bubbles. The theory predicts that the critical bubble radius for these irradiation conditions could be as large as 16.0 nm so that the lack of void growth is not surprising. The bubble distribution in the specimen that was helium implanted and aged prior to irradiation [Figure 4.9(b)] has not changed appreciably. It is similar to both the unirradiated control [Figure 4.5(c)] and a corresponding specimen irradiated at 350°C [Figure 4.8(c)]. An interesting observation in the specimens irradiated at 600°C was the presence of a large number of stacking fault tetrahedra. These were also observed in some of the 550°C irradiated specimens and will be discussed further below.

The specimens irradiated at 550°C showed the highest swelling and the greatest variation in their behavior. The microstructure of the solution annealed specimen that was irradiated at 550°C without helium preinjection is shown in Figure 4.10. The dislocation structure is shown in Figure 4.10(a) and consisted of a low density of Frank faulted loops with ~100 nm radii and a loose dislocation network. The network dislocation density was ~3.3×10^{13} m^{-2} and the loop density was $\leq 10^{18}$ m^{-3}. The cavity distribution was approximately bimodal as shown in Figure 4.10(b) and (c). The cavity density was 2.3×10^{20} m^{-3} and the average radius was 10.8 nm. The cavity distribution is plotted in Figure 4.11. The cavity volume fraction observed in this specimen was 0.19% and was primarily due to the fairly uniformly distributed population of octahedral voids shown in Figure 4.10(b).

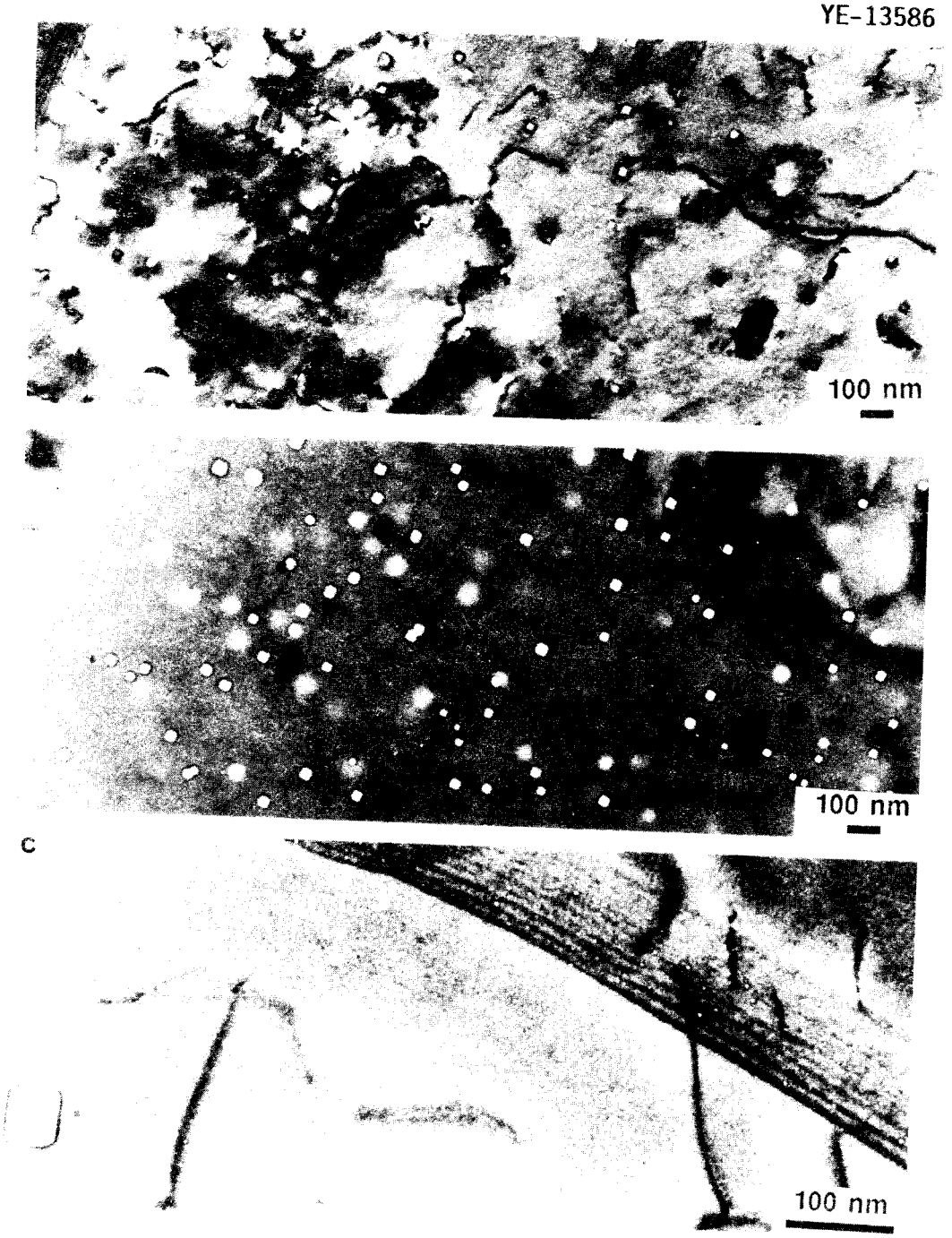

Figure 4.10. The microstructure of solution-annealed P7 observed after irradiation to 4.7 dpa at 550°C with no helium preinjection. The dislocation structure is shown in (a) and the cavities are shown in (b) and (c).

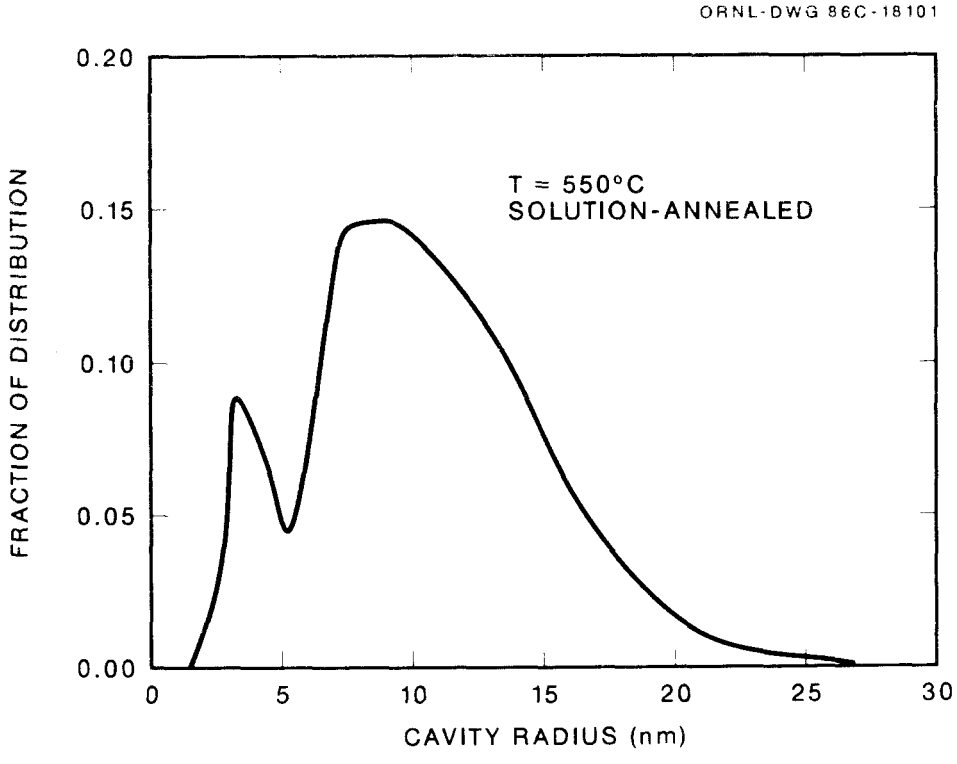

Figure 4.11. Observed cavity distribution in solution-annealed P7 after irradiation to 4.7 dpa at 550°C.

These voids had an average equivalent radius of 18.7 nm. The large number of small grain boundary bubbles and matrix bubbles is shown in Figure 4.10(c). The measured immersion density change was -0.054%. Brager and coworkers have reported somewhat higher cavity densities and smaller sizes in a nominally identical specimen.[321-323] They report a cavity volume fraction of 0.08% and an immersion density change of -0.15%.[321,322] The systematic error in the immersion density measurements used here is ≤0.1% for a TEM-disk-sized specimen[324] and Brager et al.[322] report a similar degree of accuracy.

Therefore, the immersion density and cavity volume fraction measurements are in reasonable agreement.

The critical bubble radius appears to be about 4.5 nm in Figure 4.11. Using the comprehensive model and the nominal model parameters discussed in Section 3.3.2, the predicted critical radius is between 3.9 and 4.3 nm. The range given in the predicted values of the critical radius reflect the fact that there is some uncertainty about the damage rate experienced by these specimens in the MFE-II experiment. No dosimeters were included in the capsules that contained the TEM disks.[310,325] The two values given here represent damage rates of 2.5 and 2.0 $\times 10^{-7}$ dpa/sec, respectively. The good agreement between the observed critical radius and the values calculated with the nominal model parameters is probably somewhat fortuitous. Small changes in either the assumed self-diffusion energy or the surface free energy will significantly alter the predicted values [see Equation (3.81)]. The predicted critical radius is also sensitive to changes in other model parameters because of their influence on the vacancy supersaturation as discussed in Chapter 3.

The specimen irradiated in the 20% cold-worked condition at 550°C with no helium pre-injection exhibited a somewhat higher density of smaller cavities than the solution annealed specimen. Cavity formation was also less uniform from grain to grain in the cold-worked material. Typical microstructures at an intermediate and high magnification are shown in Figure 4.12 and the cavity distribution is

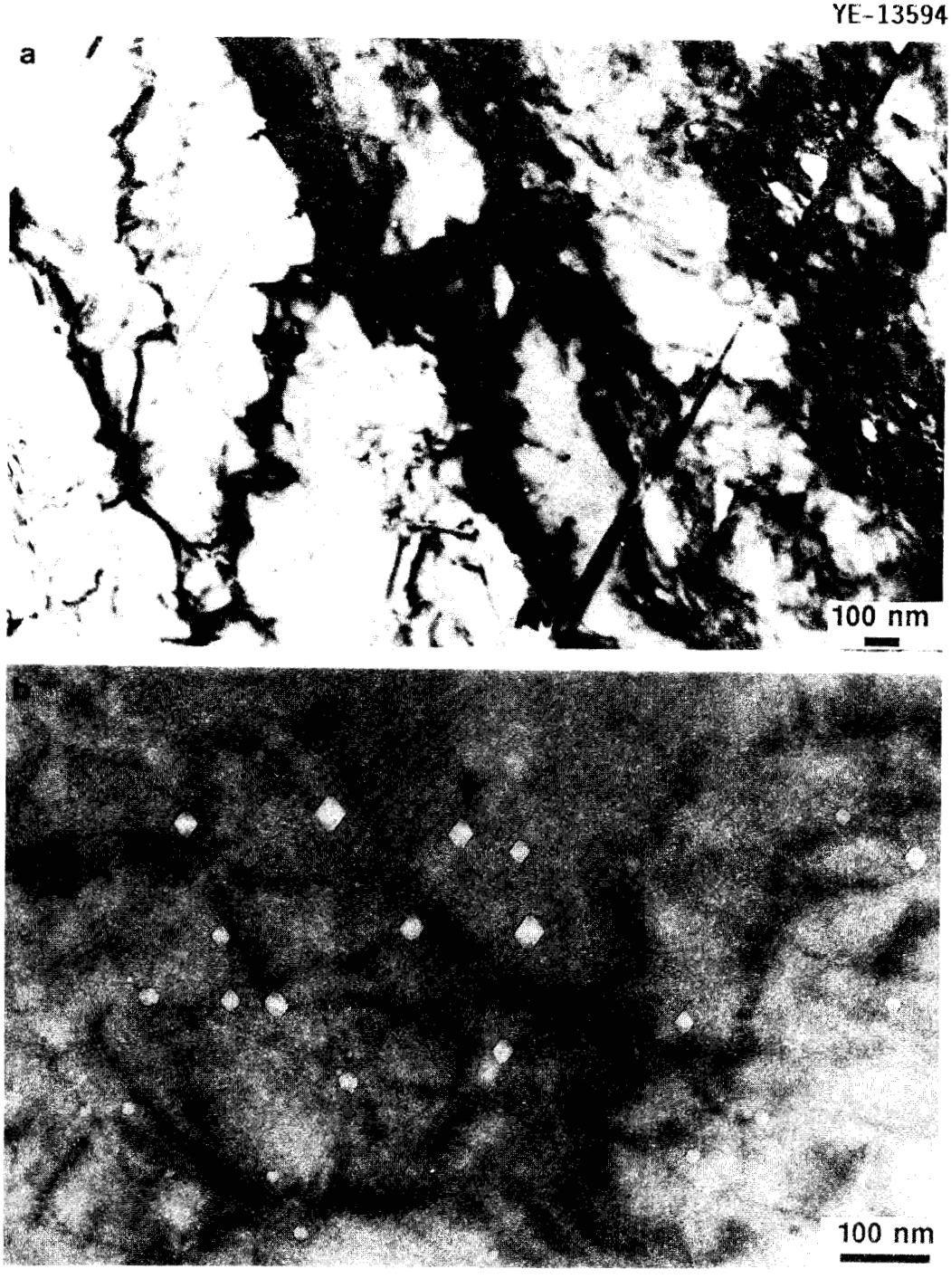

Figure 4.12. The microstructure of 20% cold-worked P7 observed after irradiation to 4.7 dpa at 550°C with no helium preinjection. The dislocation structure is shown in (a) and the cavities are shown at higher magnification in (b).

plotted in Figure 4.13. The average cavity density in the voided regions of this specimen was 1.2×10^{21} m^{-3} with an average radius of 2.91 nm. The cavity volume fraction was 0.049%. The network dislocation density was 1.2×10^{14} in the voided regions and no faulted loops were observed. These results are generally similar to the values reported by Brager et al.[321-323] for a similar specimen. They report a larger average cavity radius (8 nm), a cavity volume fraction of 0.03% and an immersion density change of -0.22%.[321,322] This immersion density change seems inconsistent with the measured cavity volume fractions, but no similar specimen was available to permit an additional measurement as part of this work.

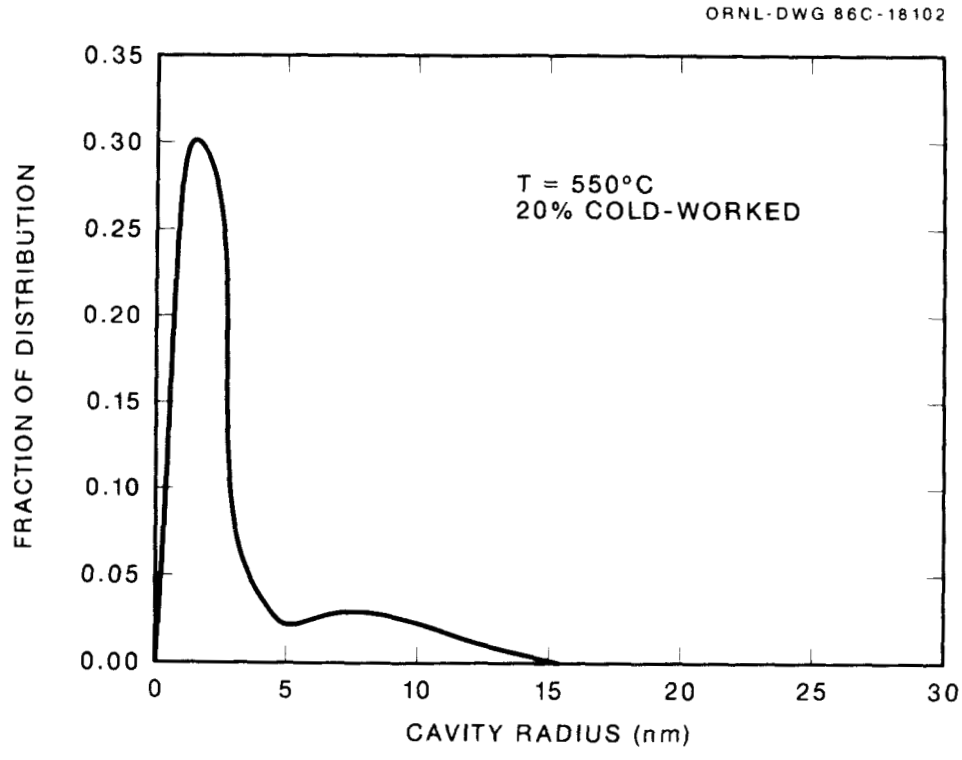

Figure 4.13. Observed cavity distribution in 20% cold-worked P7 after irradiation to 4.7 dpa at 550°C.

Although the swelling values measured in the two specimens are very similar, a comparison of the cavity distributions observed in solution-annealed (Figure 4.11) and 20% cold-worked (Figure 4.13) specimens indicates that the initial cold work has extended the swelling incubation time. While the larger cavities in the cold-worked specimen are clearly voids, the shape of the size distribution in the cold-worked material is nearly exponential. This indicates that the specimen is still in the void nucleation/incubation regime at this dose. The bimodal distribution in the solution-annealed specimen is indicative of a more mature cavity population and suggests that void growth rather than nucleation was the dominant process at the time the irradiation was terminated. It appears that one way in which the initial cold working extends the incubation time is by promoting a higher bubble density. This would require the available helium (~65 appm) to be distributed to more bubbles, thereby delaying the time for any one bubble to obtain the critical number of gas atoms.

The calculated critical radius for the cold-worked specimen ranges from 8.3 to 10.3 nm. This value is much higher than that calculated for the solution-annealed specimen because the higher dislocation density suppresses the effective vacancy supersaturation. Figure 4.13 indicates that the actual critical radius is closer to 5.0 nm. As mentioned above, this predicted value is quite sensitive

to a number of model parameters and parameter adjustment within a limited range could improve the agreement between the observed and calculated values. The fact that the dislocations are not uniformly distributed also makes a direct comparison difficult for the cold-worked material. The model assumes a homogeneous distribution of dislocations while the actual dislocation density is very heterogeneous; in particular, lower dislocation densities were observed in the regions in which voids had formed. For a dose rate of 2.5×10^{-7} dpa/sec, the dislocation density was predicted to be 4.4×10^{14} m^{-2} when the first bubbles converted to voids with a critical radius of 8.3 nm. Later, with additional dislocation recovery to a value of 1.7×10^{14} m^{-2} the critical radius became 5.4 nm. This latter value is in good agreement with the value suggested by Figure 4.13. This sensitivity of the critical number to the dislocation density provides a second mechanism by which cold working can extend the swelling incubation time. In light of this sensitivity, the fact that the apparent critical radii are so similar in Figures 4.11 and 4.13 is surprising. The overlap of the regions of the size distribution that are less than (bubbles) and greater than (voids) the critical size makes it impossible to precisely determine the critical radius experimentally. The values of the critical radii quoted above roughly correspond to the minima in the size distributions. Since the distributions are so different, the offset between the actual critical radius and the minimum in the size distribution may not be the

same for both specimens. Of course, experimental error may also be responsible for some shift in the measured critical radius.

The influence of helium implantation before irradiation at 550°C is to suppress cavity formation at low doses. The microstructure of a specimen irradiated in the as-helium-injected condition consisted of primarily unfaulted dislocation loops and a few dislocation line segments. The loop density was 8×10^{19} m^{-3} with an average radius of 34 nm. A typical micrograph and the loop size distribution for a solution annealed specimen, pre-injected with 50 appm of helium is shown in Figure 4.14. No cavities were observed. The preirradiation microstructure for this specimen was a high density of small interstitial clusters (Figure 4.2) observable only as black dots. Based on the evolution of the as-implanted microstructure during thermal annealing, the implanted helium was trapped in many small vacancy clusters. This results in a high overall system sink strength for point defects that enhances point defect recombination, thereby reducing the effective vacancy supersaturation. The lower supersaturation inhibits cavity formation; for example, the critical bubble size is increased [Equation (3.9)]. In addition, the high density of helium/vacancy clusters can be compared to a state of "over-nucleation." The number of sites available to which the helium and vacancies can partition is too high for any bubbles to grow large enough to become visible during the subsequent irradiation. Therefore, the helium remains trapped in many small bubbles that are not

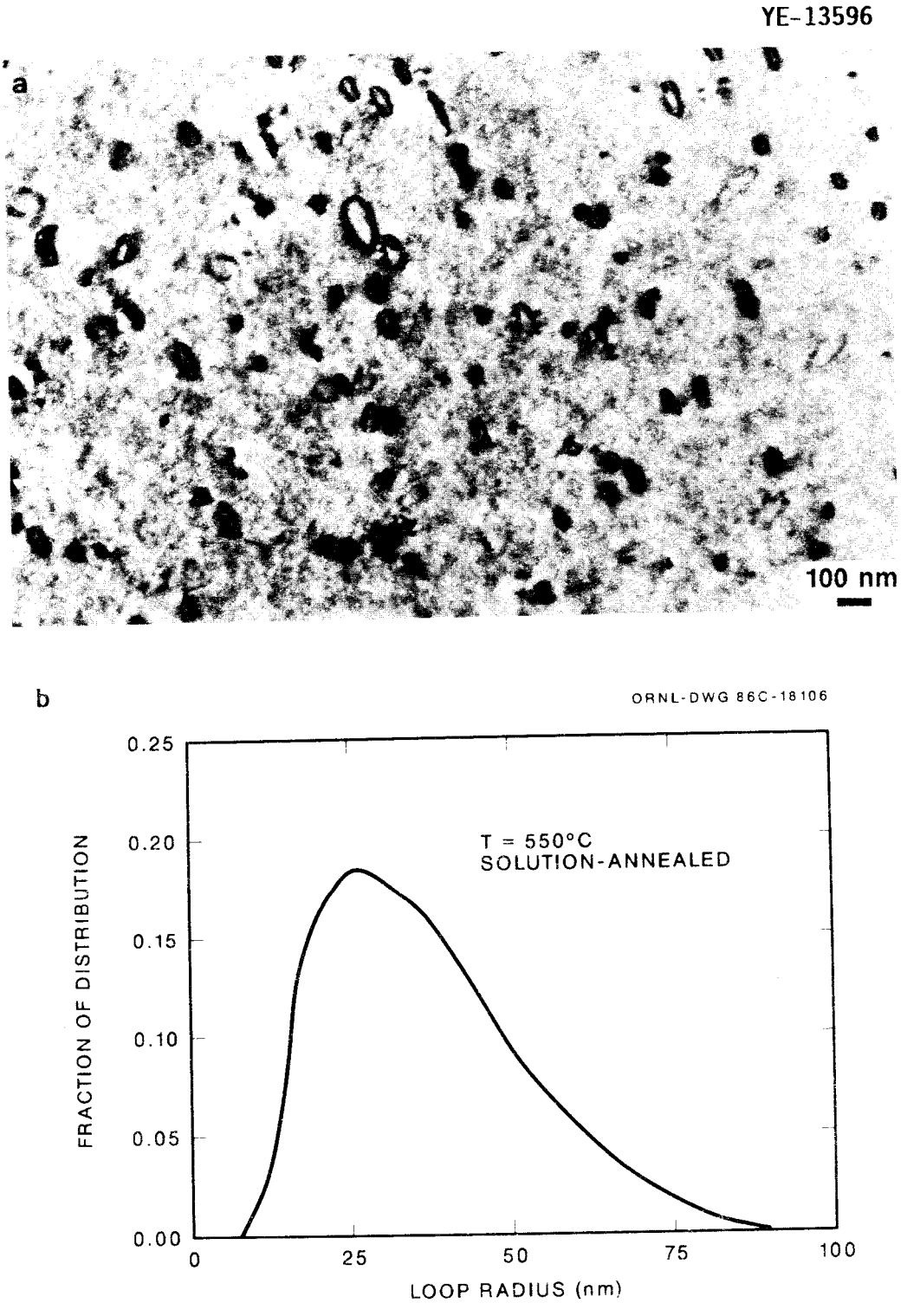

Figure 4.14. Observed dislocation loop distribution in solution-annealed P7 after room temperature implantation of 51 appm He and subsequent irradiation to 4.7 dpa at 550°C.

visible by TEM. Support for this inference is provided by the similar results of Packan and Farrell[61,308] and the fact that post-irradiation annealing at 900°C of a nominally identical specimen by Brager and Garner resulted in the formation of observable bubbles.[323] The work of Packan and Farrell[61,103,308] suggests that irradiation to a higher dose would have resulted in a higher void density in this specimen than in the specimen without helium preinjection.

All of the solution-annealed specimens that were annealed following helium implantation exhibited generally similar microstructures after irradiation to 4.7 dpa at 550°C. This microstructure consisted of a low density of unfaulted loops and dislocation line segments, helium bubbles and stacking fault tetrahedra. The dislocation loop density was ~1-3 x $10^{19}/m^3$, about one-third the density of the unannealed specimen. The average loop size was larger than the unannealed specimen, $\bar{r}_\ell$ ~ 120 nm. The typical dislocation structure is shown in a bright field/weak-beam dark field comparison in Figure 4.15. This specimen was implanted with 36 appm He and annealed for one hour at 750°C prior to irradiation. The small triangular defects in Figure 4.15 are stacking fault tetrahedra.

Because of the low damage level attained in this experiment, the cavity distributions observed in the helium-implanted-and-aged specimens were largely unchanged from those that were formed during the post-helium-implantation anneal. The one exception to this was a specimen that had been implanted with 42 appm He and annealed for one

YE-13595

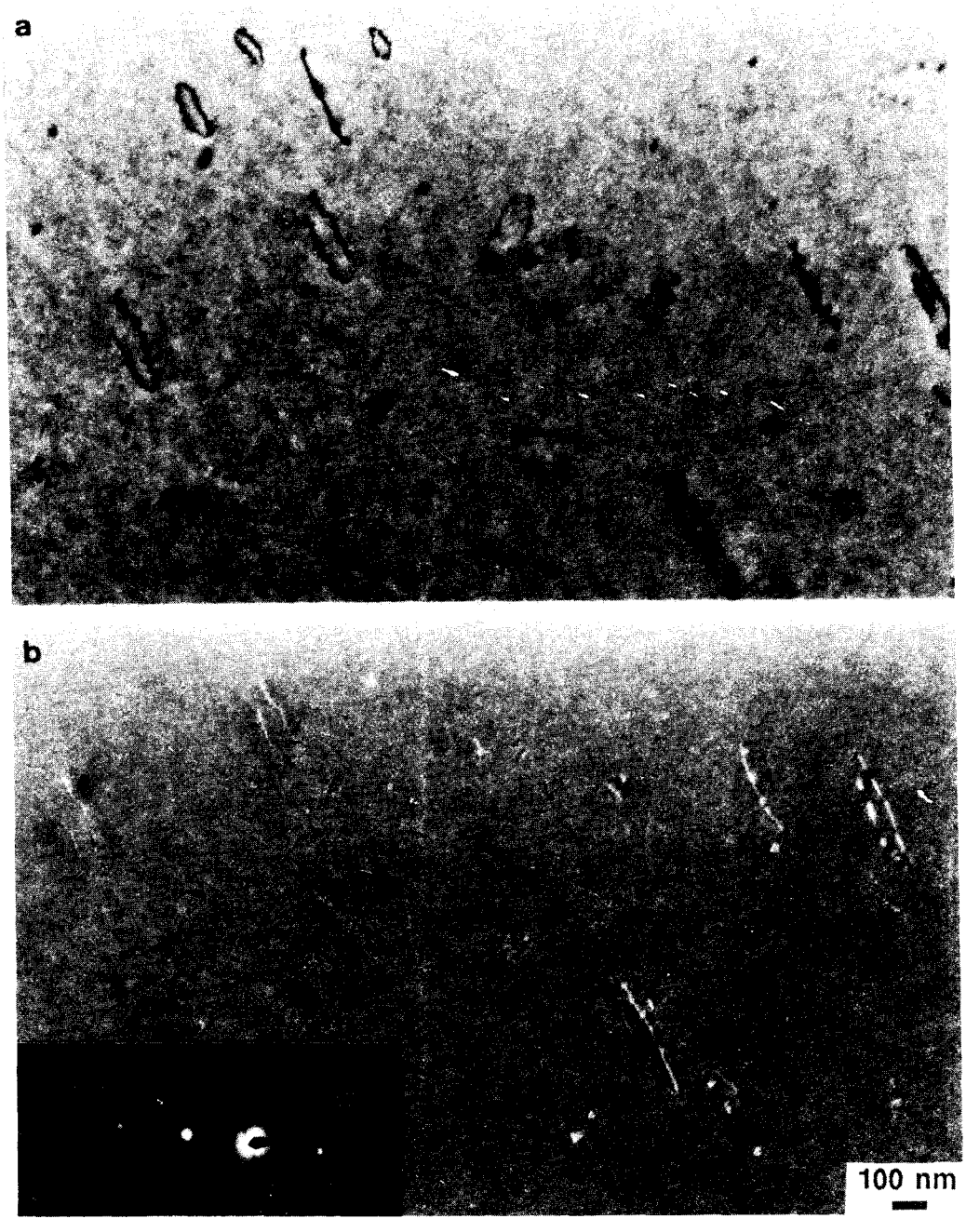

Figure 4.15. Typical dislocation loop distribution in solution-annealed P7 after room temperature helium implantation with subsequent aging prior to irradiation to 4.7 dpa at 550°C. This specimen was implanted with 36 appm He and aged at 750°C. Stacking fault tetrahedra are visible as small triangular defects in the weak-beam dark field image in (b).

hour at 750°C. This specimen exhibited voids in a narrow band adjacent to the grain boundaries. These voids are shown at low magnification in Figure 4.16 (a) and (b). Figure 4.16 (a) shows a region along a straight segment of grain boundary that has been preferentially thinned during electropolishing. Figure 4.16 (b) demonstrates that this behavior was fairly uniform in this specimen by showing a grain boundary triple point in another region of the specimen. The voids form in a band that is about 400 nm in width and the edge of this band lies about 400 nm from the grain boundary. The local density of these larger voids is 6.8×10^{20} m^{-3} with an average radius of 11.7 nm. This leads to a local swelling level of 0.49%. Thus, the local swelling is about two and one-half-times greater than in the specimen irradiated without helium preinjection. The fact that voids seem to form most easily in a region near, but not immediately adjacent to, grain boundaries has been reported earlier by Leitnaker et al. for another model austenitic alloy[326] and by Horsewell and Singh and van Witzenburg and Mastenbroek for pure aluminum.[301,302] In addition to the voids, this specimen also exhibited a higher density of small bubbles. This bimodal distribution is shown at higher magnification in Figure 4.16(c). The average radius of the bubbles in this specimen was 1.1 nm with a density of 9.9×10^{21} m^{-3}. The absence of voids in other specimens that were subject to similar irradiation conditions and levels of helium preinjection may reflect only specimen-to-specimen variations or a strong sensitivity to the level of helium implantation in the 30 to 70 appm range. As

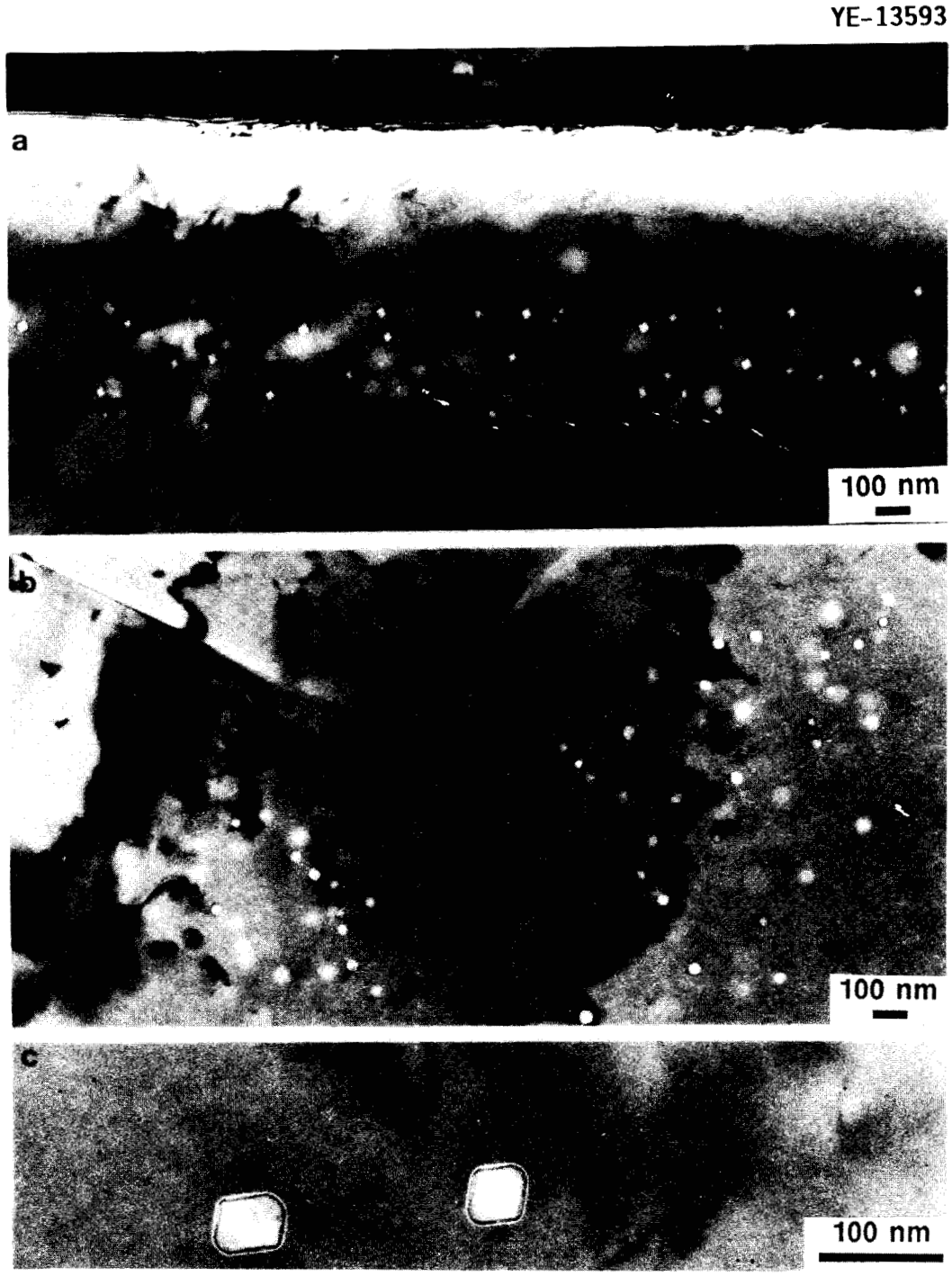

Figure 4.16. Observation of void formation near grain boundaries in solution-annealed P7 that was implanted with 42 appm He and aged at 750°C prior to irradiation at 550°C. Several grain boundaries are shown in (a) and (b) at low magnification, and (c) shows a bimodal cavity distribution at higher magnification.

discussed above, such a sensitivity was observed in three specimens that were preinjected with 47, 65 and 41 appm He and annealed for one hour at 800, 850 and 900°C, respectively [cf. Figures 4.5(c) and (d) with Figure 4.7].

The dislocation structure in the grain interior of the specimen that developed the voided bands was similar to the other helium-implanted-and-aged specimens. This structure is shown in Figure 4.17. For purposes of comparison with Figure 4.15, both a bright field and a weak-beam dark field image are shown. For this specimen orientation (foil normal near <200>) the stacking fault tetrahedra appear as nearly square defects.[327] They are most clearly seen in the weak-beam dark field image.

The observation of such large stacking fault tetrahedra (SFT) in these specimens was quite surprising since they have not been reported previously in austenitic steel that was neutron irradiated at elevated temperatures. The fact that the defects were SFTs and not triangle loops was verified by imaging them with g_{200} with a foil normal near both the <110> and <200> poles. In these two orientations the SFT will appear as a triangle and a square, respectively.[63,327] Such a sequence of micrographs is shown in Figure 4.18, along with the appropriate diffraction patterns. This specimen is the helium-implanted-and-aged one that exhibited a band of voids near the grain boundaries. Figure 4.18 shows that the voids and SFTs have grown to a similar size in roughly overlapping regions. There was some indication that the SFTs were being eliminated in the

YE-13608

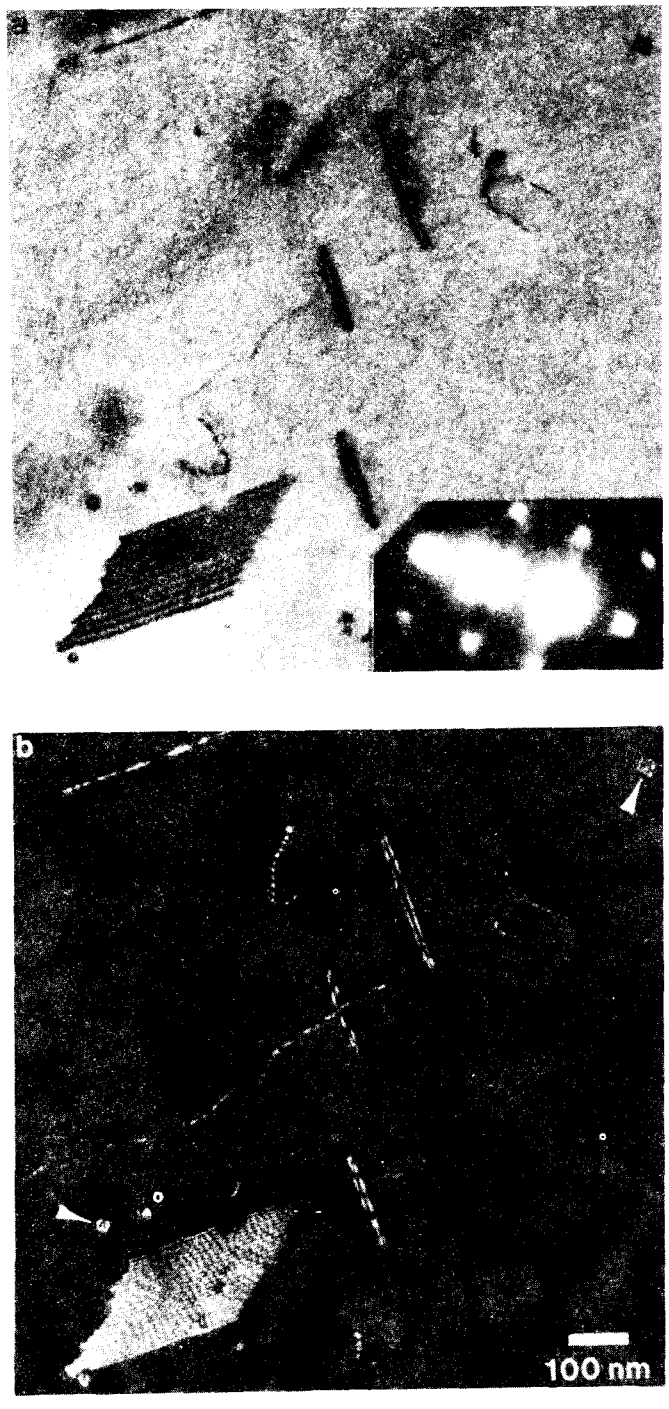

Figure 4.17. Dislocations and stacking fault tetrahedra observed in the grain interior in solution-annealed P7 that was implanted with 42 appm He and aged at 750°C prior to irradiation to 4.7 dpa at 550°C. The stacking fault tetrahedra are visible as small square defects in the weak-beam dark field image in (b), two are highlighted by small arrows.

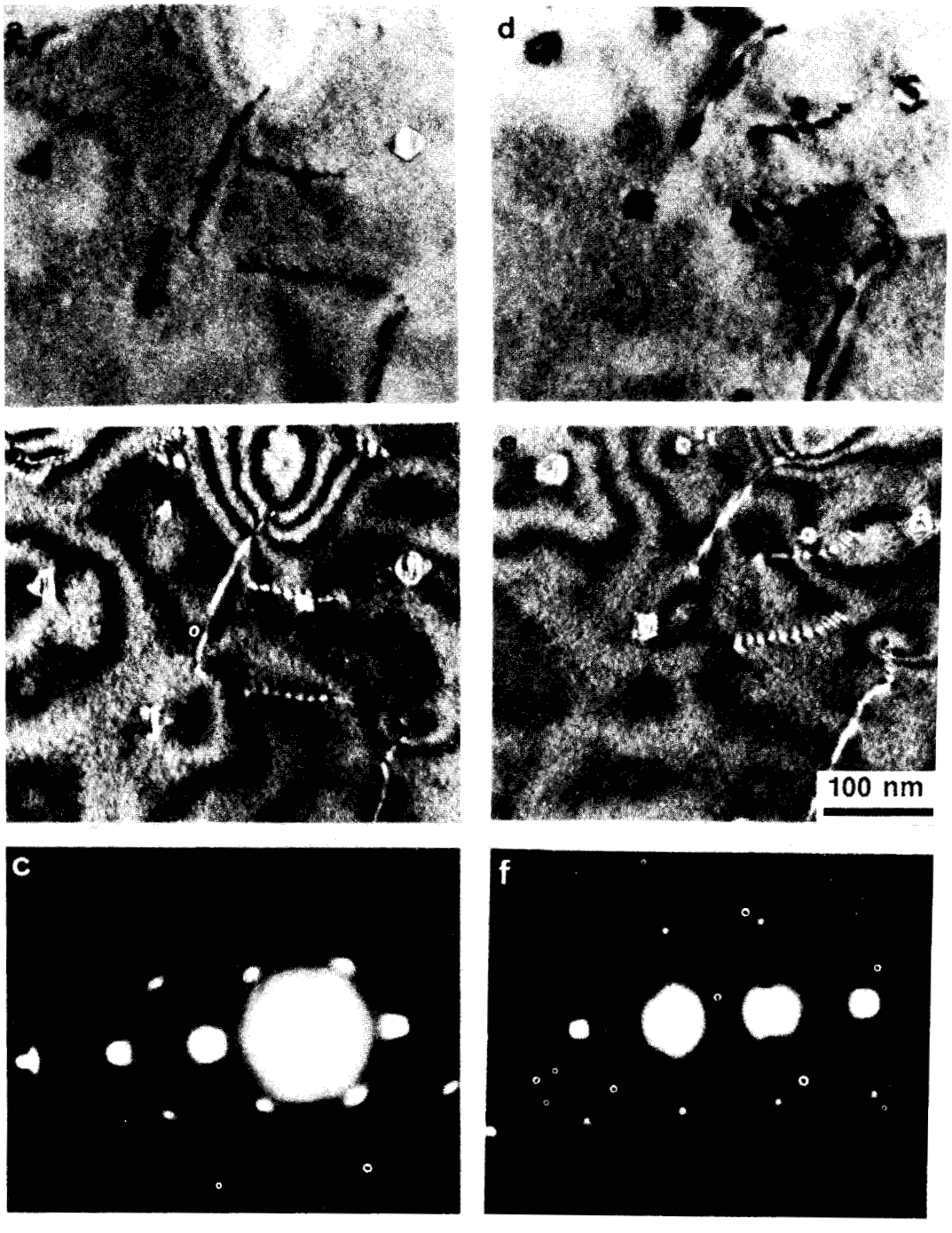

Figure 4.18. Verification of the observation of stacking fault tetrahedra in solution-annealed P7 that was implanted with 42 appm He and aged at 750°C prior to irradiation to 4.7 dpa at 550°C. The sequences (a–c) and (d–f) show the bright field and weak-beam dark field images and the diffraction pattern for g_{200} near the <110> and <100> poles, respectively.

voided band, but the present data are inconclusive with respect to this issue. The appearance of the SFTs was quite general in this experiment – they were observed in specimens irradiated at 550 and 600°C, with and without helium preinjection, and with and without post-helium-implantation heat treatment. The average edge length was ~20 nm and the density varied between 1×10^{19} and 1×10^{20} m^{-3}. The highest density was observed in a solution-annealed specimen irradiated at 600°C with no helium preinjection.

The only known previously verified observations of SFTs in irradiated austenitic stainless steel have been under charged particle irradiation at low temperatures. Yoshida et al.[328] indicate that some small (<1.0 nm) SFTs may be present in an Fe-Cr-Ni ternary alloy after 14 MeV neutron irradiation at 25°C. In a later publication,[46] some of these same authors state that the defects were too small to verify their morphology. Sindelar[47] reported observing a few defects that appeared to be SFTs near the end-of-range in a specimen of alloy P7 that had been irradiated at 400°C with nickel ions to a dose of 10 dpa. Kojima et al. performed high voltage electron irradiations of an Fe-13Cr-14Ni alloy and reported SFTs for irradiation temperatures below 325°C (ref. 46). It is not known whether the SFT is more commonly present in irradiated austenitic stainless steels and has not been reported, or if the present work has fortuitously examined specimens in a narrow fluence/temperature window that permitted their observation. This latter possibility is likely since relatively few neutron irradiation experiments have explored

the dose regime below 5 dpa. Certainly these observations lend credibility to calculations which suggest that, for some conditions and parameter choices, voids and SFTs should have similar stability.[36-38] Assuming that the SFTs form by the Silcox-Hirsch mechanism,[327] these data also confirm the growth of vacancy loops to reasonably large sizes under neutron irradiation.

In summary, the results of the MFE-II irradiation experiment are generally consistent with the theoretical concepts discussed in Chapter 3. One of the key concepts was that helium promotes void formation by stabilizing bubbles and providing a driving force for bubble growth until the bubbles reach the critical size beyond which gas pressure is not required to permit continued growth. The observation that the swelling incubation time was longer for the cold-worked material in which the bubble density was about five times greater than the solution-annealed material supports this concept. The higher bubble density provides more sites to which the available helium is partitioned; hence, the time for any one bubble to obtain the critical number of gas atoms is extended. The suppression of void formation by room-temperature helium implantation is in agreement with the arguments advanced and verified with the models that a high overall system sink strength could extend the swelling incubation time by reducing the effective vacancy supersaturation. The as-implanted microstructure also provides a high density of sites to which helium can be partitioned during the subsequent irradiation so

that no observable bubbles were formed. If sufficient coarsening took place and near critically sizes bubbles were formed during post-implantation anneals, the theory indicates that the swelling incubation time should be reduced compared to that of the unimplanted material. Although the greatest overall swelling was observed in the solution-annealed specimen irradiated without helium implantation, the local swelling in the voided regions of one of the helium-implanted-and-annealed specimens was three times that in the former. This also provides support for the concept of voids forming from the conversion of bubbles that reach the critical radius. More detailed comparisons between the theory and the MFE-II experiment are inhibited by the fact that the experiment was terminated after an exposure of only about 4 dpa. At this dose, most of the specimens were still in the swelling incubation regime so that any differences that might have evolved at a higher dose cannot be detected.

4.3.3 Results of Postirradiation Annealing Experiment

Postirradiation annealing studies in austenitic stainless steels have previously yielded somewhat conflicting results.[87,328-333] The results of Porter et al.[333] agreed with work by Cawthorne and Fulton[87] and Holmes et al.[330] that there were two annealing stages evident in irradiated material. Below about 600°C dislocation loop annealing leads to softening of the material with little change in density; while above about 700-750°C voids begin to anneal, leading

to additional softening and an increase in the density of the specimen. Most early studies, such as those by Cawthorne and Fulton,[87] Holmes et al.[330] and Stiegler and Bloom[331] reported complete void annealing by about 900°C. Straalsund et al.[332] observed void coarsening in the grain interiors while a void denuded zone gradually grew into the grain. Both Cawthorne[329] and Porter et al.[333] observed a persistent, stable population of large voids after annealing at high temperatures (~1000-1050°C).

The factors that determine void annealing behavior appear to be both the void size and the void size distribution with the dislocation network playing a role in some cases.[333,334] The studies that reported complete void annealing were conducted on specimens irradiated to low doses at fairly low temperatures. For such conditions the void sizes tend to be fairly small [e.g., Holmes et al. report an average radius of 7.5 nm (ref. 330)]. Such voids anneal quickly because the vacancy emission rate is large. For the case of voids, where the internal gas pressure is negligible, Equation (3.2) can be reduced to show that the rate of vacancy emission from a void with radius, r_v, is proportional to $\exp\left(\frac{2\gamma\Omega}{r_v kT}\right)$. This exponential term approaches unity for large voids. For example, taking $\gamma = 1.0$ J/m^2 at 900°C, this term is 1.76, 1.07 and 1.01 for voids with radii of 2.5, 25 and 100 nm, respectively.

Thus, small voids emit vacancies much more rapidly than large voids. The largest voids would tend to have vacancy emission rates

similar to dislocations and would therefore not be expected to shrink under thermal annealing. Consequently, for specimens irradiated to higher doses and characterized by a broader size distribution, coarsening of the distribution occurs during annealing as the small voids shrink and the larger voids grow in an Ostwald ripening process. Both Cawthorne[328] and Straalsund et al.[332] report that the coarsening of the void distribution in their materials was consistent with the theory of Ostwald ripening[335] developed by Wagner[336] and Lifshitz and Slyozov.[337] This latter theory also predicts the formation and growth of denuded zones adjacent to grain boundaries and twins as observed by Straalsund et al.[332] The data of Porter et al.[333] also appear to be consistent with Ostwald ripening and they report that the large voids that persisted after 900 and 1054°C anneal were interconnected by dislocation segments.

This earlier work suggested that the recovery of the radiation produced microstructure in the material chosen for the present study could be reasonably followed by a combination of microhardness and immersion density measurements. Annealing at 600°C and above was expected to show only a limited amount of recovery of the dislocation structure because of the relatively high irradiation temperature of 650°C. Therefore, both the softening of the material and the density recovery would be due to the annealing of the voids and a similar activation energy should be observed for both processes. It was expected that these measurements would lead to an estimate of the activation energy for self-diffusion in this alloy.

The results of the microhardness and immersion density measurements from the post-irradiation annealing experiment are shown in Figures 4.19 and 4.20. Two isothermal annealing curves, at 750 and 900°C, and a one-hour isochronal annealing curve are shown. Values for the as-irradiated condition and unirradiated control material are also indicated. The error bars on the microhardness data points (Figure 4.19) reflect the range of 8 to 10 measurements and the symbols indicate the average value at each condition. Additional data points are included to show the scatter in measurements on duplicate specimens (one hour at 600°C) and the effect of 1000 rather than 500 g loading (as-irradiated and one hour at 900°C). These microhardness data are seen to be very systematic and a least-squares polynomial fit to the data is also shown. For the immersion density data in Figure 4.20, the error bars reflect the observed scatter in repeated measurements on a single sample, approximately ±0.1%. The two values shown at 600°C in the isochronal annealing curve again indicate measurements on nominally duplicate specimens. Here the apparent specimen-to-specimen scatter is quite large, leading to significant uncertainty in determining a "best fit" to the data.

Following the example of Jostsons et al.,[338] these data were analyzed using the method developed by Meechan and Brinkman.[339] This analysis requires only the use of a single isothermal annealing curve and an isochronal annealing curve. For initially identical specimens, equivalent changes in the measured property (immersion density or microhardness) are observed after a time τ_i during the isothermal

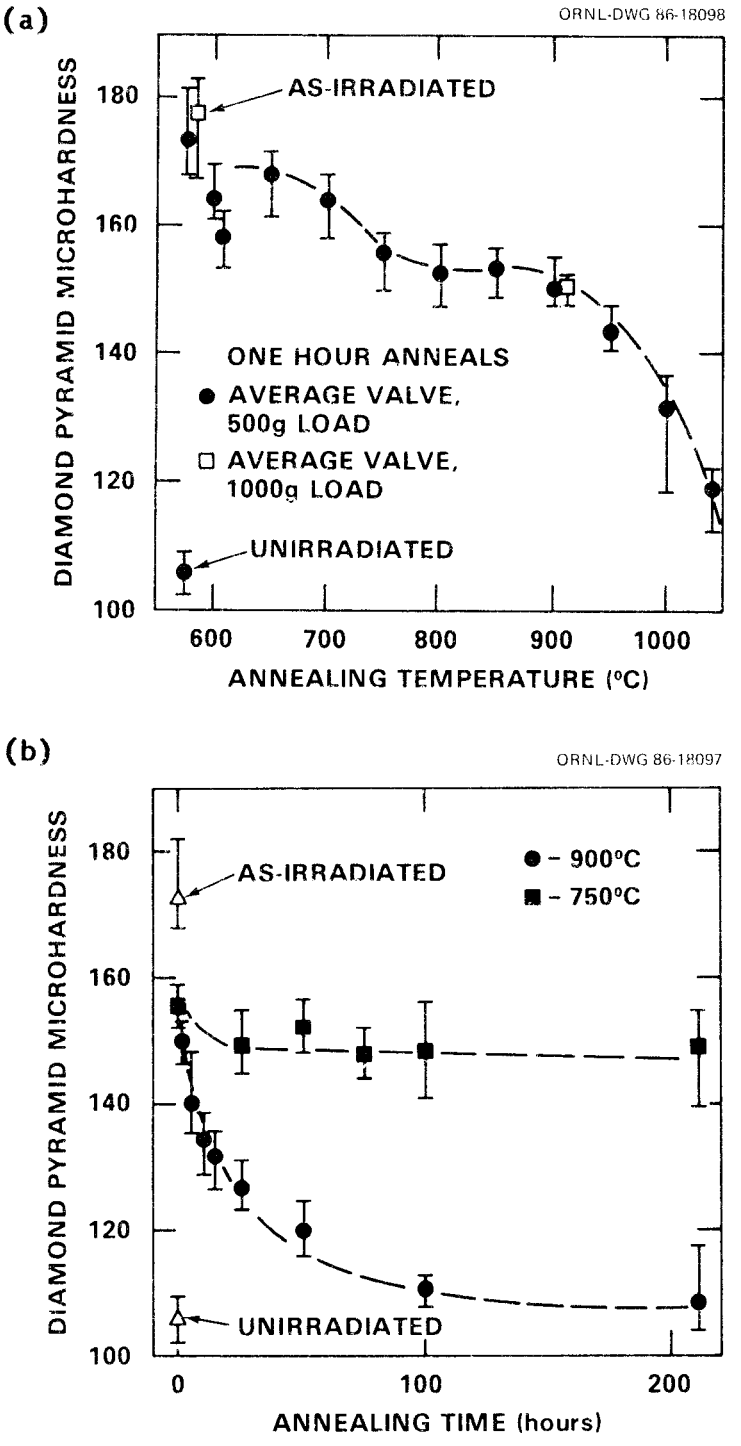

Figure 4.19. Diamond pyramid microhardness results from post-irradiation annealing experiment, one hour isochronal annealing curve (a) and isothermal annealing curves at 750 and 900°C (b). Starting material was P7, irradiated to 12.5 dpa at 650°C in the EBR-II.

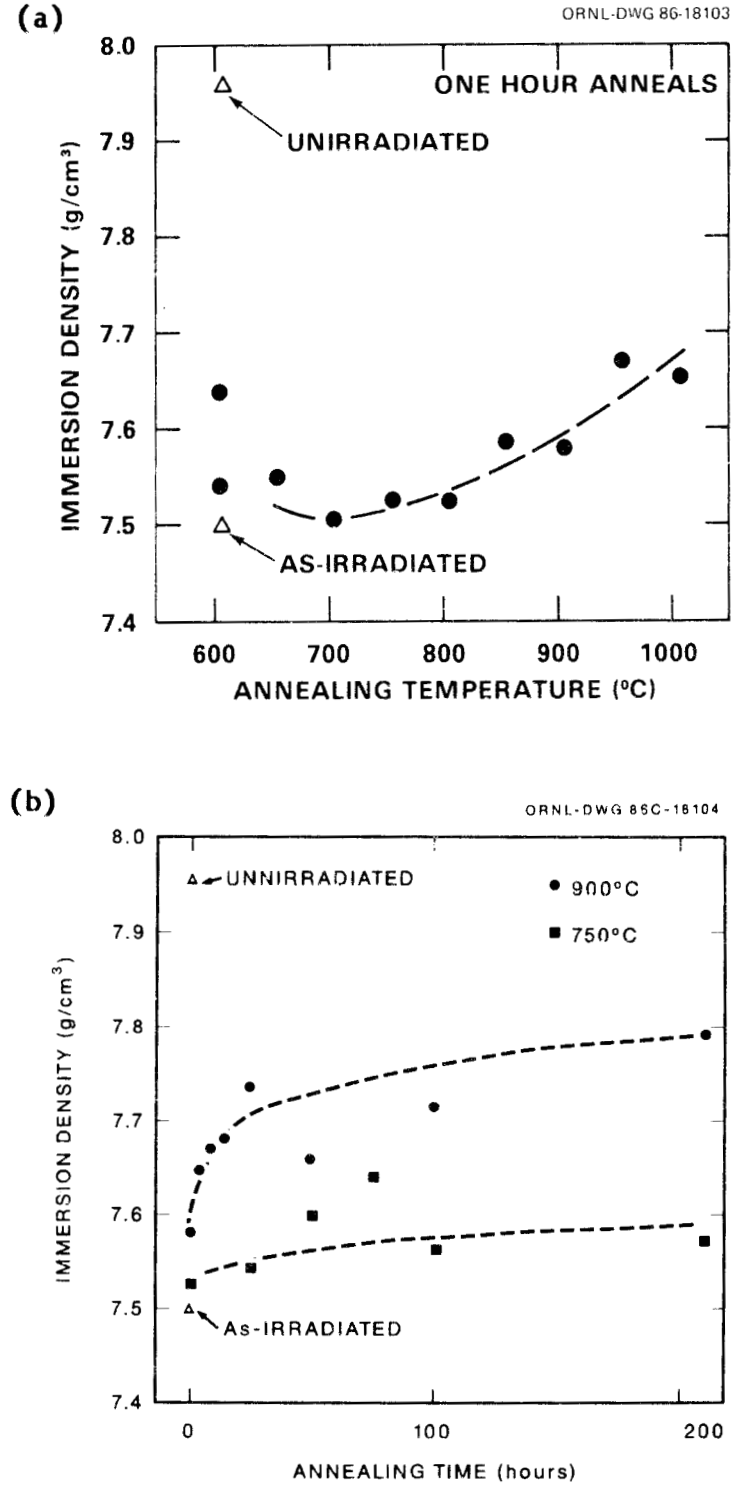

Figure 4.20. Immersion density results from postirradiation annealing experiment, one hour isochronal annealing curve (a) and isothermal annealing curves at 750 and 900°C (b). Starting material was P7, irradiated to 12.5 dpa at 650°C in the EBR-II.

anneal at T_1 and a temperature T_a during isochronal anneals for a time t_a. This occurs when an integal parameter defined by Meechan and Brinkman as the temperature-compensated time[338] is equal for the two annealing conditions. For this condition they show that:

$$\ln t_a - E_a/kT_a = \ln \tau_1 - E_a/kT_1, \qquad (4.1)$$

where E_a is the activation energy for the process responsible for the property change. Therefore, a plot of $\ln \tau_1$ versus T_a^{-1} should yield a straight line with a slope equal to E_a/k if the recovery process is characterized by a single activation energy. Regions of curvature in this plot indicate that more than one process is responsible for the property change.

The results presented here were obtained using the 900°C isothermal annealing curve because it provided the best overlap with the isochronal annealing data. Figure 4.21 shows the $\ln \tau_1$ versus T_a^{-1} curves obtained from the data in Figures 4.19 and 4.20. The microhardness data in Figure 4.21 (a) shows a fairly straight line from about 925°C to 1000°C. The apparent activation energy obtained from these data is 4.3 eV. The immersion density data shown in Figure 4.21(b) are less systematic and more difficult to interpret. This result is expected from the data scatter in Figure 4.20. If Figure 4.21(b) is a reliable indicator of the annealing behavior, the constantly changing slope would indicate that multiple mechanisms are at work. Two regions of near linear behavior are visible. The slope

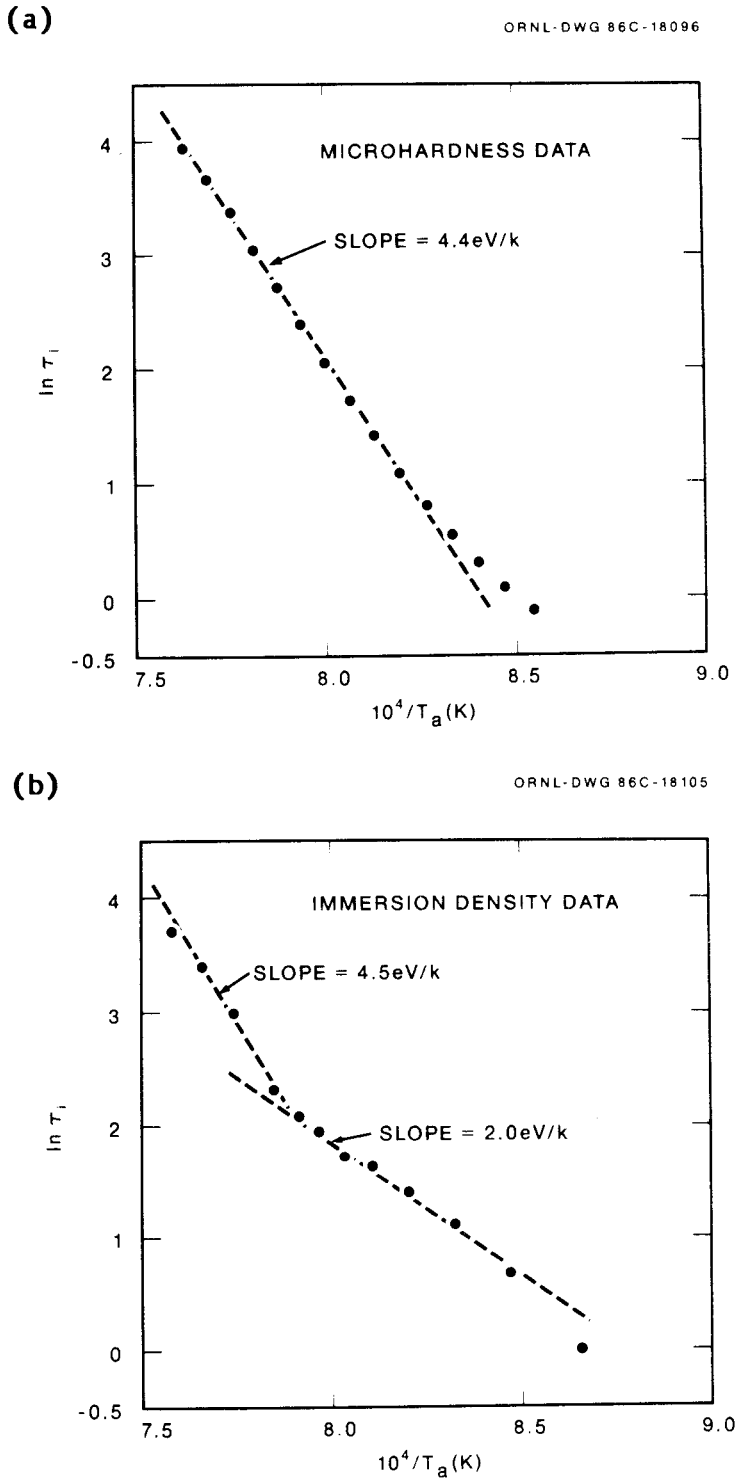

Figure 4.21. Results of Meechan-Brinkman[338] analysis of post-irradiation annealing experiment, microhardness data (a) and immersion density data (b).

of the lower temperature linear region yields an activation energy of 2.0 eV while for the higher temperature region an activation energy of 4.5 is calculated. This latter value is similar to that calculated for the recovery of the microhardness.

The activation energy of 4.3 to 4.5 eV observed in the high temperature immersion density data and the microhardness data is much too high to be a self-diffusion energy. For materials such as alloy P7, the activation energy for self-diffusion is measured to be ~2.8 to 3.0 eV.[225,226,266,267] A TEM study of the annealed specimens was conducted to verify that the voids remained and to attempt to gain some insight into the reasons for the apparent stability of the irradiation-produced microstructure. Representative micrographs from this survey are shown in Figure 4.22. The density recovery observed at short times appeared to be due to the more rapid annealing of voids near the grain boundaries and the gradual growth of a denuded zone into the grains [Figure 4.22(a)]. This growth of the grain boundary denuded zones was verified by scanning electron microscopy of specimens that had been lightly etched. Although the grain-to-grain scatter in the denuded zone widths was too great to permit quantitative analysis of the process responsible for the growth of the denuded zones, the growth was easy to observe. Representative micrographs are shown in Figure 4.23. Within the grain interiors, the void population appeared to be evolving by Ostwald ripening as predicted by the theory[335-337] and also observed by others.[320,332,333] [Figure 4.22(b,c)]. As mentioned above, there

YE-13584

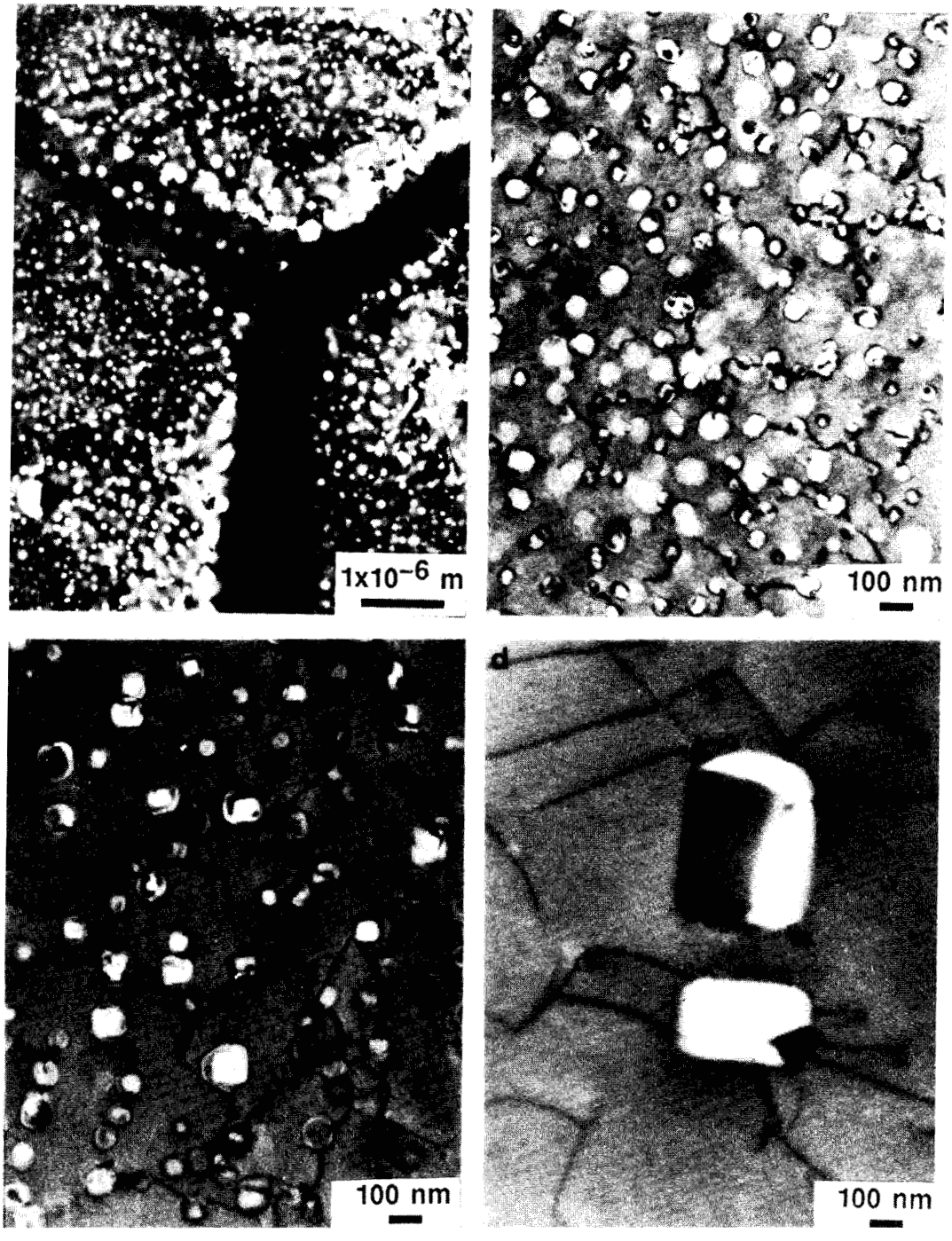

Figure 4.22. Postirradiation annealing behavior of austenitic alloy P7 irradiated in the EBR-II to 12.5 dpa at 650°C. Grain boundary denuded zones after two hour anneal at 800°C (a), evolution of the void and dislcoation structure within the grains after two hours (b) and ten hours (c) at 950°C, and after 210 hours at 900°C.

YE-13588

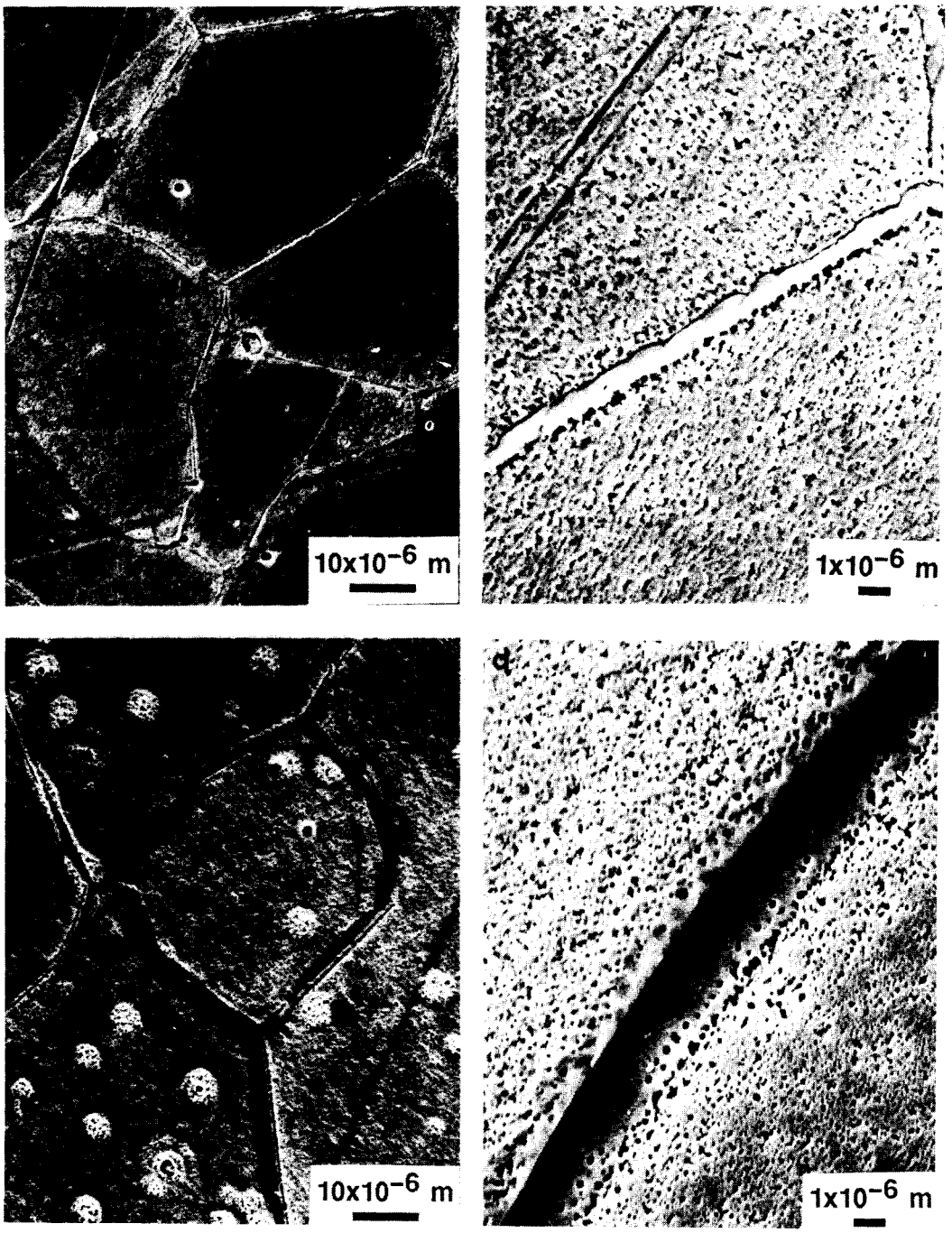

Figure 4.23. Scanning electron micrographs of grain boundary denuded zones after postirradiation annealing of austenitic alloy P7 for one hour at 600°C (a,b) and 900°C (c,d).

is little driving force for large voids to shrink. After about 20 hours at 900°C further recovery was very slow [Figure 4.20(b)]. Even after 210 hours at 900°C [Figure 4.22(d)], a stable void population with a density of about 1×10^{18} m^{-3} and an average radius of 100 nm remained. Larger voids with radii up to 300 nm were also formed, apparently by coalescence. This void population accounts for the ~2% swelling that was measured by immersion density for this condition.

The high apparent activation energy measured here seems to reflect the fact that the recovery of the voids and dislocations was the result of several interacting processes. These processes include fairly rapid void annealing near the grain boundaries, the growth of a void denuded zone into the grain interior and void coarsening within the grains. To the degree that the immersion density data are reliable, Figure 4.21(b) also verifies that more than one mechanism is responsible for the observed behavior. Some correlated annealing behavior of the voids and dislocations may also be partially responsible for the high apparent activation energy. Figure 4.22 indicates that many of the voids were interconnected by dislocation segments. Evidence of dislocation-void attachment was also seen in the as-irradiated material. Porter et al.[333] have reported that they observed stable void-dislocation arrays after postirradiation annealing of type-304L stainless steel. They observed these arrays after annealing for one hour at temperatures as high as 1054°C. This

indicates that such a defect geometry is highly resistant to recovery. One possible explanation for this stability is that the dislocations are not free to climb as a result of being pinned by the voids. This prevents them from absorbing excess vacancies. This leads to nearly equal vacancy absorption and emission rates for both the voids and the dislocations. This complexity further limits the ability of any simple kinetic analysis of this experiment to yield conclusive results.

CHAPTER 5

SUMMARY AND CONCLUSIONS

An effort has been made to discuss in some detail the implications of the present work as the results were presented in Chapters 3 and 4. Therefore, this final chapter will primarily present a summary of the work along with some further discussion where it is appropriate. Some unanswered questions which this work has raised will be described and further work that could help resolve these questions will be proposed.

5.1 Summary of Theoretical Work

Several theoretical models were presented and discussed in Chapter 3. These models were built on the foundation of the chemical rate theory description of microstructural evolution. Section 3.4 in Chapter 3 provides a detailed summary of the theoretical work so only the key results will be mentioned here.

First, because of the important role that helium is thought to play in promoting void formation, the use of a hard-sphere equation-of-state (HSEOS) for helium was adopted here.[233] The use of this HSEOS eliminates the ability to obtain closed-form mathematical solutions for the bubble radius and the critical bubble parameters. In order to be able to implement the HSEOS in computer programs without excessive iterative calculations, analytical solutions for these bubble parameters were developed that preserve the physics of

the HSEOS. This was confirmed by a comparison of results generated using the exact iterative method and the approximate analytical solutions.

Next, a direct comparison of the relative importance of two alternate paths of void formation was carried out. These two paths were: (1) gas-aided, classical void nucleation due to stochastic fluctuations in the vacancy cluster population, and (2) bubble growth driven by helium accumulation. This work concluded that stochastic nucleation was not a significant void formation mechanism for damage rates and temperatures typical of either fast fission reactors or DT fusion reactors. It demonstrated that the mechanism of gas-driven bubble growth to a critical size could account for void formation under these conditions while using realistic physical parameters in the calculations. A key assumption in these latter calculations is that sufficient vacancies are available to allow the bubble to grow as gas is added. This condition is easily met under irradiation-induced vacancy supersaturations. In addition, the annealing of helium-implanted materials discussed above indicates that highly pressurized helium-vacancy clusters can create vacancies if necessary.

Two primary models of microstructural evolution were developed here. The first was a cavity evolution model in which the other point defect sinks were treated in a simple time-independent, parametric manner. Consistent with the finding of the nucleation work just mentioned, void formation in this model was treated as the

result of gas-driven bubble growth to a critical size. The swelling data from the RS-1 experiment in the EBR-II was used to provide calibration points for the model. Using physically realistic model parameters, this relatively simple model was able to predict the dose and temperature dependence of swelling in 20% cold-worked type-316 stainless steel observed in this fairly large data base. This model was then used in a predictive fashion to explore the potential swelling behavior of this same material in an irradiation environment typical of a DT fusion reactor first wall. The degree to which the higher He/dpa ratio (~30 times the EBR-II value) will affect swelling has been the subject of some controversy.[54,288,290]

The significant prediction was that swelling may not be a monotonic function of the He/dpa ratio and that peak swelling may occur for He/dpa ratios of 5 to 10 appm He/dpa. This result follows from the effect of higher helium generation rates on the cavity density. Starting from fast reactor irradiation conditions as a reference point, for modest increases in the He/dpa ratio the cavity density increases only slightly. This higher helium generation rate leads to a reduced incubation time and, in some cases, a slightly higher swelling rate. For very high He/dpa ratios the cavity density can increase to such a degree that the available helium must partition to so many sites that few cavities reach the critical size. This extends the swelling incubation time and can also lower the swelling rate due to enhanced point defect recombination. Hence, swelling is

maximum at an intermediate He/dpa ratio. This predictive work led to the development of a set of model-based swelling design equations for 20% cold-worked type-316 stainless steel in a DT fusion reactor wall.

Recent experimental results appear to have confirmed this prediction. An experiment was conducted in the ORR in which the neutron spectrum was tailored to produce a He/dpa ratio of about 10 appm He/dpa in type-316 stainless steels. Slightly over 1% swelling was observed in a specimen of 25% cold-worked, titanium-modified type-316 stainless steel irradiated to only 12 dpa (ref. 288). Such a level of swelling would not have been observed in a conventional fast reactor (~0.5 appm He/dpa) or mixed-spectrum reactor (~70 appm He/dpa) until a dose greater than 75 dpa had been achieved.[183] Additional corroboration of the mechanisms responsible for this swelling peak is provided by an experiment that involved sequential irradiation of the same specimens of type-316 stainless steel in first the HFIR and then the FFTF.[230] The initial irradiation in the HFIR was to a dose of 22 dpa and 1475 appm He. For the 20% cold-worked n-lot material the swelling was less than 0.5% at both 500 and 600°C. Following an additional 35 dpa irradiation in the FFTF the swelling was 0.5% at 600°C and 1.8% at 500°C. The expected swelling of this material for a 60 dpa irradiation in the FFTF only is around 10%.[230] The fact that much lower swelling was observed is consistent with swelling suppression due to the formation of a high bubble density during the HFIR phase of the irradiation.

The second major component of the theoretical work was the development of a more comprehensive model of microstructural evolution. This model included the cavity evolution model just discussed but also incorporated models for the explicit dose and temperature dependence of both the dislocation network and Frank faulted dislocation loops. One crucial aspect of the dislocation loop evolution model was a scheme for dividing the loop size space into two distinct regions to reduce the number of equations necessary to describe the loop population. Different physical descriptions of loop evolution were used in the two regions and they were joined in a self-consistent manner. This scheme preserved the essential features of the loop distribution while reducing the required number of equations from $>10^4$ to about 20. Good agreement was observed between the predictions of the comprehensive model and fast reactor swelling and dislocation data over a broad range of irradiation temperatures and doses. A high degree of coupling between the evolution of the various microstructural features was observed. The success of the rate-theory in this work provides a measure of its potency as an analytical tool.

The results of extensive parametric evaluations with the comprehensive model emphasized the major role of microstructural sink balances and point defect partitioning in determining microstructural evolution under irradiation. The results of some of these sensitivity studies are summarized in Figures 5.1 through 5.4. The sensitivity of the incubation time (dose to 1% swelling), the peak swelling rate, the network dislocation density at 100 dpa, and the

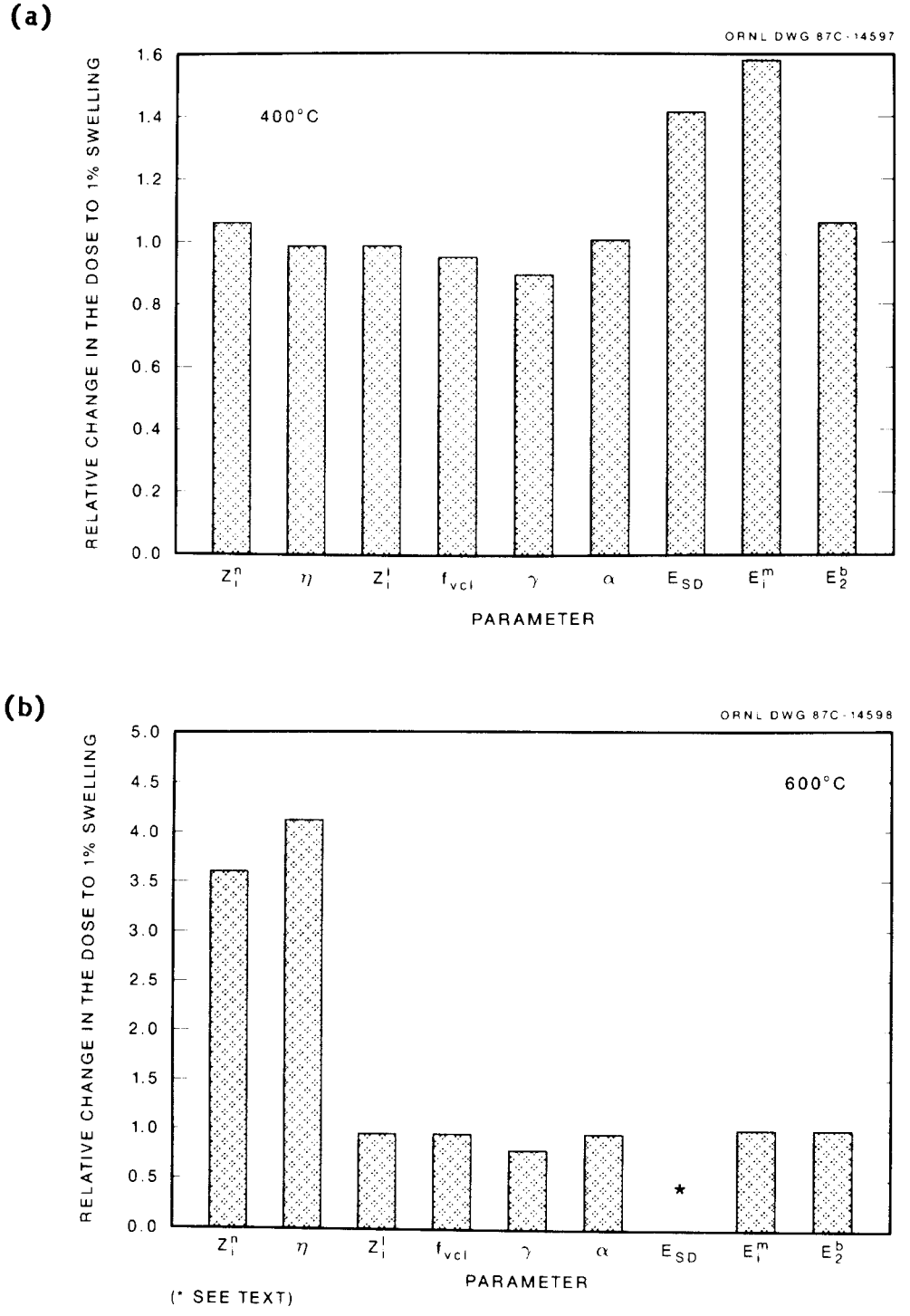

Figure 5.1. Relative influence of several parameters on the dose to 1% swelling predicted by the comprehensive model at 400 (a) and 600°C (b).

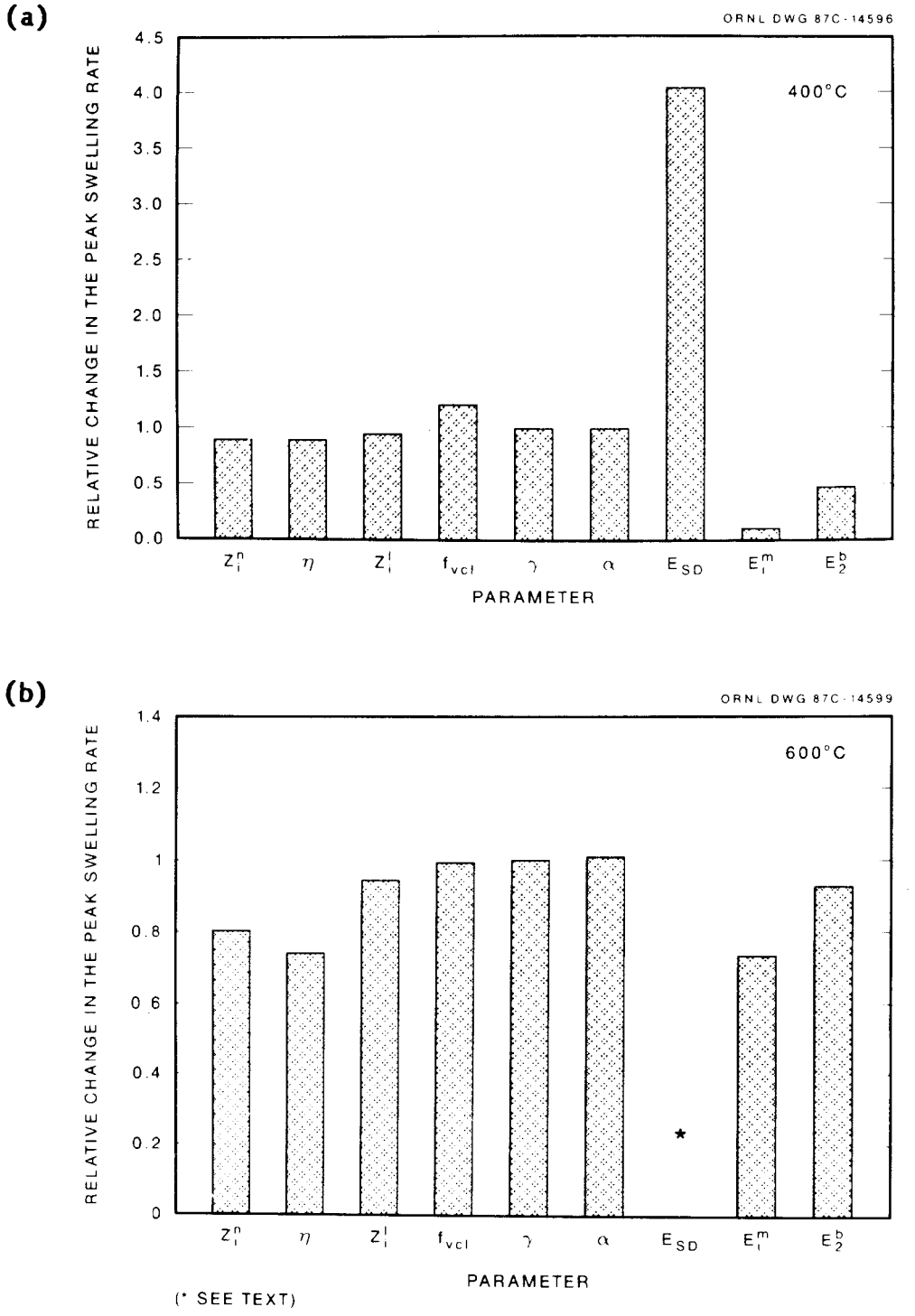

Figure 5.2. Relative influence of several parameters on the peak swelling rate predicted by the comprehensive model at 400 (a) and 600°C (b).

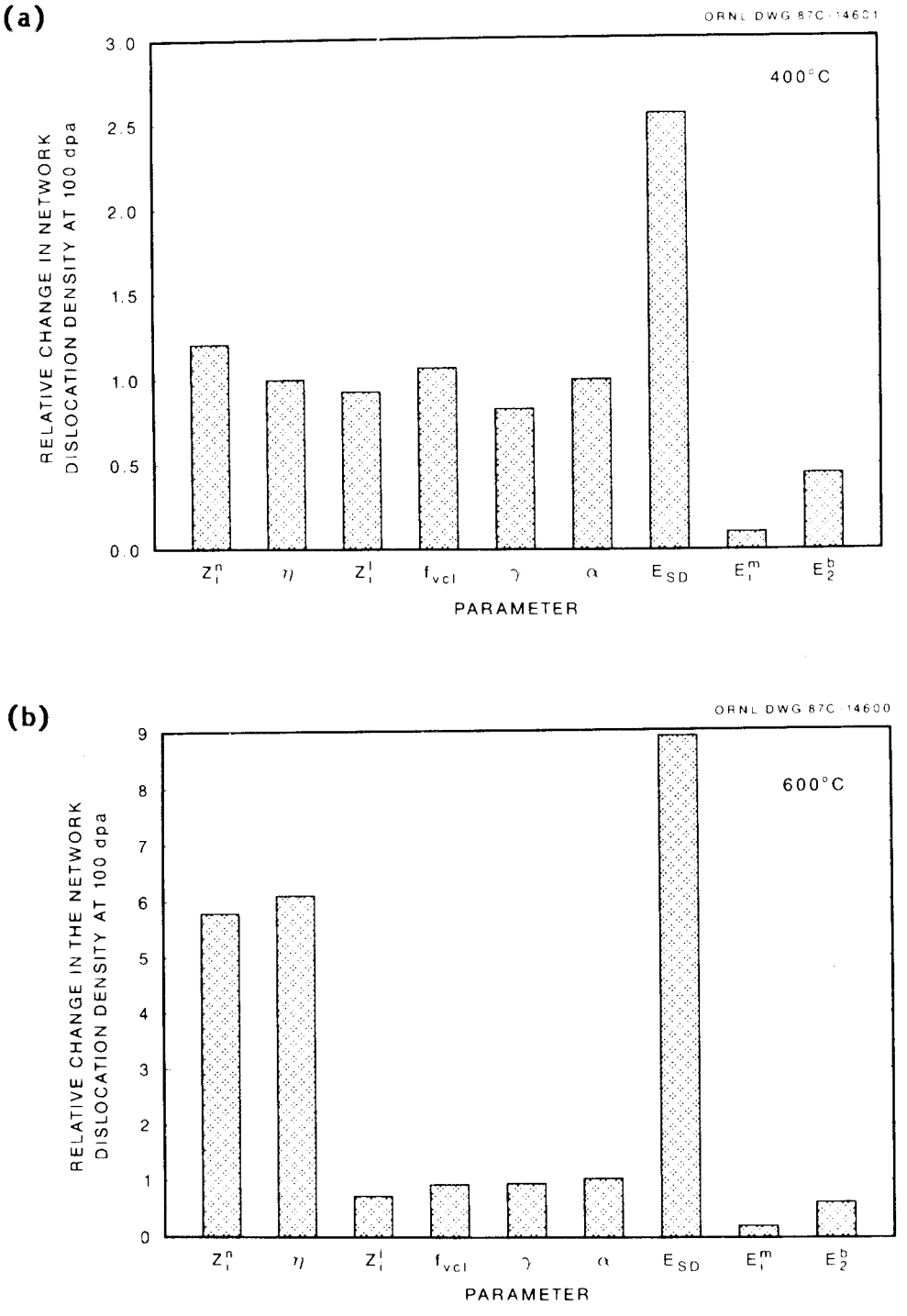

Figure 5.3. Relative influence of several parameters on the network dislocation density at 100 dpa predicted by the comprehensive model at 400 (a) and 600°C (b).

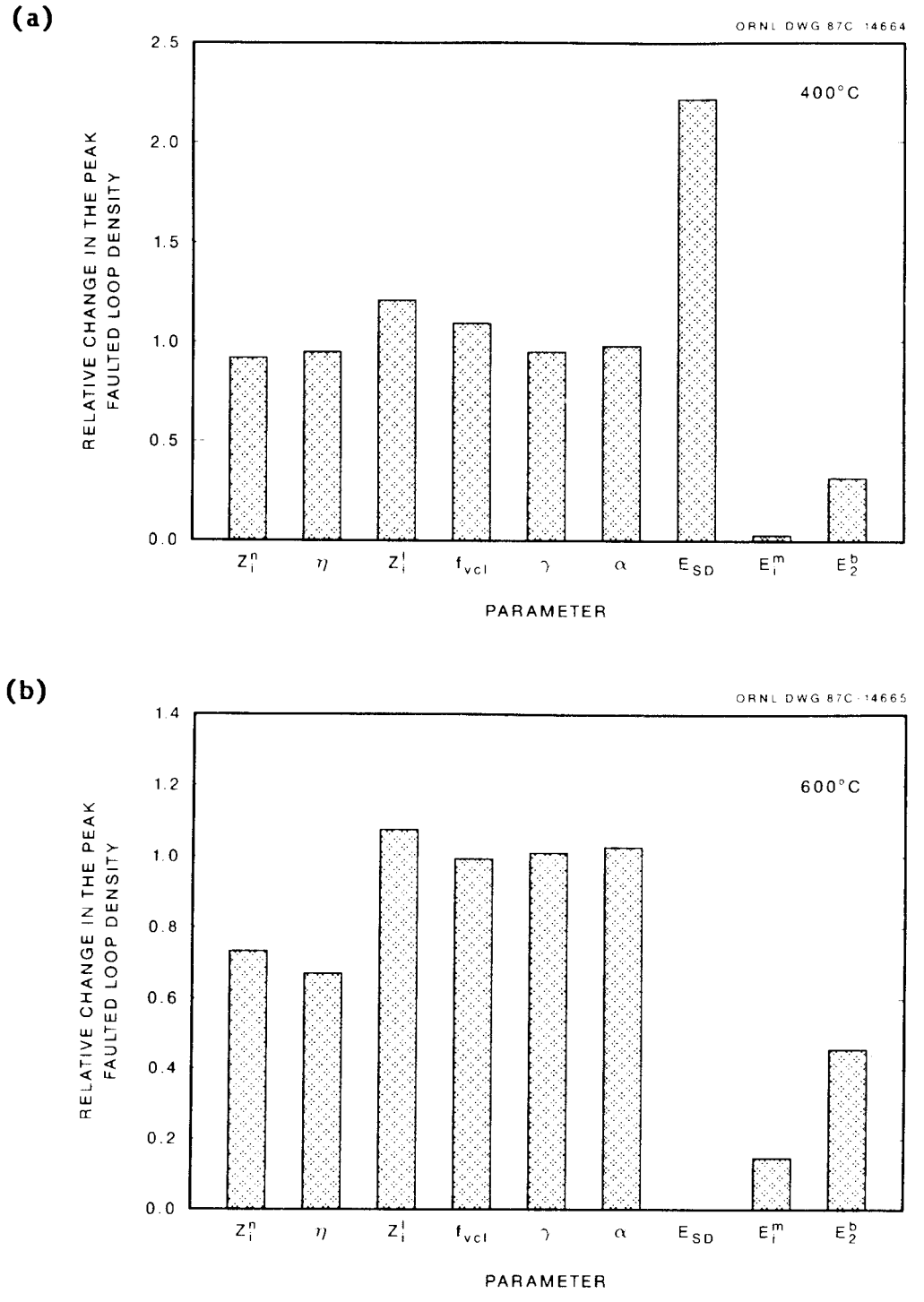

Figure 5.4. Relative influence of several parameters on the peak faulted loop density predicted by the comprehensive model at 400 (a) and 600°C (b).

peak faulted loop density to several key parameters is shown. The parameters are:

Z_i^n, the network dislocation/interstitial bias;

η, the cascade efficiency;

Z_i^ℓ, the faulted loop/interstitial bias;

f_{vcl}, the fraction of vacancies surviving intracascade annealing that cluster;

γ, the surface free energy;

α, the bulk recombination coefficient;

E_{SD}, the activation energy for self diffusion;

E_i^m, the interstitial migration energy; and

E_2^b, the di-interstitial binding energy.

The ratios shown in these four figures were obtained by dividing the results calculated with a reduction in the indicated parameter with the same values calculated with the base parameter set from Table 3.9. The ratios reflect similar relative changes in the various parameters. These figures indicate that the parameters of most general significance are η, E_{SD}, and Z_i^n. This dependence is expected from simple theoretical relationships such as Equation (3.61). However, the results shown in Figures 5.1 through 5.4 indicate that other parameters also have temperature and dose regimes in which they are of importance. One notable example is the interstitial migration energy. Because of its influence on the faulted loop density, and through that on the network dislocation density, E_i^m is very significant at

low to intermediate temperatures. It was pointed out in Chapter 3 that simple void swelling models are not sensitive to the value of E_i^m. The comprehensive model required a value of E_i^m = 0.85 eV in order to obtain agreement with fast-reactor dislocation data. This is much greater than the pure metal value used by other workers, but it is in agreement with recent measurements of this parameter in austenitic alloys.[270,274]

The fact that the parametric sensitivity varies between the results shown at 400 and 600°C is partly due to the temperature dependence of the sink strengths, as discussed in Chapter 3. For example, the incubation time is much more sensitive to the value of the dislocation bias at 600 than at 400°C. This is a result of the fact that at 600°C the dislocations are the major point defect sink while at 400°C dislocation loops and vacancy clusters are also significant. The predicted microstructures are also more sensitive to the self-diffusion coefficient at 600°C than at 400°C. At 600°C, the swelling incubation time exceeded 200 dpa for a 0.2 eV reduction in the self-diffusion energy; hence, the fractional change is off scale for the histograms shown here. Two correlated factors are responsible for this large increase in the incubation time. First, the higher self-diffusion coefficient leads to a lower effective vacancy supersaturation [see Equation (3.3)]; this increases the critical number of gas atoms required for bubble-to-void conversion. In addition, as Figure 5.3 shows, a higher network dislocation density is

obtained with the higher self-diffusion coefficient. This further suppresses the effective supersaturation since the dislocations are the dominant sink at 600°C.

Finally, it was shown that even minor sinks, such as the subgrain structure in cold-worked material, can be important if they promote differential point defect partitioning. Because only a small fraction of the total defects generated survive, small changes in the absolute number of vacancies that survive can cause large changes in the observed swelling. Such additional sensitivity to both sink strengths and parameter variations is believed to be physically meaningful because it reflects the coordinated evolution of the individual microstructural components.

The comprehensive model was also used to predict the swelling of a DT fusion reactor first wall (10 appm He/dpa). The results corroborated the conclusions drawn from the studies with the cavity evolution model. Shorter incubation times were predicted for the higher He/dpa ratio at all temperatures from 350 to 700°C and the swelling at low temperatures was significantly enhanced. These results are significant because designs for near-term fusion devices have begun to emphasize lower operating temperatures in the belief that swelling of austenitic materials would not be a problem for doses up to 30 to 50 dpa.[6,234,303] A major conclusion of this work is that making such a decision based on fast- or mixed-spectrum reactor swelling data may be erroneous.

5.2 Summary of Experimental Results

The experimental component of this work consisted of two major parts. The first was a postirradiation annealing study that employed specimens of a model austenitic alloy that had been irradiated in the EBR-II to a dose of 12.5 dpa at 650°C. These specimens exhibited about 6% swelling. The irradiation-induced microstructure was found to be surprisingly stable. After annealing for one hour at 1042°C the swelling remained slightly in excess of 3 and 2% swelling remained even after annealing for 210 hours at 900°C. Recovery of the microstructure was also followed through the use of microhardness measurements and a similar stability was observed. The apparent activation for recovery obtained by both sets of measurements was 4.3 to 4.5 eV. This is much greater than the measured activation energy for self-diffusion in this material.

No simple explanation was found for this high activation energy. The stable array of large voids and interconnecting dislocations that were observed may in part be responsible. The voids and dislocations can recover only if the two defect types can exchange vacancies. The dislocations must absorb excess vacancies and climb. This climb is inhibited when the dislocations are pinned by voids. In addition, the voids coarsened by Ostwald ripening and coalescence, leading to a population of large voids. Voids with radii up to 300 nm were formed. Voids of this size are nearly equilibrium defects and emit vacancies at a rate similar to the dislocations. Because there is no

substantial driving force for a net vacancy exchange, both defect types remain stable. The apparent correlated evolution of the voids and dislocations during postirradiation annealing is consistent with their behavior under irradiation. The theoretical models that were developed for this work verify the importance of this coupling. In this light, it is not surprising that their behavior would also be complex during postirradiation annealing.

The second component of the experimental work was the examination and analysis of alloy P7 after irradiation in the ORR in the MFE-II experiment. This experiment involved the irradiation of solution-annealed and 20% cold-worked P7 at 350, 550 and 600°C. The irradiation dose was 4.7 dpa with 65 appm He generated by neutron-induced transmutation reactions. Some of the specimens were preinjected with 10 to 40 appm He and subjected to post-helium-implantation anneals at temperatures between 600 and 900°C prior to the irradiation. In order to provide unirradiated control specimens for the MFE-II experiment, additional TEM disks were implanted with helium to similar levels and similarly aged. These control specimens were also examined by TEM in order to characterize the preirradiation microstructure.

The microstructure of the as-helium-implanted material was comprised of a high density of "black-dot" defect clusters. Under thermal annealing this evolved to produce two primary defects. For annealing temperatures between 600 and 750°C a population of Frank faulted loops was formed. This population was observed to grow and

coarsen with temperature. At 800°C and above, no loops were observed. Helium bubbles became visible after annealing at 700°C. The average bubble radius increased with an approximately constant density for temperatures up to 800°C. Above 800°C the distribution coarsened. The calculated helium content of the visible bubbles accounts for about one-third of the implanted helium after 700°C annealing, two-thirds after the 750°C anneal, and essentially all the helium after annealing at 800 to 900°C. The interstitial content of the faulted loops appeared to increase during the lower temperature anneals. Interstitial loop growth may be driven by the demand of small, overpressurized helium-vacancy clusters for additional vacancies. The coupling of the evolution of the bubbles and loops during thermal annealing is illustrated by their sensitivity to the level of helium implantation. Increasing this level from ~40 to 65 appm resulted in the stability of Frank loops under annealing up to 850°C. A lower than expected bubble density also resulted, in part because of the formation of larger than expected bubbles that were found decorating these loops. The evolution of the faulted loop and bubble microstructure observed here is consistent with and supplements similar work by others.[48,146,157-159] In particular, Maziasz[48] has also noted the relationship between the growth of apparently overpressurized bubbles and Frank faulted loop growth.

The overall behavior of the specimens irradiated in the MFE-II experiment was similar at all three temperatures. It was not possible to determine the detailed influence of the various preirradiation

heat treatments because of the low total damage level. The comparisons were particularly limited for the 350 and 600°C irradiations because of the longer swelling incubation time at these temperatures. For example, at 350°C cavities were visible only for the solution annealed specimen that had been implanted with 37 appm He and aged at 800°C prior to irradiation. This cavity distribution was little changed from the as-aged condition. Similarly, at 600°C cavities were observed in only two solution-annealed specimens. The first had been implanted with 32 appm He and aged at 800°C and the second was irradiated with no helium preinjection. In both of these specimens the cavities appeared to be helium bubbles. The lack of void growth at 350 and 600°C is consistent with the theoretical predictions of the model developed here. At 350°C, the model predicts a small critical bubble radius, but also a very slow void growth rate. At 600°C, the model predicts a critical bubble radius that is about eight times the observed average bubble radius so that no voids have formed by 4.7 dpa. At both 350 and 600°C either initial cold-working or helium preinjection without a subsequent anneal led to the suppression of visible cavity formation.

For this low dose, the maximum swelling temperature for P7 appears to be near 550°C. Bloom and Wolfer found a similar value for specimens irradiated in the EBR-II.[305] Voids were observed in solution-annealed and 20% cold-worked specimens that had received no helium preinjection and in a specimen that had been implanted with

42 appm He and aged at 750°C. This latter specimen exhibited voids only along a fairly narrow band near the grain boundaries. This corroborates the observations of Leitnaker et al.[326] and Horsewell and Singh[301] that voids form first and appear to grow fastest in a region that is near, but not immediately adjacent to grain boundaries. This enhanced swelling near grain boundaries may also explain why Bloom et al. observed much higher swelling in a very fine-grained type-316 stainless steel than in solution-annealed material.[340] The cavity distributions in several other helium-implanted-and-aged specimens irradiated at 550°C showed little change as a result of the irradiation. Helium preinjection without subsequent heat treatment resulted in no visible cavity formation after 4.7 dpa irradiation at 550°C. This result is the same as observed at 350 and 600°C and lends support to the suggestion by Packan and Farrell[193] that cold preimplantation of helium not be pursued further as a method of simulating high He/dpa ratios.

A comparison of the solution-annealed and 20% cold-worked specimens irradiated at 550°C indicates a somewhat shorter incubation time for the solution annealed material. The measured cavity volume fractions are 0.19% in the annealed specimen and 0.05% in the cold-worked specimen. It is difficult to conclude much from such low levels of swelling. In fact, Brager and Garner concluded from their examination of similar specimens that cold-work has essentially no effect on the swelling of P7.[322] However, the shape of the cavity distributions

indicated that the cold-worked specimen was still in the incubation regime while the solution annealed specimen appeared to be in a more advanced stage of microstructural evolution. Specifically, the solution annealed specimen exhibited a bimodal cavity distribution with a critical cavity radius of about 4.5 nm and the cold-worked specimen an approximately exponential distribution. In addition, the cavity density in the cold-worked specimen was five times that in the solution-annealed. This is believed to be the result of the high initial dislocation density providing many preferential nucleation sites by acting as traps for helium. Similar behavior was also reported for a commercial type-316 stainless steel irradiated in the HFIR.[54] This result emphasizes the important role of helium in void formation.

Finally, a significant new observation was that of a high density (10^{19} to 10^{20} m^{-3}) of stacking fault tetrahedra in an austenitic stainless steel that was neutron-irradiated at elevated temperatures. These SFTs had an average edge length of about 20 nm and were observed in a variety of specimens. This observation is consistent with the low stacking fault energy of the austenitic stainless steels and lends credibility to theoretical calculations that indicate this defect should be stable in these materials.

5.3 Unresolved Issues and Future Directions

A major simplification in the models developed here is their limited treatment of the effects of solute segregation and precipitation. Both of these phenomena are known to be significant factors

that influence microstructural evolution. Some of the influences of solute depletion can be thought of as being approximately accounted for in the theory by the use of effective diffusion and bias parameters that represent essentially time averages of the actual parameters. The success of the present theory indicates that the major role of what has been termed microchemical evolution[221] may be to influence these parameters as opposed to being a controlling mechanism in void swelling. The details of precipitation under irradiation are extremely complex[255] and worthy of further theoretical investigation. Several ways in which precipitates can affect void swelling were mentioned in Chapter 3; only one has been investigated here. One potentially useful extension of the present work and that done by others[176,177,253] would be to perform a detailed comparison of the relative importance of these various mechanisms.

Further development of the comprehensive model is required to enhance its usefulness for low temperature irradiation simulations. The predicted faulted loop density is too low below about 400°C. This seems to indicate that the model does not adequately balance the relative contributions of the dislocation network and the faulted loops at low temperatures. The problem appears to be one of loop stability rather than one of loop formation. The model for the evolution of the dislocation network under irradiation should also be refined. The equations and parameters in the thermally activated components of this model do not currently reflect an appropriate

influence of irradiation. For example, under irradiation, the thermal dislocation climb velocity should be replaced by the bias-driven climb velocity and the thermal source density should be dependent on the evolving microstructure. In order to maintain the calibration in the absence of irradiation, the terms in the present model need to be limiting cases of any new formulation. A further refinement of the comprehensive model would be to include an explicit clustering calculation for vacancies and helium to provide an input to the cavity evolution component of the model. This calculation could replace the current temperature-dependent cluster density that is treated as an input parameter.

Both the theoretical and the experimental components of this work have indicated that grain boundaries and hence the grain size of materials may significantly influence microstructural evolution under irradiation. Work by others[301,302,326,340] also corroborates this conclusion. Further investigation of the dependence of swelling on grain size may suggest ways to help extend the swelling incubation time. The comprehensive model developed here provides a theoretical tool for this investigation. The use of specific preirradiation thermomechanical treatments to tailor the grain size would permit experiments to be carried out to examine this variable. Finally, additional investigation of the alternate mathematical formulations of the point defect sink strengths is warranted. To date the comprehensive model has been used to examine the influence of assuming surface-limited or diffusion-limited kinetics on the faulted loop

evolution and the effect of multiple sink strength correction terms on the nominal model predictions. More detailed analysis of various point defect sink strength formulations could shed further light on their range of applicability. It is only with a comprehensive model that such determinations can be made.

The model's predictions of swelling at the DT fusion He/dpa ratio are dependent on the assumed scaling of the cavity density with the He/dpa ratio. Guidance for the present work was provided by charged particle studies in which the He/dpa ratio could be varied, and to a lesser degree by comparisons of cavity densities from experiments in the EBR-II and HFIR. In order to verify this scaling, an experiment has been planned for irradiation in the HFIR in which the fraction of the various nickel isotopes will be tailored to yield several different He/dpa ratios in a single reactor environment. This experiment will also provide a direct test of the model's predictions for fusion because the He/dpa ratio in one of the alloys in this experiment is 12 appm He/dpa.

REFERENCES

1. Energy in Transition: 1985-2010, Committee on Nuclear and Alternative Energy Systems, National Research Council, National Academy of Sciences, Washington, DC, 1979.

2. "Design, Construction and Operating Experience of Demonstration LMFBR's," Proceedings of International Symposium, Bologna, Italy, April 10–14, 1978, IAEA-SM-225/79, IAEA, Vienna, 1978.

3. B. A. Chin, R. J. Neuhold and J. L. Straalsund, Nucl. Tech. 57 (1982) 426–435.

4. Fusion Reactor Materials Program Plan: Section I, Alloy Development for Irradiation Performance, DOE/ET-0032/1, U.S. DOE, Office of Fusion Energy, Washington, DC, July, 1978.

5. R. E. Gold, E. E. Bloom, F. W. Clinard, D. L. Smith, R. D. Stephenson and W. G. Wolfer. Nucl. Tech./Fusion 1 (1978) 169–237.

6. M. A. Abdou et al., Blanket Comparison and Selection Study, ANL/FPP-83-1, Argonne National Laboratory, October 1983.

7. D. R. Olander, Fundamental Aspects of Nuclear Reactor Fuel Elements, TIC-26711-P1, U.S. ERDA, Washington, DC, 1976.

8. F. F. Chen, Introduction to Plasma Physics, Plenum Press, New York, 1974.

9. C. C. Baker, G. A. Carlson and R. A. Krakowski, Nucl. Tech./Fusion 1 (1981) 5-78.

10. CRC Handbook of Radiation Protection and Measurement, Section A, Vol. 1, CRC Press, West Palm Beach, 1978.

11. J. B. Marion and F. C. Young, Nuclear Reaction Analysis, North Holland Publishers, Amsterdam, 1968.

12. G. Carter and J. Collington, Ion Bombardment of Solids, American Elsevier Publishing, New York, 1968.

13. G. L. Kulcinski, R. G. Brown, R. G. Lott and P. A. Sanger, Nucl. Tech. 22 (1974) 20-35.

14. Technical Assessment of the Critical Issues and Problem Areas in the Plasma Materials Interaction Field, R. W. Conn, W. B. Gauster, D. Hiefetz, E. Marmar and K. L. Wilson, Eds., PPG-765, University of California, Los Angeles, 1984.

15. M. Kaminski, IEEE Trans., Nucl. Sci. NS-18 (1971) 208-217.

16. M. W. Thompson, Defects and Radiation Damage in Metals, Cambridge Press, Cambridge, 1969.

17. D. S. Billington and J. H. Crawford, Radiation Damage in Metals, Princeton Press, Princeton, 1961.

18. See for example the series of meetings sponsored by the American Society for Testing and Materials and published as Special Technical Publications: ASTM STP 484, 529, 570, 611, 683, 725, 782 and 870 or the series of Topical Meetings on Fusion Reactor Materials published by the Journal of Nuclear Materials as Volumes 85 & 86, 103 & 104, 122 & 123, 133 & 134, and 141-143.

19. R. D. Evans, The Atomic Nucleus, McGraw-Hill, New York, 1955.

20. D. G. Doran, Fundamental Aspects of Displacement Production in Irradiated Metals, HEDL-SA-1012, Hanford Engineering Development Laboratory, 1975.

21. L. K. Mansur, "Mechanisms and Kinetics of Radiation Effects in Metals and Alloys," Kinetics of Nonhomogeneous Processes, Wiley-Interscience, New York, to be published.

22. M. J. Makin, S. N. Buckley and G. P. Walters, J. Nucl. Mater. 68 (1977) 161-167.

23. D. G. Doran, R. L. Simons and W. N. McElroy, "Properties of Reactor Structural Alloys after Neutron or Particle Irradiation," Conf. Proc., ASTM STP 570, ASTM, Philadelphia, 1974, pp. 290-310.

24. M. T. Robinson, "Fundamental Aspects of Radiation Damage in Metals," Proc. of Int. Conf., CONF-751006, Vol. I, U.S. ERDA, Washington, DC, 1975, pp. 1-20.

25. D. G. Doran and J. O. Schiffgens, "Correlation of Neutron and Charged Particle Damage," Workshop Proc., CONF-760673, U.S. ERDA, Washington, DC, 1976, pp. 3-20.

26. J. I. Bramman, E. W. Etherington, R. S. Nelson and M. J. Norgett, "Irradiation Embrittlement and Creep in Fuel Cladding and Core Components," Conf. Proc., BNES, London, 1972, pp. 27-31.

27. G. R. Odette and D. G. Doran, "The Technology of Controlled Nuclear Fusion," Proc. of the Second Topical Meeting, CONF-760935, Vol. IV, U.S. ERDA, Washington, DC, 1976, pp. 1485-1500.

28. G. H. Kinchin and R. S. Pease, Rep. Prog. Phys. 18 (1955) 1-51.

29. J. Lindhard, V. Nielson, M. Scharff and P. V. Thomsen, Kgl. Dan. Vidensk. Selsk. Mat.-Fys. Meld. 33 (1963) 1-42.

30. J. R. Beeler, "Radiation-Induced Voids in Metals," Proc. of Int. Conf., CONF-710601, U.S. AEC, Washington, DC, 1972, pp. 684-738.

31. I. M. Torrens and M. T. Robinson, "Radiation-Induced Voids in Metals," Proc. of Int. Conf., CONF-710601, U.S. AEC, Washington, DC, 1972, pp. 739-756.

32. J. B. Roberto and J. Narayan, "Fundamental Aspects of Radiation Damage in Metals," Proc. of Int. Conf., CONF-751006, Vol. I, U.S. ERDA, Washington, DC, 1975, pp. 120-126.

33. D. N. Seidman, "Radiation Damage in Metals," ASM Seminar, ASM, Metals Park, OH, 1975, pp. 28-57.

34. H. L. Heinisch and F. M. Mann, J. Nucl. Mater. 122 & 123 (1984) 1023-1027.

35. R.M.J. Cotterill, "Lattice Defects in Quenched Metals," Proc. of Int. Conf., Academic Press, New York, 1965, pp. 97-157.

36. D. Kuhlmann-Wilsdorf, "Lattice Defects in Quenched Metals," Proc. of Int. Conf., Academic Press, New York, 1965, pp. 269-313.

37. J. A. Sigler and D. Kuhlmann-Wilsdorf, "The Nature of Small Defect Clusters," Proc. of Int. Conf., AERE-R5269, AERE Harwell, 1966, pp. 125-143.

38. S. J. Zinkle, L. E. Seitzman and W. G. Wolfer, Phil. Mag. A. 55 (1987) 111-125.

39. R. A. Johnson, Phys. Rev. 152 (1966) 629-634.

40. R. A. Johnson, J. Nucl. Mater. 83 (1979) 147-159.

41. K. W. Ingle, R. C. Perrin and H. R. Schober, J. Phys. F.: Metal Phys. 11 (1981) 1161–1173.

42. A. F. Rowcliffe and R. B. Nicholson, Acta Met. 20 (1972) 143–156.

43. A. Azarian, M. D. Conhabelo and J. Leteurtre, Scripta Met. 9 (1975) 185–192.

44. F. Artigue, M. Condat and M. Fayard, Scripta Met. 11 (1977) 623–626.

45. O. Vingsbro, Acta Met. 15 (1967) 615–621.

46. S. Kojima, Y. Sano, T. Yoshiie, N. Yoshida and M. Kiritani, "Conversion of Stacking Fault Tetrahedra to Voids in Electron Irradiated Fe-Cr-Ni," Proc. Second Int. Conf. on Fusion Reactor Materials, Chicago, April 14–17, 1986, to be published in Journal of Nuclear Materials.

47. R. L. Sindelar, A Comparison of the Response of 316SS and the P7 Alloy to Heavy Ion Irradiation, UWFDM-637, University of Wisconsin, Madison, 1985.

48. P. J. Maziasz, Effect of Helium Content on Microstructural Development in Type 316 Stainless Steel Under Neutron Irradiation, ORNL-6121, Oak Ridge National Laboratory, 1985.

49. G. L. Kulcinski, "Radiation Effects and Tritium Technology For Fusion Reactors," Proc. of Int. Conf., CONF-750989, Vol. I, U.S. ERDA, Washington, DC, 1976, pp. 17-72.

50. R. L. Simons, "Radiation Effects On Structural Materials: Ninth Conf.," ASTM STP 683, ASTM, Philadelphia, 1978, pp. 365-379.

51. T. A. Gabriel, B. L. Bishop and F. W. Wiffen, Nucl. Tech. 38 (1978) 427-433.

52. F. A. Mann, Transmutation of Alloys in MFE Facilities as Calculated by REAC, HEDL-TME 81-37, Hanford Engineering Development Laboratory, 1982.

53. J. F. Bates, F. A. Garner and F. N. Mann, J. Nucl. Mater. 104 (1981) 999-1003.

54. G. R. Odette, P. J. Maziasz and J. A. Spitznagel, J. Nucl. Mater. 103&104 (1981) 1289-1303.

55. G. L. Kulcinski, D. G. Doran and M. A. Abdou, "Properties of Reactor Structural Alloys after Neutron or Particle Irradiation," Conf. Proc., ASTM STP 570, ASTM, Philadelphia, 1974, pp. 329-351.

56. D. J. Reed, Rad. Effects 31 (1977) 129-177.

57. K. Farrell, Rad. Effects 53 (1980) 175-194.

58. W. N. McElroy and H. Farrar, "Radiation Induced Voids in Metals," Proc. of Int. Conf., CONF-710601, U.S. AEC, Washington, DC, 1972, pp. 187-228.

59. D. B. Bullen, G. L. Kulcinski and R. A. Dodd, J. Nucl. Mater. 133&134 (1985) 455–458.

60. R. H. Jones, J. Nucl. Mater. 141&143 (1986) 468–475.

61. N. H. Packan and K. Farrell, J. Nucl. Mater. 85&86 (1979) 677–681.

62. J. Bardeen and C. Herring, "Imperfections in Nearly Perfect Crystals," Symp. Proc., John Wiley and Sons, New York, 1952, pp. 261–288.

63. J. P. Hirth and J. Lothe, Theory of Dislocations, McGraw-Hill, New York, 1968.

64. C. R. Barrett, W. D. Nix and A. S. Tetelman, The Principles of Engineering Materials, Prentice-Hall, Englewood Cliffs, N.J., 1973.

65. G. E. Dieter, Mechanical Metallurgy, McGraw-Hill, New York, 1976.

66. R. W. Cahn, Physical Metallurgy, North-Holland, Amsterdam, 1970.

67. P. J. Maziasz, Alloy Development for Irradiation Performance: Quarterly Progress Report, DOE/ER-0045-3, U.S. DOE Office of Fusion Energy, Washington, DC, October 1980, pp. 75-129.

68. T. M. Williams, "Effects of Irradiation on Materials: Eleventh Conf.," ASTM STP 782, ASTM, Philadelphia, 1982, pp. 166-185.

69. P. T. Heald, Phil. Mag. 3 (1975) 551-558.

70. W. G. Wolfer and M. Ashkin, J. Appl. Phys. 46 (1975) 547–557 and erratum, J. Appl. Phys. 46 (1975) 4108.

71. W. G. Wolfer and M. Ashkin, J. Appl. Phys. 47 (1976) 791–800.

72. W. A. Coghlan and M. H. Yoo, "Dislocation Modeling of Physical Systems," Proc. of Int. Conf., Pergamon Press, New York, 1980, pp. 152–157.

73. F. F. Nichols and Y. Y. Liu, "Effects of Radiation on Materials: Tenth Conf.," ASTM STP 725, ASTM, Philadelphia, 1981, pp. 145-165.

74. L. K. Mansur, Nucl. Tech. 40 (1978) 5–34.

75. R. Bullough and M. R. Hayns, Sm. Archives, Noordhoof International Publishing, The Netherlands 3 (1978) pp. 73-106.

76. G. R. Odette, J. Nucl. Mater. 85&86 (1979) 533-545.

77. H. R. Brager, F. A. Garner, E. R. Gilbert, J. E. Flinn and W. G. Wolfer, "Radiation Effects in Breeder Reactor Structural Materials," Proc. of Int. Conf., AIME, New York, 1977, pp. 727-755.

78. H. R. Brager and J. L. Straalsund, J. Nucl. Mater. 46 (1973) 134–158.

79. K. C. Russell, Acta Met. 19 (1971) 753–758.

80. J. L. Katz and H. Wiedersich, "Radiation-Induced Voids in Metals," Proc. of Int. Conf., CONF-710601, U.S. AEC, Washington, DC, 1972, pp. 825-839.

81. W. G. Wolfer and A. Si-Ahmed, Phil. Mag. A46 (1982) 723–736.

82. C. A. Parker and K. C. Russell, "Effects of Irradiation on Materials: Eleventh Conf.," ASTM STP 782, ASTM, Philadelphia, 1982, pp. 1042–1053.

83. K. C. Russell, Acta Met. 26 (1978) 1615–1630.

84. W. G. Wolfer, L. K. Mansur and J. A. Sprague, "Radiation Effects In Breeder Reactor Structural Materials," Proc. of Int. Conf., AIME, New York, 1977, pp. 841-864.

85. A. Si-Ahmed and W. G. Wolfer, "Effects of Irradiation on Materials: Eleventh Conf.," ASTM STP 782, ASTM, Philadelphia, 1982, pp. 1008-1022.

86. R. L. Sindelar, R. A. Dodd and G. L. Kulcinski, "Effects of Radiation on Materials: Twelfth Conf.," ASTM STP 870, ASTM, Philadelphia, 1985, pp. 330–343.

87. C. A. Parker and K. C. Russell, J. Nucl. Mater. 119 (1983) 82–94.

88. N. M. Ghoniem, S. Sharafat and L. K. Mansur, "Point Defects and Defect Interactions in Metals," Proc. of Int. Conf., University of Tokyo Press, Tokyo, 1982, pp. 865–916.

89. C. F. Melius, W. D. Wilson and C. L. Bisson, Rad. Effects 53 (1980) 111–120.

90. N. H. Packan and D. N. Braski, J. Nucl. Mater. 34 (1970) 307–314.

91. P. J. Barton, B. L. Eyre and D. A. Stow, J. Nucl. Mater. 67 (1977) 181-197.

92. W.J.S. Yang and F. A. Garner, "Effects of Radiation on Materials: Eleventh Conf.," ASTM STP 782, ASTM, Philadelphia, 1982, pp. 186-206.

93. J. F. Bates and M. K. Korenko, Nucl. Tech. 48 (1980) 303–314.

94. B. J. Makenas, "Effects of Radiation on Materials: Twelfth Conf.," ASTM STP 870, ASTM, Philadelphia, 1985, pp. 202–211.

95. P. J. Maziasz and M. L. Grossbeck, J. Nucl. Mater. 103&104 (1981) 987-991.

96. H. R. Brager and F. A. Garner, J. Nucl. Mater. 117 (1983) 159-176.

97. C. Cawthorne and E. J. Fulton, "The Nature of Small Defect Clusters," Proc. of Int. Conf., AERE-R5269, AERE Harwell, 1966, pp. 446-454.

98. C. Cawthorne and E. J. Fulton, Nature 216 (1967) 575-576.

99. J. H. Shively, "Radiation Damage in Reactor Materials," Proc. of Int. Symp., STI/PUB/230, IAEA, Vienna, 1969, pp. 253–255.

100. R. Bullough and R. C. Perrin, "Radiation Damage in Reactor Materials," Proc. of Int. Symp., STI/PUB/230, IAEA, Vienna, 1969, pp. 233–251.

101. K. Farrell, P. J. Maziasz, E. H. Lee and L. K. Mansur, Rad. Effects 78 (1983) 277–295.

102. G. R. Odette and M. W. Frei, "The Technology of Controlled Nuclear Fusion," Proc. of Topical Meeting, CONF-740402, Vol. 2, U.S. AEC, Washington, DC, 1974, pp. 485–498.

103. G. R. Odette and S. C. Langley, "Radiation Effects and Tritium Technology for Fusion Reactors," Proc. of Int. Conf., CONF-750989, Vol. I, U.S. ERDA, Washington, DC, 1976, pp. 395–416.

104. B. N. Singh and A.J.E. Foreman, J. Nucl. Mater. 103&104 (1981) 1469–1474.

105. P. J. Maziasz, J. A. Horak and B. L. Cox, "Phase Stability During Irradiation," AIME Symp., AIME, New York, 1980, pp. 271-294.

106. E. H. Lee, P. J. Maziasz and A. F. Rowcliffe, "Phase Stability During Irradiation," AIME Symp., AIME, New York, 1980, pp. 191–218.

107. E. A. Kenik and E. A. Lee, "Phase Stability During Irradiation," AIME Symp, AIME, New York, 1980, pp. 493-503.

108. R. E. Stoller and G. R. Odette, "Effects of Irradiation on Materials: Eleventh Conf.," ASTM STP 782, ASTM, Philadelphia, 1982, pp. 275-294.

109. G. W. Greenwood, A.J.E. Foreman and D. E. Rimmer, J. Nucl. Mater. 1 (1959) 305–324.

110. S. D. Harkness and Che-Yu Li, "Radiation Damage in Reactor Materials," Proc. of Int. Symp., STI/PUB/230, IAEA, Vienna, 1969, pp. 189–214.

111. A. D. Brailsford and R. Bullough, J. Nucl. Mater. 44 (1972) 121–135.

112. H. Wiedersich, Rad. Effects 12 (1972) 111–125.

113. A. D. Brailsford, R. Bullough and M. R. Hayns, J. Nucl. Mater. 60 (1976) 246–256.

114. A. D. Brailsford, J. Nucl. Mater. 60 (1976) 257–278.

115. A. D. Brailsford and R. Bullough, The Theory of Sink Strengths, TP.854, AERE Harwell, 1980.

116. R. Bullough and T. M. Quigley, J. Nucl. Mater. 113 (1983) 179–191.

117. L. K. Mansur, P. R. Okamoto, A. Taylor and Che-Yu Li, "Properties of Reactor Structural Alloys after Neutron or Particle Irradiation," Conf. Proc., ASTM STP 570, ASTM, Philadelphia, 1975, pp. 272–289.

118. L. K. Mansur, A. D. Brailsford and W. G. Wolfer, J. Nucl. Mater. 105 (1982) 36–38.

119. P. T. Heald and K. M. Miller, J. Nucl. Mater. 66 (1976) 107–111.

120. P. T. Heald and J. E. Harbottle, J. Nucl. Mater. 67 (1977) 229–233.

121. M. H. Yoo, Dislocation Loop Growth and Void Swelling in Bounded Media by Charged Particle Damage, ORNL-TM-5789, Oak Ridge National Laboratory, 1977.

122. M. H. Yoo, J. Nucl. Mater. 68 (1977) 193–204.

123. U. Gösele, J. Nucl. Mater. 78 (1978) 83–95.

124. L. K. Mansur and W. A. Coghlan, J. Nucl. Mater. 119 (1983) 1–25.

125. M. R. Hayns and L. K. Mansur, "Effect of Irradiation on Materials: Tenth Conf.," ASTM STP 725, ASTM, Philadelphia, 1981, pp. 213–230.

126. B. B. Glasgow and W. G. Wolfer, "Effect of Irradiation on Materials: Twelfth Conf.," ASTM STP 870, ASTM, Philadelphia, 1985, pp. 453–467.

127. M. H. Yoo and J. O. Stiegler, Phil. Mag. 36 (1977) 1305–1315.

128. M. H. Yoo, Phil. Mag. 40 (1979) 193–211.

129. L. K. Mansur and M. H. Yoo, J. Nucl. Mater. 74 (1978) 228–241.

130. G. R. Odette and R. E. Stoller, J. Nucl. Mater. 122&123 (1984) 514–519.

131. A. D. Brailsford and R. Bullough, J. Nucl. Mater. 48 (1973) 87–106.

132. R. M. Mayer, L. M. Brown and U. Gösele, J. Nucl. Mater. 95 (1980) 44–107.

133. N. M. Ghoniem and D. D. Cho, The Influence of Vacancy Clustering on the Early Stages of Interstitial Loop Formation and Growth, UCLA-ENG-7845, University of California, Los Angeles, 1978.

134. N. M. Ghoniem and M. L. Takata, J. Nucl. Mater. **105** (1982) 276–292.

135. S. Sharafat and N. M. Ghoniem, J. Nucl. Mater. **122&123** (1984) 531–536.

136. N. M. Ghoniem and D. D. Cho, Numerical Solution to the Time-Dependent 2-D Fokker-Planck Equation Representing Stochastic Atomic Clustering in Solids, UCLA-ENG-8630, University of California, Los Angeles, 1986.

137. M. F. Wehner and W. G. Wolfer, Vacancy Cluster Evolution in Metals Under Irradiation, UWFDM-590, University of Wisconsin, Madison, 1984.

138. M. R. Hayns, A Composite Numerical Scheme for the Nucleation of Secondary Defect Aggregates: I. Interstitial Loop Nucleation, AERE-R9708, AERE Harwell, 1980.

139. M. R. Hayns, A Composite Numerical Scheme for the Nucleation of Secondary Defect Aggregates: II. Void Nucleation, AERE-R9708, AERE Harwell, 1980.

140. M. R. Hayns, J. Nucl. Mater. **56** (1975) 267–274.

141. R. W. Powell, "Radiation Effects in Breeder Reactor Structural Materials," Proc. of Int. Conf., AIME, New York, 1977, pp. 757–772.

142. K. C. Russell and R. W. Powell, Acta Met. **21** (1973) 187–194.

143. F. A. Garner and W. G. Wolfer, "Effects of Irradiation on Materials: Eleventh Conf.," ASTM STP 782, ASTM, Philadelphia, 1982, pp. 1073–1087.

144. D.I.R. Norris, Rad. Effects **15** (1972) 1–22.

145. D. J. Mazey and S. Francis, "The Physics of Irradiation Produced Voids," Consultants Symp., AERE R-7934, AERE Harwell, 1975, pp. 257–262.

146. A. D. Brailsford and L. K. Mansur, Time Dependent Rate Theory for Diffusional Defect Processes, ORNL-6122, Oak Ridge National Laboratory, 1985.

147. L. K. Mansur, A. D. Brailsford and W. A. Coghlan, A Cascade Diffusion Theory of Sink Capture During Irradiation of a Solid, ORNL-6123, Oak Ridge National Laboratory, 1985.

148. A. D. LeClaire, J. Nucl. Mater. 69&70 (1978) 70–96.

149. W. G. Wolfer, F. A. Garner and L. E. Thomas, "Effects of Irradiation on Materials: Eleventh Conf.," ASTM STP 782, ASTM, Philadelphia, 1982, pp. 1023–1041.

150. E. E. Bloom and J. O. Stiegler, "Effect of Radiation on Substructure and Mechanical Properties of Metals and Alloys," Conf. Proc., ASTM STP 529, ASTM, Philadelphia, 1973, pp. 360–382.

151. B. L. Eyre, "Fundamental Aspects of Radiation Damage in Metals," Proc. of Int. Conf., CONF-751006, Vol. II, U.S. ERDA, Washington, DC, 1975, pp. 729–763.

152. F. A. Garner, "Optimizing Materials for Nuclear Applications," AIME Symp. Proc., AIME, New York, 1984, pp. 111–139.

153. P. J. Maziasz, J. Nucl. Mater. 122&123 (1984) 472–486.

154. R. T. King, "Uses of Cyclotrons in Chemistry, Metallurgy and Biology," Proc. of Int. Conf., Butterworths, London, 1970, pp. 294–315.

155. J. H. Worth, "Uses of Cyclotrons in Chemistry, Metallurgy and Biology," Proc. of Int. Conf., Butterworths, London, 1970, pp. 282–293.

156. J. H. Worth, The Problem of Obtaining a Uniform Volume Concentration of Implanted Ions, AERE-R5704, AERE Harwell, 1968.

157. D. J. Mazey and R. S. Nelson, "Radiation Effects and Tritium Technology for Fusion Reactors," Proc. of Int. Conf., CONF-750989, Vol. I, U.S. ERDA, Washington, DC, 1976, pp. 240–258.

158. F. A. Smidt and A. G. Pieper, "Radiation Effects and Tritium Technology for Fusion Reactors," Proc. of Int. Conf., CONF-750989, Vol. II, U.S. ERDA, Washington, DC, 1976, pp. 250–279.

159. J. Rothaut and H. Schroeder, J. Nucl. Mater. 103&104 (1981) 1023–1034.

160. Metals Handbook, Vol. 4, Ninth Edition, ASM, Metals Park, OH, 1981.

161. H. R. Brager and J. L. Straalsund, J. Nucl. Mater. 47 (1973) 105–109.

162. H. R. Brager, E. R. Gilbert and J. L. Straalsund, Rad. Effects 21 (1974) 37–50.

163. D. Fahr, E. E. Bloom and J. O. Stiegler, "Irradiation Embrittlement and Creep in Fuel Cladding and Core Components," Proc. of Int. Conf., BNES, London, 1972, pp. 167–172.

164. M. M. Paxton and J. J. Holmes, Recovery and Recrystallization of Prototypic FTR Fuel Cladding, HEDL-TME 71-126, Hanford Engineering Development Laboratory, 1971.

165. P. J. Maziasz, Trans. Am. Nucl. Soc. 39 (1981) 433–435.

166. J. I. Bramman, C. Brown, J. S. Watkin, C. Cawthorne, E. J. Fulton, P. J. Barton and E. A. Little, "Radiation Effects in Breeder Reactor Structural Materials," Proc. of Int. Conf., AIME, New York, 1977, pp. 479–507.

167. L. Le Naour, M. Vovillon and V. Levy, "Effects of Irradiation on Materials: Eleventh Conf.," ASTM STP 782, ASTM, Philadelphia, 1982, pp. 310–324.

168. E. E. Bloom, W. R. Martin, J. O. Stiegler and J. R. Weir, J. Nucl. Mater. 22 (1967) 68–76.

169. H. R. Brager, F. A. Garner and G. L. Guthrie, J. Nucl. Mater. 66 (1977) 181–197.

170. H. R. Brager, J. Nucl. Mater. 57 (1975) 103–118.

171. J. Bramman, C. Brown, C. Cawthorne, E. J. Fulton and G. Linekar, "The Physics of Irradiation Produced Voids," Consultants Symp., AERE-R7934, AERE Harwell, 1975, pp. 71–77.

172. P. J. Maziasz, Alloy Development for Irradiation Performance: Semiannual Progress Report, DOE/ER-0045/7, U.S. DOE Office of Fusion Energy, Washington, DC, March 1982, pp. 54–97.

173. P. B. Hirsch, A. Howie, R. B. Nicholson, D. W. Pashley and M. J. Whelan, Electron Microscopy of Thin Crystals, Butterworths, London, 1971.

174. E. H. Lee, A. F. Rowcliffe and E. A. Kenik, J. Nucl. Mater. 83 (1979) 79–89.

175. T. A. Kenfield, W. K. Appleby, H. J. Busboom and W. L. Bell, J. Nucl. Mater. 75 (1978) 85–97.

176. L. K. Mansur, Phil. Mag. A44 (1981) 867–877.

177. L. K. Mansur, M. R. Hayns and E. H. Lee, "Phase Stability During Irradiation," AIME Symp., AIME, New York, 1980, pp. 359–382.

178. L. K. Mansur, E. H. Lee, P. J. Maziasz and A. F. Rowcliffe, "Control of Helium Effects in Irradiated Materials Based on Theory and Experiment," Proc. Second Int. Conf. on Fusion Reactor Materials, Chicago, April 14–17, 1986, to be published in Journal of Nuclear Materials.

179. P. J. Maziasz, F. W. Wiffen and E. E. Bloom, "Radiation Effects and Tritium Technology for Fusion Reactors," Proc. of Int. Conf., CONF-750989, Vol. I, U.S. ERDA, Washington, DC, 1976, pp. 259–288.

180. A. Hishinuma, J. M. Vitek, J. A. Horak and E. E. Bloom, "Effects of Radiation on Materials: Eleventh Conf.," ASTM STP 782, ASTM, Philadelphia, 1982, pp. 92–107.

181. H. R. Brager and F. A. Garner, J. Nucl. Mater. 103&104 (1981) 993–998.

182. H. R. Brager and F. A. Garner, J. Nucl. Mater. 108&109 (1982) 347–358.

183. H. R. Brager and F. A. Garner, "Dimensional Stability and Mechanical Behavior of Irradiated Metals and Alloys," Proc. of Int. Conf., BNES, London, 1984, pp. 1–4.

184. P. J. Maziasz and D. N. Braski, J. Nucl. Mater. 122&123 (1984) 305–310.

185. D. Imeson, M. Lee, J. B. Vander Sande, N. J. Grant and O. K. Harling, J. Nucl. Mater. 122&123 (1984) 266–271.

186. J. A. Spitznagel, W. J. Choyke, N. J. Doyle, R. B. Irwin, J. R. Townsend and J. R. McGruer, J. Nucl. Mater. 108&109 (1982) 537–543.

187. A. Kohyama, G. Aryault and N. Igata, J. Nucl. Mater. 122&123 (1984) 224–229.

188. R. L. Sindelar, G. L. Kulcinski and R. A. Dodd, J. Nucl. Mater. 122&123 (1984) 246–251.

189. R. L. Sindelar, G. L. Kulcinski and R. A. Dodd, J. Nucl. Mater. 133&134 (1985) 544–548.

190. E. H. Lee, N. H. Packan and L. K. Mansur, J. Nucl. Mater. 117 (1983) 123–133.

191. V. Levy, D. Gilbon and C. Rivera, "Effects of Radiation on Materials: Twelfth Conf.," ASTM STP 870, ASTM, Philadelphia, 1985, pp. 317–329.

192. E. H. Lee and L. K. Mansur, Phil. Mag. A52 (1985) 493–508.

193. N. H. Packan and K. Farrell, Nucl. Tech./Fusion 3 (1983) 392–404.

194. S. G. Agarwal, G. Ayrault, D. I. Potter, A. Taylor and F. V. Nolfi, J. Nucl. Mater. 85&86 (1979) 653–657.

195. E. A. Kenik, J. Nucl. Mater. 85&86 (1979) 659–663.

196. W. J. Choyke, J. N. McGruer, J. R. Townsend, J. A. Spitznagel, N. J. Doyle and F. J. Venskytis, J. Nucl. Mater. 85&86 (1979) 647–651.

197. S. Wood, J. A. Spitznagel, W. J. Choyke, N. J. Doyle, J. N. McGruer and J. R. Townsend, "Effects of Radiation on Materials: Tenth Conf.," ASTM STP 725, ASTM, Philadelphia, 1981, pp. 455–469.

198. G. Ayrault, H. A. Hoff, F. V. Nolfi and A.P.L. Turner, J. Nucl. Mater. 103&104 (1981) 1035–1040.

199. R. W. Clark, Dimensional Change Correlations for 20% Cold-Worked AISI 316 Stainless Steel for Fusion Applications, Master's Degree Thesis, University of Missouri, Rolla, 1985.

200. B. J. Makenas, J. F. Bates and J. W. Yost, "Effects of Radiation on Materials: Eleventh Conf.," ASTM STP 782, ASTM, Philadelphia, 1982, pp. 17–29.

201. J. F. Bates and D. S. Gelles, J. Nucl. Mater. 71 (1978) 365–367.

202. J. F. Bates, J. Nucl. Mater. 98 (1981) 71–85.

203. F. A. Garner, H. R. Brager and R. J. Puigh, J. Nucl. Mater. 133&134 (1985) 535-539.

204. J. L. Seran and J. M. Dupouy, "Effects of Radiation on Materials: Eleventh Conf.," ASTM STP 782, ASTM, Philadelphia, 1982, pp. 5-16.

205. J. F. Bates and E. R. Gilbert, J. Nucl. Mater. 71 (1978) 286-291.

206. F. A. Garner, E. R. Gilbert and D. L. Porter, "Effects of Irradiation on Materials: Tenth Conf.," ASTM STP 725, ASTM, Philadelphia, 1981, pp. 680-697.

207. D. L. Porter, M. L. Takata and E. L. Wood, J. Nucl. Mater. 116 (1983) 272-276.

208. D.I.R. Norris and J. T. Buswell, J. Nucl. Mater. 59 (1976) 316-320.

209. M. J. Makin, J. Nucl. Mater. 107 (1982) 133-147.

210. R. E. Stoller and G. R. Odette, J. Nucl. Mater. 131 (1985) 118-125.

211. R. E. Stoller and G. R. Odette, J. Nucl. Mater. 122&123 (1984) 514-519.

212. G. R. Odette, J. Nucl. Mater. 133&134 (1985) 127-133.

213. N. H. Packan, K. Farrell and J. O. Stiegler, J. Nucl. Mater. 78 (1978) 143-145.

214. L. K. Mansur, J. Nucl. Mater. 78 (1978) 156-160.

215. R. Bullough and R. C. Perrin, "Irradiation Effects on Structural Alloys for Nuclear Reactor Applications," Conf. Proc., ASTM STP 484, ASTM, Philadelphia, 1970, pp. 317-331.

216. P. J. Maziasz, J. Nucl. Mater. 122&123 (1984) 236-241.

217. P. J. Maziasz and D. N. Braski, J. Nucl. Mater. 122&123 (1984) 311-316.

218. F. A. Garner, J. Nucl. Mater. 122&123 (1984) 459-471.

219. F. A. Garner and H. R. Brager, "Optimizing Materials for Nuclear Applications," AIME Symp. Proc., AIME, New York, 1984, pp. 87–109.

220. F. A. Garner, "Phase Stability During Irradiation," AIME Symp., AIME, New York, 1980, pp. 165–189.

221. H. R. Brager and F. A. Garner, "Effects of Radiation on Materials: Tenth Conf.," ASTM STP 725, ASTM, Philadelphia, 1981, pp. 470–483.

222. F. A. Garner and W. G. Wolfer, J. Nucl. Mater. 122&123 (1984) 201–206.

223. B. Weiss and R. Stickler, Met. Trans. 3 (1972) 851–865.

224. W.J.S. Yang, "Precipitate Evolution in 316-Type Stainless Steel Irradiated in EBR-II," Proc. of Thirteenth Conference on Radiation Effects in Materials, Seattle, June 22–25, 1986, to be published by ASTM.

225. W. Assassa and P. Guiraldenq, Met. Sci. 12 (1978) 123–128.

226. S. J. Rothman, L. J. Nowicki and G. E. Murch, J. Phys. F.: Metal Phys. 10 (1980) 383–398.

227. F. A. Garner and W. G. Wolfer, J. Nucl. Mater. 102 (1981) 143–150.

228. H. R. Brager and F. A. Garner, "Advanced Techniques for Characterizing Microstructures," AIME Symp., AIME, New York, 1982, pp. 97–114.

229. P. J. Maziasz, J. Nucl. Mater. 108&109 (1982) 359–384.

230. H. R. Brager and P. J. Maziasz, "Results of Continued Irradiation in FFTF of Various Austenitic Stainless Steels Previously Irradiated in HFIR," presented in a poster session at the Second Topical Meeting on Fusion Reactor Materials, Chicago, April 14–17, 1986, to be published in a future Damage Analysis and Fundamental Studies Quarterly progress report by the U.S. DOE Office of Fusion Energy.

231. R. E. Stoller and G. R. Odette, Damage Analysis and Fundamental Studies: Quarterly Progress Report, DOE/ER-0046/10, U.S. DOE Office of Fusion Energy, Washington, DC, August 1982, pp. 199–232.

232. Standard Mathematical Tables, 24th Ed., CRC Press, Cleveland, Ohio, 1973.

233. I. R. Brearley and D. A. MacInnes, J. Nucl. Mater. 95 (1980) 239–252.

234. R. F. Mattas, F. A. Garner, M. L. Grossbeck, P. J. Maziasz, G. R. Odette and R. E. Stoller, J. Nucl. Mater. 122&123 (1984) 230–235.

235. J. A. Spitznagel, S. Wood, N. J. Doyle, W. J. Choyke, J. N. McGruer, J. R. Townsend and R. B. Irwin, J. Nucl. Mater. 103&104 (1981) 1463–1468.

236. W. A. Coghlan and L. K. Mansur, J. Nucl. Mater. 122&123 (1984) 495–501.

237. H. Trinkaus and L. K. Mansur, unpublished research.

238. S. D. Harkness and Che-Yu Li, Met. Trans. 2 (1971) 1457-1470.

239. J. L. Katz and H. Wiedersich, J. Chem. Phys. 55 (1971) 1414-1425.

240. K. C. Russell, "The Physics of Irradiation Produced Voids," Consultants Symp., AERE-R7934, AERE Harwell, 1975, pp. 158–179.

241. S. A. Seyyedi, M. Hadji-Mirzai and K. C. Russell, "Irradiation Behavior of Metallic Materials for Fast Reactor Core Components," Proc. of Int. Conf., Organisee Par Le Commissariat a L'Energie Atomique, Gif-sur-Yvette, France, 1979, pp. 101–106.

242. M. F. Wehner and W. G. Wolfer, Phil. Mag. A52 (1985) 189–205.

243. V. F. Sears, J. Nucl. Mater. 39 (1971) 18–26.

244. L. L. Horton and L. K. Mansur, "Effects of Radiation on Materials, Twelfth Conf.," ASTM STP 870, ASTM, Philadelphia, 1985, pp. 344–357.

245. R. E. Stoller and G. R. Odette, J. Nucl. Mater. 103&104 (1981) 1361–1366.

246. K. Farrell and N. H. Packan, J. Nucl. Mater. 85&86 (1979) 683-687.

247. See the discussion following ref. 244, "Effects of Radiation on Materials, Twelfth Conf.," STP 870, ASTM, Philadelphia, 1985, pp. 357–362.

248. H. Wiedersich, "The Physics of Irradiation Produced Voids," Consultants Symp. AERE-R7934, AERE Harwell, 1975, pp. 147–157.

249. C. F. Clement and M. H. Wood, J. Nucl. Mater. 89 (1980) 1-8.

250. L. K. Mansur and W. G. Wolfer, A Study of the Effect of Void Coatings on the Radiation-Induced Swelling, ORNL/TM-5670, Oak Ridge National Laboratory, 1977.

251. M. H. Yoo and L. K. Mansur, J. Nucl. Mater. 85&86 (1979) 571–575.

252. L. K. Mansur and W. A. Coghlan, "Effects of Radiation on Materials, Twelfth Conf.," ASTM STP 870, ASTM, Philadelphia, 1985, pp. 481–492.

253. W. G. Wolfer and L. K. Mansur, J. Nucl. Mater. 91 (1980) 265–276.

254. J. E. Harris, Met. Sci. J. 7 (1973) 1–6.

255. P. J. Maziasz, "Phase Stability During Irradiation," AIME Symp., AIME, New York, 1980, pp. 477–492.

256. R. Raj and M. F. Ashby, Acta Met. 23 (1975) 653–666.

257. R. Raj and M. F. Ashby, Acta Met. 26 (1978) 995–1006.

258. L. E. Murr, Interfacial Phenomena in Metals and Alloys, Addison-Wesley, Reading, 1975.

259. L. E. Murr, G. I. Wong and R. J. Horylev, Acta Met. 21 (1973) 593–603.

260. B. O. Hall, J. Nucl. Mater. 103&104 (1981) 1391–1396.

261. H. L. Heinisch, Damage Analysis and Fundamental Studies: Quarterly Progress Report, DOE/ER-0046/2, U.S. DOE Office of Fusion Energy, Washington, DC, August 1980, pp. 60–72.

262. H. Saka, Phil. Mag. A42 (1980) 185–194.

263. C. Brown, J. K. Butler and E. J. Fulton, "Irradiation Behavior of Metallic Materials for Fast Reactor Core Components," Proc. of Int. Conf., Organisee Par Le Commissariot a L'Energie, Atomique, Gif-sur-Yvette, France, 1979, pp. 129–136.

264. A. C. Hindmarsh, SIGNUM, Newsletter of the A.C.M. 15 (1980) 10–11.

265. N. L. Peterson, J. Nucl. Mater. 69&70 (1978) 3–37.

266. R. A. Perkins, Met. Trans. 4 (1973) 1665–1669.

267. R. A. Perkins, R. A. Padgett and N. K. Tunali, Met. Trans. 4 (1973) 2535–2539.

268. S. K. Khanna and S. Sonnenberg, Rad. Effects 59 (1981) 91–92.

269. L. C. Smedskjaer, M. J. Fluss, D. G. Legnini, M. K. Chason and R. W. Seigel, J. Phys. F: Metal Phys. 11 (1981) 2221–2230.

270. O. Dimitrov and C. Dimitrov, J. Nucl. Mater. 105 (1982) 39–47.

271. A.O.O. Mekhrabov, E. Sato, M. Shimotomai, M. Doyama, T. Iwata and T. Kawanishi, J. Nucl. Mater. 133&134 (1985) 549–552.

272. L. K. Mansur, J. Nucl. Mater. 83 (1979) 109–127.

273. F. W. Young, J. Nucl. Mater. 69&70 (1978) 310–330.

274. J. T. Stanley and J. R. Cost, J. Phys. F: Metal Phys. 14 (1984) 1801–1810.

275. N. Housseau and J. Pelissier, J. Nucl. Mater. 119 (1983) 317–325.

276. S. J. Zinkle, W. G. Wolfer, G. L. Kulcinski, and L. E. Seitzman, Phil. Mag. A. 55 (1987) 127–140.

277. L. E. Seitzman, L. M. Wang, G. L. Kulcinski, and R. A. Dodd, "The Effect of Oxygen on Void Stability in Nickel and Austenitic Stainless Steels," presented at the Second Int. Conf. on Fusion Reactor Materials, Chicago, April 14–17, 1986, to be published in Journal of Nuclear Materials.

278. E. H. Lee, Oak Ridge National Laboratory, unpublished research, private communication, 1986.

279. C. A. English, J. Nucl. Mater. 108&109 (1982) 104–123.

280. J. W. Muncie, B. L. Eyre and C. A. English, Phil. Mag. A52 (1985) 309–331.

281. M. R. Hayns, J. Nucl. Mater. 79 (1979) 323–337.

282. W. G. Wolfer and A. Si-Ahmed, J. Nucl. Mater. 99 (1981) 117–123.

283. T. Leffers and B. N. Singh, Rad. Effects 59 (1981) 83–89.

284. T. Leffers and B. N. Singh, J. Nucl. Mater. 91 (1980) 336–342.

285. O. Dimitrov, M. C. Belo and C. Dimitrov, J. Phys. F: Metal Phys. 10 (1980) 1653–1654.

286. K. M. Miller, J. Nucl. Mater. 84 (1980) 167–172.

287. M. L. Grossbeck and K. R. Thoms, Alloy Development for Irradiation Performance: Quarterly Progress Report, DOE/ER-0045/3, U.S. DOE Office of Fusion Energy, Washington, DC, October 1980, pp. 10–23.

288. P. J. Maziasz and M. P. Tanaka, Oak Ridge National Laboratory, unpublished reseach in progress, private communication, 1986.

289. P. J. Maziasz and M. L. Grossbeck, Alloy Development for Irradiation Performance: Semiannual Progress Report, DOE/ER-0045/7, U.S. DOE Office of Fusion Energy, Washington, DC, March 1982, pp. 98–109.

290. F. A. Garner, P. J. Maziasz and W. G. Wolfer, Damage Analysis and Fundamental Studies: Quarterly Progress Report, DOE/ER-0046/3, U.S. DOE Office of Fusion Energy, Washington, DC, November 1980, pp. 159–177.

291. P. J. Maziasz and M. L. Grossbeck, Alloy Development for Irradiation Performance: Quarterly Progress Report, DOE/ER-0045/6, U.S. DOE Office of Fusion Energy, Washington, DC, July 1981, pp. 28–56.

292. F.R.N. Nabarro, Phil. Mag. 16 (1967) 231–237.

293. J. Gittus, Creep, Viscoelasticity and Creep Fracture in Solids, John Wiley and Sons, New York, 1975.

294. W. D. Nix, R. Gasca-Neri, and J. P. Hirth, Phil. Mag. 23 (1971) 1339–1349.

295. G. B. Gibbs, Phil. Mag. 23 (1971) 771–780.

296. G. D. Johnson, F. A. Garner, H. R. Brager and R. L. Fish, "Effects of Irradiation on Materials: Tenth Conf.," ASTM STP 725, ASTM, Philadelphia, 1981, pp. 393–412.

297. Materials Handbook for Fusion Energy Systems, DOE/TIC-10122, U.S. DOE Office of Fusion Energy, Washington, DC.

298. A. C. Damask and G. J. Dienes, Point Defects in Metals, Gordon and Breach, New York, 1971.

299. H. R. Schober and R. Zeller, J. Nucl. Mater. 69&70 (1978) 341–349.

300. N. H. Packan and K. Farrell, "Effects of Irradiation on Materials: Eleventh Conf.," ASTM STP 782, ASTM, Philadelphia, 1982, pp. 885–894.

301. A. Horsewell and B. N. Singh, "Effects of Radiation on Materials: Twelfth Conf.," ASTM STP 870, ASTM, Philadelphia, 1985, pp. 248–261.

302. W. van Witzenburg and A. Mastenbroek, J. Nucl. Mater. 133&134 (1985) 553–557.

303. D. R. Harries, The European Community Fusion Materials Programme, EUR-FU/XII-80/86/85, Commission of the European Communities Directorate General XII, Fusion Programme, Brussels, 1986.

304. E. E. Bloom, J. O. Stiegler, A. F. Rowcliffe, and J. M. Leitnaker, Scripta Met. 10 (1976) 303–308.

305. E. E. Bloom and W. G. Wolfer, "Effects of Radiation on Structural Materials," Conf. Proc., ASTM STP 683, ASTM, Philadelphia, 1979, pp. 656–672.

306. K. Farrell, and N. H. Packan, "Effects of Radiation on Materials: Eleventh Conf.," ASTM STP 782, ASTM, Philadelphia, 1982, pp. 953-962.

307. N. H. Packan, J. Nucl. Mater. 103&104 (1981) 1029–1034.

308. N. H. Packan and K. Farrell, A.N.S. Trans. 33 (1979) 290–291.

309. G. R. Odette, R. W. Powell, and F. V. Nolfi, Damage Analysis and Fundamental Studies: Quarterly Progress Report, DOE/ET-0065/5, U.S. DOE, Office of Fusion Energy, Washington, DC, May 1979, pp. 5–8.

310. S. D. Harkness, B. J. Kestel, and S. G. McDonald, J. Nucl. Mater. 46 (1973) 159-168.

311. D. Kramer, Energy Systems Group, Rockwell International, Canoga Park, CA, by letter to J. McCurdy of Crocker Nuclear Laboratory, University of California, Davis, 83ESG-336, January 5, 1983.

312. I. Manning and G. P. Mueller, Computer Phys. Comm. 7 (1974) 85-94.

313. J. M. Leitnaker, E. E. Bloom, and J. O. Stiegler, J. Nucl. Mater. 49 (1973) 57-66.

314. J. W. Edington, Practical Electron Microscopy in Materials Science, Philips Gloeilampenfabrieken, Eindhoven, The Netherlands, 1975.

315. W. Kesternich, "Electon Microscopy," Proc. of Eighth European Congress, Volume 2, Budapest, 1984, pp. 837–838.

316. H. Farrar, Energy Systems Group, Rockwell International, by letter to R. E. Stoller, University of California, Santa Barbara, 84ESG-777, February 20, 1984.

317. K. Shiraishi, K. Fukaya and K. Fukai, J. Nucl. Mater. 119 (1983) 268–277.

318. R. S. Barnes and D. J. Mazey, Phil. Mag. 5 (1960) 1247–1253.

319. L. R. Greenwood, Damage Analysis and Fundamental Studies: Quarterly Progress Report, DOE/ER-0046/6, U.S. DOE, Office of Fusion Energy, Washington, DC, August 1981, pp. 17–21.

320. M. L. Grossbeck, Oak Ridge National Laboratory, by letter to H. R. Brager of Hanford Engineering Development Laboratory, March 21, 1981.

321. H. R. Brager, F. A. Garner, and R. L. Gaines, Damage Analyses and Fundamental Studies: Quarterly Progress Report, DOE/ER-004616, U.S. DOE, Office of Fusion Energy, Washington, DC, August, 1981, pp. 144–147.

322. H. R. Brager and F. A. Garner, Damage Analyses and Fundamental Studies: Quarterly Progress Report, DOE/ER-004616, U.S. DOE Office of Fusion Energy, Washington, DC, August, 1981, pp. 148–161.

323. H. R. Brager and F. A. Garner, Damage Analyses and Fundamental Studies: Quarterly Progress Report, DAFS, DOE/ER-0046/7, U.S. DOE, Office of Fusion Energy, Washington, DC, November, 1981, pp. 172–179.

324. R. A. Buhl and L. J. Turner, Remote-Controlled Immersion Densitometer, to be published as ORNL/TM-10378, Oak Ridge National Laboratory, 1987.

325. L. R. Greenwood, Damage Analysis and Fundamental Studies: Quarterly Progress Report, DOE/ER-0046/5, U.S. DOE, Office of Fusion Energy, Washington, DC, May 1981, pp. 13–17.

326. J. M. Leitnaker, E. E. Bloom, and J. O. Stiegler, Fuels and Materials Development: Quarterly Progress Report, ORNL-TM-4105, Oak Ridge National Laboratory, December, 1972, pp. 3.19–3.29.

327. J. Silcox and P. B. Hirsch, Phil. Mag. 4 (1959) 72–89.

328. N. Yoshida, Y. Akashi, K. Kitajima, and M. Kiritani, J. Nucl. Mater. 133&134 (1985) 405–409.

329. C. Cawthorne, "The Physics of Irradiation Produced Voids," Consultants Symposium, AERE-R7934, AERE Harwell, 1975, pp. 78–81.

330. J. J. Holmes, R. E. Robbins, J. L. Brimhall, and B. Mastel, Acta Met. 16 (1968) 955–967.

331. J. O. Stiegler and E. E. Bloom, J. Nucl. Mater. 33 (1969) 173–185.

332. J. L. Straalsund, J. J. Holmes, H. R. Brager, and R. L. Fish, abstract of paper presented at 1969 Spring meeting of TMS AIME, J. Metals 21 (1969) 44a.

333. D. L. Porter, G. L. McVay, and L. C. Walters, "Effects of Radiation on Materials: Tenth Conf.," ASTM STP 725, ASTM, Philadelphia, 1981, pp. 500–511.

334. K. Q. Bagley, J. I. Bramman, and C. Cawthorne, "Voids Formed by Irradiation of Reactor Materials," Proc. of BNES European Conf., AERE Harwell, 1971, pp. 1-26.

335. R. A. Oriani, Acta Met. 12 (1964) 1399-1409.

336. C. Wagner, Z. Electrochem. 65 (1961) 581–591.

337. I. M. Lifshitz and V. V. Slyozov, J. Phys. Chem. Solids 19 (1961) 35-50.

338. A. Jostsons, E. L. Long, J. O. Stiegler, K. Farrell and D. N. Braski, "Radiation-Induced Voids in Materials," Proc. of Int. Conf., CONF-750989, U.S. ERDA, Washington, DC, 1976, pp. 363-375.

339. C. J. Meechan and J. A. Brinkman, Phys. Rev. 103 (1956) 1193–1202.

340. E. E. Bloom, J. O. Stiegler, and G. A. Reimann, Irradiation Effects on Reactor Structural Materials: Quarterly Progress Report, HEDL-TME-71-116, Hanford Engineering Development Laboratory, September 1971, pp. ORNL/5–ORNL/12.

APPENDIX A

COMPUTER CODE MICROEV

This Appendix contains the listing of a computer code called MICROEV that implements the major microstructural models discussed in Chapter 3. The code was written to conform to the FORTRAN-77 standards and has been successfully compiled and executed on a number of different computers using various FORTRAN-77 compilers without difficulty. Numerous comments are included in the code to describe the input parameters and the execution sequence.

A sample data file for MICROEV follows the code listing. The first line of data read by MICROEV contains only a parameter called "ictr". The value of ictr determines the number of twenty-line data files that will subsequently be read. Each twenty-line data set describes the irradiation conditions and material parameters for a given run. The input parameter called "iclflg" is read as the first number on the fifteenth line of each twenty-line set of data. The value of iclflg determines whether the calculations will be done using only the cavity evolution model with a constant dislocation density (iclflg=0) or if the comprehensive model with simultaneously evolving dislocations will be used (iclflg=1). The sample data file included here is for a fast reactor irradiation to 100 dpa at 500 C with iclflg set to 1 so that the comprehensive microstructural model

is used. Several representative output parameters from this run follow the data file.

A.1 Listing of Computer Code MICROEV

```
ccccccccccccccccccccccccccccccccccccccccccccccccccccccccccccccccccccccccc
c                                                                       c
c               MICROEV                 MICROEV                       c
c                                                                       c
c     A Theoretical Model of Microstructural Evolution                  c
c                                                                       c
c    Roger E. Stoller, January 1987                                     c
c                                                                       c
c   This code is written to use the Livermore Solver of Ordinary       c
c   Differential Equations (LSODE) to intgrate the differential        c
c   equations.  With appropriate changes to the code, an equivalent    c
c   integrator could be used.                                          c
c                                                                       c
c   'nclass' size classes of spherical sinks are allowed to grow and   c
c   shrink.  The defects may convert from bubbles to voids based on    c
c   the amount of helium they contain.  The conversion criterion       c
c   is that the helium content exceed the critical number computed     c
c   using the master curve solution obtained from the Brearley and     c
c   Macinnes hard sphere equation of state (J.N.M. 95 (1980)).         c
c   The bubble radius is also computed using the appropriate master    c
c   curve.  The helium generation rate can either be constant as       c
c   input (hfrflg.eq.0) or time dependent to simulate the hfir         c
c   (hfrflr.eq.1 and hegnrr=3.5e-12).  The cavities in class 1         c
c   collect helium by a dislocaton trapping mechanism while they      c
c   are bubbles; after conversion they capture helium with their      c
c   own sink strength only.  'hefrac' is a parameter multiplying       c
c   the dislocation sink strength to obtain the dislocation sink       c
c   strength for helium (both before and after class 1 converts).     c
c   The cavities in classes 2 - (nclass-1) are pure matrix cavities    c
c   while class nclass can be either pure matrix or precipiate        c
c   assisted.  For ppt-assisted, these cavities collect helium with    c
c   the ppt. sink strength (pptsnk) for times greater than the ppt.    c
c   nucleation time (ppttau).  For pure matrix cavities, input         c
c   ppttau.gt.stop and pptcon.lt.0.  To deal with cases when the       c
c   vacancy supersaturation (sprsat) is less than 0; bubble radii      c
c   are computed for sprsat=0 (ie. equilibrium bubbles).               c
c                                                                       c
c   For iclflg.ne.1, the code uses a constant dislocation density      c
c   (disntd) as input; while for iclflg.eq.1 a rate-theory based       c
c   model of dislocation evolution is used.  'lclass' size classes     c
c   of faulted loops grow and unfault to provide a source of network   c
c   dislocations.  This network is simultaneously annihilated via      c
c   climb which is both thermally and irradiation induced.  The        c
c   faulted loop bias factor can either be input as a parmaeter        c
c   or Wolfer & Ashkin's size dependent biases (J.A.P. 46 (1975)       c
c   and later erratum) can be used.  The alternate sets of code        c
c   lines with 'zil-r' in columns 73-80 need to be interchanged to     c
c   use the alternate biases.  These lines are in the main routine,    c
c   the subroutine grow and the function subroutine fcnlpg.            c
c                                                                       c
c   Transients vacancy clusters as microvoids are also included.       c
c   The clusters can be computed either at steady-state or using       c
c   a time-dependent calculation.  The alternate sets of code lines    c
c   with 'ssvcl' in columns 73-80 need to be interchanged to alter     c
c   the solution method.  These lines are in the main routine and      c
c   in the subroutine grow.                                            c
c                                                                       c
c   When computing the point defect calculations the input parameter   c
c   'pptflg' specifies whether or not the precipitate sink strength,   c
c   'pptsnk' is used.  In this version of the code, pptflg=0 is the    c
c   recommmended value so that ppsink=0.  There are alternate lines    c
c   of code in the subroutine pntdef to determine whether the full     c
c   multiple sink correction is applied to the subgrain sink strength  c
c   (ksbgi) and the cavity sink strength (cfaci).  The lines of code   c
c   that need to be interchanged in pntdef are marked with 'subg-i'    c
```

```
c   and 'cfac-i' respectively in columns 73-80.                          c
c                                                                       c
c   Temperature changes can be called for by setting tmpchg.gt.0        c
c   (up to 9) on input.  New temperatures and the dose (dpa) at         c
c   which the changes are to occur are then required.                   c
c                                                                       c
ccccccccccccccccccccccccccccccccccccccccccccccccccccccccccccccccccccccc
      implicit real*8 (a-z)
      external grow,dumsub
      common /intgr/ bblflg(5),flpcls,hfrflg,iclflg,jtemp,lclas1,
     1  lclas2,lclass,lmns1,lpls1,nclass,netcls,noeq,nplt,nplus1,
     2  nqmns1,nqmns2,outsw,pfact,pntcls,pptflg,
     3  tempno,title1(20),title2(20),tmpchg,vclcls,vdflg(5)
      common /cavprm/ bbconv(5),bbsnk,bbsnk0,cvsnki,cvsnkv,comprs(5),
     1  cfaci(5),cfacv(5),cvsnk0,cvv(5),delhe(5),fs(5),fv(5),gamma(5),
     2  helium(5),mpa(5),ncritr(5),press(5),rhohe(5),
     3  ttconv(5),vdsnk,vdsnk0,voidcn(5),voidrd(5)
      common /disprm/ avlprd,bi1o,bi2o,bv2o,bi3o,bi4o,bv3o,bv4o,
     1  c2dis,c3dis,cvl(45),cvn,dicon,displd,disn0,disntd,distot,
     2  ec2dis,ec3dis,irrann,irrsrc,lpnum(45),lprad(45),ncrate,numilp,
     3  ilpmax,prmt1,prmt2,prmt3,prmt4,rate(45),rc,rhosnk,ro,shrmod,
     4  tauimx,snkerr,snknew,snktst,srcden,stckft,stfeng,tau4,
     5  tetcon,thrann,thrsrc,tricon,zil(45),zil0,zin,zi1,zi2,zi3,zi4,
     6  zvl(45),zvl0,zvn,zv2,zv3,zv4
      common /defprm/ alpha,ao,bvectd,bvectf,cvcls,cvemit,diffi,diffv,
     1  ef,eim,em,fracls,gamvcl,genvcl,intcon,intgn2,intgnr,kt,
     2  numvac,numvcl,omega,radvcl,sprsat,tauvcl,vaccne,vaccon,
     3  vacgnr,vclsnk,cilo,cihi,cvgues,iflux,vflux,delflx
      common /balrl/ appmhe,bubble,cavhe,clster,dery(50),diffhe,
     1  disloc,doschg(10),doschk,ehemig,embbl,emdisl,emflp,emppt,emsubg,
     2  emvcl,emvoid,floop,gasd,graind,grnd0,grnmax,grntau,hefrac,
     7  intbbl,intflp,intnet,intppt,intrec,intsbg,intvcl,intvd,ksbgi,
     3  hegnr0,hegnrr,ksbgv,mtrxhe,ntdhe,pi,pltflg,pptcon,pptrad,
     4  pptsnk,ppttau,precip,prntdt,prntnw,recomb,stop,stress,
     5  subghe,subgrn,swell,swlcmp,swlto1,taup,tauto1,tc(10),temp,
     6  time,tk,totdos,tsinki,tsinkv,tvdvac,vdemit,vdrecm,voids
      common /mscoef/ a0,a1,a2,a3,a4,a5,a6,a7,a8,a9,a10,
     1                b0,b1,b2,b3,b4,b5,b6,b7,b8,b9,b10,
     2                c0,c1,c2,c3,c4,c5,c6,c7,c8,c9,c10
      integer outsw,pfact,pptflg,nplt,nclass,flpcls,netcls,vclcls,
     *  bblflg,vdflg,i,j,k,title1,title2,hfrflg,nplus1,tempno,
     *  noeq,nqmns1,nqmns2,lclass,lclas1,lclas2,lmns1,lpls1,
     *  pntcls,swlflg,iclflg,jtemp,ict,ictr,
     *  neq(1),iwork(70),cnvchk,l1mns1,l1pls1,cavflg,
     *  itol,itask,istate,iopt,lrw,liw,mf
      dimension rwork(2972),y(50),rtol(1),atol(50),idealr(5),idlrad(3),
     *   swlplt(110,2),dntplt(110,2),dlpplt(110,2),
     *   dttplt(110,2),lnmplt(110,2)
 898  format('  For this run, p-cav=',f4.2,' cavity density=',f5.2,
     1 ' times EBR-2 value')
 899  format(8g10.2)
 900  format(8i10)
 901  format(6g12.4)
 902  format(20a4)
 903  format(' ****  input edit  ****')
 904  format('1')
 905  format(/,30x,'% swell vs. dose in dpa',//)
 906  format(/,30x,'disntd (cm-2) vs. dose in dpa',//)
 907  format(/,30x,'displd (cm-2) vs. dose in dpa')
 908  format(/,30x,'numilp (cm-3) vs. dose in dpa',//)
 909  format(/,30x,'distot (cm-2) vs. dose in dpa')
 918  format(/,' dose=',1pd8.2,' (',d8.2,' secs)',2x,'swell=',d9.2,
     1 2x,'swlrate=',d9.2,2x,'sprsat=',d12.6)
 919  format(' vaccon=',1pd12.6,'  intcon=',d12.6,2x,'delflx=',d10.4,
     1 2x,'vacgnr=',d10.4,2x,'snk.ratio(disl/cav)=',d8.2)
 920  format(' cvsnkv=',1pd9.2,2x,'vdsnk=',d9.2,2x,'bbsnk=',d9.2,2x,
     1 'cvsnk0=',d9.2,2x,'vdsnk0=',d9.2,2x,'bbsnk0=',d9.2)
 921  format(' zin=',f5.2,2x,'distot=',1pd9.2,2x,'ksbgv=',d9.2,2x,
     1 'ksbgi=',d9.2,2x,'graind=',d9.2,2x,'pptsnk=',d9.2)
 922  format(' hegnrr=',1pd9.2,2x,'appmhe=',d9.2,
     1 2x,'mtrxhe=',d9.2,2x,'cavhe=',d9.2,2x,'subghe=',d9.2,
     2 2x,'ntdhe=',d9.2)
 923  format(' vclsnk=',1pd10.3,2x,'numvcl=',d10.3,2x,'tauvcl=',d10.3,
     1 2x,'genvcl=',d10.3,2x,' dery=',d10.3,2x,2x,'sschk=',d10.3)       ssvcl
c    1 2x,'genvcl=',d10.3,2x,'sschk=',d10.3)                           ssvcl
 925  format(/,'  bflg  voidrd',4x,'voidcn',5x,'dr/dt',5x,'ncrit',4x,
     1 'helium',5x,'delhe',5x,'press',4x,'comprs',6x,'cvv',8x,
     2 'cfac(for v,i)')
 926  format(i4,1p8d10.2,d11.3,2d10.2)
```

```
 927  format(/,' >> mf, time, last dt, next dt =',
     1 i2,3(1pd12.3) )
 928  format(5x,' i=',i2,6x,'y(i)=',1pd14.6,6x,'dery(i)=',d14.6)
 929  format('  conversion time, bubble class=',i2,t42,1pd10.3,t54,
     1  'secs',t69,'zz')
 930  format('  bubble radius at conversion, class=',i2,t42,1pd10.3,t54,
     1   'cm',t69,'xx')
 932  format('  for class=',i3,'  bubble did not convert')
 933  format(/,'  At approximately 1% swell (',1pd9.2,'%) dose=',d9.2)
 934  format('  maximum swelling rate=',1pd10.3,' %/dpa at ',0pf7.3,
     1 ' dpa',/,'  final swelling=',f7.3,' at ',f7.3,' dpa.',t69,'zz')
 935  format('    calculated dose (dpa)=',1pd10.3)
 936  format('    dose for initial bubble distribution=',1pd10.3)
 937  format('  maximum swelling rate=',1pd10.3,' %/dpa at ',0pf7.3,
     1 ' dpa',/,'  maximum faulted loop density=',1pd10.3,' at',0pf7.3,
     2 ' dpa',/,'  final swelling=',f7.3,' at ',f7.3,' dpa.',t69,'zz')
 939  format('  istate=',i2,', # lsode steps=',i7,
     1 ', # grow calls=',i7,', # pntdef calls=',i7)
 940  format(/,' for class ',i1,' initial radius calculation failed',
     1 ', radius set to ',1pd10.4)
 941  format(' >>> initial sprsat calculation: i, vclsnk, sprsat=',
     1 i4,1p2d13.4)
 942  format(/,'  temp=',f5.1,2x,'disn0=',1pd8.1,2x,'zin=',0pf6.3,
     1 2x,'grnd0=',1pd9.2,2x,'graind=',d9.2)
 943  format('  eim=',f5.2,2x,'evm=',f5.2,2x,'evf=',f5.2,2x,
     1 'diffi0=',f5.2,2x,'diffv0=',f5.2)
 944  format('  alfodi=',1pd9.2,2x,'intgn2=',d9.2,2x,'caseff=',0pf5.3,
     1 2x,'voidcn=',1p5d10.2,//)
 945  format('  prmt1=',f5.2,4x,'prmt2=',f5.2,4x,'prmt3=',f5.2,4x,
     1  'prmt4=',f5.2,//)
 946  format(f7.2,1p5d11.2,' xyz')
 947  format(//,' at',f9.2,' dpa the temperature changed from',f6.1,
     1 ' c to',f6.1,' c',//)
 948  format(' emvoid=',1pd10.3,2x,'embbl=',d10.3,2x,'emdisl=',d10.3,
     1 2x,'emvcl=',d10.3,2x,'emsubg=',d10.3,2x,'emppt=',d10.3)
 949  format(' recmb. ratios, vacrec=',1pd9.2,2x,
     1 'intrec=',d9.2,2x,'tsinki=',d9.2,2x,'tsinkv=',d9.2,2x,
     2 'rhosnk=',d9.2)
 950  format('  ec2dis=',f5.2,' ec3dis=',f5.2,' zi1=',f4.0,' zi2=',f4.0,
     1 ' zi3=',f4.0,' zi4=',f4.0,' zv2=',f4.0,' zv3=',f4.0,' zv4=',f4.0)
 951  format('  di-inter=',1pd10.4,2x,'tri-inter=',d10.4,2x,
     1 'tetra-int=',d10.4,2x,'ncl-rate',d11.4,2x,'tau4=',d10.3)
 952  format(/,4x,'loop rad.',3x,'loop den.',4x,'zil',5x,'zvl',4x,
     1 'cv(loop)',6x,'dn/dt',7x,'rate')
 953  format(' ',1p2d12.3,0p2f8.4,1pd12.3,4x,'-------',5x,'-------')
 954  format(' ',1p2d12.3,0p2f8.4,1p3d12.3)
 955  format(' ',1p2d12.3,0p2f8.4,1pd12.3,4x,'-------',d13.3)
 956  format(/,' disntd=',1pd10.4,'  irrann=',d11.4,'  thrann=',d11.4,
     1 '  irrsrc=',d11.4,'  thrsrc=',d11.4,'  dery(netcls)=',d11.4)
 957  format('  numilp=',1pd11.4,2x,'displd=',d11.4,2x,'avlprd=',
     1 d11.4,2x,'emflp=',d11.4)
 958  format('    dose',4x,'swell',6x,'disntd',5x,'displd',5x,
     1    'numilp',5x,'distot',' T=',f6.1)
 959  format('    dose',4x,'swell',4x,'T=',f6.1)
 960   format(/,'   >>>>> in dlsode, rwork(13,11,12)=',1p3e11.2)
ccccccccccccccccccccccccccccccccccccccccccccccccccccccccccccccccccccccc
c                                                                      c
c        main program loop for up to ictr data decks                   c
c                                                                      c
ccccccccccccccccccccccccccccccccccccccccccccccccccccccccccccccccccccccc
      read(5,900) ictr
      write(6,900) ictr
      do 9999 ict=1,ictr
      do 1001 i=1,2972
 1001 rwork(i)=0.d0
      do 1002 i=1,70
 1002 iwork(i)=0
      do 1003 i=1,50
      dery(i)=0.d0
 1003 y(i)=0.d0
      do 1004 i=1,45
      zil(i)=0.d0
      zvl(i)=0.d0
      lpnum(i)=0.d0
      lprad(i)=0.d0
      rate(i)=0.d0
 1004 cvl(i)=0.d0
      noeq=0
      cnvchk=0
```

```
      nplt=1
      totdos=0.0d0
      tauimx=totdos
      ilpmax=-1.
      tausmx=totdos
      ratemx=-1.
      time=0.0d0
      prntnw=0.
      swlat1=-1.d0
      tauto1=-1.d0
      recomb=0.0d0
      subgrn=0.d0
      precip=0.d0
      clster=0.d0
      voids=0.0d0
      swlcmp=0.0d0
      swlrat=0.d0
      bubble=0.0d0
      disloc=0.0d0
      floop=0.0d0
      vdrecm=0.0d0
      vdemit=0.0d0
      tvdvac=0.0d0
      intbbl=0.0d0
      intflp=0.0d0
      intnet=0.0d0
      intppt=0.0d0
      intrec=0.0d0
      intsbg=0.0d0
      intvcl=0.0d0
      intvd=0.0d0
      appmhe=0.0d0
      mtrxhe=0.0d0
      ntdhe=0.0d0
      intcon=0.d0
      vaccon=0.d0
      vacgnr=0.d0
      pntcls=0
      read(5,902)title1
      read(5,902)title2
ccccccccccccccccccccccccccccccccccccccccccccccccccccccccccccccccccccccc
c                                                                      c
c                                                                      c
c       several switches giving the user program control are           c
c       read in initially. their meanings are given here:              c
c                                                                      c
c       tmpchg = the number of temperature changes which occur         c
c                during the run (.le.9) at totdos=doschg,              c
c                tempno=tmpchg+1=number of temperatures                c
c                                                                      c
c                                                                      c
c       hfrflg = 0,  constant helium generation rate (ebr-ii)          c
c              = 1,  time dependent helium generation rate (hfir)      c
c                                                                      c
c       pfact;   a table of intermediate output is printed after       c
c                every 'pfact' converged time steps, pfact = 0 will    c
c                suppress this output                                  c
c                                                                      c
cccccccccccccccccccccccccccccccccccccccccccccccccccccccccccccccccccccccc
      write(6,904)
      write(6,903)
      read(5,901)  em,ef,eim,ec2dis,ec3dis,ehemig
      write(6,901) em,ef,eim,ec2dis,ec3dis,ehemig
      read(5,901)  diffv0,diffi0,alfodi,hegnrr,hefrac
      write(6,901) diffv0,diffi0,alfodi,hegnrr,hefrac
      read(5,901)  intgnr,caseff,zin,zvn,zil0,zvl0
      write(6,901) intgnr,caseff,zin,zvn,zil0,zvl0
      read(5,901)  tc(1),disntd,stress,stfeng,rc
      write(6,901) tc(1),disntd,stress,stfeng,rc
      read(5,901)  fracls,numvcl,radvcl,gamvcl,snkerr
      write(6,901) fracls,numvcl,radvcl,gamvcl,snkerr
      read(5,901)  dumrad,srcden,prmt1,prmt2,prmt3,prmt4
      write(6,901) dumrad,srcden,prmt1,prmt2,prmt3,prmt4
      read(5,901)  relerr,aberr1,aberr2,aberr3,aberr4
      write(6,901) relerr,aberr1,aberr2,aberr3,aberr4
      read(5,899)  zi1,zi2,zi3,zi4,zv2,zv3,zv4
      write(6,899) zi1,zi2,zi3,zi4,zv2,zv3,zv4
      read(5,901)   pptrad,pptcon,ppttau
      write(6,901) pptrad,pptcon,ppttau
```

```
      read(5,901)   graind,grnmax,grntau
      write(6,901) graind,grnmax,grntau
      read(5,901)   stop,prntdt,bgdlt0,dtinit,dtmax,dtrtrn
      write(6,901)  stop,prntdt,bgdlt0,dtinit,dtmax,dtrtrn
      read(5,900)   pptflg,mf,hfrflg,pfact,tmpchg
      write(6,900) pptflg,mf,hfrflg,pfact,tmpchg
      read(5,900)   iclflg,lclas1,lclas2,nclass,cavflg
      write(6,900)  iclflg,lclas1,lclas2,nclass,cavflg
cccccccccccccccccccccccccccccccccccccccccccccccccccccccccccccccccccccccc
c                                                                       c
c         read cavity parameters for each class                         c
c                                                                       c
cccccccccccccccccccccccccccccccccccccccccccccccccccccccccccccccccccccccc
      read(5,901)  (voidcn(i),i=1,nclass)
      write(6,901) (voidcn(i),i=1,nclass)
      read(5,901)  (fv(i),i=1,nclass)
      write(6,901) (fv(i),i=1,nclass)
      read(5,901)  (fs(i),i=1,nclass)
      write(6,901) (fs(i),i=1,nclass)
      read(5,901)  (gamma(i),i=1,nclass)
      write(6,901) (gamma(i),i=1,nclass)
      read(5,901) (helium(i),i=1,nclass )
      write(6,901) (helium(i),i=1,nclass )
      if(cavflg.le.0) go to 1
      read(5,*) pcav
      cavfct=(hegnrr/3.50d-13)**pcav
      write(6,898) pcav,cavfct
      go to 2
 1    cavfct=1.0d0
 2    vclcls=nclass+1
      nplus1=nclass+1
      if(iclflg.ne.1) go to 5
      lclass=lclas1+lclas2
      flpcls=nclass+lclass-1
      vclcls=nclass+lclass+1
      netcls=nclass+lclass
      l1mns1=lclas1-1
      l1pls1=lclas1+1
      lmns1=lclass-1
      lpls1=lclass+1
      do 3 i=1,lpls1
 3    lpnum(i)=1.0d0
 5    disn0=disntd
      distot=disntd
      displd=0.0d0
      numilp=0.d0
      hegnr0=hegnrr
      grnd0=graind
      snktst=0.d0
      intgn2=intgnr
      intgnr=intgnr*caseff
      pi=3.14159265d0
cccccccccccccccccccccccccccccccccccccccccccccccccccccccccccccccccccccccc
c                                                                       c
c    set switches to signal printing of table and plotting              c
c                                                                       c
cccccccccccccccccccccccccccccccccccccccccccccccccccccccccccccccccccccccc
      outsw=pfact-1
      delout=stop/50.0
      pltflg=delout
cccccccccccccccccccccccccccccccccccccccccccccccccccccccccccccccccccccccc
c                                                                       c
c     the following are the polynomial master curve coefficients        c
c      ai for ncrit; bi for rcrit; ci for real gas radius               c
c      Stoller and Odette, J.N.M. 131 (1985)                            c
c                                                                       c
cccccccccccccccccccccccccccccccccccccccccccccccccccccccccccccccccccccccc
      a0= 1.1802288d+00
      a1=-7.9391797d-01
      a2= 5.7059961d-01
      a3=-2.7545689d-01
      a4= 8.4271137d-02
      a5=-1.6549585d-02
      a6= 2.1091198d-03
      a7=-1.7313693d-04
      a8= 8.8188621d-06
      a9=-2.5326847d-07
      a10=3.1317501d-09
      b0= 1.3368825d+00
```

```
      b1= 3.8733464d-01
      b2=-3.2338567d-01
      b3= 1.6904814d-01
      b4=-5.4081633d-02
      b5= 1.0909847d-02
      b6=-1.4139331d-03
      b7= 1.1733086d-04
      b8=-6.0190901d-06
      b9= 1.7369785d-07
      b10=-2.1550751d-09
      c0=-7.3006207d-03
      c1= 4.5820315d+00
      c2=-1.3153813d+01
      c3= 4.0631158d+01
      c4=-1.1590146d+02
      c5= 2.3303617d+02
      c6=-3.0597821d+02
      c7= 2.5718364d+02
      c8=-1.3349066d+02
      c9= 3.8976532d+01
      c10=-4.8969485d+00
      pptsnk=0.0
      if(time.ge.ppttau) pptsnk=4.*pi*pptcon*pptrad
      do 10 i=1,nclass
      ttconv(i)=-1.0
      bbconv(i)=-1.0
      press(i)=0.0
      delhe(i)=0.0
      bblflg(i)=1
      vdflg(i)=0
      ncritr(i)=1.0d+8
      voidcn(i)=cavfct*voidcn(i)
      if(fs(i) .gt. 0.0d0) go to 6
      fs(i)=4.*pi
      go to 7
 6    fs(i)=fs(i)*4.*pi
 7    if(fv(i) .gt. 0.0d0) go to 8
      fv(i)=4.*pi/3.
      go to 10
 8    fv(i)=fv(i)*4.*pi/3.
 10   continue
ccccccccccccccccccccccccccccccccccccccccccccccccccccccccccccccccccccccc
c                                                                       c
c         initialization of necesary parameters and variables.          c
c                                                                       c
c      kboltz = boltzmann's constant ( ergs/deg. k )                    c
c      kt = kt                                                          c
c      bvectd = dislocation burger's vector (cm)                        c
c      bvectf = faulted loop burger's vector (cm)                       c
c      omega = atomic volume (cm 3)                                     c
c      diffv0 = vacancy diffusivity pre-exponential                     c
c      diffi0 = interstitial diffusivity pre-exponential                c
c      graind = grain diameter                                          c
c      comprs = compressability of helium                               c
c      ao = lattice parameter (cm)                                      c
c      shrmod = shear modulus (ergs/cm**3) from nsmh                    c
c                                                                       c
c      where it appears, the value 8.524d16 represents the atomic       c
c      density of 316ss divided by 1.0d6 to yield appm                  c
c                                                                       c
ccccccccccccccccccccccccccccccccccccccccccccccccccccccccccccccccccccccc
      ao=3.58d-8
      omega=ao**3/4.
      bvectf=ao/dsqrt(3.0d0)
      bvectd=ao/dsqrt(2.0d0)
      if(rc.lt.0.5 .or. rc.gt.5) write(6,*) 'BAD rc value, rc=2*b'
      if(rc.lt.0.5 .or. rc.gt.5) rc=2.d0*bvectd
      if(rc.gt.0.49) rc=rc*bvectd
      ro=1./dsqrt(pi*distot)
      rhosnk=2.*pi/dlog(ro/rc)
      stckft=omega*stfeng/bvectf
      kboltz=1.38062d-16
      numvac=4.*pi*radvcl**3/3./omega
      genvcl=intgnr*fracls/numvac/omega
      if(iclflg .ne. 1) go to 18
      lprad(1)=dsqrt(dsqrt(3.d0)/pi)*ao
      lprad(lclas1)=dumrad
      lprad(lpls1)=1.d0/prmt1/dsqrt(distot)
      delr=(lprad(lclas1)-lprad(1)) / l1mns1
```

```
      tmpr=lprad(1)
      do 12 i=2,l1mns1
 12   lprad(i)=tmpr+delr*(i-1)
      lprad(lclass)=1.0/prmt1/dsqrt(5.d11)
      delr=( lprad(lclass)-lprad(lclas1) ) / lclas2
      j=0
      tmpr=lprad(lclas1)
      do 14 i=l1pls1,lmns1
      j=j+1
 14   lprad(i)=tmpr+delr*(j)
ccccccccccccccccccccccccccccccccccccccccccccccccccccccccccccccccccccccc
c                                                                      c
c     initialize all temperature dependent parameters                  c
c                                                                      c
ccccccccccccccccccccccccccccccccccccccccccccccccccccccccccccccccccccccc
 18   tempno=tmpchg+1
      doschg(1)=intgn2*stop*1.01
      if(tempno.eq.1) go to 20
      read(5,901) (tc(i), i=2,tempno)
      write(6,901) (tc(i), i=2,tempno)
      read(5,901)  (doschg(i), i=1,tmpchg)
      write(6,901) (doschg(i), i=1,tmpchg)
      doschg(tempno)=intgn2*stop*1.01
 20   write(6,903)
      do 9991 jtemp=1,tempno
      doschk=doschg(jtemp)
      temp=tc(jtemp)
      tk=temp+273.16
      tf=temp*1.8d0 + 32.0d0
      kt=kboltz*tk
      omovkt=omega/kt
      diffv=diffv0*dexp(-em*1.602d-12/kt)
      diffi=diffi0*dexp(-eim*1.602d-12/kt)
      alpha=diffi*alfodi
      vaccne=dexp(-ef*1.602d-12/kt)
      cvn=vaccne*dexp(stress*omovkt)
      cvemit=2.*vaccne/3.+cvn/3.
      gasd=3.135d-8*(0.8542 - 0.03996*dlog(tk/9.16d0) )
      if(gamvcl .gt. 2.d0) go to 23
      gamvcl=gamvcl*(4050.d0 - 1.75d0*temp)
 23   continue
      cvcls=vaccne*dexp(2.*gamvcl*omovkt/radvcl)
      do 25 i=1,nclass
      cvv(i)=vaccne
      if(gamma(i) .gt. 2.d0) go to 25
      gamma(i)=gamma(i)*(4050.d0 - 1.75d0*temp)
 25   continue
      shrmod=11.2476-tf*(1.64275d-3+tf*(1.330819d-6-tf*3.567476d-10))
      shrmod=shrmod*6.894757d10
      if(iclflg.ne.1) go to 28
ccccccccccccccccccccccccccccccccccccccccccccccccccccccccccccccccccccccc
c         initialize some values for dislocation calculation           c
c                                                                      c
c       ro=1/2 mean dislocation spacing                                c
c       rc=effective capture radius of dislocation                     c
c       ec2dis=dissociation energy of di-interstitial                  c
c       e32dis=dissociation energy of tri-interstitial                 c
c                                                                      c
c       calculate critical radius and set loop class radii             c
c                                                                      c
c     if size dependent loop bias of Wolfer and Ashkin are used,       c
c     compute root terms for loop bias (zil0, zvl0)                    c
c                                                                      c
c     vv and vi are vacancy and interstitial relaxation volumes        c
c     avk, aik, avg & aig are the bulk and shear polarizabiliies       c
c     for vacancies and interstitials                                  c
c                                                                      c
ccccccccccccccccccccccccccccccccccccccccccccccccccccccccccccccccccccccc
      vv=-0.2*omega
      vi=1.4*omega
      avg=-15.
      aig=-150.
      avk=-150.
      aik=100.
      kev=8.61727d-5
      nu=.3
c     zltmp1=-1./21.*((1.+nu)/(1.-nu))**2/1024./kev                    zil-r
c     zltmp2=(3./32./(1-nu))**2*(4./3.)**2                             zil-r
c     zltmp3=3./7.*(2./7.*(1.-2.*nu)*3.25/kboltz)**2                   zil-r
```

```
c      zltmp4=73./1155.*(1.-2.*nu)**2/kev                                zil-r
c      zltmp5=(-530.-1460.*nu+1371*nu**2)/11./9./7./5./3./kev            zil-r
c      zil0=bvectf**2 * (zltmp1*aig + zltmp2 *                           zil-r
c     1 ( zltmp3*vi*shrmod**2*vi/tk + zltmp4*aik + zltmp5*aig) ) / tk    zil-r
c      zvl0=bvectf**2 *                                                  zil-r
c     1 (zltmp1*avg+zltmp2*(zltmp3*vv*shrmod**2*vv/tk+zltmp4*avk        zil-r
c     2 +zltmp5*avg))/tk                                                zil-r
       bi1o=zi1*diffi/ao**2
       bi2o=zi2*diffi/ao**2
       bi3o=zi3*diffi/ao**2
       bi4o=zi4*diffi/ao**2
       bv2o=zv2*diffv/ao**2
       bv3o=zv3*diffv/ao**2
       bv4o=zv4*diffv/ao**2
       c2dis=diffi*dexp(-ec2dis*1.602d-12/kt)/ao**2
       c3dis=diffi*dexp(-ec3dis*1.602d-12/kt;/ao**2
       do 27 i=1,lpls1
       zil(i)=zil0                                                       zil-r
       zvl(i)= zvl0                                                      zil-r
c      zil(i)=dmin1(3.5d0, (zin + zil0/lprad(i)**2) )                    zil-r
c      zvl(i)= zvn + zvl0/lprad(i)**2                                    zil-r
       linetn=shrmod*bvectf*omega/2.8/pi/lprad(i)*
      1 dlog(4.d0*lprad(i)/bvectf)
       dedm=dmin1(30.0d0,linetn+stckft)
 27    cvl(i)=vaccne*dexp(-dedm/kt)
 28    if( jtemp.gt. 1 ) go to 285
ccccccccccccccccccccccccccccccccccccccccccccccccccccccccccccccccccccc
c                                                                       c
c         compute initial bubble radius and pressure                    c
c         equation of state from:                                       c
c            brearley & macinnes, j.nuc.mat,(95),1980                   c
c                                                                       c
c         1.  compute voidrd for zero supersaturation                   c
c         2.  compute ci and cv with approx. voidrd and vclsnk.  then   c
c             recompute vclsnk (std. st. approx.) and then new ci, cv   c
c             to obtain better guess of sprsat.                         c
c         3. recompute voidrd using master curve with new sprsat        c
c                                                                       c
ccccccccccccccccccccccccccccccccccccccccccccccccccccccccccccccccccccc
c 1.  **********                                                        c
       do 40 i=1,nclass
       j=0
       rad=2.0d-8
 30    rho=helium(i)/fv(i)/rad**3
       j=j+1
       if(j.gt.100) go to 35
       yz=pi*gasd**3*rho/6.d0
       z=(1. + yz + yz**2 - yz**3) / (1. - yz)**3
       if(yz .gt. 0.5) z=3.0573d-1*dexp(yz*7.5d0)
       radprt=helium(i)*kt/2./gamma(i)/fv(i)/rad**2
       voidrd(i)=( helium(i)*gasd**3/8./
      1 (1.-(radprt*(1.+yz*yz**2-yz**3) )**(1./3.)) )**(1./3.)
       if( dabs(voidrd(i)-rad) .lt. 1.d-6*rad ) go to 40
       rad=voidrd(i)
       go to 30
 35    voidrd(i)=2.50d-8*dsqrt(3.*helium(i)*kt*1.d+16/8./pi/gamma(i))
       write(6,940) i,voidrd(i)
 40    continue
ccccccccccccccccccccccccccccccccccccccccccccccccccccccccccccccccccccc
c 2.  **********                                                        c
       vclsnk=dmin1( 1.d13, fracls*intgn2*3.86d32*dexp(-0.0472*tk) )
       write(6,*) '  -->> vclsnk initialization=',vclsnk
       sprsat=1.d0
       tmpspr=sprsat
       cvsnk0=fcnsnk(voidrd,voidcn,nclass,fs,pi,bblflg,bbsnk0,vdsnk0)
       i=0
       cilo=1.d-15
       cihi=1.0d-07
       cvgues=5.d-08
 42    call pntdef
       i=i+1
       tauvcl=dmax1(0.0d0,
      1 -radvcl**2/3./(diffv*(vaccon-cvcls)-diffi*intcon))
       numvcl=genvcl*tauvcl
       vclsnk=4.*pi*numvcl*radvcl
       if( dabs((tmpspr-sprsat)/sprsat) .lt. 1.d-3) go to 43
       tmpspr=sprsat
       go to 42
 43    write(6,941) i,vclsnk,sprsat
```

```
ccccccccccccccccccccccccccccccccccccccccccccccccccccccccccccccccccccccc
c 3.  **********                                                        c
      lns=dlog(sprsat)
      do 50 i=1,nclass
      if(sprsat.le.1.00001d0) go to 46
      tmp=gamma(i)*omega/lns/kt
      y2=helium(i)*omega/lns
      p2=2./3.*tmp
      angle=(1.d0-27.d0*y2/16./fv(i)/tmp**3)
      theta=dacos(angle)/3.
      idlrad(1)=p2*(1.+2.*dcos(theta))
      idlrad(2)=p2*(1.+2.*dcos(theta+2.*pi/3.))
      idlrad(3)=p2*(1.+2.*dcos(theta+4./3.*pi))
      idealr(i)=1.d30
      do 44 j=1,3
      if(idlrad(j) .lt. 0.d0) go to 44
      idealr(i)=dmin1(idealr(i),idlrad(j))
 44   continue
      rs=(idealr(i)*kt/gamma(i))**(1./3.)*1.d7
       f3=c0+rs*(c1+rs*(c2+rs*(c3+rs*(c4+rs*(c5+rs*(c6+rs*
     1 (c7+rs*(c8+rs*(c9+rs*c10)))))))))
      voidrd(i)=idealr(i)/f3
 46   rhohe(i)=helium(i)/fv(i)/voidrd(i)**3
      yz=pi*gasd**3*rhohe(i)/6.d0
      comprs(i)=(1.d0+yz+yz**2-yz**3)/(1.d0-yz)**3
      if(yz .gt. 0.5) comprs(i)=3.0573d-1*dexp(yz*7.5d0)
      press(i)=rhohe(i)*kt*comprs(i)
      cvv(i)=fcncvv(kt,omega,vaccne,gamma(i),voidrd(i),press(i),i)
  50  continue
      cvsnk0=fcnsnk(voidrd,voidcn,nclass,fs,pi,bblflg,bbsnk0,vdsnk0)
ccccccccccccccccccccccccccccccccccccccccccccccccccccccccccccccccccccccc
c                                                                       c
c        compute bubble nucleation dose                                 c
c                                                                       c
ccccccccccccccccccccccccccccccccccccccccccccccccccccccccccccccccccccccc
      taupo=0.0d0
      cavhe=0.0d0
      do 60 i=1,nclass
      cavhe=cavhe+voidcn(i)*helium(i)/8.524d+16
  60  taupo=taupo+voidcn(i)*helium(i)
      taup=taupo*omega/hegnrr*intgnr
ccccccccccccccccccccccccccccccccccccccccccccccccccccccccccccccccccccccc
c                                                                       c
c     compute initial point defect concentrations using  the            c
c     values of voidrd and vclsnk computed above.  make initial         c
c     calls to const and table.                                         c
c                                                                       c
ccccccccccccccccccccccccccccccccccccccccccccccccccccccccccccccccccccccc
      call pntdef
c     tauvcl=dmax1(0.0d0,                                                ssvcl
c    1 -radvcl**2/3./(diffv*(vaccon-cvcls)-diffi*intcon))                ssvcl
c     numvcl=genvcl*tauvcl                                               ssvcl
c     vclsnk=4.*pi*numvcl*radvcl                                         ssvcl
      hespr=dmax1(1.d0,sprsat)
      diffhe=hespr*dexp(-ehemig*1.602d-12/kt)
      snkrat=rhosnk*distot/cvsnkv
      call const(aberr1,aberr2,aberr3,aberr4,caseff,relerr)
      call table(snkrat,swlrat)
      if(time .lt. 1.0) go to 250
 70   if(iclflg .eq. 1) go to 85
 80   tplsdt=time+dtrtrn
ccccccccccccccccccccccccccccccccccccccccccccccccccccccccccccccccccccccc
c                                                                       c
c       for the case with no equations to integrate, subroutine         c
c       bgrow takes individual time steps.                              c
c                                                                       c
ccccccccccccccccccccccccccccccccccccccccccccccccccccccccccccccccccccccc
      call bgrow( bgdlt0,dtmax,
     1  disntd,rhosnk,tplsdt,bblflg,vdflg,cnvchk,hfrflg,nclass)
      go to 125
 85   if(time .lt. 1.0) tplsdt=time+dtrtrn
ccccccccccccccccccccccccccccccccccccccccccccccccccccccccccccccccccccccc
c                                                                       c
c       initialize values for use by dlsode                             c
c                                                                       c
ccccccccccccccccccccccccccccccccccccccccccccccccccccccccccccccccccccccc
      istate=1
      itask=1
      itol=2
```

```
      iopt=1
      rwork(5)=dtinit
      rwork(6)=dtmax
      iwork(6)=10000
      rtol(1)=relerr
      lrw=2972
      liw=70
      crntim=time
c     noeq=0                                                          ssvcl
      noeq=1                                                          ssvcl
      if(iclflg .eq. 1) noeq=noeq+lclass
      j=0
      do 90 i=1,nclass
      if(bblflg(i).eq.1) go to 90
      noeq=noeq+1
      j=j+1
      y(j)=voidrd(i)
      atol(j)=aberr1
 90   dery(i)=1.d-18
      if(iclflg .ne. 1) go to 100
      k=nclass
      do 95 i=2,lclass
      k=k+1
      j=j+1
      y(j)=lpnum(i)
      atol(j)=aberr2
 95   dery(k)=1.d-17
      y(j+1)=disntd
      atol(j+1)=aberr3
      dery(netcls)=1.d-16
 100  continue
      nqmns1=noeq-1
      nqmns2=noeq-2
      y(noeq)=numvcl                                                  ssvcl
      atol(noeq)=aberr4                                               ssvcl
      dery(vclcls)=1.d-15                                             ssvcl
      neq(1)=noeq
      cnvchk=0
      if(time .gt. 1.0) call table(snkrat,swlrat)
cccccccccccccccccccccccccccccccccccccccccccccccccccccccccccccccccccccccc
c                                                                       c
c     call dlsode to integrate the rate quations for cavities and       c
c     dislocation loops and network (if iclflg=1)                       c
c                                                                       c
cccccccccccccccccccccccccccccccccccccccccccccccccccccccccccccccccccccccc
 120  call lsode( grow, neq, y, crntim, tplsdt, itol, rtol, atol,
     1 itask,istate,iopt,rwork,lrw,iwork,liw,dumsub,mf)
cccccccccccccccccccccccccccccccccccccccccccccccccccccccccccccccccccccccc
c                                                                       c
c     update helium level, vacancy accounting and bubble radii          c
c                                                                       c
cccccccccccccccccccccccccccccccccccccccccccccccccccccccccccccccccccccccc
      call vaccnt(dtrtrn,bblflg,iclflg,lclass,nclass,pptflg,vdflg)
      call helprt(dtrtrn,disntd,omega,rhosnk,bblflg,vdflg,hfrflg,nclass)
      call bubrad(bblflg,vdflg,cnvchk,dtrtrn,nclass)
      time=crntim
cccccccccccccccccccccccccccccccccccccccccccccccccccccccccccccccccccccccc
c                                                                       c
c     check for error state upon return, terminate if istate<-1         c
c                                                                       c
cccccccccccccccccccccccccccccccccccccccccccccccccccccccccccccccccccccccc
      if(istate .le. -2) go to 310
      if(istate .eq. 2) go to 125
      write(6,927) mf,rwork(13),rwork(11),rwork(12)
      write(6,939) istate,iwork(11),iwork(12),pntcls
      istate=2
 125  totdos=intgn2*time
      swlrat=0.d0
      do 130 i=1,nclass
      swlrat=swlrat+3.*fv(i)*voidcn(i)*voidrd(i)**2*dery(i)*100./intgn2
      mpa(i)=press(i)*1.d-07
 130  continue
      if(swlrat.gt.ratemx) tausmx=totdos
      ratemx=dmax1(ratemx,swlrat)
      if(time.ge.ppttau) pptsnk=4.*pi*pptcon*pptrad
      if(time.lt.prntnw) go to 250
       write(6,960) rwork(13),rwork(11),rwork(12)
      sschk=vclsnk*(diffi*intcon+diffv*(cvcls-vaccon))
      vacrec=alpha*intcon/diffv/tsinkv
```

```
      intrec=alpha*vaccon/diffi/tsinki
      snkrat=rhosnk*distot/cvsnkv
      swell=fcntvv(voidcn,voidrd,fv,nclass)*100.
      write(6,918) totdos,time,swell,swlrat,sprsat
      write(6,919) vaccon,intcon,delflx,vacgnr,snkrat
      write(6,949) vacrec,intrec,tsinki,tsinkv,rhosnk
      write(6,948) emvoid,embbl,emdisl,emvcl,emsubg,emppt
      write(6,920) cvsnkv,vdsnk,bbsnk,cvsnk0,vdsnk0,bbsnk0
      write(6,921) zin,distot,ksbgv,ksbgi,graind,pptsnk
      write(6,922) hegnrr,appmhe,mtrxhe,cavhe,subghe,ntdhe
      write(6,923) vclsnk,numvcl,tauvcl,genvcl,dery(vclcls),sschk        ssvcl
c     write(6,923) vclsnk,numvcl,tauvcl,genvcl,sschk                     ssvcl
      if(iclflg.ne.1) go to 160
      write(6,956) disntd,irrann,thrann,irrsrc,thrsrc,dery(netcls)
      write(6,951) dicon,tricon,tetcon,ncrate,tau4
      write(6,957) numilp,displd,avlprd,emflp
      write(6,952)
      write(6,953) lprad(1),lpnum(1),zil(1),zvl(1),cvl(1)
      do 150 i=2,lclass
      j=nclass+i-1
 150  write(6,954) lprad(i),lpnum(i),zil(i),zvl(i),cvl(i),dery(j),
     1 rate(i)
      write(6,955) lprad(lpls1),lpnum(lpls1),zil(lpls1),zvl(lpls1),
     1 cvl(lpls1),rate(lpls1)
 160  write(6,925)
      write(6,926)  (bblflg(i),voidrd(i),voidcn(i),dery(i),ncritr(i),
     1 helium(i),delhe(i),mpa(i),comprs(i),cvv(i),cfacv(i),cfaci(i),
     2 i=1,nclass)
      prntnw=prntnw+prntdt
ccccccccccccccccccccccccccccccccccccccccccccccccccccccccccccccccccccc
c                                                                      c
c     update array containing microstructural data for plot at end     c
c                                                                      c
ccccccccccccccccccccccccccccccccccccccccccccccccccccccccccccccccccccc
 250  if ( time .ge. 0.999999*stop ) go to 255
      if ( time .lt. pltflg) go to 270
      pltflg=pltflg+delout
 255  nplt=nplt+1
      swlplt(nplt,1)=totdos
      swlplt(nplt,2)=fcntvv(voidcn,voidrd,fv,nclass)*100.
      if(iclflg.ne.1)go to 257
      dntplt(nplt,1)=totdos
      dlpplt(nplt,1)=totdos
      dttplt(nplt,1)=totdos
      lnmplt(nplt,1)=totdos
      dntplt(nplt,2)=disntd
      dlpplt(nplt,2)=displd
      dttplt(nplt,2)=distot
      lnmplt(nplt,2)=numilp
 257  if(swlplt(nplt,2).lt.1.0 .or. tauto1.gt.0.d0) go to 260
      swlto1=swlplt(nplt,2)
      tauto1=totdos
 260  continue
      if( time .ge. 0.999999*stop ) go to 290
c270  if (time .lt. 1.0) go to 70                                       ssvcl
 270  if (time .lt. 1.0) go to 85                                       ssvcl
ccccccccccccccccccccccccccccccccccccccccccccccccccccccccccccccccccccc
c                                                                      c
c     check for temperature change and adjust if appropriate           c
c                                                                      c
ccccccccccccccccccccccccccccccccccccccccccccccccccccccccccccccccccccc
      if(totdos.lt.0.999d0*doschk) go to 285
      go to 330
 285  continue
      if(noeq.eq.0 .and. cnvchk.eq.0) go to 80
      tplsdt=time+dtrtrn
      if(cnvchk.ne.0) go to 85
      go to 120
ccccccccccccccccccccccccccccccccccccccccccccccccccccccccccccccccccccc
c                                                                      c
c      stoping time reached: make final variable printout and          c
c      plot microstructural parameters vs time                         c
c                                                                      c
ccccccccccccccccccccccccccccccccccccccccccccccccccccccccccccccccccccc
 290  continue
      call table(snkrat,swlrat)
      swlplt(1,1)=0.
      swlplt(1,2)=0.0
      write(6,904)
```

```
      swlflg=1
       call plot(swlplt,nplt,22,110,swlflg)
      write(6,905)
      write(6,942) temp,disn0,zin,grnd0,graind
      write(6,943) eim,em,ef,diffi0,diffv0
      if(iclflg.eq.1)
     1    write(6,950) ec2dis,ec3dis,zi1,zi2,zi3,zi4,zv2,zv3,zv4
      write(6,944) alfodi,intgn2,caseff,(voidcn(i),i=1,nclass)
      if(iclflg.eq.1)write(6,945) prmt1,prmt2,prmt3,prmt4
      do 295 i=1,nclass
      if(ttconv(i).ge.0.0) write(6,929) i,ttconv(i)
      if(ttconv(i).ge.0.0) write(6,930) i,bbconv(i)
      if(ttconv(i).lt.0.0) write(6,932) i
 295  continue
      taut=tauto1+taup
      write(6,933) swlto1,taut
      write(6,935) tauto1
      write(6,936) taup
      if(iclflg.eq.1)
     1 write(6,937) ratemx,tausmx,ilpmax,tauimx,swell,totdos
      if(iclflg.ne.1) write(6,934) ratemx,tausmx,swell,totdos
      write(6,939) istate,iwork(11),iwork(12),pntcls
      if(iclflg.ne.1) go to 292
      write(6,904)
      swlflg=0
      dntplt(1,1)=0.
      dntplt(1,2)=disn0
      dttplt(1,1)=0.
      dttplt(1,2)=disn0
      dlpplt(1,1)=0.
      dlpplt(1,2)=0.
      lnmplt(1,1)=0.
      lnmplt(1,2)=0.
       call plot(dntplt,nplt,22,110,swlflg)
      write(6,906)
       call plot(dlpplt,nplt,22,110,swlflg)
      write(6,907)
      write(6,904)
       call plot(lnmplt,nplt,22,110,swlflg)
      write(6,908)
       call plot(dttplt,nplt,22,110,swlflg)
      write(6,909)
 292  write(6,904)
      if(iclflg.eq.1)write(6,958) temp
      if(iclflg.ne.1)write(6,959) temp
      do 300 i=1,nplt
      if(iclflg.ne.1)write(6,946) swlplt(i,1),swlplt(i,2)
 300  if(iclflg.eq.1)write(6,946) swlplt(i,1),swlplt(i,2),dntplt(i,2),
     1   dlpplt(i,2),lnmplt(i,2),dttplt(i,2)
      go to 9999
 310  write(6,927) mf,rwork(13),rwork(11),rwork(12)
      write(6,939) istate,iwork(11),iwork(12),pntcls
      do 320 i=1,noeq
 320  write(6,928) i,y(i),dery(i)
      go to 9999
 330  write(6,947) totdos,temp,tc(jtemp+1)
ccccccccccccccccccccccccccccccccccccccccccccccccccccccccccccccccccccc
c                                                                     c
c    reduce time step if needed for a temperature change run          c
c                                                                     c
ccccccccccccccccccccccccccccccccccccccccccccccccccccccccccccccccccccc
c     delta=delta/100.
 9991 continue
 9999 continue
      stop
      end


ccccccccccccccccccccccccccccccccccccccccccccccccccccccccccccccccccccc
c                                                                     c
c                                BGROW                                c
c                                                                     c
c     subroutine to advance time and compute bubble radii if          c
c     dlsode has not been called yet                                  c
c                                                                     c
ccccccccccccccccccccccccccccccccccccccccccccccccccccccccccccccccccccc
      subroutine bgrow ( bgdlt0,dtmax,
     1 disntd,rhosnk,tplsdt,bblflg,vdflg,cnvchk,hfrflg,nclass)
```

```
      implicit real*8 (a-z)
      common /cavprm/ bbconv(5),bbsnk,bbsnk0,cvsnki,cvsnkv,comprs(5),
     1  cfaci(5),cfacv(5),cvsnk0,cvv(5),delhe(5),fs(5),fv(5),gamma(5),
     2  helium(5),mpa(5),ncritr(5),press(5),rhohe(5),
     3  ttconv(5),vdsnk,vdsnk0,voidcn(5),voidrd(5)
      common /defprm/ alpha,ao,bvectd,bvectf,cvcls,cvemit,diffi,diffv,
     1  ef,eim,em,fracls,gamvcl,genvcl,intcon,intgn2,intgnr,kt,
     2  numvac,numvcl,omega,radvcl,sprsat,tauvcl,vaccne,vaccon,
     3  vacgnr,vclsnk,cilo,cihi,cvgues,iflux,vflux,delflx
      common /balrl/ appmhe,bubble,cavhe,clster,dery(50),diffhe,
     1  disloc,doschg(10),doschk,ehemig,embbl,emdisl,emflp,emppt,emsubg,
     2  emvcl,emvoid,floop,gasd,graind,grnd0,grnmax,grntau,hefrac,
     7  intbbl,intflp,intnet,intppt,intrec,intsbg,intvcl,intvd,ksbgi,
     3  hegnr0,hegnrr,ksbgv,mtrxhe,ntdhe,pi,pltflg,pptcon,pptrad,
     4  pptsnk,ppttau,precip,prntdt,prntnw,recomb,stop,stress,
     5  subghe,subgrn,swell,swlcmp,swlto1,taup,tauto1,tc(10),temp,
     6  time,tk,totdos,tsinki,tsinkv,tvdvac,vdemit,vdrecm,voids
      integer bblflg(5),vdflg(5),cnvchk,hfrflg,nclass
cccccccccccccccccccccccccccccccccccccccccccccccccccccccccccccccccccccccc
c                                                                       c
c     update helium level, vacancy accounting, bubble radii            c
c     and cavity sink strengths                                         c
c                                                                       c
cccccccccccccccccccccccccccccccccccccccccccccccccccccccccccccccccccccccc
      bgdelt=bgdlt0
 10   time=time+bgdelt
      call vaccnt(bgdelt,bblflg,iclflg,lclass,nclass,pptflg,vdflg)
      call helprt(bgdelt,disntd,omega,rhosnk,bblflg,vdflg,hfrflg,nclass)
      call bubrad(bblflg,vdflg,cnvchk,bgdelt,nclass)
      cvsnk0=fcnsnk(voidrd,voidcn,nclass,fs,pi,bblflg,bbsnk0,vdsnk0)
      if(cnvchk.ne.0) return
cccccccccccccccccccccccccccccccccccccccccccccccccccccccccccccccccccccccc
c                                                                       c
c     compute new point defect concentrations                           c
c                                                                       c
cccccccccccccccccccccccccccccccccccccccccccccccccccccccccccccccccccccccc
      if( graind .lt. grnmax )
     1 graind=(grnmax - grnd0)*(1.0-dexp(-time/grntau))+grnd0
      oldint=intcon
      oldvac=vaccon
      call pntdef
c     tauvcl=dmax1(0.0d0,                                               ssvcl
c    1 -radvcl**2/3./(diffv*(vaccon-cvcls)-diffi*intcon))               ssvcl
c     numvcl=genvcl*tauvcl                                              ssvcl
c     vclsnk=4.*pi*numvcl*radvcl                                        ssvcl
      hespr=dmax1(1.d0,sprsat)
      diffhe=hespr*dexp(-ehemig*1.602d-12/kt)
cccccccccccccccccccccccccccccccccccccccccccccccccccccccccccccccccccccccc
c                                                                       c
c     scale bgdelt and take one time step                               c
c                                                                       c
cccccccccccccccccccccccccccccccccccccccccccccccccccccccccccccccccccccccc
      deltst=dabs(oldint-intcon)/oldint+dabs(oldvac-vaccon)/oldvac
      if(deltst.le.1.d-2) bgdelt=dmin1(dtmax,1.5d0*bgdelt)
      if(deltst.ge.5.d-2) bgdelt=bgdelt/2.
      if(time.ge.tplsdt) return
      go to 10
      end



cccccccccccccccccccccccccccccccccccccccccccccccccccccccccccccccccccccccc
c                                                                       c
c                                BUBRAD                                 c
c                                                                       c
c     subroutine to compute the critical helium bubble parameters and   c
c     check for bubble-to-void conversion.  while the cavities are      c
c     still bubbles the bubble radius is computed here and this value   c
c     is used rather than the one computed by dlsode.                   c
c                                                                       c
cccccccccccccccccccccccccccccccccccccccccccccccccccccccccccccccccccccccc
      subroutine bubrad(bblflg,vdflg,cnvchk,timdlt,nclass)
      implicit real*8 (a-z)
      common /cavprm/ bbconv(5),bbsnk,bbsnk0,cvsnki,cvsnkv,comprs(5),
     1  cfaci(5),cfacv(5),cvsnk0,cvv(5),delhe(5),fs(5),fv(5),gamma(5),
     2  helium(5),mpa(5),ncritr(5),press(5),rhohe(5),
     3  ttconv(5),vdsnk,vdsnk0,voidcn(5),voidrd(5)
      common /defprm/ alpha,ao,bvectd,bvectf,cvcls,cvemit,diffi,diffv,
     1  ef,eim,em,fracls,gamvcl,genvcl,intcon,intgn2,intgnr,kt,
```

```
     2  numvac,numvcl,omega,radvcl,sprsat,tauvcl,vaccne,vaccon,
     3  vacgnr,vclsnk,cilo,cihi,cvgues,iflux,vflux,delflx
      common /balrl/ appmhe,bubble,cavhe,clster,dery(50),diffhe,
     1  disloc,doschg(10),doschk,ehemig,embbl,emdisl,emflp,emppt,emsubg,
     2  emvcl,emvoid,floop,gasd,graind,grnd0,grnmax,grntau,hefrac,
     7  intbbl,intflp,intnet,intppt,intrec,intsbg,intvcl,intvd,ksbgi,
     3  hegnr0,hegnrr,ksbgv,mtrxhe,ntdhe,pi,pltflg,pptcon,pptrad,
     4  pptsnk,ppttau,precip,prntdt,prntnw,recomb,stop,stress,
     5  subghe,subgrn,swell,swlcmp,swlto1,taup,tauto1,tc(10),temp,
     6  time,tk,totdos,tsinki,tsinkv,tvdvac,vdemit,vdrecm,voids
      common /mscoef/ a0,a1,a2,a3,a4,a5,a6,a7,a8,a9,a10,
     1                b0,b1,b2,b3,b4,b5,b6,b7,b8,b9,b10,
     2                c0,c1,c2,c3,c4,c5,c6,c7,c8,c9,c10
      integer cnvchk,nclass,bblflg(5),vdflg(5),i,j
      dimension idealr(5),idlrad(3)
      do 250 i=1,nclass
      oldrad=voidrd(i)
      if(sprsat.le.1.d0) go to 236
      lns=dlog(sprsat)
      tmp=gamma(i)*omega/lns/kt
      f1=a0+lns*(a1+lns*(a2+lns*(a3+lns*(a4+lns*(a5+lns*(a6+lns*
     1 (a7+lns*(a8+lns*(a9+lns*a10)))))))))
      f2=b0+lns*(b1+lns*(b2+lns*(b3+lns*(b4+lns*(b5+lns*(b6+lns*
     1 (b7+lns*(b8+lns*(b9+lns*b10)))))))))
      ncritr(i)=f1*fv(i)*tmp*tmp*gamma(i)/kt
      rcritr=f2*tmp
      if(bblflg(i).eq.0) go to 250
      if(helium(i).ge.ncritr(i)) go to 248
cccccccccccccccccccccccccccccccccccccccccccccccccccccccccccccccccccccc
c                                                                      c
c      here compute the ideal gas roots using an analytical solution.  c
c                                                                      c
cccccccccccccccccccccccccccccccccccccccccccccccccccccccccccccccccccccc
      y2=helium(i)*omega/lns
      p2=2./3.*tmp
      angle=(1.d0-27.d0*y2/16./fv(i)/tmp**3)
      theta=dacos(angle)/3.
      idlrad(1)=p2*(1.+2.*dcos(theta))
      idlrad(2)=p2*(1.+2.*dcos(theta+2.*pi/3.))
      idlrad(3)=p2*(1.+2.*dcos(theta+4./3.*pi))
      idealr(i)=1.d30
      do 232 j=1,3
      if(idlrad(j) .lt. 0.d0) go to 232
      idealr(i)=dmin1(idealr(i),idlrad(j))
 232  continue
cccccccccccccccccccccccccccccccccccccccccccccccccccccccccccccccccccccc
c                                                                      c
c     shift the ideal gas radius to fit master curve                   c
c                                                                      c
cccccccccccccccccccccccccccccccccccccccccccccccccccccccccccccccccccccc
      rs=(idealr(i)*kt/gamma(i))**(1./3.)*1.d7
      f3=c0+rs*(c1+rs*(c2+rs*(c3+rs*(c4+rs*(c5+rs*(c6+rs*
     1 (c7+rs*(c8+rs*(c9+rs*c10)))))))))
      voidrd(i)=idealr(i)/f3
      go to 246
cccccccccccccccccccccccccccccccccccccccccccccccccccccccccccccccccccccc
c                                                                      c
c   if sprsat.le.0, compute voidrd as if sprsat=0                      c
c                                                                      c
cccccccccccccccccccccccccccccccccccccccccccccccccccccccccccccccccccccc
 236  j=0
      rad=voidrd(i)
 238  rho=helium(i)/fv(i)/rad**3
      j=j+1
      if(j.gt.100) go to 240
      yz=pi*gasd**3*rho/6.d0
      z=(1. + yz + yz**2 - yz**3) / (1. - yz)**3
      if(yz .gt. 0.5) z=3.0573d-1*dexp(yz*7.5d0)
      radprt=helium(i)*kt/2./gamma(i)/fv(i)/rad**2
      newrad=( helium(i)*gasd**3/8./
     1 (1.-(radprt*(1.+yz*yz**2-yz**3) )**(1./3.)) )**(1./3.)
      if( dabs(newrad-rad) .lt. 1.d-6*rad ) go to 244
      rad=newrad
      go to 238
 240  voidrd(i)=1.01*oldrad
      write(6,8900) i,j,time,newrad,oldrad,helium(i),sprsat
 8900 format(' ','i,j,time,newrad,oldrad,helium(i),sprsat=',/,' ',
     1 2i3,1p5d10.2)
      go to 246
```

```
 244  voidrd(i)=newrad
 246  rhohe(i)=helium(i)/fv(i)/voidrd(i)**3
      yz=pi*gasd**3*rhohe(i)/6.d0
      comprs(i)=(1.d0+yz+yz**2-yz**3)/(1.d0-yz)**3
      if(yz .gt. 0.5) comprs(i)=3.0573d-1*dexp(yz*7.5d0)
      press(i)=rhohe(i)*kt*comprs(i)
      cvv(i)=fcncvv(kt,omega,vaccne,gamma(i),voidrd(i),press(i),i)
      dery(i)=(voidrd(i)-oldrad)/timdlt
      go to 250
cccccccccccccccccccccccccccccccccccccccccccccccccccccccccccccccccccccc
c                                                                      c
c      the bubble has become a void.  change bblflg to 0 and          c
c      change other parameters to reflect the time, radius,           c
c      etc.  print the proper message.                                 c
c                                                                      c
cccccccccccccccccccccccccccccccccccccccccccccccccccccccccccccccccccccc
 248  bblflg(i)=0
      vdflg(i)=1
      ttconv(i)=time
      bbconv(i)=voidrd(i)
      write(6,910)
      write(6,911)
      write(6,912) time,i,voidrd(i),helium(i),delhe(i),rcritr,
     1   ncritr(i),idealr(i),comprs(i),sprsat
      write(6,911)
      write(6,913)
      voidrd(i)=rcritr*1.01
      cnvchk=1
 250  continue
      return
 910  format(//,2x,69('*'))
 911  format('  *',t71,'*')
 912  format('  * at ',1pd9.3,' secs. the number of helium',
     1 ' atoms in class',i2,' bubbles',t71,'*',/,'  * ',
     2 'has passed the critical number.  these cavities now',
     3 ' grow as voids' ,t71,'*',/,'  *',7x,'radius=',8pf8.3,' ang',
     4 3x,'helium(i)=',0pf10.2,2x,'delhe=',f9.3,t71,'*',/,'  *',7x,
     6 'rcritr=',1pd12.5,2x,'ncritr=',d10.3,2x,'idealr=',d10.3,t71,'*',
     5 /,'  *',7x,'comprs=',d10.3,3x,'sprsat=',d11.4,t71,'*')
 913  format('  ',69('*'),//)
      end


cccccccccccccccccccccccccccccccccccccccccccccccccccccccccccccccccccccc
c                                                                      c
c                                CONST                                 c
c                                                                      c
c     subroutine to print out table of constants                       c
c                                                                      c
cccccccccccccccccccccccccccccccccccccccccccccccccccccccccccccccccccccc
      subroutine const(aberr1,aberr2,aberr3,aberr4,caseff,relerr)
      implicit real*8 (a-z)
      common /intgr/ bblflg(5),flpcls,hfrflg,iclflg,jtemp,lclas1,
     1  lclas2,lclass,lmns1,lpls1,nclass,netcls,noeq,nplt,nplus1,
     2  nqmns1,nqmns2,outsw,pfact,pntcls,pptflg,
     3  tempno,title1(20),title2(20),tmpchg,vclcls,vdflg(5)
      common /cavprm/ bbconv(5),bbsnk,bbsnk0,cvsnki,cvsnkv,comprs(5),
     1  cfaci(5),cfacv(5),cvsnk0,cvv(5),delhe(5),fs(5),fv(5),gamma(5),
     2  helium(5),mpa(5),ncritr(5),press(5),rhohe(5),
     3  ttconv(5),vdsnk,vdsnk0,voidcn(5),voidrd(5)
      common /disprm/ avlprd,bi1o,bi2o,bv2o,bi3o,bi4o,bv3o,bv4o,
     1  c2dis,c3dis,cvl(45),cvn,dicon,displd,disn0,disntd,distot,
     2  ec2dis,ec3dis,irrann,irrsrc,lpnum(45),lprad(45),ncrate,numilp,
     3  ilpmax,prmt1,prmt2,prmt3,prmt4,rate(45),rc,rhosnk,ro,shrmod,
     4  tauimx,snkerr,snknew,snktst,srcden,stckft,stfeng,tau4,
     5  tetcon,thrann,thrsrc,tricon,zil(45),zil0,zin,zi1,zi2,zi3,zi4,
     6  zvl(45),zvl0,zvn,zv2,zv3,zv4
      common /defprm/ alpha,ao,bvectd,bvectf,cvcls,cvemit,diffi,diffv,
     1  ef,eim,em,fracls,gamvcl,genvcl,intcon,intgn2,intgnr,kt,
     2  numvac,numvcl,omega,radvcl,sprsat,tauvcl,vaccne,vaccon,
     3  vacgnr,vclsnk,cilo,cihi,cvgues,iflux,vflux,delflx
      common /balrl/ appmhe,bubble,cavhe,clster,dery(50),diffhe,
     1  disloc,doschg(10),doschk,ehemig,embbl,emdisl,emflp,emppt,emsubg,
     2  emvcl,emvoid,floop,gasd,graind,grnd0,grnmax,grntau,hefrac,
     7  intbbl,intflp,intnet,intppt,intrec,intsbg,intvcl,intvd,ksbgi,
     3  hegnr0,hegnrr,ksbgv,mtrxhe,ntdhe,pi,pltflg,pptcon,pptrad,
     4  pptsnk,ppttau,precip,prntdt,prntnw,recomb,stop,stress,
     5  subghe,subgrn,swell,swlcmp,swlto1,taup,tauto1,tc(10),temp,
```

```
     6  time,tk,totdos,tsinki,tsinkv,tvdvac,vdemit,vdrecm,voids
      integer outsw,pfact,pptflg,nplt,nclass,flpcls,netcls,vclcls,
     *  bblflg,vdflg,i,title1,title2,hfrflg,nplus1,tmpchg,tempno,
     *  noeq,nqmns1,nqmns2,lclass,lclas1,lclas2,lmns1,lpls1,
     *  pntcls,iclflg,jtemp
10    format('1',t89,'!',/,33x,'t a b l e  o f  c o n s t a n t s',t89,
     1 '!',/,33x,'                                ',t89,'!')
20    format(t89,'!',/,t89,'!')
30    format(' interstitial generation rate',t42,1pd15.5,
     1 t60,'intgnr',t70,'dpa/sec',t89,'!',/
     2 ' cascade efficiency',t42,d15.5,t60,'caseff',t70,'-----',t89,'!')
40    format(' helium generation rate',t42,1pd15.5,t60,
     1'hegnrr',t70,'he atom/atom/sec',t89,'!')
50    format(' recombination coefficient',t42,1pd15.5,
     1 t60,'alpha',t70,'/sec',t89,'!')
60    format(' vacancy diffusivity',t42,1pd15.5,t60,
     1 'diffv',t70,'cm**2/sec',t89,'!')
70    format(' interstitial diffusivity',t42,1pd15.5,t60,
     1'diffi',t70,'cm**2/sec',t89,'!')
80    format(' helium atom diffusivity',t42,1pd15.5,t60,
     1 'diffhe',t70,'cm**2/sec',t89,'!')
90    format(' temperature',t42,1pd15.5,t60,'temp',
     1 t70,'deg c',t89,'!')
100   format(' kt',t42,1pd15.5,t60,'kt',t70,'ergs',t89,'!')
110   format(' stopping time',t42,1pd15.5,t60,'stop',
     1 t70,'secs',t89,'!')
120   format(' grain diameter',t42,1pd15.5,t60,'graind',
     1 t70,'cm',t89,'!')
130   format(' defect free eq. vacancy concentration',t42,1pd15.5,
     1 t60,'vaccne',t70,'-----',t89,'!')
140   format(' energy of motion (vacancy)',t42,1pd15.5,t60,
     1'em',t70,'ev',t89,'!')
150   format(' energy of motion (interstitial)',t42,1pd15.5,
     1 t60,'eim',t70,'ev',t89,'!')
160   format(' energy of formation (vacancy)',t42,1pd15.5,
     1 t60,'ef',t70,'ev',t89,'!')
170   format(' eq. vac. conc. near network dis.',t42,1pd15.5,
     1 t60,'cvn',t70,'-----',t89,'!')
180   format(' network dislocation/int. bias',t42,1pd15.5,t60,
     1 'zin',t70,'-----',t89,'!')
200   format(' network dislocation/vac. bias',t42,1pd15.5,t60,
     1 'zvn',t70,'-----',t89,'!')
192   format(' frank loop, int. bias root term',t42,1pd15.5,t60,
     1 'zil0',t70,'-----',t89,'!')
194   format(' frank loop, vac. bias root term',t42,1pd15.5,t60,
     1 'zvl0',t70,'-----',t89,'!')
210   format(' initial dislocation network density',t42,1pd15.5,
     1 t60,'disntd',t70,'/cm**2',t89,'!')
212   format(' lattice parameter',t42,1pd15.5,t60,'ao',t70,'cm',
     1  t89,'!')
214   format(' atomic volume',t42,1pd15.5,t60,'omega',t70,'cm**3',
     1  t89,'!')
216   format(' frank loop b-vector',t42,1pd15.5,t60,'bvectf',t70,'cm',
     1  t89,'!')
218   format(' dislocation b-vector',t42,1pd15.5,t60,'bvectd',t70,'cm',
     1  t89,'!')
220   format(' stress',t42,1pd15.5,t60,'stress',t70,'ergs/cm**3',
     1  t89,'!')
230   format(' stacking fault energy',
     1  t42,1pd15.5,t60,'stfeng',t70,'ergs/cm**2',t89,'!')
240   format(' shear modulus',
     1  t42,1pd15.5,t60,'shrmod',t70,'ergs/cm**3',t89,'!')
250   format(' fv(i), 1 to nclass',t42,3f10.4,t89,'!')
260   format(' fs(i), 1 to nclass',t42,3f10.4,t89,'!')
270   format(' gamma(i), 1 to nclass (ergs/cm**2)',t42,3f10.1,t89,'!')
280   format(' frac. of vacancies in cluster',t42,1pd15.5,t60,
     1 'fracls',t70,'-----',t89,'!')
290   format(' vac. cluster radius',t42,1pd15.5,t60,
     1 'radvcl',t70,'cm',t89,'!')
300   format(' vacancies/cluster',t42,1pd15.5,t60,
     1 'numvac',t70,'-----',t89,'!')
310   format(' cluster surface energy',t42,1pd15.5,t60,
     1 'gamvcl',t70,'ergs/cm**2',t89,'!')
320   format(' eq. vac. conc. near clstr',t42,1pd15.5,t60,
     1 'cvcls',t70,'-----',t89,'!')
330   format(t89,'!',/,t89,'!',/,t89,'!',/,t5,'program parameters',
     1  t89,'!',/,t5,'------------------',t89,'!')
332   format(' constant dislocation density used, no frank loops',
     1  t89,'!')
```

```
334   format(' full dislocation evolution used',t89,'!')
340   format(' relative error limit in lsode =',1pd12.3,t89,'!',/,
     1 ' frac. change in sink strength between pntdef calls=',d12.3,
     2  t89,'!')
342   format(' absolute error limits in lsode (aberr1-aberr4)=',
     1  t89,'!',/,5x,1p4d12.3,t89,'!')
350   format(' print factor (iterations per plot) =',i5,t89,'!')
390   format(t89,'!',/t89,'!',/,' comments:',t89,'!')
400   format(20a4,t89,'!',/,20a4,/,t89,'!')
      write(6,10)
      write(6,20)
      write(6,30) intgn2,caseff
      if(hfrflg.eq.1) hegnrr=hegnr0/0.45*(1.+100.*(1.-dexp(-totdos/9.)))
      write(6,40)hegnrr
      write(6,50)alpha
      write(6,60)diffv
      write(6,70)diffi
      write(6,80) diffhe
      write(6,90)temp
      write(6,100)kt
      write(6,110)stop
      write(6,120)graind
      write(6,130)vaccne
      write(6,140) em
      write(6,150) eim
      write(6,160) ef
      write(6,170)cvn
      write(6,180)zin
      write(6,192) zil0
      write(6,194) zvl0
      write(6,200)zvn
      write(6,210)disntd
      write(6,212) ao
      write(6,214) omega
      write(6,216) bvectf
      write(6,218) bvectd
      write(6,220)stress
      write(6,230)stfeng
      write(6,240)shrmod
      write(6,250) (fv(i),i=1,nclass)
      write(6,260) (fs(i),i=1,nclass)
      write(6,270) (gamma(i),i=1,nclass)
      write(6,280)fracls
      write(6,290)radvcl
      write(6,300)numvac
      write(6,310)gamvcl
      write(6,320)cvcls
      write(6,330)
      if(iclflg .ne. 1) write(6,332)
      if(iclflg .eq. 1) write(6,334)
      write(6,340) relerr,snkerr
      write(6,342) aberr1,aberr2,aberr3,aberr4
      write(6,350)pfact
      write(6,390)
      write(6,400)title1,title2
      return
      end


ccccccccccccccccccccccccccccccccccccccccccccccccccccccccccccccccccccccc
c                                                                       c
c                                GROW                                   c
c                                                                       c
c     subroutine to calculate derivatives for 'dlsode'                  c
c                                                                       c
ccccccccccccccccccccccccccccccccccccccccccccccccccccccccccccccccccccccc
      subroutine grow(neq,crntim,y,yprime)
      implicit real*8 (a-z)
      common /intgr/ bblflg(5),flpcls,hfrflg,iclflg,jtemp,lclas1,
     1  lclas2,lclass,lmns1,lpls1,nclass,netcls,noeq,nplt,nplus1,
     2  nqmns1,nqmns2,outsw,pfact,pntcls,pptflg,
     3  tempno,title1(20),title2(20),tmpchg,vclcls,vdflg(5)
      common /cavprm/ bbconv(5),bbsnk,bbsnk0,cvsnki,cvsnkv,comprs(5),
     1  cfaci(5),cfacv(5),cvsnk0,cvv(5),delhe(5),fs(5),fv(5),gamma(5),
     2  helium(5),mpa(5),ncritr(5),press(5),rhohe(5),
     3  ttconv(5),vdsnk,vdsnk0,voidcn(5),voidrd(5)
      common /disprm/ avlprd,bi1o,bi2o,bv2o,bi3o,bi4o,bv3o,bv4o,
     1  c2dis,c3dis,cvl(45),cvn,dicon,displd,disn0,disntd,distot,
```

```
     2  ec2dis,ec3dis,irrann,irrsrc,lpnum(45),lprad(45),ncrate,numilp,
     3  ilpmax,prmt1,prmt2,prmt3,prmt4,rate(45),rc,rhosnk,ro,shrmod,
     4  tauimx,snkerr,snknew,snktst,srcden,stckft,stfeng,tau4,
     5  tetcon,thrann,thrsrc,tricon,zil(45),zil0,zin,zi1,zi2,zi3,zi4,
     6  zvl(45),zvl0,zvn,zv2,zv3,zv4
      common /defprm/ alpha,ao,bvectd,bvectf,cvcls,cvemit,diffi,diffv,
     1  ef,eim,em,fracls,gamvcl,genvcl,intcon,intgn2,intgnr,kt,
     2  numvac,numvcl,omega,radvcl,sprsat,tauvcl,vaccne,vaccon,
     3  vacgnr,vclsnk,cilo,cihi,cvgues,iflux,vflux,delflx
      common /balrl/ appmhe,bubble,cavhe,clster,dery(50),diffhe,
     1  disloc,doschg(10),doschk,ehemig,embbl,emdisl,emflp,emppt,emsubg,
     2  emvcl,emvoid,floop,gasd,graind,grnd0,grnmax,grntau,hefrac,
     7  intbbl,intflp,intnet,intppt,intrec,intsbg,intvcl,intvd,ksbgi,
     3  hegnr0,hegnrr,ksbgv,mtrxhe,ntdhe,pi,pltflg,pptcon,pptrad,
     4  pptsnk,ppttau,precip,prntdt,prntnw,recomb,stop,stress,
     5  subghe,subgrn,swell,swlcmp,swlto1,taup,tauto1,tc(10),temp,
     6  time,tk,totdos,tsinki,tsinkv,tvdvac,vdemit,vdrecm,voids
      integer outsw,pfact,pptflg,nplt,nclass,flpcls,netcls,vclcls,
     *  bblflg,vdflg,i,j,k,l,m,title1,title2,hfrflg,nplus1,tmpchg,
     *  tempno,noeq,nqmns1,nqmns2,lclass,lclas1,lclas2,lmns1,lpls1,
     *  pntcls,iclflg,jtemp,jj,kk,neq(1),snkflg
      dimension y(50),yprime(50),fof(17)
ccccccccccccccccccccccccccccccccccccccccccccccccccccccccccccccccccccc
c                                                                      c
c     update sink parameters from dlsode and compute                   c
c     new point defect concentrations for the next time step           c
c                                                                      c
ccccccccccccccccccccccccccccccccccccccccccccccccccccccccccccccccccccc
      snkflg=1
      j=0
      do 20 i=1,nclass
      if(bblflg(i).eq.1) go to 20
      j=j+1
      voidrd(i)=y(j)
      rhohe(i)=helium(i)/fv(i)/voidrd(i)**3
      yz=pi*gasd**3*rhohe(i)/6.d0
      comprs(i)=(1.d0+yz+yz**2-yz**3)/(1.d0-yz)**3
      if(yz .gt. 0.5) comprs(i)=3.0573d-1*dexp(yz*7.5d0)
      press(i)=rhohe(i)*kt*comprs(i)
      cvv(i)=fcncvv(kt,omega,vaccne,gamma(i),voidrd(i),press(i),i)
 20   continue
      numvcl=y(noeq)                                                   ssvcl
      vclsnk=4.*pi*numvcl*radvcl                                       ssvcl
      cvsnk0=fcnsnk(voidrd,voidcn,nclass,fs,pi,bblflg,bbsnk0,vdsnk0)
      if(iclflg.ne.1) go to 50
      do 30 i=2,lclass
      j=j+1
 30   lpnum(i)=dmax1(y(j),1.d0)
      disntd=dmax1(1.d8,y(j+1))
      displd=0.0
      numilp=0.0
      do 40 i=2,lclass
      displd=displd+2.0*pi*lprad(i)*lpnum(i)
      numilp=numilp+lpnum(i)
 40   continue
      if(numilp.gt.ilpmax) tauimx=totdos
      ilpmax=dmax1(ilpmax,numilp)
      distot=displd+disntd
      lprad(lpls1)=1.d0/prmt1/dsqrt(dmax1(distot,1.d8))
      zil(lpls1)=zil0                                                  zil-r
      zvl(lpls1)=zvl0                                                  zil-r
c     zil(lpls1)=dmin1(3.5d0, (zin + zil0/lprad(lpls1)**2) )           zil-r
c     zvl(lpls1)= zvn + zvl0/lprad(lpls1)**2                           zil-r
      linetn=shrmod*bvectf*omega/2.8/pi/lprad(lpls1)*
     1 dlog(4.d0*lprad(lpls1)/bvectf)
      dedm=dmin1(30.0d0,linetn+stckft)
      cvl(lpls1)=vaccne*dexp(-dedm/kt)
      avlprd=displd/numilp/2./pi
 50   continue
      ro=1.0/dsqrt(pi*distot)
      rhosnk=2.d0*pi/dlog(ro/rc)
      if( graind .lt. grnmax )
     1 graind=(grnmax - grnd0)*(1.0-dexp(-time/grntau))+grnd0
ccccccccccccccccccccccccccccccccccccccccccccccccccccccccccccccccccccc
c                                                                      c
c     check for significant (>snkerr) change in total sink strength    c
c     to determine how much recalculation to do                        c
c                                                                      c
ccccccccccccccccccccccccccccccccccccccccccccccccccccccccccccccccccccc
```

```
          if(pntcls.le.5) go to 53
      snknew=disntd+cvsnk0+displd+vclsnk
      if(dabs(snknew-snktst) .le. snkerr*snktst) snkflg=0
      if(snkflg.eq.0) go to 55
      snktst=snknew
 53   call pntdef
c     tauvcl=dmax1(0.0d0,                                                    ssvcl
c    1 -radvcl**2/3./(vflux-diffv*cvcls-iflux))                              ssvcl
c     numvcl=genvcl*tauvcl                                                   ssvcl
c     vclsnk=4.*pi*numvcl*radvcl                                             ssvcl
      hespr=dmax1(1.d0,sprsat)
      diffhe=hespr*dexp(-ehemig*1.602d-12/kt)
 55   j=0
cccccccccccccccccccccccccccccccccccccccccccccccccccccccccccccccccccccccccc
c                                                                           c
c     compute cavity radii derivatives                                      c
c                                                                           c
cccccccccccccccccccccccccccccccccccccccccccccccccccccccccccccccccccccccccc
      do 100 i=1,nclass
      if(bbiflg(i) .eq. 1) go to 100
      j=j+1
      if( y(j) .gt. 0.0d0 ) go to 60
      write(6,600) time,i,y(i),yprime(i),sprsat,press(i),comprs(i)
      y(i)=dsqrt(3.d0*helium(i)*comprs(i)*kt/gamma(i)/pi/8.d0)
      stop
 60   yprime(j)=fs(i)/y(j)/3./fv(i) *
     1  (cfacv(i)*(vflux-diffv*cvv(i)) - cfaci(i)*iflux)
      dery(i)=yprime(j)
 100  continue
cccccccccccccccccccccccccccccccccccccccccccccccccccccccccccccccccccccccccc
c                                                                           c
c     compute derivative of vacancy cluster density                         c
c                                                                           c
cccccccccccccccccccccccccccccccccccccccccccccccccccccccccccccccccccccccccc
      tauvcl=-radvcl**2/3./(vflux-diffv*cvcls-iflux)                        ssvcl
      yprime(noeq)=genvcl-numvcl/tauvcl                                     ssvcl
      dery(vclcls)=yprime(noeq)                                             ssvcl
      if( iclflg .ne. 1) return
cccccccccccccccccccccccccccccccccccccccccccccccccccccccccccccccccccccccccc
c                                                                           c
c      calculate derivative of frank loop number density                    c
c                                                                           c
c      rate(i)=rate of transfer of loops between classes i-1 and i          c
c      note: lpnum(1) assigned in subroutine pntdef                         c
c      a simpson's rule integration with fixed delta is used to             c
c      calculate the rates.                                                 c
c                                                                           c
cccccccccccccccccccccccccccccccccccccccccccccccccccccccccccccccccccccccccc
       if(snkflg.eq.0) go to 130
      do 120 i=2,lpls1
      tempsm=0.0
      delh=( lprad(i) - lprad(i-1) ) / 16.0
      do 110 jj=1,17
      kk=jj-1
      temprd=lprad(i-1)+kk*delh
      fof(jj)=fcnlpg(temprd,pi,rhosnk,shrmod,stckft,zin,zvn,zil0,zvl0)
 110  continue
      do 115 jj=2,16,2
 115  tempsm=tempsm + ( fof(jj-1) + 4.*fof(jj) + fof(jj+1) )
 120  rate(i)=3.0/delh/tempsm
 130  k=nclass
      do 150 i=2,lclass
      j=j+1
      k=k+1
      if( rate(i) .lt. 0.0 ) m=0
      if( rate(i) .ge. 0.0) m=1
      if ( rate(i+1) .lt. 0.0 ) l=1
      if ( rate(i+1) .ge. 0.0 ) l=0
      yprime(j)=rate(i)*lpnum(i-m)-rate(i+1)*lpnum(i+l)
      dery(k)=yprime(j)
 150  continue
cccccccccccccccccccccccccccccccccccccccccccccccccccccccccccccccccccccccccc
c                                                                           c
c     compute derivative of network dislocation density                     c
c                                                                           c
cccccccccccccccccccccccccccccccccccccccccccccccccccccccccccccccccccccccccc
      irrann=dabs(zin*iflux - zvn*(vflux-diffv*cvemit) )*
     1 prmt3*dsqrt(disntd)/bvectd*rhosnk
      thrvel=prmt4*shrmod*omega*diffv*vaccne*rhosnk*dsqrt(disntd)/kt
```

```
      thrann=prmt3*dsqrt(disntd)*thrvel
      annrat=thrann + irrann
      thrsrc=2.d0*pi*thrvel*srcden
      irrsrc=dmax1( 0.d0,
     1  prmt2*2.0*pi*lprad(lpls1)*rate(lpls1)*lpnum(lclass) )
      srcrat=irrsrc + thrsrc
      yprime(j+1)=srcrat - annrat*disntd
      dery(netcls)=yprime(j+1)
      return
600   format(6h time=,1pd11.4,4h  i=,i2,6h  rad=,d11.4,7h  dery=,
     1 d11.4,9h  sprsat=,d11.4,8h  press=,d11.4,9h  comprs=,d11.4)
      end


ccccccccccccccccccccccccccccccccccccccccccccccccccccccccccccccccccccccc
c                                                                       c
c                                HELPRT                                 c
c                                                                       c
c      subroutine to generate helium for completed time step and        c
c      distribute it amoung the various sinks present.                  c
c                                                                       c
ccccccccccccccccccccccccccccccccccccccccccccccccccccccccccccccccccccccc
      subroutine helprt(timdlt,disntd,omega,rhosnk,bblflg,vdflg,
     1  hfrflg,nclass)
      implicit real*8 (a-z)
      common /cavprm/ bbconv(5),bbsnk,bbsnk0,cvsnki,cvsnkv,comprs(5),
     1  cfaci(5),cfacv(5),cvsnk0,cvv(5),delhe(5),fs(5),fv(5),gamma(5),
     2  helium(5),mpa(5),ncritr(5),press(5),rhohe(5),
     3  ttconv(5),vdsnk,vdsnk0,voidcn(5),voidrd(5)
      common /balrl/ appmhe,bubble,cavhe,clster,dery(50),diffhe,
     1  disloc,doschg(10),doschk,ehemig,embbl,emdisl,emflp,emppt,emsubg,
     2  emvcl,emvoid,floop,gasd,graind,grnd0,grnmax,grntau,hefrac,
     7  intbbl,intflp,intnet,intppt,intrec,intsbg,intvcl,intvd,ksbgi,
     3  hegnr0,hegnrr,ksbgv,mtrxhe,ntdhe,pi,pltflg,pptcon,pptrad,
     4  pptsnk,ppttau,precip,prntdt,prntnw,recomb,stop,stress,
     5  subghe,subgrn,swell,swlcmp,swlto1,taup,tauto1,tc(10),temp,
     6  time,tk,totdos,tsinki,tsinkv,tvdvac,vdemit,vdrecm,voids
      integer bblflg(5),vdflg(5),hfrflg,nclass,i
      snktmp=0.0
      do 187 i=1,nclass
      if(i.eq.nclass .and. pptcon.gt.0.) go to 187
      snktmp=snktmp+fs(i)*voidcn(i)*voidrd(i)*cfacv(i)
 187  continue
      snk1=fs(1)*voidcn(1)*voidrd(1)*cfacv(1)
      sumk=snktmp+hefrac*rhosnk*disntd+pptsnk+ksbgv
      timexp=dexp(-dmin1(15.d0,sumk))
      if(hfrflg .ne. 1) go to 200
      hegnrr=hegnr0/0.45*( 1.0 + 100.*( 1.0 - dexp(-totdos/9.0) ) )
 200  hegprm=hegnrr/omega
      mtrxhe=hegprm*(1.d0-timexp)/diffhe/sumk/8.524d16
      appmhe=appmhe+hegnrr*timdlt*1.0d6
      temprs=timdlt*hegprm*(1.0-timexp)/sumk
      cavhe=0.0d0
      do 210 i=1,nclass
      if(i.eq.nclass .and. pptcon.gt.0.) go to 208
      if(bblflg(1).eq.1 .and. i.eq.1) go to 202
      delhe(i)=fs(i)*temprs*voidrd(i)*cfacv(i)
      go to 209
 202  delhe(i)=fs(i)*temprs*voidrd(i)*cfacv(i)*
     1 (hefrac*rhosnk*disntd+snk1)/snk1
      go to 209
 208  delhe(i)=temprs*pptsnk/voidcn(i)
 209  helium(i)=helium(i)+delhe(i)
      cavhe=cavhe+helium(i)*voidcn(i)/8.524d16
 210  continue
      subghe=subghe+temprs*ksbgv/8.524d16
      if(bblflg(1).eq.0)ntdhe=ntdhe+temprs*hefrac*rhosnk*disntd/8.524d16
      return
      end


ccccccccccccccccccccccccccccccccccccccccccccccccccccccccccccccccccccccc
c                                                                       c
c                                PLOT                                   c
c                                                                       c
c     plots microstructual data on line printer                         c
c                                                                       c
```

```
ccccccccccccccccccccccccccccccccccccccccccccccccccccccccccccccccccccccccccc
      subroutine plot(dumvar,nplt,numlin,trusiz,swlflg)
      implicit real*8 (a-z)
      real*4 sngl,sx
      dimension dumvar(1),xlin(11)
      integer i,i1,ifix,ix,ixpos(2000),isym(2),k,line(101),nplt,numlin,
     1  swlflg,trusiz,l
      data isym/' ','*'/
 1    format(' ',1pd10.3,' ^',61a1,'^')
 2    format(' ',11x,'+',6('^---------'),'^+')
 3    format(' ',7x,7(f10.2))
 4    format(' ',g10.4,' ^',61a1,'^')
      ymax=-1.d+30
      ymin=1.d+30
ccccccccccccccccccccccccccccccccccccccccccccccccccccccccccccccccccccccccccc
c                                                                            c
c        determine max and min for y values                                  c
c                                                                            c
ccccccccccccccccccccccccccccccccccccccccccccccccccccccccccccccccccccccccccc
      xmin=0.0
      xmax=dumvar(nplt)
      do 100 i=1,nplt
      l=trusiz+i
      if(dumvar(l).le.ymax)go to 50
      ymax=dumvar(l)
50    if(dumvar(l).ge.ymin)go to 100
      ymin=dumvar(l)
100   continue
ccccccccccccccccccccccccccccccccccccccccccccccccccccccccccccccccccccccccccc
c                                                                            c
c      establish integer column positions for the x axis                     c
c                                                                            c
ccccccccccccccccccccccccccccccccccccccccccccccccccccccccccccccccccccccccccc
      do 200 i=1,nplt
      x=((dumvar(i)-xmin)/(xmax-xmin))*60.+1.5
      sx=sngl(x)
200   ixpos(i)=ifix(sx)
      y=ymax
      ystep=(ymax-ymin)/dfloat(numlin-1)
      xstep=(xmax-xmin)/60.
      do 300 i=1,7
300   xlin(i)=xmin+xstep*dfloat(i-1)*10.
      write(6,3)(xlin(i),i=1,7)
      write(6,2)
ccccccccccccccccccccccccccccccccccccccccccccccccccccccccccccccccccccccccccc
c                                                                            c
c      print plot                                                            c
c                                                                            c
ccccccccccccccccccccccccccccccccccccccccccccccccccccccccccccccccccccccccccc
      do 600 ix=1,numlin
      do 400 k=1,61
400   line(k)=isym(1)
      do 500 i=1,nplt
      l=trusiz+i
      if(dabs(dumvar(l)-y).gt.(ystep/2.))go to 500
      line(ixpos(i))=isym(2)
500   continue
      if(swlflg .eq. 0) write(6,1)y,(line(i1),i1=1,61)
      if(swlflg .eq. 1) write(6,4)y,(line(i1),i1=1,61)
      y=y-ystep
600   continue
      write(6,2)
      write(6,3)(xlin(i),i=1,7)
      return
      end


ccccccccccccccccccccccccccccccccccccccccccccccccccccccccccccccccccccccccccc
c                                                                            c
c                                PNTDEF                                      c
c                                                                            c
c      computes vacancy and interstial concentration                         c
c         method depends on whether or not interstitial                      c
c         clusters are included (iclflg=1) or not (iclflg=0)                 c
c                                                                            c
ccccccccccccccccccccccccccccccccccccccccccccccccccccccccccccccccccccccccccc
      subroutine pntdef
      implicit real*8 (a-z)
```

```
      common /intgr/ bblflg(5),flpcls,hfrflg,iclflg,jtemp,lclas1,
     1  lclas2,lclass,lmns1,lpls1,nclass,netcls,noeq,nplt,nplus1,
     2  nqmns1,nqmns2,outsw,pfact,pntcls,pptflg,
     3  tempno,title1(20),title2(20),tmpchg,vclcls,vdflg(5)
      common /cavprm/ bbconv(5),bbsnk,bbsnk0,cvsnki,cvsnkv,comprs(5),
     1  cfaci(5),cfacv(5),cvsnk0,cvv(5),delhe(5),fs(5),fv(5),gamma(5),
     2  helium(5),mpa(5),ncritr(5),press(5),rhohe(5),
     3  ttconv(5),vdsnk,vdsnk0,voidcn(5),voidrd(5)
      common /disprm/ avlprd,bi1o,bi2o,bv2o,bi3o,bi4o,bv3o,bv4o,
     1  c2dis,c3dis,cvl(45),cvn,dicon,displd,disn0,disntd,distot,
     2  ec2dis,ec3dis,irrann,irrsrc,lpnum(45),lprad(45),ncrate,numilp,
     3  ilpmax,prmt1,prmt2,prmt3,prmt4,rate(45),rc,rhosnk,ro,shrmod,
     4  tauimx,snkerr,snknew,snktst,srcden,stckft,stfeng,tau4,
     5  tetcon,thrann,thrsrc,tricon,zil(45),zil0,zin,zi1,zi2,zi3,zi4,
     6  zvl(45),zvl0,zvn,zv2,zv3,zv4
      common /defprm/ alpha,ao,bvectd,bvectf,cvcls,cvemit,diffi,diffv,
     1  ef,eim,em,fracls,gamvcl,genvcl,intcon,intgn2,intgnr,kt,
     2  numvac,numvcl,omega,radvcl,sprsat,tauvcl,vaccne,vaccon,
     3  vacgnr,vclsnk,cilo,cihi,cvgues,iflux,vflux,delflx
      common /balrl/ appmhe,bubble,cavhe,clster,dery(50),diffhe,
     1  disloc,doschg(10),doschk,ehemig,embbl,emdisl,emflp,emppt,emsubg,
     2  emvcl,emvoid,floop,gasd,graind,grnd0,grnmax,grntau,hefrac,
     7  intbbl,intflp,intnet,intppt,intrec,intsbg,intvcl,intvd,ksbgi,
     3  hegnr0,hegnrr,ksbgv,mtrxhe,ntdhe,pi,pltflg,pptcon,pptrad,
     4  pptsnk,ppttau,precip,prntdt,prntnw,recomb,stop,stress,
     5  subghe,subgrn,swell,swlcmp,swlto1,taup,tauto1,tc(10),temp,
     6  time,tk,totdos,tsinki,tsinkv,tvdvac,vdemit,vdrecm,voids
      integer outsw,pfact,pptflg,nplt,nclass,flpcls,netcls,vclcls,
     *  bblflg,vdflg,i,j,k,title1,title2,hfrflg,nplus1,tmpchg,tempno,
     *  noeq,nqmns1,nqmns2,lclass,lclas1,lclas2,lmns1,lpls1,
     *  pntcls,iclflg,jtemp,j1,j2
      dimension yof(2),fof(17)
      pntcls=pntcls+1
      cvsnkv=0.0d0
      cvsnki=0.0d0
      vdsnk=0.0d0
      bbsnk=0.0d0
      ppsink=0.0
      if(pptflg.eq.1) ppsink=pptsnk
      if(iclflg.ne.1) go to 201
cccccccccccccccccccccccccccccccccccccccccccccccccccccccccccccccccccccc
c                                                                      c
c       when interstitial clusters are included, set initial guesses   c
c       (cihi and cilo) to bracket root for false-position root        c
c       finding method of calculating intcon.                          c
c       1. bi1, bi2,bi3, bv2, bv3, bv4 are impingement rates of        c
c          point defects on interstitial clusters of various sizes.    c
c       2. tau4 is life time of tetra-inter. in transit to next        c
c          loop size class                                             c
c                                                                      c
cccccccccccccccccccccccccccccccccccccccccccccccccccccccccccccccccccccc
      j1=0
      j2=0
      sdisli=zin*disntd
      sdislv=zvn*disntd
      do 5 i=2,lclass
      sdislv=sdislv + 2.*pi*zvl(i)*lprad(i)*lpnum(i)
 5    sdisli=sdisli + 2.*pi*zil(i)*lprad(i)*lpnum(i)
      tsnkv0=dsqrt( rhosnk*sdislv + cvsnk0 + ppsink + vclsnk )
      tsnki0=dsqrt( rhosnk*sdisli + cvsnk0 + ppsink + vclsnk )
      ksbgv=6.d0*tsnkv0/graind
c     ksbgi=6.d0*tsnki0/graind                                         subg-i
      ksbgi=ksbgv                                                      subg-i
      tsnkv=dsqrt(tsnkv0**2+ksbgv)
      tsnki=dsqrt(tsnki0**2+ksbgi)
      do 10 i=1,nclass
      cfacv(i)=1.+voidrd(i)*tsnkv
c     cfaci(i)=1.+voidrd(i)*tsnki                                      cfac-i
      cfaci(i)=cfacv(i)                                                cfac-i
      tmpvac=voidrd(i)*voidcn(i)*cfacv(i)
      tmpint=voidrd(i)*voidcn(i)*cfaci(i)
      vdsnk=vdsnk+tmpvac*fs(i)*vdflg(i)
      bbsnk=bbsnk+tmpvac*fs(i)*bblflg(i)
      cvsnkv=cvsnkv+tmpvac*fs(i)
 10   cvsnki=cvsnki+tmpint*fs(i)
      vacgnr=fcnvgr(bblflg,iclflg,lclass,nclass,pptflg,vdflg)
      tsinki=rhosnk*sdisli + cvsnki+ksbgi+vclsnk+ppsink
      tsinkv=rhosnk*sdislv +cvsnkv+ksbgv+vclsnk+ppsink
      ciprt1=diffi*tsinki
```

```
      ciold=cilo
      bv2=bv2o*cvgues
      bv3=bv3o*cvgues
      bv4=bv4o*cvgues
40    cisto=cilo
      do 50 k=1,2
      tempsm=0.0
      delh=( lprad(2) - lprad(1) ) / 8.0
      delh2=delh/2.0
      do 95 j=1,17
      i=j-1
      temprd=lprad(1)+i*delh2
      fof(j)=fcnlpg(temprd,pi,rhosnk,shrmod,stckft,zin,zvn,zil0,zvl0)
95    continue
      do 100 j=2,16,2
100   tempsm=tempsm + ( fof(j-1) + 4.*fof(j) + fof(j+1) )
      tau4=tempsm*delh/6.d0
      rate4=dmax1(0.d0,1.d0/tau4)
      bi1=bi1o*cisto
      bi2=bi2o*cisto
      bi3=bi3o*cisto
      bi4=bi4o*cisto
      part3=bi3/(bv4+rate4)
      part2=bi2/(bv3+bi3+c3dis-bv4*part3)
      part1=bi1/(c2dis+bi2+bv2-part2*(bv3+c3dis))/2.0d0
      cvpart=diffv*part1*(zv2+zv3*part2+zv4*part2*part3)/ao**2
      cvgues=vacgnr / ( cisto*(alpha+cvpart) + diffv*tsinkv )
      bv2=bv2o*cvgues
      bv3=bv3o*cvgues
      bv4=bv4o*cvgues
      ciprt2=bi1 + alpha*cvgues
      ciprt3=part1*(2.0*c2dis + bv2 + part2*(c3dis-bi3-bi4*part3) - bi2)
      yof(k)=intgnr + cisto*(ciprt3 - ciprt1 - ciprt2)
      cisto=cihi
50    continue
      if( dabs(yof(2)-yof(1)) .lt. 1.0d-30) go to 90
      cinew=cihi - yof(2)*(cihi-cilo)/(yof(2)-yof(1))
      if(dabs((ciold - cinew)/ciold) .lt. 1.0d-6) go to 90
      bi1=bi1o*cinew
      bi2=bi2o*cinew
      bi3=bi3o*cinew
      bi4=bi4o*cinew
      tempsm=0.0
      delh=( lprad(2) - lprad(1) ) / 8.0
      delh2=delh/2.0
      do 195 j=1,17
      i=j-1
      temprd=lprad(1)+i*delh2
      fof(j)=fcnlpg(temprd,pi,rhosnk,shrmod,stckft,zin,zvn,zil0,zvl0)
195   continue
      do 200 j=2,16,2
200   tempsm=tempsm + ( fof(j-1) + 4.*fof(j) + fof(j+1) )
      tau4=tempsm*delh/6.d0
      rate4=dmax1(0.d0,1.d0/tau4)
      part3=bi3/(bv4+rate4)
      part2=bi2/(bv3+bi3+c3dis-bv4*part3)
      part1=bi1/(c2dis+bi2+bv2-part2*(bv3+c3dis))/2.0d0
      cvpart=diffv*part1*(zv2+zv3*part2+zv4*part2*part3)/ao**2
      cvgues=vacgnr / ( cinew*(alpha+cvpart) + diffv*tsinkv )
      bv2=bv2o*cvgues
      bv3=bv3o*cvgues
      bv4=bv4o*cvgues
      ciprt2=bi1 + alpha*cvgues
      ciprt3=part1*(2.0*c2dis + bv2 + part2*(c3dis-bi3-bi4*part3) - bi2)
      ynew=intgnr + cinew*(ciprt3 - ciprt1 - ciprt2)
      if(yof(1)*ynew) 60,90,70
60    cihi=cinew
      j2=0
      j1=j1+1
      if(j1 .le. 2) go to 80
      cilo=(3.0*cilo+cihi)/4.0
      go to 80
70    cilo=cinew
      j1=0
      j2=j2+1
      if(j2 .le. 2) go to 80
      cihi=(3.0*cihi+cilo)/4.0
80    ciold=cinew
      go to 40
```

```
 90   intcon=cinew
      bi1=bi1o*intcon
      bi2=bi2o*intcon
      bi3=bi3o*intcon
      bi4=bi4o*intcon
      tempsm=0.0
      delh=( lprad(2) - lprad(1) ) / 8.0
      delh2=delh/2.0
      do 295 j=1,17
      i=j-1
      temprd=lprad(1)+i*delh2
      fof(j)=fcnlpg(temprd,pi,rhosnk,shrmod,stckft,zin,zvn,zil0,zvl0)
 295  continue
      do 300 j=2,16,2
  300 tempsm=tempsm + ( fof(j-1) + 4.*fof(j) + fof(j+1) )
      tau4=tempsm*delh/6.d0
      rate4=dmax1(0.d0,1.d0/tau4)
      part3=bi3/(bv4+rate4)
      part2=bi2/(bv3+bi3+c3dis-bv4*part3)
      part1=bi1/(c2dis+bi2+bv2-part2*(bv3+c3dis))/2.0d0
      cvpart=diffv*part1*(zv2+zv3*part2+zv4*part2*part3)/ao**2
      vaccon=vacgnr / ( intcon*(alpha+cvpart) + diffv*tsinkv )
      dicon=intcon*part1
      tricon=intcon*part1*part2
      tempsm=0.0
      delh=( lprad(2) - lprad(1) ) / 8.0
      delh2=delh/2.0
      do 395 j=1,17
      i=j-1
      temprd=lprad(1)+i*delh2
      fof(j)=fcnlpg(temprd,pi,rhosnk,shrmod,stckft,zin,zvn,zil0,zvl0)
 395  continue
      do 400 j=2,16,2
  400 tempsm=tempsm + ( fof(j-1) + 4.*fof(j) + fof(j+1) )
      tau4=tempsm*delh/6.d0
      rate4=dmax1(0.d0,1.d0/tau4)
      lpnum(1)=dmax1( 1.d0, part1*part2*part3*intcon/omega)
      tetcon=lpnum(1)*omega
      ncrate=lpnum(1)*rate4
      cilo=0.95*intcon
      cihi=1.05*intcon
      cvgues=vaccon
       iflux=diffi*intcon
       vflux=diffv*vaccon
      delflx=vflux-iflux
      sprsat=delflx/diffv/vaccne
      return
ccccccccccccccccccccccccccccccccccccccccccccccccccccccccccccccccccccccc
c                                                                      c
c       without interstitial clusters, solve for vaccon and intcon     c
c       by solving a quadratic equation for vaccon and subsitute       c
c       for intcon                                                     c
c                                                                      c
ccccccccccccccccccccccccccccccccccccccccccccccccccccccccccccccccccccccc
 201  tsnki0=dsqrt( zin*rhosnk*disntd +  cvsnk0 + ppsink + vclsnk )
      tsnkv0=dsqrt( zvn*rhosnk*disntd + cvsnk0 + ppsink + vclsnk )
      ksbgv=6.d0*tsnkv0/graind
c     ksbgi=6.d0*tsnki0/graind                                         subg-i
      ksbgi=ksbgv                                                      subg-i
      tsnkv=dsqrt(tsnkv0**2+ksbgv)
      tsnki=dsqrt(tsnki0**2+ksbgi)
      do 210 i=1,nclass
      cfacv(i)=1.+voidrd(i)*tsnkv
c     cfaci(i)=1.+voidrd(i)*tsnki                                      cfac-i
      cfaci(i)=cfacv(i)                                                cfac-i
      tmpvac=voidrd(i)*voidcn(i)*cfacv(i)
      tmpint=voidrd(i)*voidcn(i)*cfaci(i)
      vdsnk=vdsnk+tmpvac*fs(i)*vdflg(i)
      bbsnk=bbsnk+tmpvac*fs(i)*bblflg(i)
      cvsnkv=cvsnkv+tmpvac*fs(i)
 210  cvsnki=cvsnki+tmpint*fs(i)
 230  vacgnr=fcnvgr(bblflg,iclflg,lclass,nclass,pptflg,vdflg)
      tsinkv= zvn*rhosnk*disntd + cvsnkv + ppsink + vclsnk + ksbgv
      tsinki= zin*rhosnk*disntd +  cvsnki + ppsink + vclsnk + ksbgi
      a=alpha*diffv*tsinki
      b=(alpha*(intgnr-vacgnr)+diffi*diffv*tsinki*tsinkv)
      c=-vacgnr*diffi*tsinki
      vaccon=(-b+dsqrt(b**2-4.*a*c))/2./a
      intcon=intgnr/(alpha*vaccon+diffi*tsinki)
```

```
      cilo=0.95*intcon
      cihi=1.05*intcon
      cvgues=vaccon
       iflux=diffi*intcon
       vflux=diffv*vaccon
      delflx=vflux-iflux
      sprsat=delflx/diffv/vaccne
      return
      end


ccccccccccccccccccccccccccccccccccccccccccccccccccccccccccccccccccccccccc
c                                                                       c
c                                TABLE                                  c
c                                                                       c
c     subroutine to print out table of variables                        c
c                                                                       c
ccccccccccccccccccccccccccccccccccccccccccccccccccccccccccccccccccccccccc
      subroutine table(snkrat,swlrat)
      implicit real*8 (a-z)
      common /intgr/ bblflg(5),flpcls,hfrflg,iclflg,jtemp,lclas1,
     1  lclas2,lclass,lmns1,lpls1,nclass,netcls,noeq,nplt,nplus1,
     2  nqmns1,nqmns2,outsw,pfact,pntcls,pptflg,
     3  tempno,title1(20),title2(20),tmpchg,vclcls,vdflg(5)
      common /cavprm/ bbconv(5),bbsnk,bbsnk0,cvsnki,cvsnkv,comprs(5),
     1  cfaci(5),cfacv(5),cvsnk0,cvv(5),delhe(5),fs(5),fv(5),gamma(5),
     2  helium(5),mpa(5),ncritr(5),press(5),rhohe(5),
     3  ttconv(5),vdsnk,vdsnk0,voidcn(5),voidrd(5)
      common /disprm/ avlprd,bi1o,bi2o,bv2o,bi3o,bi4o,bv3o,bv4o,
     1  c2dis,c3dis,cvl(45),cvn,dicon,displd,disn0,disntd,distot,
     2  ec2dis,ec3dis,irrann,irrsrc,lpnum(45),lprad(45),ncrate,numilp,
     3  ilpmax,prmt1,prmt2,prmt3,prmt4,rate(45),rc,rhosnk,ro,shrmod,
     4  tauimx,snkerr,snknew,snktst,srcden,stckft,stfeng,tau4,
     5  tetcon,thrann,thrsrc,tricon,zil(45),zil0,zin,zi1,zi2,zi3,zi4,
     6  zvl(45),zvl0,zvn,zv2,zv3,zv4
      common /defprm/ alpha,ao,bvectd,bvectf,cvcls,cvemit,diffi,diffv,
     1  ef,eim,em,fracls,gamvcl,genvcl,intcon,intgn2,intgnr,kt,
     2  numvac,numvcl,omega,radvcl,sprsat,tauvcl,vaccne,vaccon,
     3  vacgnr,vclsnk,cilo,cihi,cvgues,iflux,vflux,delflx
      common /balrl/ appmhe,bubble,cavhe,clster,dery(50),diffhe,
     1  disloc,doschg(10),doschk,ehemig,embbl,emdisl,emflp,emppt,emsubg,
     2  emvcl,emvoid,floop,gasd,graind,grnd0,grnmax,grntau,hefrac,
     7  intbbl,intflp,intnet,intppt,intrec,intsbg,intvcl,intvd,ksbgi,
     3  hegnr0,hegnrr,ksbgv,mtrxhe,ntdhe,pi,pltflg,pptcon,pptrad,
     4  pptsnk,ppttau,precip,prntdt,prntnw,recomb,stop,stress,
     5  subghe,subgrn,swell,swlcmp,swlto1,taup,tauto1,tc(10),temp,
     6  time,tk,totdos,tsinki,tsinkv,tvdvac,vdemit,vdrecm,voids
      integer outsw,pfact,pptflg,nplt,nclass,flpcls,netcls,vclcls,
     *  bblflg,vdflg,i,title1,title2,hfrflg,nplus1,tmpchg,tempno,
     *  noeq,nqmns1,nqmns2,lclass,lclas1,lclas2,lmns1,lpls1,
     *  pntcls,iclflg,jtemp
  5   format('1',t89,'!')
 10   format(t89,'!',/t89,'!',/,33x,'t a b l e  o f  v a r i a b l e s',
     1  t89,'!',/,33x,'_____________________________',t89,'!')
 20   format(t89,'!',/,t89,'!')
 30   format(' time',t42,1pd15.5,t60,'time',t70,'secs',t89,'!')
 50   format(' total damage dose',t42,1pd15.5,
     1 t60,'totdos',t70,'dpa',t89,'!')
 60   format(' swell',t42,1pd15.5,t60,'swell',t70,'%',t89,'!',/,
     1 ' swelling rate',t42,1pd15.5,t60,'swlrat',t70,'%/dpa',t89,'!')
 70   format(' swell contribution of bubbles',t42,1pd15.5,
     1 t60,'bblswl',t70,'%',t89,'!')
 80   format(' swell contribution of voids',t42,1pd15.5,
     1 t60,'vdswl',t70,'%',t89,'!')
 90   format(' vacancy generation rate',t42,1pd15.5,
     1 t60,'vacgnr',t70,'dpa/sec',t89,'!')
100   format(' intersitial generation rate',t42,1pd15.5,
     1 t60,'intgnr',t70,'dpa/sec',t89,'!')
110   format(' fractional vacancy concentration',t42,1pd15.5,
     1 t60,'vaccon',t70,'-----',t89,'!')
120   format(' fractional interstitial concentration',t42,1pd15.5,
     1 t60,'intcon',t70,'-----',t89,'!')
130   format(' vacancy flux',t42,1pd15.5,t60,
     1 'vflux',t70,'cm**2/sec',t89,'!')
140   format(' interstitial flux',t42,1pd15.5,t60,
     1 'iflux',t70,'cm**2/sec',t89,'!')
150   format(' net vacancy flux (dv*cv-di*ci)',t42,1pd15.5,
     1 t60,'delflx',t70,'cm**2/sec',t89,'!')
```

```
170  format(' cavity emission term',t42,1pd15.5,t60,
    1 'emcav',t70,'-----',t89,'!')
180  format(' saturation term  (vaccon/vaccne)',t42,1pd15.5,
    1 t60,'sat',t70,'-----',t89,'!')
190  format(' supersaturation term',t42,1pd15.5,t60,
    1'sprsat',t70,'-----',t89,'!')
195  format(' vacancy cluster sink strengt!',t42,1pd15.5,t60,
    1'vclsnk',t70,'-----',t89,'!')
200  format(' summation of 4*pi*voidrd*voidcn',t42,1pd15.5,
    1 t60,'cvsnk0',t70,'/cm**2',t89,'!')
210  format(' network dislocation density',t42,1pd15.5,
    1 t60,'disntd',t70,'/cm**2',t89,'!')
212  format(' ','faulted loop dislocation density',t42,
    1 1pd15.5,t60,'displd',t70,'/cm**2',t89,'!')
214  format(' ','total dislocation density',t42,1pd15.5,
    1 t60,'distot',t70,'/cm**2',t89,'!')
216  format(' ','total interstitial loop density',t42,1pd15.5,t60,
    1'numilp',t70,'/cm**3',t89,'!')
218  format(' ','total dislocation to cavity sink ratio',t42,1pd15.5,
    1 t60,'snkrat',t70,'-----',t89,'!')
220  format(' void vacancies lost to recombination =',1pd10.3,
    1 ' (',0pf5.2,'%)',t89,'!')
230  format(' void vacancies lost through emission =',1pd10.3,
    1 ' (',0pf5.2,'%)',t89,'!')
232  format(t89,'!',/,' total vacancies absorbed at voids (tvdvac)=',
    1 1pd10.3,' (#/atom)',t89,'!')
234  format(' surviving vacancy concentration in voids (swlcmp)=',
    1 1pd10.3,' (#/atom)',t89,'!')
240  format(t89,'!',/t89,'!',/t89,'!',/,' Point Defect',9x,
    1 '>> VACANCIES <<',12x,'>> INTERSTITIALS <<',t89,'!',/,4x,'Sinks',
    2 7x,'total abs  percent  ','inst %  total abs  percent  inst %',
    3 t89,'!',/,x,70('-'),t89,'!',/,' bulk recomb.',t14,
    4 2(1pd12.3,0pf8.2,f9.2),t89,'!',/,' voids',t14,
    5 2(1pd12.3,0pf8.2,f9.2),t89,'!',/,' bubbles',t14,
    6 2(1pd12.3,0pf8.2,f9.2),t89,'!',/,' dislocations',t14,
    7 2(1pd12.3,0pf8.2,f9.2),t89,'!',/,' frank loops',t14,
    8 2(1pd12.3,0pf8.2,f9.2),t89,'!',/,' sub grains',t14,
    9 2(1pd12.3,0pf8.2,f9.2),t89,'!',/,' vac. clusters',t14,
    * 2(1pd12.3,0pf8.2,f9.2),t89,'!',/,' precipitates',t14,
    1 2(1pd12.3,0pf8.2,f9.2),t89,'!',/,x,70('-'),t89,'!',/,
    2 ' total',t14,2(1pd12.3,0pf8.2,f9.2),t89,'!')
250  format(t89,'!',/t89,'!',/t89,'!',/,'   void radii',3x,
    1 'void concentration',5x,'dr/dt',9x,'pressure',5x,
    2 '# of helium',t89,'!',/,7x,'(a)',11x,'(/cm**3)',8x,
    3 '(cm/sec)',10x,'(mpa)',5x,'atoms per void',t89,'!',/,t89,'!')
260  format(i2,8pf8.3,4x,1p2d17.5,1pd15.5,0pf12.3,t89,'!')
270  format(t89,'!',/,' 1   means defect is a bubble',t89,'!')
     swell=fcntvv(voidcn,voidrd,fv,nclass)*100.
     bblswl=0.0
     do 300 i=1,nclass
     if(bblflg(i).eq.1) bblswl=bblswl+fv(i)*voidrd(i)**3*
    1  voidcn(i)*100.0
     mpa(i)=press(i)*1.0d-7
300  continue
     vdswl=dmax1(0.0d0,swell-bblswl)
     write(6,5)
     write(6,10)
     write(6,20)
     write(6,30)time
     write(6,50)totdos
     write(6,60) swell,swlrat
     write(6,70)bblswl
     write(6,80)vdswl
     write(6,90)vacgnr
     write(6,100) intgnr
     write(6,110)vaccon
     write(6,120)intcon
     write(6,130) vflux
     write(6,140) iflux
     delflx=vflux-iflux
     write(6,150) delflx
     emcav=embbl+emvoid
     write(6,170) emcav
     sat=vaccon/vaccne
     write(6,180) sat
     write(6,190)sprsat
     write(6,195) vclsnk
     write(6,200) cvsnk0
     write(6,210)disntd
```

```
      write(6,212) dispid
      write(6,214) distot
      write(6,216) numilp
      write(6,218) snkrat
      ppsink=0.d0
      if(pptflg.eq.1) ppsink=pptsnk
      totalv=recomb+voids+bubble+disloc+subgrn+clster+precip+floop
      totali=recomb+intvd+intbbl+intnet+intsbg+intvcl+intppt+intflp
      if(totalv.lt.1.d-6) go to 320
      rt=recomb/totalv*100.
      vt=voids/totalv*100.
      bbt=bubble/totalv*100.
      dt=disloc/totalv*100.
      ft=floop/totalv*100.
      st=subgrn/totalv*100.
      ct=clster/totalv*100.
      prt=precip/totalv*100.
      ttlt=rt+vt+bbt+dt+ft+st+ct+prt
      irt=recomb/totali*100.
      ivt=intvd/totali*100.
      ibbt=intbbl/totali*100.
      idt=intnet/totali*100.
      ift=intflp/totali*100.
      ist=intsbg/totali*100.
      ict=intvcl/totali*100.
      iprt=intppt/totali*100.
      ittlt=irt+ivt+ibbt+idt+ift+ist+ict+iprt
      if(voids.le.1.d-6) go to 302
      write(6,232) tvdvac
      write(6,234) swlcmp
      vdrc=vdrecm/tvdvac*100.
      write(6,220) vdrecm,vdrc
      vdem=vdemit/tvdvac*100.
      write(6,230) vdemit,vdem
302   vi=0.0d0
      bbi=0.0d0
       ivi=0.d0
       ibbi=0.d0
      do 310 i=1,nclass
      tmpvac=fs(i)*voidrd(i)*voidcn(i)*cfacv(i)
      tmpint=fs(i)*voidrd(i)*voidcn(i)*cfaci(i)
      if(bblflg(i) .eq. 1) go to 305
      vi=vi+tmpvac*(vflux-diffv*cvv(i))
      ivi=ivi+tmpint*iflux
      go to 310
305   bbi=bbi+tmpvac*(vflux-diffv*cvv(i))
      ibbi=ibbi+tmpint*iflux
310   continue
      fi=0.d0
      ifi=0.d0
      if(iclflg.ne.1) go to 318
      do 315 i=2,lclass
      ifi=ifi + zil(i)*rhosnk*2.*pi*lprad(i)*lpnum(i)*iflux
315   fi=fi+zvl(i)*rhosnk*2.*pi*lprad(i)*lpnum(i)*(vflux-diffv*cvl(i))
318   si=ksbgv*(vflux-diffv*cvemit)
      pri=ppsink*(vflux-diffv*cvemit)
      ci=vclsnk*(vflux-diffv*cvcls)+intgnr*fracls
      di=zvn*rhosnk*disntd*(vflux-diffv*cvemit)
      ri=alpha*vaccon*intcon
      ttli=ri+vi+bbi+di+fi+si+ci+pri
      isi=ksbgj*iflux
      ipri=ppsink*iflux
      ici=vclsnk*iflux
      idi=zin*rhosnk*disntd*iflux
      iri=alpha*vaccon*intcon
      ittli=iri+ivi+ibbi+idi+ifi+isi+ici+ipri
      ri=ri/ttli*100.0
      vi=vi/ttli*100.0
      bbi=bbi/ttli*100.0
      di=di/ttli*100.0
      fi=fi/ttli*100.0
      si=si/ttli*100.
      ci=ci/ttli*100.
      pri=pri/ttli*100.
      ttli=ri+vi+bbi+di+si+fi+ci+pri
      iri=iri/ittli*100.0
      ivi=ivi/ittli*100.0
      ibbi=ibbi/ittli*100.0
      idi=idi/ittli*100.0
```

```
      ifi=ifi/ittli*100.0
      isi=isi/ittli*100.
      ici=ici/ittli*100.
      ipri=ipri/ittli*100.
      ittli=iri+vi+bbi+di+si+fi+ci+pri
      write(6,240) recomb,rt,ri,recomb,irt,iri,
     1  voids,vt,vi,intvd,ivt,ivi,
     2  bubble,bbt,bbi,intbbl,ibbt,ibbi,
     3  disloc,dt,di,intnet,idt,idi,
     4  floop,ft,fi,intflp,ift,ifi,
     5  subgrn,st,si,intsbg,ist,isi,
     6  clster,ct,ci,intvcl,ict,ici,
     7  precip,prt,pri,intppt,iprt,ipri,
     8  totalv,ttlt,ttli,totali,ittlt,ittli
 320  write(6,250)
      write(6,260)  (bblflg(i),voidrd(i),voidcn(i),dery(i),
     1    mpa(i),helium(i), i=1,nclass )
      write(6,270)
      write(6,5)
      return
      end


ccccccccccccccccccccccccccccccccccccccccccccccccccccccccccccccccccccccc
c                                                                       c
c                              VACCNT                                   c
c                                                                       c
c      subroutine to keep track of where the vacancies are going        c
c         tvdvac=net number of vacancies absorbed by voids              c
c         vdrecm=number void vacancies lost to recombination,           c
c                equals the number of interstitials absorbed            c
c         vdemit=the number of vacancies emitted from voids             c
c         voids=the net vacancy absorbtion at vois                      c
c         bubble,subgrn,disloc,clster,floop,precip analogous to voids   c
c                                                                       c
ccccccccccccccccccccccccccccccccccccccccccccccccccccccccccccccccccccccc
      subroutine vaccnt(timdlt,bblflg,iclflg,lclass,nclass,pptflg,
     1   vdflg)
      implicit real*8 (a-z)
      common /cavprm/ bbconv(5),bbsnk,bbsnk0,cvsnki,cvsnkv,comprs(5),
     1  cfaci(5),cfacv(5),cvsnk0,cvv(5),delhe(5),fs(5),fv(5),gamma(5),
     2  helium(5),mpa(5),ncritr(5),press(5),rhohe(5),
     3  ttconv(5),vdsnk,vdsnk0,voidcn(5),voidrd(5)
      common /disprm/ avlprd,bi1o,bi2o,bv2o,bi3o,bi4o,bv3o,bv4o,
     1  c2dis,c3dis,cvl(45),cvn,dicon,displd,disn0,disntd,distot,
     2  ec2dis,ec3dis,irrann,irrsrc,lpnum(45),lprad(45),ncrate,numilp,
     3  ilpmax,prmt1,prmt2,prmt3,prmt4,rate(45),rc,rhosnk,ro,shrmod,
     4  tauimx,snkerr,snknew,snktst,srcden,stckft,stfeng,tau4,
     5  tetcon,thrann,thrsrc,tricon,zil(45),zil0,zin,zi1,zi2,zi3,zi4,
     6  zvl(45),zvl0,zvn,zv2,zv3,zv4
      common /defprm/ alpha,ao,bvectd,bvectf,cvcls,cvemit,diffi,diffv,
     1  ef,eim,em,fracls,gamvcl,genvcl,intcon,intgn2,intgnr,kt,
     2  numvac,numvcl,omega,radvcl,sprsat,tauvcl,vaccne,vaccon,
     3  vacgnr,vclsnk,cilo,cihi,cvgues,iflux,vflux,delflx
      common /balrl/ appmhe,bubble,cavhe,clster,dery(50),diffhe,
     1  disloc,doschg(10),doschk,ehemig,embbl,emdisl,emflp,emppt,emsubg,
     2  emvcl,emvoid,floop,gasd,graind,grnd0,grnmax,grntau,hefrac,
     7  intbbl,intflp,intnet,intppt,intrec,intsbg,intvcl,intvd,ksbgi,
     3  hegnr0,hegnrr,ksbgv,mtrxhe,ntdhe,pi,pltflg,pptcon,pptrad,
     4  pptsnk,ppttau,precip,prntdt,prntnw,recomb,stop,stress,
     5  subghe,subgrn,swell,swlcmp,swlto1,taup,tauto1,tc(10),temp,
     6  time,tk,totdos,tsinki,tsinkv,tvdvac,vdemit,vdrecm,voids
      integer bblflg(5),vdflg(5),iclflg,lclass,nclass,pptflg,i
      ppsink=0.0d0
      if(pptflg.eq.1) ppsink=pptsnk
      recomb=recomb+alpha*vaccon*intcon*timdlt
      do 175 i=1,nclass
      tmpvac=fs(i)*voidrd(i)*voidcn(i)*cfacv(i)
      tmpint=fs(i)*voidrd(i)*voidcn(i)*cfaci(i)
      voids=voids+tmpvac*(vflux-diffv*cvv(i))*timdlt*vdflg(i)
      intvd=intvd+tmpint*iflux*timdlt*vdflg(i)
      vdrecm=vdrecm+tmpint* iflux*timdlt*vdflg(i)
      vdemit=vdemit+tmpvac*diffv*cvv(i)*timdlt*vdflg(i)
      tvdvac=tvdvac+tmpvac*vflux*timdlt*vdflg(i)
      swlcmp=swlcmp + ( tmpvac*diffv*(vaccon-cvv(i))
     1  tmpint* iflux ) * timdlt*vdflg(i)
      bubble=bubble+tmpvac*(vflux-diffv*cvv(i))*timdlt*bblflg(i)
      intbbl=intbbl+tmpint*iflux*timdlt*bblflg(i)
```

```
 175  continue
      subgrn=subgrn+ksbgv*(vflux-diffv*cvemit)*timdlt
      precip=precip+ppsink*(vflux-diffv*cvemit)*timdlt
      clster=clster +
     1 (vclsnk*(vflux-diffv*cvcls)+intgnr*fracls)*timdlt
      disloc=disloc +
     1 zvn*rhosnk*disntd*(vflux-diffv*cvemit)*timdlt
      intsbg=intsbg+ksbgi*iflux*timdlt
      intppt=intppt+ppsink*iflux*timdlt
      intvcl=intvcl + vclsnk*iflux*timdlt
      intnet=intnet + zin*rhosnk*disntd*iflux*timdlt
      if(iclflg.ne.1) go to 185
      do 180 i=2,lclass
      intflp=intflp + zil(i)*rhosnk*2.*pi*lprad(i)*lpnum(i)*
     1  iflux*timdlt
 180  floop=floop + zvl(i)*rhosnk*2.*pi*lprad(i)*lpnum(i)*
     1  (vflux-diffv*cvl(i))*timdlt
 185  return
      end


ccccccccccccccccccccccccccccccccccccccccccccccccccccccccccccccccccccccccc
c                                                                       c
c                                FCNCVV                                 c
c                                                                       c
c    function to calculate value of cvv, vacancy concentration in       c
c    equilibrium with cavity                                            c
c                                                                       c
ccccccccccccccccccccccccccccccccccccccccccccccccccccccccccccccccccccccccc
      function fcncvv (kt,omega,vaccne,gamma,rvoid,gpress,i)
      implicit real*8 (a-z)
      integer i
      cvvexp=(2.*gamma/rvoid-gpress)*omega/kt
      if(cvvexp.gt.15. .or. cvvexp.lt.-15.) write(6,901) i,cvvexp
      cvvexp=dmax1( -15.d0, dmin1(15.d0,cvvexp) )
      fcncvv=vaccne*dexp(cvvexp)
      return
 901  format(5x,'>>  for i=',i2,' fcncvv exp. term=',1pd11.3,'  <<')
      end


ccccccccccccccccccccccccccccccccccccccccccccccccccccccccccccccccccccccccc
c                                                                       c
c                                FCNLPG                                 c
c                                                                       c
c      function to calculate the loop growth rates                      c
c                                                                       c
c      dedm=change of loop energy w/ respect to loop no. of inter.      c
c      linetn=line tension contribution of loop energy                  c
c      stckft=stacking fault contribution to loop energy                c
c      cvl=equilibrium vacancy concentration at loop suface             c
c                                                                       c
ccccccccccccccccccccccccccccccccccccccccccccccccccccccccccccccccccccccccc
      function fcnlpg(lrad,pi,rhosnk,g,stckft,zin,zvn,zil0,zvl0)
      implicit real*8 (a-z)
      common /defprm/ alpha,ao,bvectd,bvectf,cvcls,cvemit,diffi,diffv,
     1  ef,eim,em,fracls,gamvcl,genvcl,intcon,intgn2,intgnr,kt,
     2  numvac,numvcl,omega,radvcl,sprsat,tauvcl,vaccne,vaccon,
     3  vacgnr,vclsnk,cilo,cihi,cvgues,iflux,vflux,delflx
      zilr=zil0                                                         zil-r
      zvlr=zvl0                                                         zil-r
c     zilr=dmin1(3.5d0, (zin + zil0/lrad**2) )                          zil-r
c     zvlr= zvn + zvl0/lrad**2                                          zil-r
      linetn=g*bvectf*omega/2.8/pi/lrad*dlog(4.d0*lrad/bvectf)
      dedm=dmin1(30.0d0,linetn+stckft)
      cvlr=vaccne*dexp(-dedm/kt)
      fcnlpg=bvectf / rhosnk /
     1  (zilr*diffi*intcon - zvlr*(diffv*vaccon-diffv*cvlr))
      return
      end


ccccccccccccccccccccccccccccccccccccccccccccccccccccccccccccccccccccccccc
c                                                                       c
c                                FCNSNK                                 c
c                                                                       c
```

```
c      function subprogram to calculate summation 4*pi*voidrd          c
c      *voidcn (geometry term of weighted sink)                        c
c                                                                      c
ccccccccccccccccccccccccccccccccccccccccccccccccccccccccccccccccccccccc
      function fcnsnk(voidrd,voidcn,nclass,fs,pi,bblflg,bbsnk0,vdsnk0)
      implicit real*8 (a-z)
      dimension voidrd(1),voidcn(1),fs(1)
      integer bblflg(1), i, nclass
      fcnsnk=0.0d0
      vdsnk0=0.0d0
      bbsnk0=0.0d0
      do 100 i=1,nclass
      tmpsnk=fs(i)*voidrd(i)*voidcn(i)
      if(bblflg(i) .eq. 1) go to 50
      vdsnk0=vdsnk0+tmpsnk
      go to 100
 50   bbsnk0=bbsnk0+tmpsnk
 100  fcnsnk=fcnsnk+tmpsnk
      return
      end


ccccccccccccccccccccccccccccccccccccccccccccccccccccccccccccccccccccccc
c                                                                      c
c                                FCNTVV                                c
c                                                                      c
c         function to calculate total void volume (swell)              c
c                                                                      c
ccccccccccccccccccccccccccccccccccccccccccccccccccccccccccccccccccccccc
      function fcntvv(voidcn,voidrd,fv,nclass)
      implicit real*8 (a-z)
      dimension voidcn(1),voidrd(1),fv(1)
      integer i, nclass
      fcntvv=0.
      do 100 i=1,nclass
100   fcntvv=fcntvv+fv(i)*voidrd(i)**3*voidcn(i)
      return
      end


ccccccccccccccccccccccccccccccccccccccccccccccccccccccccccccccccccccccc
c                                                                      c
c                                FCNVGR                                c
c                                                                      c
c         function to calculate new vacancy generation rate            c
c                                                                      c
ccccccccccccccccccccccccccccccccccccccccccccccccccccccccccccccccccccccc
      function fcnvgr(bblflg,iclflg,lclass,nclass,pptflg,vdflg)
      implicit real*8 (a-z)
      common /cavprm/ bbconv(5),bbsnk,bbsnk0,cvsnki,cvsnkv,comprs(5),
     1  cfaci(5),cfacv(5),cvsnk0,cvv(5),delhe(5),fs(5),fv(5),gamma(5),
     2  helium(5),mpa(5),ncritr(5),press(5),rhohe(5),
     3  ttconv(5),vdsnk,vdsnk0,voidcn(5),voidrd(5)
      common /disprm/ avlprd,bi1o,bi2o,bv2o,bi3o,bi4o,bv3o,bv4o,
     1  c2dis,c3dis,cvl(45),cvn,dicon,displd,disn0,disntd,distot,
     2  ec2dis,ec3dis,irrann,irrsrc,lpnum(45),lprad(45),ncrate,numilp,
     3  ilpmax,prmt1,prmt2,prmt3,prmt4,rate(45),rc,rhosnk,ro,shrmod,
     4  tauimx,snkerr,snknew,snktst,srcden,stckft,stfeng,tau4,
     5  tetcon,thrann,thrsrc,tricon,zil(45),zil0,zin,zi1,zi2,zi3,zi4,
     6  zvl(45),zvl0,zvn,zv2,zv3,zv4
      common /defprm/ alpha,ao,bvectd,bvectf,cvcls,cvemit,diffi,diffv,
     1  ef,eim,em,fracls,gamvcl,genvcl,intcon,intgn2,intgnr,kt,
     2  numvac,numvcl,omega,radvcl,sprsat,tauvcl,vaccne,vaccon,
     3  vacgnr,vclsnk,cilo,cihi,cvgues,iflux,vflux,delflx
      common /balrl/ appmhe,bubble,cavhe,clster,dery(50),diffhe,
     1  disloc,doschg(10),doschk,ehemig,embbl,emdisl,emflp,emppt,emsubg,
     2  emvcl,emvoid,floop,gasd,graind,grnd0,grnmax,grntau,hefrac,
     7  intbbl,intflp,intnet,intppt,intrec,intsbg,intvcl,intvd,ksbgi,
     3  hegnr0,hegnrr,ksbgv,mtrxhe,ntdhe,pi,pltflg,pptcon,pptrad,
     4  pptsnk,ppttau,precip,prntdt,prntnw,recomb,stop,stress,
     5  subghe,subgrn,swell,swlcmp,swlto1,taup,tauto1,tc(10),temp,
     6  time,tk,totdos,tsinki,tsinkv,tvdvac,vdemit,vdrecm,voids
      integer bblflg(5),vdflg(5),iclflg,lclass,nclass,pptflg,i
      embbl=0.
      emvoid=0.
      emflp=0.0
      ppsink=0.0d0
```

```
      if(pptflg.eq.1) ppsink=pptsnk
      emdisl=zvn*rhosnk*disntd*diffv*cvemit
      emppt=ppsink*diffv*cvemit
      emsubg=ksbgv*diffv*cvemit
      emvcl=vclsnk*diffv*cvcls
      if(iclflg.ne.1) go to 80
      do 50 i=2,lclass
      emflp=emflp +
     1 zvl(i)*rhosnk*2.*pi*lprad(i)*lpnum(i)*diffv*cvl(i)
 50   continue
 80   do 100 i=1,nclass
      tmpvac=fs(i)*voidrd(i)*voidcn(i)*cfacv(i)
      emvoid=emvoid + tmpvac*diffv*cvv(i)*vdflg(i)
      embbl=embbl + tmpvac*diffv*cvv(i)*bblflg(i)
100   continue
      fcnvgr=intgnr*(1.d0-fracls)
     1  + (emdisl+emppt+emsubg+embbl+emvoid+emvcl+emflp)
      return
      end


ccccccccccccccccccccccccccccccccccccccccccccccccccccccccccccccccccccccc
c                                                                       c
c                                DUMSUB                                 c
c                                                                       c
c     a dummy subroutine for dlsode, see documentation                  c
c                                                                       c
ccccccccccccccccccccccccccccccccccccccccccccccccccccccccccccccccccccccc
      subroutine dumsub(neq, t, y, ml, mu, pd, nrowpd)
      implicit real*8 (a-z)
      integer neq,nrowpd,ml,mu
      dimension y(neq),pd(nrowpd,neq)
      return
      end
```

A.2 Sample Data File for MICROEV

See the Introduction to this Appendix and the comments in the MICROEV source listing for an explanation of the input parameters.

```
      1
data file for MICROEV, 100 dpa irradiation at 500 C
base case parmeters, January 1987
     1.400       1.600       0.850       1.350       1.750       2.500
      .800       .0800    2.00e+17    3.50e-13        0.50
  1.00e-06      0.3333        1.25        1.00       1.500       1.000
     500.0    3.00e+11         0.0        15.0        2.00
     0.600    1.00e+01    8.00e-08   0.800e+00    2.00e-03
1.3291e-07    2.00e+15       1.773       1.000      0.3545       0.050
  1.00e-04    1.00e-09    1.00e+09    1.00e+08    1.00e+14
    63.0        90.0       110.0       127.0        33.0        38.0        42.0
  1.00e-05   3.183e+14    3.20e+07          ppt. radius, conc, time
  1.00e-04    1.00e-04    1.00e+08          subgrain diameter
  1.00e+08    2.50e+07    1.00e+04    1.00e+01    1.00e+04    1.00e+04
         0          22           0       10000           0
         1          16           8           2          -1
  2.28e+15    2.53e+14                       void densities line
     1.000       0.400                       fv line
     1.000       0.434                       fs line
 0.800e+00   0.800e+00                       gamma line
      2.00        2.00                       helium line
```

A.3 Partial Results from Sample MICROEV Run

These results are printed at the end of each run. More detailed output is printed at intermediate doses as requested by the input parameter "prntdt" on the thirteenth line of the input data set. Additional output includes an echo of the input data set, a table of calculated material and irradiation parameters for the current data set (see the subroutine CONST), a table of selected variables that is printed when a size class of bubbles converts to voids (see the subroutine TABLE) and line-printer plots of dose versus swelling, Frank faulted loop number density, and the network and total dislocation densities (see the subroutine PLOT).

```
For cavity size class 1: bubbles did not convert to voids.
For cavity size class 2:
     bubble-to void-conversion dose = 36.1 dpa,
     bubble radius at conversion = 1.274 nm.

Approximate dose to 1% swelling = 44.1 dpa.

Maximum swelling rate = 1.365d+00 %/dpa at 99.7 dpa.

Maximum faulted loop density = 1.318e+20 at 68.0 dpa.
```

dose (dpa)	swelling (%)	network dislocation density (/m**2)	faulted loop density (/m**3)
0.	0.00e+00	3.00e+15	0.00e+00
10.00	3.37e-04	6.36e+14	9.96e+19
20.00	7.39e-04	6.31e+14	1.01e+20
30.00	1.22e-03	6.28e+14	1.01e+20
40.00	4.19e-01	5.89e+14	1.10e+20
50.00	4.82e+00	5.24e+14	1.23e+20
60.00	1.30e+01	4.71e+14	1.31e+20
70.00	2.38e+01	4.36e+14	1.32e+20
80.00	3.61e+01	4.09e+14	1.29e+20
90.00	4.91e+01	3.90e+14	1.27e+20
100.00	6.25e+01	3.73e+14	1.23e+20

ORNL-6430
Dist. Category UC-25

INTERNAL DISTRIBUTION

1–2. Central Research Library
3. Document Reference Section
4–5. Laboratory Records Department
6. Laboratory Records, ORNL RC
7. ORNL Patent Section
8. J. Bentley
9. T. M. Besmann
10. E. E. Bloom
11. R. A. Buhl
12. R. R. Coltman
13. G. L. Copeland
14. D. F. Craig
15. K. Farrell
16. M. L. Grossbeck
17. F. M. Haggag
18. P. N. Haubenreich
19. J. A. Horak
20. T. J. Huxford
21. E. A. Kenik
22. O. F. Kimball
23. R. L. Klueh
24. E. H. Lee
25. L. K. Mansur
26. P. J. Maziasz
27. M. K. Miller
28. N. H. Packan
29. D. F. Pedraza
30. A. F. Rowcliffe
31. M. J. Saltmarsh
32. M. A. Schmidt
33. T. E. Shannon
34. J. Sheffield
35. J. H. Smith
36. J. O. Stiegler
37-41. R. E. Stoller
42–44. P. T. Thornton
45. F. W. Wiffen
46. F. W. Young
47. S. J. Zinkle
48. H. D. Brody (Consultant)
49. G. Y. Chin (Consultant)
50. F. F. Lange (Consultant)
51. W. D. Nix (Consultant)
52. D. P. Pope (Consultant)
53. E. R. Thompson (Consultant)

EXTERNAL DISTRIBUTION

54–58. AERE HARWELL, Oxfordshire, OX11, ORA, United Kingdom

R. Bullough
M. R. Hayns
J. R. Matthews
S. M. Murphy
T. Williams

59–60. ARGONNE NATIONAL LABORATORY, 9700 S. Cass Avenue, Argonne, IL 60439

B. Loomis
R. Mattas

61. ARIZONA STATE UNIVERSITY, Department of Mechanical and Aerospace Engineering, Tempe, AZ 85281

W. A. Coghlan

62. AUBURN UNIVERSITY, Department of Mechanical Engineering, Auburn, AL 36849

B. A. Chin

63-68. BATTELLE PACIFIC NORTHWEST LABORATORY, P.O. Box 999, Richland, WA 99352

H. R. Brager
D. G. Doran
F. A. Garner
D. S. Gelles
H. L. Heinisch
C. H. Henager

69-73. CENTRE d'ETUDE NUCLEAIRES de SACLAY, B.P. No. 2, 91190, Gif-sur-yvette, France

L. Le Naour
V. Levy
G. Martin
A. Terlain
V. Vouillon

74. C.E.C. — Joint Research Centre, Materials Science Division, 21020 – ISPRA (Varese) Italy

P. Schiller

75. CULHAM LABORATORY, U.K.A.E.A., Abingdon, Oxon OX14 3DB, United Kingdom

J. Butterworth

76. ECN PETTEN, Materials Department, P.O. Box 1, 1755 ZG Petten, The Netherlands

W. Von Witzenburg

77. FORD MOTOR CO., 21500 Oakwood Ave., P.O. Box 2053, Dearborn, MI 48121

A. D. Brailsford

78. GA TECHNOLOGIES, INC., P.O. Box 81608, San Diego, CA 92138

T. A. Lechtenberg

79. GENERAL DYNAMICS/CONVAIR, Mail Zone 43-6320, P.O. Box 85357, San Diego, CA 92138

H. Gurol

80. HOKKAIDO UNIVERSITY, Faculty of Engineering, Kita 13 nishi 8, Kitaku, Sapporo 060, Japan

A. Okada

81-82. IFF, Kernforschungsanlage, Postfach 1913, D-5170 Jülich 1, F.R. Germany

H. Trinkaus
H. Ullmaier

83. INSTITUT FÜR MATERIAL — UND FESTKÖRPERFORSCHUNG, Kernforschungszentrum Karlsruhe, D-7500 Karlsruhe, F.R. Germany

K. Ehrlich

84. IPP NAGOYA UNIVERSITY, Department of Nuclear Engineering, Chikusa-ku Furocho, Nagoya, 464, Japan

M. Kiritani

85–86. J.A.E.R.I., Nuclear Fuel Research Division, Tokai-mura, Naka-gun 319–11, Ibaraki-ken, Japan

A. Hishinuma
M. P. Tanaka

87–88. KYUSHU UNIVERSITY, Research Institute of Applied Mechanics, Hokozaki, Fukuoka, 812, Japan

K. Kitajima
T. Muroga

89. McDONNELL DOUGLAS ASTRONAUTICS COMPANY, EAST, P.O. Box 516, St. Louis, MO 63166

J. W. Davis

90. NATIONAL RESEARCH INSTITUTE FOR METALS, Tsukuba, Japan

H. Shiraishi

91. OAK RIDGE ASSOCIATED UNIVERSITIES, University Programs Division, P.O. Box 117, Oak Ridge, TN 37831–0117

Billie Stooksbury

92. POWER REACTOR AND NUCLEAR FUEL DEVELOPMENT CORP., O–ARA1 Engineering Center, 4002, Oraria, Ibarage, Japan

M. Ito

93. RISO NATIONAL LABORATORY, Metallurgy Department, DK 4000, Roskilde, Denmark

B. N. Singh

94. SANDIA NATIONAL LABORATORIES, P.O. Box 5800, Albuquerque, NM 87185

W. Beezhold

95. SANDIA NATIONAL LABORATORIES, Livermore Division 8316, Livermore, CA 94550

W. Wolfer

96. SAMFORD UNIVERSITY, 800 Lakeshore Drive, Birmingham, AL 35229

J. Trang

97. SCIENCE UNIVERSITY OF TOKYO, Faculty of Engineering, Kagurazaka, Shinjuku-ku, tokyo, 162, Japan

R. R. Hasiguti

98. TOHOKU UNIVERSITY, Institute for Materials Research, 2-1-1 Katahira, Sendai 980, Japan

H. Matsui

99-100. UNIVERSITY OF CALIFORNIA, 5532 Boelter Hall, Los Angeles, CA 90024

R. W. Conn
N. Ghoniem

101-102. UNIVERSITY OF CALIFORNIA, Department of Chemical and Nuclear Engineering, Santa Barbara, CA 93106

G. E. Lucas
G. R. Odette

103. UNIVERSITY OF MISSOURI, Nuclear Engineering, Rolla, MO 65401

A. Kumar

104. UNIVERSITY OF TOKYO, Engineering Research Institute, Bunko-ku, Tokyo, 113, Japan

S. Ishino

105-106. UNIVERSITY OF TOKYO, Materials Science Department, Bunko-ku, Tokyo, 113, Japan

N. Igata
A. Kohyama

107. UNIVERSITY OF WISCONSIN, Nuclear Engineering Department, Madison, WI 53706

G. L. Kulcinski

108. WESTINGHOUSE ELECTRIC CORP., Advanced Energy Systems Division, P.O. Box 10864, Pittsburgh, PA 15236

R. Bajaj

109. WESTINGHOUSE RESEARCH LABORATORY, 1310 Beulah Road, Churchill Boro, Pittsburgh, PA 15235

J. A. Spitznagel

110-113. DOE, OFFICE OF FUSION ENERGY, Reactor Technologies Branch, MS G-234 (GTN), Washington, DC 20545

J. F. Clarke
M. M. Cohen
R. E. Nygren
T. C. Reuther

114. DOE, OAK RIDGE OPERATIONS OFFICE, P.O. Box E, Oak Ridge, TN 37831

Office of Assistant Manager for Energy Research and Development

115-241. DOE, TECHNICAL INFORMATION CENTER, Office of Information Services, P.O. Box 62, Oak Ridge, TN 37831

For distribution as shown in DOE/TIC-4500, Distribution Category UC-25 (MFE - Reactor Materials)

☆U.S. GOVERNMENT PRINTING OFFICE 1988—548-118/60142